

PERI-OPERATIVE DIGITAL PLANNING IN ROBOT-ASSISTED PARTIAL NEPHRECTOMY

Bridging the Gap between
Artificial Intelligence,
Augmented Reality
and Surgical Data Science

PIETER
DE BACKER



**Peri-operative Digital Planning in Robot-Assisted Partial Nephrectomy:
Bridging the Gap between
Artificial Intelligence, Augmented Reality and Surgical Data Science**

Pieter De Backer


Thesis submitted to fulfil the requirements for the degree of
Doctor of Health Sciences and of Biomedical Engineering

Academic year 2023-2024

Promotors: Prof. Dr. K. Decaestecker, Prof. dr. ir. C. Debbaut, Prof. Dr. A. Mottrie



Voor mijn mama, papa en zus

Voor Tine, Suzan en 

© copyright by Pieter De Backer, 2023, Belgium.

All rights reserved. No part of this publication may be produced or transmitted in any form or by any other means, electronic or mechanical, including photocopying, recording or by any other information storage and retrieval system, without written permission of the author. Please treat these results as confidential and do not perform any actions that may obstruct patent approval or publication.

Peri-operative Digital Planning in Robot-Assisted Partial Nephrectomy: Bridging the Gap between A.I., A.R. and Surgical Data Science

Doctoral school: Doctoral School of Life Sciences and Medicine

Academic year: 2023-2024

Author: Pieter De Backer

Funding: Vlaams Agentschap voor Innovatie en Ondernemen (VLAIO)
Baekeland mandate

Affiliations: Urology Department, Ghent University Hospital
Department of Human Structure and Repair
Faculty of Medicine and Health Sciences
Ghent University, Belgium

 Institute of Biomedical Engineering and Technology (IBiTech)
 Biophysical Models for Medical Applications (BioMMedA)
 Department of Electronics and Information Systems
 Faculty of Engineering and Architecture
 Ghent University, Belgium

 Orsi Academy – Orsi Innotech
 Training institute for Minimal Invasive Surgery
 Melle, Belgium

Promotors:

PROF. DR. KAREL DECAESTECKER

Ghent University, Faculty of Medicine and Health Sciences,
Department of Human Structure and Repair, Belgium

AZ Maria Middelaes Ghent, Department of Urology, Belgium

PROF. DR. IR. CHARLOTTE DEBBAUT

Ghent University, Faculty of Engineering and Architecture,
Department of Electronics and Information Systems, Belgium

PROF. DR. ALEXANDRE MOTTRIE

OLV Hospital Aalst, Department of Urology, Belgium

CEO Orsi Academy, Melle, Belgium

Ghent University, Faculty of Medicine and Health Sciences,
Department of Human Structure and Repair, Belgium

Examination board

Chair

PROF. DR. DANIEL DE WOLF

Ghent University, Faculty of Medicine and Health Sciences, Department of Internal Medicine and Pediatrics

Ghent University Hospital, Department of Pediatrics, Belgium

Secretary

PROF. DR. ISABELLE VAN HERZEELE

Ghent University, Faculty of Medicine and Health Sciences, Department of Human Structure and Repair

Ghent University Hospital, Department of Thoracic and Vascular Surgery, Belgium

Reading Committee

PROF. DR. WESLEY DE NEVE

Ghent University, Faculty of Engineering and Architecture, Department of Electronics and Information Systems – IDLab, Belgium

Center for Biosystems and Biotech Data Science, Department of Environmental Technology, Food Technology and Molecular Biotechnology, Ghent University Global Campus, Korea

PROF. DR. PIETER DE VISSCHERE

Ghent University, Faculty of Medicine and Health Sciences, Department of Diagnostic Sciences, Belgium

Ghent University Hospital, Department of Radiology, Belgium

PROF. DR. IR. JOS VANDER SLOTEN

KU Leuven, Faculty of Engineering Science, Department of Mechanical Engineering
Faculty of Engineering Science, Belgium

PROF. DR. TEODOR GRANTCHAROV

Stanford University, Department of General Surgery, California, USA

PROF. DR. ALBERTO BREDÀ

Fundació Puigvert, Oncology Urology Unit and Kidney Transplant Unit, Barcelona, Spain

Ooit was de wereld plat

De geschiedenis van kennis
druipt van generatie op generatie
erodeert in de geest van tijd een voortschrijdend inzicht
een overlevering in conventies
huist semantiek in nuance en detail
gevoelig aan mens, cultuur en natuur

In het immer uitdijende rijk der waarheid
waar elke ontdekking nieuwe vragen stelt
zet de mens een stap dichterbij zijn beperktheid
en afhankelijkheid van nieuwe technologieën

Met onze gedachten in machines
zetten we rase schreden voorwaarts
gaat de reis naar wijsheid exponentieel
varen we steeds verder in het heelal
printen we nier en hart op maat
snijden we extra adem in onze levensduur

Desalniettemin hebben we spatie nodig voor kritische reflectie
om te doorstrepen, schaven en herschrijven
Laten we het externaliseren van onze gedachten
niet ons denkend vermogen vervangen
Laten we het kunstmatig beslissingsmodel
onze verantwoordelijkheid niet ondermijnen

Als een man die op een ladder de wolken meet
is de waarheid van vandaag
niet die van morgen

Een manifest voor humane intelligentie
Een oproep voor trage wetenschap
Een ode aan de mens

MR.

Table of Contents

Abbreviations	15
1. Preface	19
1.1. Context	21
1.2. Objectives	22
1.3. Outline	23
2. Introduction	27
2.1. Renal Anatomy and its History	29
2.2. Renal Physiology	31
2.3. Embryology	33
2.4. Surgical Renal Anatomy	33
2.4.1. Renal Anatomical Relationships	33
2.4.2. Arterial System.....	36
2.4.3. Venous System	39
2.4.4. Renal Collecting System and Ureter.....	42
2.5. Robot Assisted Partial Nephrectomy	43
2.5.1. Nephron Sparing Robotic Surgery	43
2.5.2. Trifecta in RAPN.....	44
2.5.3. Radiologic Assessment and Preoperative 3D Planning.....	45
2.5.4. Intra and Post-operative Outcomes Using 3D Models.....	52
2.5.5. RAPN Surgical Steps	53
2.5.6. Hilar control – Minimizing Healthy Tissue Ischemia.....	57
2.5.7. Tumor Resection – Minimal Healthy Tissue Resection.....	62
2.6. State-of-the-art in Augmented Reality Surgery	64
3. Nephron Sparing Surgery	67
3.1. Preoperative Prediction of Selective Arterial Clamping Strategy	69
3.1.1. Abstract	69
3.1.2. Introduction	70
3.1.3. Materials and Methods.....	71
3.1.4. Results	75
3.1.5. Discussion.....	81
3.1.6. Conclusions.....	82
3.2. Maximization of Nephron Sparing Surgery through Intra-arterial Cooling 83	
3.2.1. Abstract	83
3.2.2. Introduction	84
3.2.3. Design, Setting and Participants.....	85
3.2.4. Surgical Procedure.....	85
3.2.5. Results and Limitations	90
3.2.6. Conclusions.....	93

4. AI-Assisted Video Analysis	95
4.1. Privacy Proof Video Sharing	97
4.1.1. Introduction	97
4.1.2. Materials and Methods.....	98
4.1.3. Results	104
4.1.4. Discussion.....	108
4.1.5. Data Availability.....	110
4.1.6. Supplemental Digital Content	110
4.2. Data annotation	121
4.2.1. Abstract	121
4.2.2. Introduction	122
4.2.3. Materials and Methods.....	125
4.2.4. Results	131
4.2.5. Discussion.....	138
4.2.6. Supplemental Digital Content	141
4.3. Dataset Description and Open Sourcing	153
4.3.1. Abstract	153
4.3.2. Background & Summary	153
4.3.3. Methods	154
4.3.4. Data Records	159
4.3.5. Technical Validation	159
4.3.6. Usage Notes.....	160
4.3.7. Code Availability	160
5. 3D & A.I. Integration	163
5.1. Feasibility of Instrument De-occlusion in A.R. Guided Robotic Surgery 165	
5.1.1. Abstract	165
5.1.2. Case Series.....	166
5.1.3. Discussion.....	172
5.2. Realtime Implementation of Instrument De-occlusion through Dedicated Hardware Setup	173
5.2.1. Abstract	173
5.2.2. Introduction	173
5.2.3. Materials and Methods	174
5.2.4. Results	177
5.2.5. Conclusion and Future Work.....	181
5.2.6. Data Availability.....	182
6. Beyond 3D Models: Surgical Data Science	185
6.1. Instrument Segmentation as an Enabler for Surgical Data Science	187
6.1.1. Introduction	187
6.1.2. Materials and Methods.....	188
6.1.3. Results	190
6.1.4. Conclusion	191
6.2. Clinical value exploration of phase durations in RAPN	193
6.2.1. Abstract	193
6.2.2. Introduction	194
6.2.3. Materials and Methods.....	195

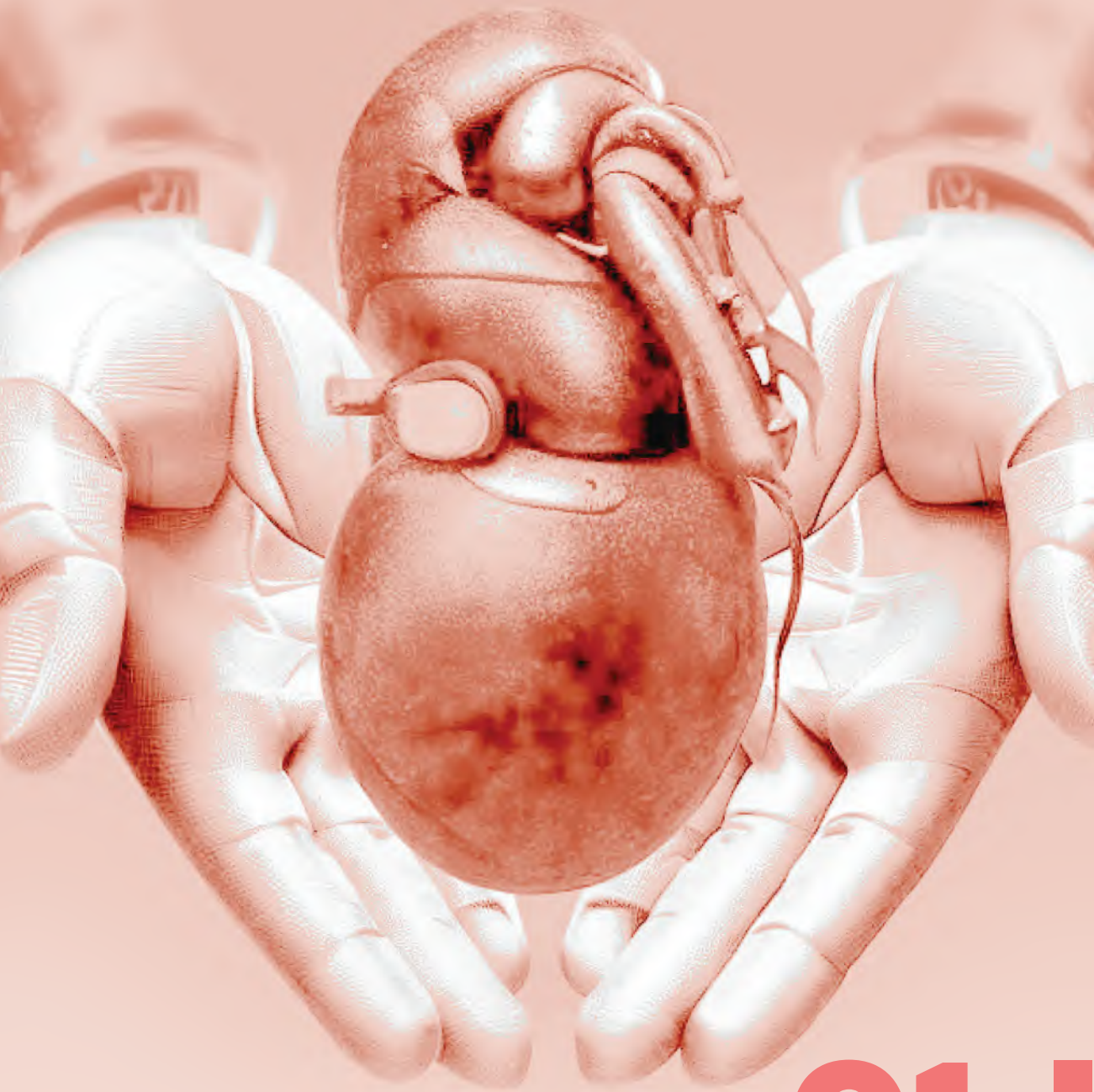
6.2.4. Results	199
6.2.5. Discussion.....	204
6.2.6. Conclusions.....	205
6.2.7. Supplemental Digital Content	206
7. Discussion and Future Perspectives	211
7.1. Pre-operative Virtual 3D Models	213
7.1.1. Steps Taken.....	213
7.1.2. Future Work.....	214
7.2. Augmented Reality	215
7.2.1. Steps Taken.....	215
7.2.2. Future Work.....	216
7.3. Surgical Phase Recognition	218
7.3.1. Steps Taken.....	218
7.3.2. Future Work.....	218
7.4. Surgical Data Science & Surgical Fingerprints	220
7.4.1. Steps Taken.....	220
7.4.2. Future Work.....	221
7.5. Closure	223
8. Summary	225
9. Samenvatting	227
10. References	231
Acknowledgments.....	251
Curriculum Vitae.....	259
Publications.....	267
PhD Related First Author Articles.....	267
Published.....	267
Under revision	268
PhD Related Patent Filed.....	268
Other Articles (First and Co-author)	275
First Author Abstracts.....	277
Co-Authored Abstracts	279
Posters	281
Book Chapters	282

Abbreviations

2D	Two-Dimensional
3D	Three-Dimensional
A.I.	Artificial Intelligence
A.R.	Augmented Reality
CAI	Computer-Assisted Intervention
ccRCC	clear cell Renal Cell Carcinoma
CKD	Chronic Kidney Disease
CLOCK	CLamp vs Off Clamp Kidney
CT	Computed Tomography
CRISP-DM	CRoss-Industry Standard Process for Data Mining
DV3+	DeepLabV3+
EAU	European Association of Urology
(e)GFR	estimated Glomerular Filtration Rate
ERUS	European Association of Urology Robotic Urology Section
EV2	EfficientNetV2-S
FCNs	Fully Convolutional Networks
FLOPs	Floating Point Operations
FN	False Negative
FP	False Positive
FP	Floating Point
FPN	Feature Pyramid Network
fps	frames per second
GDPR	General Data Protection Regulation
GV	Gonadal Vein
HU	Hounsfield Unit
IAC	Intra-Arterial Cooling
ICG	Indocyanine Green
IoU	Intersection over Union
IQR	InterQuartile Range
IVC	Inferior Vena Cava
LRV	Left Renal Vein

LV	Lumbar Vein
MAC	Multiple Accumulate operations
MDCTa	Multidetector CT angiography
MNM	MixNet-M
MRI	Magnetic Resonance Imaging
MV2	MobileNet-V2
NeRFs	Neural Radiance Fields
NPV	Negative Predictive Value
NSS	Nephron-Sparing Surgery
Orsi-RAPNI	Orsi-Robot-Assisted Partial Nephrectomy Instruments dataset
PN	Partial Nephrectomy
PNSA	Progressively Normalized Self-Attention
RA	Robot-assisted
RALM	Robot-assisted Liver Metastasectomy
RAMIE	Robot-assisted Minimal Invasive Esophagectomy
RAPN	Robot-assisted Partial Nephrectomy
RARC	Robot-assisted Radical Cystectomy
RARHC	Robot-assisted Right Hemicolectomy
RARP	Robot-assisted Radical Prostatectomy
RAS	Robot-assisted Surgery
RCC	Renal Cell Carcinoma
RCT	Randomized Controlled Trial
ROBODEN	ROBotic Out-of-body DEtector Network
ROC AUC	Receiver Operating Characteristic Area Under the Curve
RRV	Right Renal Vein
SDI	Serial Digital Interface
SDS	Surgical Data Science
SIB	Surface-Intermediate-Base
STL	Standard Triangle Language
TE	Tumor Enucleation
tiRAKAT	total intracorporeal Robot-Assisted Kidney AutoTransplantation

US	UltraSound
VR	Virtual Reality
VTK	Visualization Toolkit
WIT	Warm Ischemia Time



PREFACE

01 |

*“If I had asked people they wanted,
they would have said faster horses”*

- Henry Ford

1. Preface

1.1. Context

Although Artificial Intelligence (A.I.) is prevalent in our daily lives, ranging from email filtering to automated driving, medicine is rightfully one of the more conservative disciplines in adapting to such a revolutionary technology. The consequence of wrongly filtered email is indeed fundamentally different than that of misdiagnosing a medical condition. As often with disruptive technology, it is reasonable to understand why many are not able to see the bigger picture how A.I. has the power to interconnect multiple aspects of our daily lives. This also counts for surgery, which makes some surgeons renounce or even fear progress made in this field.

As such, Henry Ford's quote, as mentioned on the front page, particularly struck me, and flashed through my mind several times throughout the last 6 years. One particular and recurring example is the following. Whilst starting this research and presenting about the need for A.I. assisted instrument detection, I repeatedly received the following comment: "Why do we need to detect instruments? We know what they are!"

I hope this thesis will help the reader to better connect some of the dots in the blooming and exciting time that lies ahead for artificial intelligence in surgery. Likewise, it might serve as an eyeopener for clinicians and surgeons to collaborate more closely as well as provide an understanding why seemingly simple tasks such as data collection can be more time-consuming and bothersome than expected. For engineers, I hope this dissertation can show that working on small but clinically relevant problems, can be equally exciting as solving large futuristic surgical problems with technologies that are not readily used in operating rooms as of today.

Although our society has faced major A.I.-related revolutions throughout the last year with chat-GPT [1] as an intelligent text writer, or DALL-E [2] as the painter of several chapter covers, a challenging, long but interesting path lies ahead. Just recently, the European Parliament adopted its negotiation position on the A.I. Act [3], to establish rules that safeguard good A.I. practices. For surgical A.I., it is only through collaboration and building bridges between engineering and surgery that the surgical society will make this progress happen in a responsible and ethical way.

Even more important than the technological push, is the clinically driven need for new innovations. As such, one group is paramount and should constantly be on top of mind when innovating: i.e. the patients. Technology should serve them for the better and should be driven by clinical demand. It is the patient who always deserves the best possible care.

In case of surgery, the best possible care entails prevention of adverse events. These adverse events remain a worldwide cause of morbidity and mortality, of which 50% could potentially be prevented [4]. When specifically looking at these errors, 50% of these preventable errors are due to underdeveloped pre-, intra-, or post-operative performance [5]. Furthermore, robust and systemic approaches to patient safety might mitigate these surgical errors by at least 50% [6]. As such, this work aims to leverage A.I. and digital technology to improve the pre-, intra- and post-operative surgical course through the development and validation of objective algorithms.

1.2. Objectives

This PhD thesis investigates how digital applications can help the surgeon plan the surgery, improve the intra-operative guidance through A.I. and Augmented Reality (A.R.), and finally how A.I. can help in post-operative case analysis. Although the general principles apply across all of surgery, the specific procedure under investigation is robot assisted-partial nephrectomy (RAPN). In this procedure, the surgeon removes a tumoral mass from the kidney through the assistance of a robotic device whilst maximally sparing healthy renal tissue.

The objective of the thesis is providing insights into the peri-operative planning of RAPN. As such, the objective can be split up in 3 major blocks:

1. The development and validation of a **pre-operative** algorithm and pipeline to plan selective clamping for partial nephrectomy through mathematical modeling.
2. Enabling **intra-operative** 3D model information fusion (A.R.) by leveraging A.I. technology
3. **Post-operative** video evaluation, which lays the foundation for automated and objective skill and quality assessment.

As A.I. applications require significant data collection and data processing, we also share the necessary technological enablers and lessons learned along the way to build, process, analyze and subsequently share datasets.

1.3. Outline

Figure 1.1 provides an overview of the PhD. The top row depicts the peri-operative RAPN digital planning, split up according to the 3 major blocks above. The procedural digitization is possible thanks to foundational work of technological enablers, depicted inside the orange box.

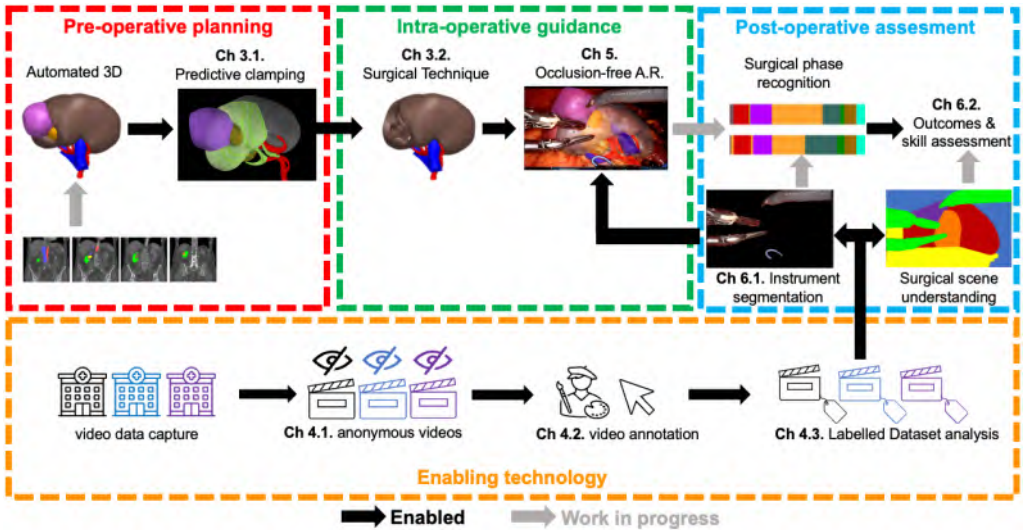


Figure 1.1: Overview of PhD work packages and their respective chapters (Ch). We differentiate between the clinical pipeline (red – green – blue), and prerequisite technological foundations in orange. Black arrows depict processes which have been implemented and published. Grey arrows depict work in progress, as discussed in the outlook and future work chapter.

As partial nephrectomy is a challenging procedure with plenty of pitfalls, the next chapter (Chapter 2) firstly provides an in-depth overview of renal anatomy and physiology as well as its implications for renal surgery. Subsequently, it elaborates on how 3D and A.I. technology is being used at present to help prevent surgical pitfalls.

Chapter 3 provides more detail on how nephron sparing surgery can be maximally optimized. We describe the results of pre-operative digital planning with a novel algorithm developed and validated throughout this PhD thesis. Next, we elaborate on a novel surgical technique using intra-arterial cooling to maximize healthy tissue preservation when the proposed algorithmic approach is less suitable but nephron sparing is still imperative.

Whilst chapter 3 elaborates on 3D technology for pre-operative surgical planning and surgical techniques, 3D visualization often remains a standalone entity in the operating room. This implies that 3D models are often viewed on distinct monitors such as laptops, tablets or a separate screen inside the robotic view. One of the major bottlenecks for endoscopic image enhancement by e.g., 3D models, is an automated and thorough understanding of the surgical scene. To address this bottleneck, we investigated A.I. assisted surgical video analysis to facilitate automated surgical video interpretation. Robotic surgery is the ideal substrate for automated analysis and subsequent surgical automatization. Nevertheless, the challenges to be tackled at present are far more fundamental than surgical automatization. A recurring quote in data science and A.I. is “data is the new oil”. A nuance to be made here is that *structured* data is probably the

new oil. Structured data typically refers to tabular, ready-to-use data. Surgical videos, just as natural language, are examples of *unstructured* data. This implies that, not purely correct data collection as such, but the addition of correct and consistent labels describing this data is what adds real value.

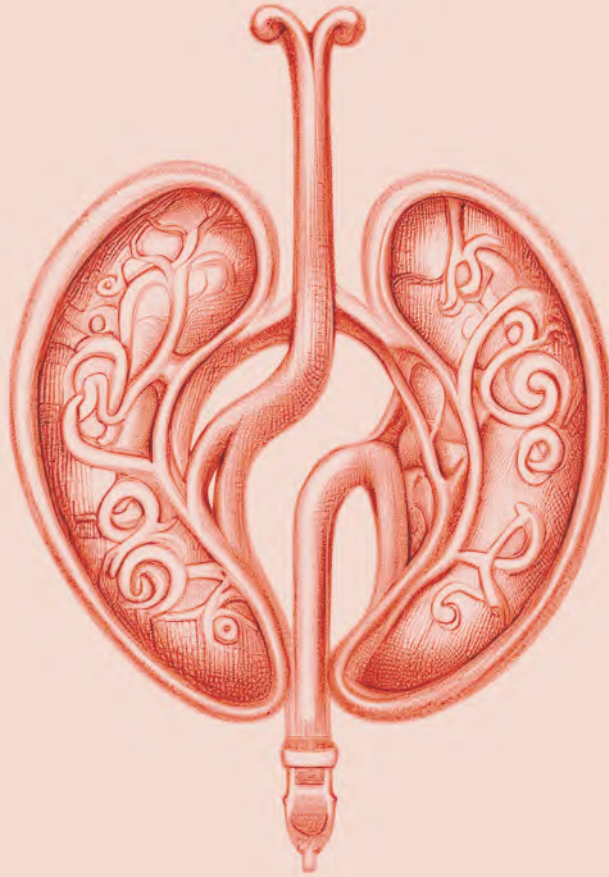
Chapter 4 firstly deals with surgical video collection in the era of General Data Protection Regulation (GDPR) and the need for intra-operative anonymization. More precisely, we describe the need for detecting video sequences when the endoscopic camera is not positioned inside the abdominal cavity, and subsequently remove them from our dataset. Secondly, we share our lessons learned whilst building a robotic surgery dataset for automated instrument segmentation. The essence of surgery is the interaction of instruments with tissue. Hence, we initially focused on surgical instrument delineation or 'segmentation' throughout the surgical scene. Thirdly, we share our newly build state-of-the-art dataset with the surgical A.I. community. As it is of unseen public magnitude on both image count and number of instruments delineated, we hope it can help break down several barriers which hinder current surgical A.I. developments.

Given sufficient annotated data, chapter 5 focuses on how 3D models can now be more efficiently integrated into the operative workflow using A.I. instrument segmentation. We present our case series in which we improve current state-of-the-art Augmented Reality (A.R.) applications by solving the problem of instrument occlusion caused by superimposed 3D models. Nevertheless, as identified during these cases, computational loads limit the usability. This computational problem was subsequently solved through the design of a dedicated computer pipeline and tested during real-time surgery. In the second part of this chapter, we report on the first real-time A.I. assisted instrument delineation cases during A.R. surgery.

Chapter 6 reaches beyond 3D models and evaluates other potential applications of A.I. assisted video analysis. As stated above, tool-tissue interaction is at the heart of surgery. Hence, our next effort focuses not only on delineating surgical instruments but also discerning between them, keeping in mind low computational requirements. As surgical instruments perform surgical actions, robust and real-time instrument segmentation paves the way for automated surgical skill assessment and a plethora of other applications. We describe our initial findings in instrument segmentation on our newly built dataset.

Apart from tool-tissue interaction, surgical skill and potential errors are very dependent on the surgical phase. As such, the second part of chapter 6 elaborates on how a dataset can be built which firstly assess surgical phase durations and subsequently explores its relevance for clinical outcomes.

The last chapter (Chapter 7) provides an outlook of ongoing research and challenges, depicted by the grey arrows in Figure 1.1. It provides preliminary results on automated 3D model development, automated surgical phase detection and automated surgical scene understanding. All three of them are once more enabled by A.I.



INTRODUCTION

02

*“There is nothing more difficult to take in hand,
more perilous to conduct, or more uncertain in its success,
than to take the lead in the introduction of a new order of things”*

- Niccolo Machiavelli

This chapter was partially rewritten and updated from following prior work:

- Robotic Urologic Surgery, 2022, edited by Peter Wiklund, Alexandre Mottrie, Mohan S Gundeti, Vipul Patel.
Chapter 31. Renal anatomy, physiology and its clinical relevance to renal surgery.
*Ruben De Groot, Chandru Sundaram, **Pieter De Backer***
Pieter De Backer was the main author.
- Robotic Surgery for Renal Cancer, 2022, edited by Sanchia S. Goonewardene, Raj Pershad, David Albala.
Chapter 6. Pushing the boundaries in robot-assisted partial nephrectomy for renal cancer.
*Charles Van Praet, **Pieter De Backer**, Riccardo Campi, Pietro Piazza, Alessio Pecoraro, Alexandre Mottrie, Andrea Minervini, Karel Decaestecker*
Pieter De Backer wrote the main technology chapter parts.

2.1. Renal Anatomy and its History

Due to its complexity, renal anatomy has a long-standing research history with a specific focus on renal vascularization, as it crucial to surgical hemostasis. Renal vascular segments were first recognized in the middle of the 18th century by Hunter and Bertin[7], [8]. Hyrtl [9] confirmed the compartmentalization hypothesis in 1882 and noted that, due to the renal artery's branching nature with blind endings, the kidney is particularly sensitive to ischemia as compared to other organs. In 1901, Brodel [10] described surgical planes of renal division to avoid blood loss, which he had defined through the production of human renal casts.

The next major breakthrough in renal vascularization was published in 1954 by Graves[11]. He described the first renal artery classification, proposing a renal division into five commonly found segments, based on the corresponding five extrarenal divisions of the renal artery (Figure 2.1). This division can be considered a gold standard up to present, although following research showed the renal vascularization to have a high degree of variation without a “one size fits all” formula.

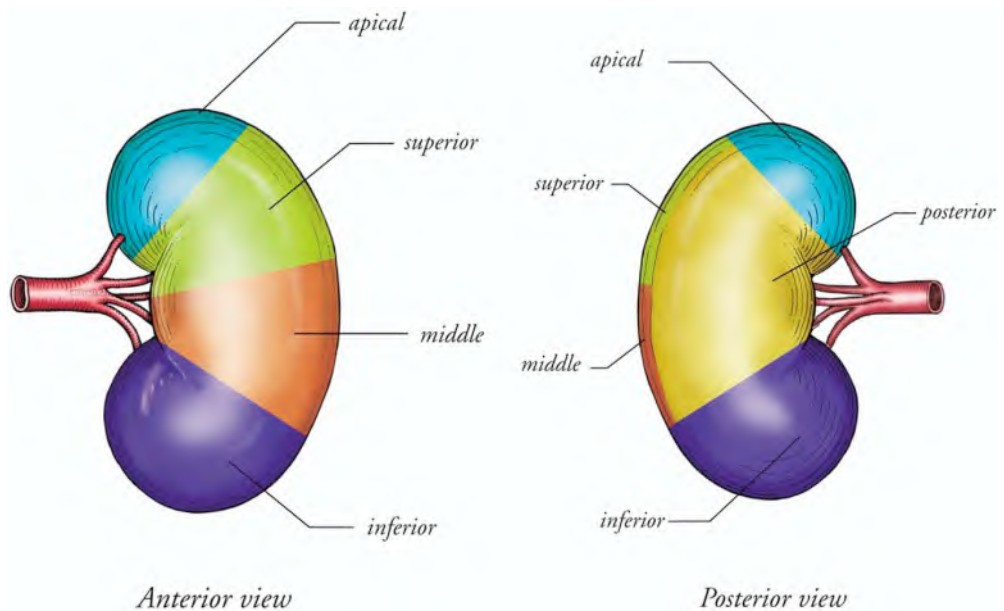


Figure 2.1: Segmental division following extrarenal arterial branching as described by Graves. The apical part encompasses the superior pole, the superior part encompasses the remainder of the anteromedial portion of the superior pole, the inferior part occupies the lower pole, middle part occupies the remaining anteromedial part and the posterior zone includes the posterior renal part between the apical and inferior segments. Image derived from Weld et al, Urology, 2005 [12].

Due to advancements in the availability and power of imaging systems, researchers continue to gain insights into normal and aberrant renal anatomy, and it remains an active topic of study. Our knowledge vastly expands due to the increase in urological, interventional radiological, vascular and renal transplantation surgeries, all of which

require profound knowledge of the vascular tree and renal anomalies[13], [14]. Shifting from open to robotic surgery further facilitates this research.

In this chapter, we describe the embryology, physiology and surgical renal anatomy in order to provide a holistic understanding to pre-operative partial nephrectomy planning. A strong emphasis is put on the detection and treatment of vascular anomalies in order to facilitate dissection of atypical vasculature. We also describe practicalities in anticipating and overcoming possible surgical difficulties. Next, we elaborate on the procedure central to this dissertation: Robot-Assisted Partial Nephrectomy (RAPN). RAPN is the procedure in which a renal tumor is removed through robotic assistance, whilst sparing the healthy surrounding kidney parenchyma

Robotic surgery has become a viable alternative for open partial nephrectomy [15]. Robotic surgery also facilitates the integration of enhanced patient-specific visualizations. The technical environment of robotic systems allows for easy image and sensor data acquisition. The surgeon is no longer scrubbed in and at the operating table which also allows easy interaction with new data sources. We close this chapter with an overview of current pre -and intra-operative technologies and surgical techniques to improve surgical care in RAPN. We also provide pointers to future chapters.

2.2. Renal Physiology

Renal function can be categorized in 3 main categories. Firstly, an excretory function, in which metabolic waste products are excreted towards the urine. Secondly, an endocrine function that controls red blood cell production by bone marrow and activates vitamin D. Thirdly, a homeostatic role in controlling blood pressure, tissue osmolality, electrolyte and water balance, and plasma pH. Both excretory and homeostatic properties are carried out through a complex process of filtration, reabsorption, secretion and excretion.

Renal anatomy and its functions are closely linked. The medial surface of the kidney consists of a hilum through which the renal artery, vein, lymphatics, renal nerves and ureter access the inner part of the kidney. On sectioning, the kidney parenchyma consists of two main regions: the cortex, seen as a pale outer region, and the medulla, which is the darker inner region. The medulla typically consists of 8-18 conical regions called renal pyramids. Each pyramid is separated by renal cortex, these septa of surrounding cortical tissue are called the columns of Bertin. The base of each medullary pyramid lies at the cortex-medullary border, and the apex ends at so-called papilla, which merges with the pyelum through a minor calyx, the start of the collecting system. These minor calyces fuse in to two or three major calyces, which subsequently form the renal pelvis, draining into the ureter. The calyceal walls, pelvis and ureters are lined with smooth muscles that can propel urine forward by peristalsis. The cortex and medulla form the functional part of the kidney and consist of about 1.3 million nephrons. A corticopapillary osmotic gradient is in place, with a renal cortex osmolality (300 mOsm/kg), being close to plasma osmolality, and a high inner medulla osmolality (1200 mOsm/kg). This osmotic gradient is essential for normal renal function as it allows to recover virtually all of the daily filtered water, which is approximately 180 liters.

The cortex contains approximately 85% of the nephrons, the other 15% are so-called juxta-medullary nephrons. The nephron is the functional kidney unit and consist of a renal corpuscle which is the initial filtering component, and a renal tubule which processes and finally carries away the filtered urine.

The renal corpuscle of the juxta-medullary nephron is situated at the border of the medulla but still in the cortex, and their proximal convoluted tubule and the associated loop of Henle occur deeper in the medulla than the cortical nephron. It is to be noted that the juxta-medullary nephrons are the most functional of all nephrons, as they have the capacity to hyperconcentrate urine. This is due to their long loops of Henle reaching deep into the hyperosmolar inner medulla. Their tubuli are the only ones surrounded by vasa recta. The vasa recta is a long looping vascular structure around the tubular loop, able to generate an hyperosmolar gradient and generate hyperconcentration. The renal pyramids, consisting mainly of the tubuli and vasa recta of juxta-medullary nephrons, can thus be considered the primary functional unit of the kidney. The juxta-medullary nephron is often depicted when explaining the function of the kidney. Each kidney filters approximately 1 liter of blood per minute. This high filtration rate has two major advantages. Firstly, circulating toxins can be cleared from the circulation in as little as 30 minutes. Secondly, the kidney is only selective on what it recovers from the large filtrate volume, so any substance that is not reabsorbed, is automatically secreted without further due.

As depicted in Figure 2.2, the vascular supply of the kidney forms a complex network. The renal artery splits into segmental arteries as discussed thoroughly in section 4. These segmental arteries subsequently divide into interlobar arteries which enter the

parenchyma at the level of the renal sinus and subsequently travel towards the cortex in the Bertin columns. As such, they extend along the boundary of each renal lobe, explaining their name. These interlobar arteries subsequently branch in right angles to arcuate arteries, found at the corticomedullary border. From these arcuate arteries, cortical radial arteries or interlobular arteries arise in a 90 degree angle, and oriented radially as their name suggest. From there on, the arterioles provide oxygen rich blood to renal corpusculi, tubuli and vasa recta. Compared to other organs, there is relatively little branching until the capillary region of the vasculature is reached, resulting in higher capillary bed pressures, necessary to sustain the high filtration rate.

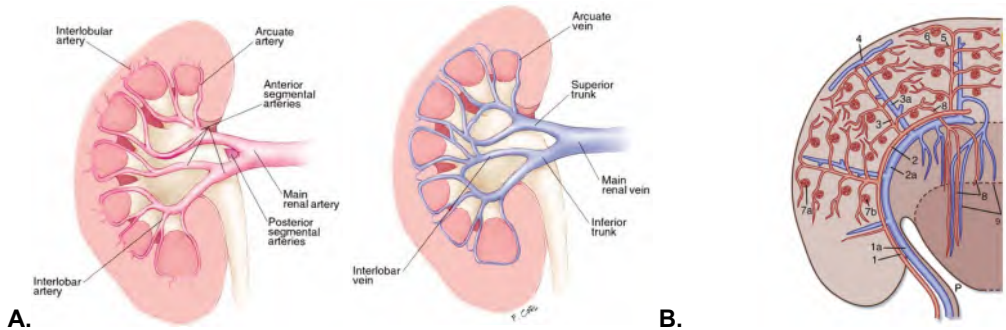


Figure 2.2: Vascular system of the kidney. A. Macrovascular network of the kidney. Derived from [16]. B. Microvascular network. . 1, interlobar arteries; 1a, interlobar vein; 2, arcuate arteries; 2a, arcuate veins; 3, cortical radial or interlobular arteries; 3a, interlobular veins; 4, stellate vein; 5, afferent arterioles; 6, efferent arterioles; 7a, 7b, glomerular capillary networks; 8, descending vasa recta; 9, ascending vasa recta. Derived from Koeppen et al, Elsevier Health Sciences, 2009 [17].

Two main factors contribute to the renal sensitivity in hypoperfusion.

Firstly, as stated above, the medullary region is crucial in renal function, yet it receives only 10% of the arterial blood supply. This is explained by the cortex having a high energy demand of sodium/potassium ATPase, responsible for 99% of the filtration reabsorption into the blood [18]. The lower medullary perfusion however implies that during restricted oxygen delivery such as trauma/crush/arterial clamping, this important functional part becomes anoxic and renal failure can follow. We also note that it is exactly this lower medullary perfusion rate which contributes the medullary region to be hyperosmolar, as compared to the medullary cortex.

Secondly, the renal branches are non-anastomotic[19]. Even though the arcuate arteries may illicit similarities to arcuate arteries in the human feet, the renal arterial system is terminal. This is also clearly noted in renal infarction, with typical triangular defects.

Venous blood drains through a similar cascade of venules, interlobular veins, arcuate, interlobar and eventually the renal vein. In contrast to the arterial system, this system is non-terminal, with several anastomosis inside the kidney but also with veins in the perinephric fat, through a subcapsular plexus of stellate veins.

2.3. Embryology

The renal organogenesis starts at the level of the three germ leaves. More specifically, the kidneys originate from the intermediate mesoderm. Nephrogenesis starts in the 4th week of gestation. In utero, renal development is characterized by 3 subsequent phases: pronephros, mesonephros and the metanephros which is the precursor of the final kidney[20].

At week 6, the metanephros ascends from the pelvis towards its final lumbar position where it meets the adrenal gland. While the kidneys are still in the pelvis, they are supplied by the median sacral artery and internal and external iliac vessels. In normal organogenesis, these arteries atrophy and newly cranial arteries are formed as the kidneys ascent. As such, the kidneys generate arteries along their path, making new cranial arteries while lower caudal arteries atrophy. Errors during this vascularization process result in the growth of accessory arteries as discussed below.

The renal and ureteral development are thought to be interdependent: normal renal development depends upon a normal ureteral bud and vice versa. The ureteral bud undergoes orderly branching and penetrates this metanephros, forming the collecting duct and pyelocaliceal system. It will also elongate, thus forming the ureter. Autopsy reports show that renal agenesis can occur when either parenchyma or ureteral bud fail to develop, emphasizing their interdependence[21].

Each adult kidney typically consists of 750,000 nephrons, though the total number can vary significantly from 250,000 to 2 million nephrons [22]. All nephrons are formed by week 32 to 36 of gestation. Although the fetal kidneys do produce urine, it is not until after birth that the glomerular filtration rate increases rapidly due to a postnatal kidney vascular resistance drop and accompanying increased renal perfusion. Nephron maturation also continues postnatally.

2.4. Surgical Renal Anatomy

2.4.1. Renal Anatomical Relationships

Renal Topology

Understanding the renal topology is of utmost importance when planning for partial nephrectomy as it helps to choose the best possible surgical access and provides insight into the procedural steps and possible surgical difficulties. The right kidney is generally located 1-2 cm lower than the left kidney due to the liver, positioned above. Both kidneys are positioned retroperitoneally and rest with their posterior upper third against the diaphragm, covered by the 12th rib. The left kidney is also covered by the 11th rib. Their longitudinal axis parallels the oblique and inclined psoas muscle, on which their posterior medial two thirds rest, while the lateral posterior two third is bordered by the quadratus lumborum. Both muscles are separated from the kidney by Gerota's fascia, a layer of posterior pararenal fat and the transversus abdominis fascia [23]. Due to the conical psoas muscle shape, the superior poles are more inclined towards posterior and medial in comparison to the inferior poles.

Anteriorly, the kidneys are lined by left and right colon with their mesentery on the respective sides. The right kidney is bordered by the liver and attached to it by the hepatorenal ligament. Its renal hilum is overlaid by the descending part of the

duodenum and the pancreatic head. The left kidney is superiorly bordered by the pancreatic tail and splenic hilum, in which the inferior mesenteric vein fuses. The posterior gastric wall can also overlie the left kidney. It is attached to the spleen by the splenorenal ligaments and care should be taking in applying excessive downward pressure on the left kidney as to avoid splenic capsular lesions.

Mean renal length is estimated at approximately 11.1 cm, with a thickness of 3.3 cm. The superior width is found to be 1.1 cm wider than the inferior pole. The left kidney is found to be 1 to 3 mm larger in every dimension. Superior poles are slightly larger in width than the inferior poles. Each kidney weighs some 100-200g, female kidneys being slightly heavier. Individual stature and length is significantly correlated to the renal size[14]. Classically, from anterior to posterior, the renal hilum consists of a single renal vein, a single renal artery and the renal pelvis. Figure 2.3 depicts the classical renal hilar configuration and the relation with adjacent vessels.

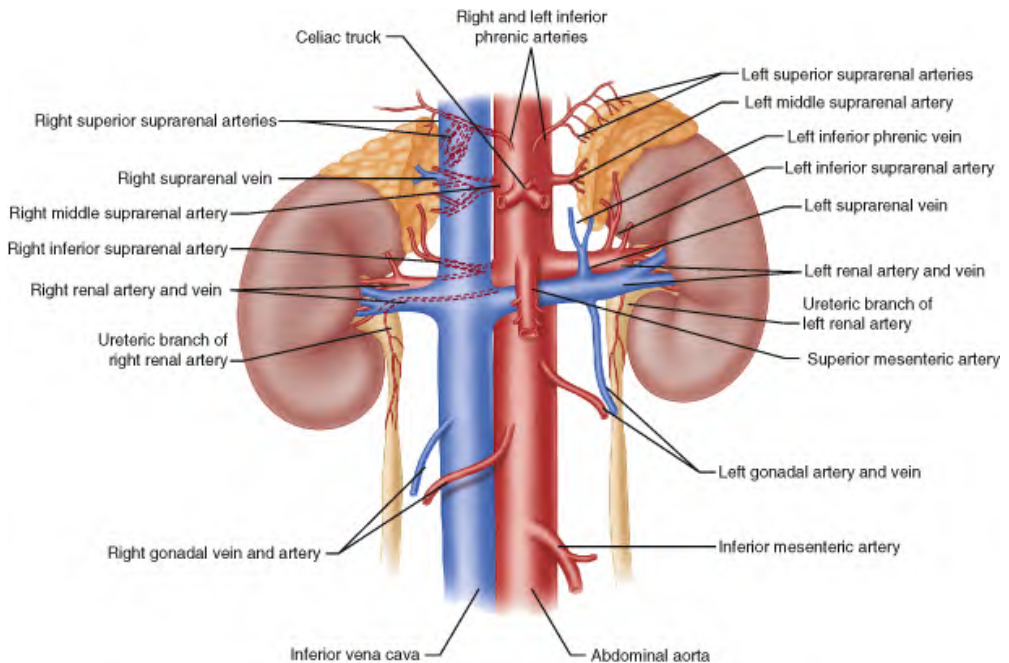


Figure 2.3: Renal and adrenal vascularization overview. Image derived from Furst et al, *Surgical Endocrinopathies*, 2015 [24]

The Retroperitoneal Space

The retroperitoneal space is divided into perirenal and the anterior and posterior pararenal space. The perirenal space is contained within the Gerota fascia and contains the kidneys, adrenals, the great vessels and the perirenal fat. The kidney's outer layer consists of a tough fibrous layer, the renal capsule. Outside the Gerota but inside the retroperitoneum, the anterior and posterior pararenal fat is found. The anterior and posterior Gerota fascia fuse laterally into the lateroconal fascia, which subsequently fuses with the peritoneum lateral to the colon, forming the white line of Toldt. Superiorly, the Gerota attaches to the diaphragmatic crura, while inferiorly, no fusion occurs and as

such leaving a potential open space. Figure 2.4 provides an overview of the renal retroperitoneal organization.

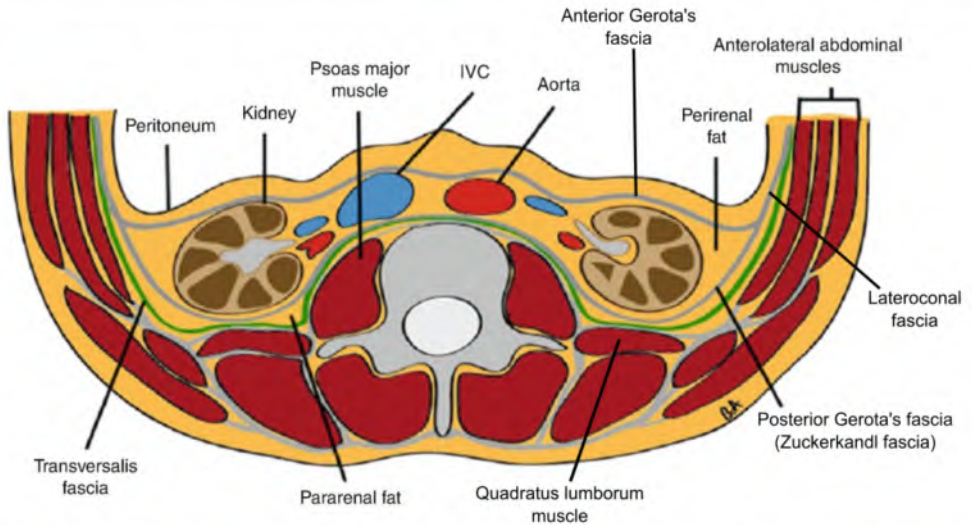


Figure 2.4: Retroperitoneal organization. Image adapted from Karam et al, "Surgical Anatomy of Kidneys and Adrenals," 2018 [25]

Surgical Impact

Several renal anatomical relationships need to be appreciated during kidney mobilization and renal surgery. Due to the vicinity of the pancreatic tail near the left renal hilum, one should always be aware of the possibility of pancreatic tail lesions during RAPN or left nephrectomy. Unlike splenic injuries, which are easily recognized per-operatively due to extensive bleeding, pancreatic lesions tend to be recognized in the post-operative period when pancreatic fistula's or peripancreatic collections become apparent. As these complications require re-interventions in most cases and have a considerable mortality rate, pancreatic lesions during renal surgery account for one of the most significant complications. Care should be given to the pancreas tail during descending colon mobilization in left-sided renal surgery during which wide exposure and a meticulous surgical technique are key[26].

The close relationship between the left kidney and the spleen demands carefulness during upper pole mobilization of the left kidney. Iatrogenic injury to the spleen is not an uncommon complication. Left nephrectomy has been reported as the second commonest cause of iatrogenic splenectomy with a reported incidence between 1.3 and 24%. Moreover, iatrogenic splenectomy is associated with significant morbidity and mortality. With the advent of hemostatic agents, smaller splenic injuries could be managed conservatively. As mobilization of the splenic flexure of the colon most often is not deemed necessary for a good exposure, this could prevent iatrogenic splenic capsule laceration and splenic vessel damage [27]–[29].

Left-sided kidney exposure demands mobilization of the descending colon along the paracolic gutter (ie. Toldt's fascia). During right-sided renal surgery, it is deemed necessary by many surgeons to completely mobilize the ascending colon along Toldt's

fascia. However, the splenic flexure lies at a higher level compared with the hepatic flexure, as it is held on to the diaphragm by a peritoneal fold, the phrenicocolic ligament on which the spleen sits. Therefore, a full ascending colon might not be necessary in the majority of cases. An alternative technique is to start the right hilar dissection at the level of the fat-free region of the inferior caval vein under the liver border and to follow it more caudally until the renal vein is met. A minimal mobilization of hepatic colic flexure and duodenum is only necessary [30].

2.4.2. Arterial System

Normal Anatomy

In general, each kidney has one single renal artery which finds its origin on the abdominal aorta slightly below the superior mesenteric artery. It is bilaterally positioned posterior to the renal vein. However, in approximately one in three patients, the renal artery is located anterior to the renal vein [31].

Due to the lowered position of the right kidney and the left sided aortic origin, the right renal artery has a longer and downwards course, traversing behind the inferior vena cava (IVC). The left renal artery however, typically arises somewhat lower on the abdominal aorta, having a horizontal orientation towards to the superiorly positioned left kidney.

The renal artery typically gives rise to an anterior and posterior trunk, which subsequently subdivide into 4 to 5 segmental arteries which supply a corresponding segmental parenchymal part (Figure 2.5). The anterior trunk is considered dominant in perfusion, carrying approximately 75% of the renal blood supply [31]. The anterior-posterior division gives rise to an avascular frontal plane, along the so-called line of Brödel as defined in 1901, passing through the row of minor posterior calyces, which is currently however less used in surgical planning.

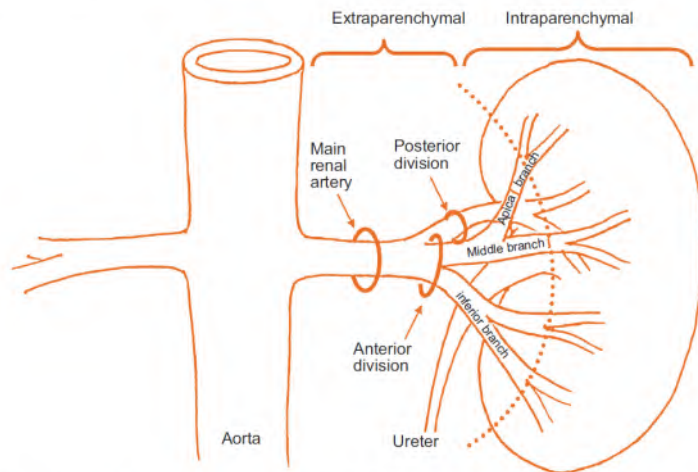


Figure 2.5: Classical extrarenal anatomic division of the renal artery into five segmental arteries: anterior trunk giving rise to an apical, upper, middle and lower segmental artery, and a posterior trunk perfusing the posterior segment. Image derived from [31].

The corresponding perfusion zones for these segmental arteries, as defined by Graves in 1954 can be seen in Figure 2.1. Subsequent division of segmental arteries up onto the interlobular level is discussed in section 2.2.

Graves' classification is considered the gold standard for the classification of the arterial renal system. Nevertheless, a high variability is present both at the level of the main renal artery and its segmental arteries. Several studies estimate the percentage deviating from Graves' classification around 40% [7], [8], [32]. Single parenchymal segment can also be perfused by one or more branches of another segmental artery [32]–[34].

Multidetector CT angiography (MDCT) provides a non-invasive way to measure the number, size, branching pattern, course and relationship between arteries, veins and the collecting system [35]. It detects accessory arteries, early branching, and renal vein anomalies with a respective accuracy of 95, 90–95, and 95–100%, respectively [36]. Nevertheless, this evaluation requires a slice by slice two-dimensional (2D) interpretation and mental reconstruction of the arterial tree. This mental load is decreased using 3D models which are currently finding their way into surgical planning. We refer to section 2.5.3 for an elaborate discussion.

Renal Artery Variations

As mentioned above, the renal vasculature has consistent patterns but it can still be very subject to variation. One reason for this variation is the renal ascent in utero in which arteries are subsequently generated and atrophied. For this reason, supernumerary or accessory renal arteries are found up to 25-30% of the population, while the other two third are estimated to have a classical single renal artery [8], [37], [38]. The presence of these multiple or accessory renal arteries is the most common anatomic variation[39]. Up to five accessory arteries have been reported.

Accessory arteries originate most commonly from the abdominal aorta, supplying the inferior pole [36]. Accessory or multiple renal arteries are more common on the right side [31] and can be present bilaterally in 10-15% of the population [38]. More arterial variation is also seen when anomalies are present contralaterally.

Some discordance is found in literature on the terminology for the classification of anomalous arterial renal anatomy. While some authors consider accessory arteries to be the general term for arteries not following a classical pattern [36], others define accessory arteries as arteries reaching the hilum and aberrant or polar arteries as the other category [40]. We choose the first definition.

Accessory arteries are thus subdivided in two main categories. The first one being hilar arteries, supernumerary arteries which enter the kidney at the hilum along with the main renal artery. When a hilar accessory artery is of a similar caliber as the main renal artery and originates from a similar abdominal aortic level, it is sometimes named 'second main renal artery'. The second category is formed by polar arteries which enter the kidney directly from the capsule outside the hilum. Both groups usually originate from the abdominal aorta or iliac arteries. Rarely, both categories of accessory arteries may also arise from the lower thoracic aorta, lumbar, mesenteric, or iliac arteries.

Both groups are not to be confused with so-called prehilum or early arterial branching, in which the first renal arterial branch arises within 1.5cm of the renal artery ostium, with an estimated prevalence of 12% of the population [40]. Early arterial branching is also more objectivated on the right side [41]–[43]. Figure 2.6 provides visualisations of arterial variations.

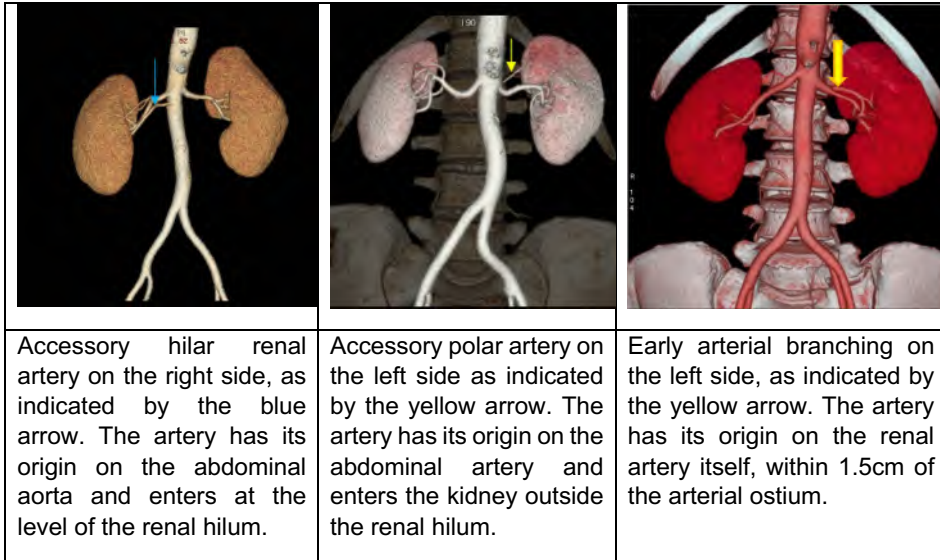


Figure 2.6: Cinematic renders of supernumerary renal artery categories. Pictures adapted from [41]

Surgical Impact

The highly variable arterial blood supply requires a tailored approach and thorough arterial tree evaluation per RAPN case. Apart from knowing the arterial location and course, it is equally important to know the corresponding perfusion zone of each artery. Several studies have shown that both parenchymal segments [26] as well as tumors are often perfused by several segmental arteries [8], [33], [34]. This means that segmental clamping of a single branch can be insufficient to reach satisfactory tumor ischemia. This variation and unpredictable nature of perfusion are one of the main drivers in developing novel digital algorithms as elaborated upon in chapter 3. The crossing vessels are most frequently found between the middle, inferior and superior segment. This implies that tumors at the posterior segment have a smaller risk of collateral blood supply from anterior segmental arteries. Bloodless resection after selective clamping is expected to follow [32] and predictive algorithms could potentially be of lesser benefit. This can be considered a present equivalent to the avascular plane as defined by Brödel.

The right renal artery has a more variant course. Although it typically originates posterior to the IVC, early bifurcation or accessory arteries can deviate part of its course anterior to the IVC. As such, surgeons should take care whilst dissecting the right renal artery to not damage the IVC. Failure to identify or recognize the presence of the accessory artery can also lead to bleeding during clamping or damaging the accessory artery during dissection [43].

Evenly important is that the renal arterial system is terminal. As stated above, this makes the parenchyma sensitive to ischemic damage. Both aspects have a direct impact on the clamping strategy. We refer to section 2.5.6 for an overview of hilar control during partial nephrectomy.

2.4.3. Venous System

Normal Anatomy

As discussed in the arterial section, the right renal artery generally crosses the inferior vena cava posteriorly. This relative position is most often maintained upon the renal hilum, where the renal vein usually lies anterior to the renal artery. Due to the IVC's rather right sided position, the left renal vein is almost three times longer than the right renal vein [25]. Unlike the right renal vein, the left renal vein receives several tributaries before joining the IVC: the left adrenal vein superiorly, the left gonadal vein inferiorly and a lumbar vein posteriorly. It reaches the IVC more cranially and anterolaterally as compared to the right renal vein. Direct confluence of gonadal or adrenal veins into the right renal vein is seen in only 7 and 30% of cases, respectively. The renal vein's position can vary up to 1-2cm cranio-caudally with respect to the artery.

Up until the level of the segmental branches, the venous anatomy correlates with the arterial system. These segmental branches next coalesce in two to five venous trunks which will eventually reach the renal vein.

In contrast to the arterial supply, the venous system has plenty of intra and extrarenal anastomotic vessels. They anastomose at the level of the sinus (first order), pyramids (second order) and marginal veins (third order) [44]. The veins are also in relation to interlobar, arciform and stellate veins. As noted earlier, the venous drainage indeed also communicates with veins inside the perinephric fat via a subcapsular venous plexus of stellate veins.

We discuss the anomalies on CT angiography. The venous anatomy is readily to be appreciated on the arterial phase. However, some large venous tributaries might require additional evaluation of nephrographic phase images [45], [46].

Renal Vein Anomalies

In contrast to the high arterial variation, venous anatomy is less variable.

The most commonly encountered venous variation is the presence of multiple renal veins, encountered in 15-30% of patients [38]. Multiple renal veins are more present on the right side [40], most probably due to the short distance to the IVC. The left renal vein is nearly always singular. Two left gonadal veins can be observed in 15% of patients, and the gonadal vein can become very large on the left side, being diagnosed a prominent gonadal vein when is 5 mm or larger (Figure 2.7). In 59-88% of patients, the retroperitoneal veins (lumbar, ascending lumbar and hemiazygos veins) drain into the left renal vein.

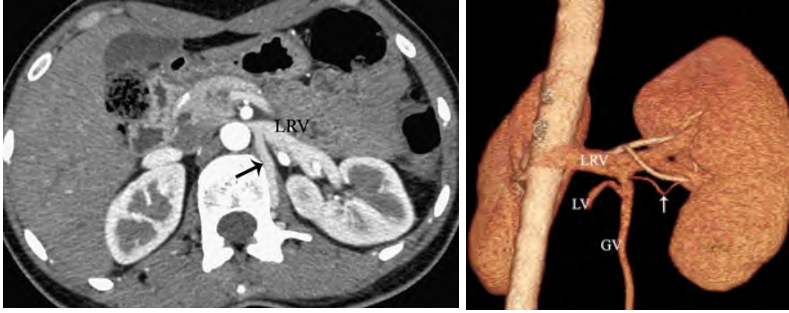


Figure 2.7: Prominent gonadal and retroperitoneal veins. A) Large lumbar vein draining into the left renal vein (LRV), as indicated by the black arrow. B) Cinematic render showing a prominent left gonadal vein (GV), draining into left renal vein (LRV), as well as a lumbar vein (LV) and small renal venous branch (arrow) draining into the left gonadal vein. Adapted from [36]

Figure 2.8 provides an overview of the most common left renal vein anomalies and peculiarities.

The most common anomaly of the left renal venous system is the circumaortic renal vein, seen in up to 17% of the population (Figure 2.8.b.) [38], [40]. Here, the left renal vein splits into an anterior and posterior part that encircles the abdominal aorta. The retro-aortic component can vary in size. The adrenal vein typically joins the anterior part, while the gonadal vein typically joins the posterior vein. The posterior component often joins the aorta at a more caudal level, which also explains its relation to the gonadal vein.

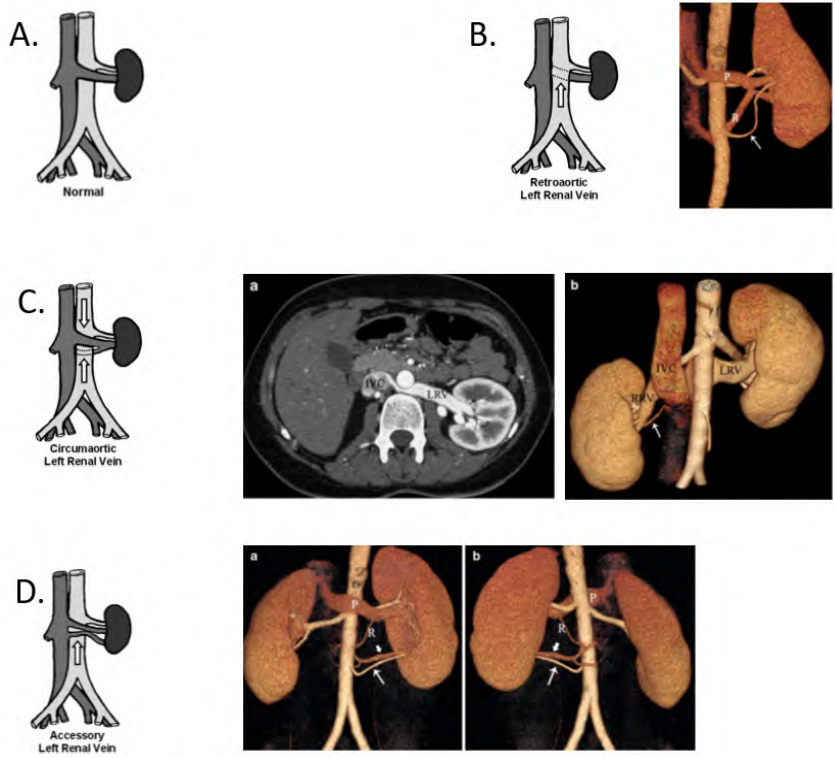


Figure 2.8: Overview of congenital left renal vein and IVC anomalies. Adapted from Türkvtan et al, Eur. Radiol. 2009 [38], [47]. A) normal anatomical situation. B) Circumaortic left renal vein. Cinematic render shows how the posterior vein is more caudally oriented. We also note the accessory hilar artery. C) Retroaortic left renal vein (LRV). Note the second small right renal vein (arrow) (RRV right renal vein, IVC inferior vena cava) D) Accessory second renal vein (short arrow), with a small retro-aortic component, and a polar artery (long arrow).

More rare is a complete retro-aortic renal vein, seen in 2-3% of patients. Here, the single left renal vein courses posterior to the aorta before draining into the IVC (Figure 2.8.c).

Less common variants include a late venous confluence, in which the venous branch coalescence within 1.5cm of the anastomosis of the renal vein with the IVC. It can be considered the venous analogy of early arterial branching.

Right sided late venous confluence is very poorly described, as almost every right sided venous drainage happens within 1.5cm of the renal vein ostium due to the short venous length.

Surgical Impact

As discussed earlier, the renal venous system is not terminal but widely collateral. This implies that segmental branches can be occluded without hampering venous outflow or without subsequent renal damage.

MDCT allows for pre-operative detection of minor venous variants such as lumbar or gonadal veins. This may facilitate dissection in partial and radical nephrectomy and help avoid hemorrhagic complications. Similar to arterial domain, 3D models can help to appreciate relative positions of the venous tree.

2.4.4. Renal Collecting System and Ureter

Renal Papillae, Calyces, and Pelvis

On average a kidney has 7 to 9 papillae, although the count can vary from 4 to 18. Each of these papillae is at the top of a medullary pyramid and is enclosed by a minor calyx. Each minor calyx tapers into an infundibulum. Much like the variation in the number of calyces, the dimensions of these infundibula show significant diversity. These infundibula come together to create two or three larger branches known as major calyces. Often referred to as upper, middle, and lower pole calyces, these structures then unite to constitute the renal pelvis. The size of the renal pelvis itself can significantly vary, ranging from a small pelvis contained within the kidney to a larger pelvis that extends beyond its confines. Eventually, the pelvis narrows down to form the point where the ureter begins, known as the ureteropelvic junction.

Ureter

The ureteropelvic junction marks the start of the ureter, positioned behind the renal artery and vein. From there, the ureter proceeds downward along the front border of the psoas muscle. Roughly one-third of the distance towards the bladder, the ureter is crossed in front by the gonadal vessels. Upon entering the pelvic region, the ureter passes in front of the iliac vessels. This crossing point generally aligns with the split of the common iliac artery into the internal and external iliac arteries, thus serving as a valuable reference point for procedures involving the pelvis. [48], [49]

Surgical Impact

Adequate management of the renal hilum is crucial for RAPN. Identifying the ureter can serve as a landmark for dissection towards the renal hilum. Knowledge of the relative position of artery, vein and collecting system allows for safe renal pedicle management. Preoperative identification of renal calyces positioned close to the tumor is equally important, as calyces can be opened during tumor resection. This subsequently requires selective suturing to avoid urinoma formation or hematuria.

2.5. Robot Assisted Partial Nephrectomy

2.5.1. Nephron Sparing Robotic Surgery

As stated above, Robot-Assisted Partial Nephrectomy is the procedure in which a renal tumor is removed through robotic assistance, whilst sparing the healthy surrounding kidney parenchyma. Robotic assistance denotes a master-slave relation in which the surgeon manipulates controllers and the robotic system transfers the surgeon's motion to its miniaturized instruments. This relation allows for precise movements, which are further enhanced thanks to scaling possibilities in which movements of the surgeons can be scaled down and correct for minor tremors, thus enabling further enhanced control. Just like classical laparoscopic surgery, robotic surgery allows for small incisions (keyhole surgery). The current EAU guidelines [15] do not specifically advise on the use of robotic surgery for partial nephrectomy. The implementation of RAPN is however increasing in urology centers with a robotic system available. RAPN has been shown to deliver at minimum equivalent outcomes to open and laparoscopic surgery[50], [51] but offers the dexterity advantages described above. RAPN has also been shown to have a shorter learning curve [52], a lower complication rate and length of stay as well as better renal outcomes when compared to open surgery and a lower blood loss when compared to laparoscopic surgery[53]. It is also suited for large tumors [54].

The incidence of renal cell carcinoma (RCC) increases worldwide [55] and is highest in developed countries. One reason for the increased incidence is the expanded use and advancements in routine radiologic imaging. This has enabled RCC to often be diagnosed incidentally and early at the clinical T1 stage with ensuing decreasing average tumor size[56].

In the absence of metastases, which may occur in up to 12% at initial diagnosis, the gold standard treatment is surgical resection [57].

Given the frequent early diagnosis, urologists are now focusing on strategies to minimize the impact of therapy in terms of overall morbidity and renal function, while maintaining optimal oncological outcome. The application of minimal-invasive surgical techniques is a general evolution across all surgical disciplines to reduce short-term morbidity whilst also allowing earlier convalescence. Minimal invasive surgery applications span a wide field and include robotic/laparoscopic endoscopic procedures such as partial nephrectomy, as well as endoluminal surgery, percutaneous procedures, and the use of natural orifice transluminal endoscopic surgery (NOTES).

In case of outcomes specific to renal cancer, cancer-specific survival of T1-2 N0M0 RCC is excellent, with cancer specific survival exceeding 92%. However, chronic kidney disease (CKD) can be acquired through renal cancer surgery and is associated with poor survival [58]. The risk of early or late CKD has been the main driver towards nephron-sparing surgery (NSS). During NSS, the urologist attempts to preserve the maximum of healthy tissue instead of complete kidney removal (as in radical nephrectomy) to optimize long-term renal function. NSS itself can be considered a synonym to partial nephrectomy and spans a wide range of partial nephrectomy techniques [59]. On one end of the spectrum, we find heminephrectomy, which is basically slicing the kidney in half and removing the tumoral part in bulk with half of the healthy kidney. On the other end of the spectrum is tumor enucleation, in which a submillimeter rim of non-tumoral tissue is kept when removing the tumor. We refer to section 2.5.7 for an in-depth discussion.

Apart from the quantity of preserved healthy renal parenchyma, postoperative renal function is considered to be influenced by the pre-operative kidney function and by a lesser extent by the warm ischemia time [60]. The kidney was initially thought to be hypersensitive to periods of ischemia. More recent insights show that the human kidney could be more tolerable to warm ischemia than expected and the concept of 20 to 25 minutes “maximal safe ischemia time” is being challenged [61], [62]. The impact of ischemia techniques, which refer to the way the arterial clamping is performed and which renal volume undergoes warm ischemia, are also heavily debated as more high level evidence accrues [63], [64]. One reason for the lack of clear evidence, is that most patients undergoing RAPN have a good functioning contralateral kidney and even a radical nephrectomy would not always have direct clinical impact when measured by renal function through blood sampling. Nonetheless, recent evidence from the CLOCK trial (CLamp vs Off Clamp Kidney) has shown subclinical renal function impairment as measured by radionuclide scans when clamping times exceed 10 minutes [65].

The European Association of Urology (EAU) guidelines panel recommends going for partial nephrectomy/NSS for all T1 tumors, as well as T2 tumors “if technically feasible”, especially in patients with a solitary kidney, bilateral tumors or CKD [15]. The EAU guidelines do not impose open, laparoscopic or robotic surgery for NSS, but do state the evidence of shorter length of stay and blood loss for the laparoscopic and robotic approach. It should be stated that ‘technically feasible’ is subject to interpretation. Digital planning of these cases can have the potential to render ‘technically impossible lesions’ to become amendable for nephron sparing surgery nonetheless.

Increased experience with robotic surgery, technological improvements and better awareness of RCC’s biological behavior are allowing T2 and even more advanced RCC cases such as T3 tumors to be safely treated with robotic partial nephrectomy. As such, robotic experts are pushing further towards surgical techniques which maximize healthy tissue preservation and simultaneously minimize warm ischemia time or volume. Pushing these boundaries through digital planning and assistance is central to this dissertation. One particular aspect of digital planning is the use of pre-operative 3D models as introduced in section 2.5.3. and chapter 3.

2.5.2. Trifecta in RAPN

Midst this rapidly evolving evidence, new surgical techniques, technological additions and sometimes conflicting, low/intermediate evidence, it is easy to get lost in the noise. A key landmark to keep in mind whilst exploring NSS and this dissertation is the so-called trifecta, three key outcomes which define a properly executed partial nephrectomy [66]:

- 1 All tumor should be removed (negative surgical margins)
- 2 Minimal renal function decrease
- 3 No urological complications

Throughout this dissertation, the trifecta plays a central role to assess if newly introduced technology is safe and/or adding clinical value. Figure 2.9 provides a schematic overview of the partial nephrectomy trifecta in black, and the different factors influencing it. It can help as a beacon through the exploration of the rest of this work. Although seemingly independent, the trifecta pillars are very interlinked. Figure 2.9 displays only the basic interlinking mechanisms in the red dotted lines.

The first pillar “Negative Surgical Margins” is evident: all tumoral tissue should be removed. Oncological margins should never be compromised, nevertheless they can be when attempting to minimize renal function decrease.

The second pillar, “Minimal Renal Function Decrease”, is itself influenced by several factors. The more healthy tissue is preserved through NSS (section 2.5.7.), the better the renal function is ought to be. Likewise, preoperative renal function is a strong predictor of postoperative renal function. Nevertheless, if the maximal amount of healthy renal tissue is spared, but every initially healthy nephron underwent a long ischemic episode, these nephrons might have accrued irreversible damage and function suboptimal. Hence, the ischemia volume and ischemia time, although possibly less impactful than NSS and preoperative kidney function [60], are also considered in the surgical strategy (section 2.5.6.).

The third pillar, avoidance of complications is equally important. The initial definition by Hung et al [66] included bleeding, urine leakage and kidney loss for whatever reason. Especially bleeding can once more be influenced by the second pillar, through several mechanisms of both NSS or minimizing ischemia.

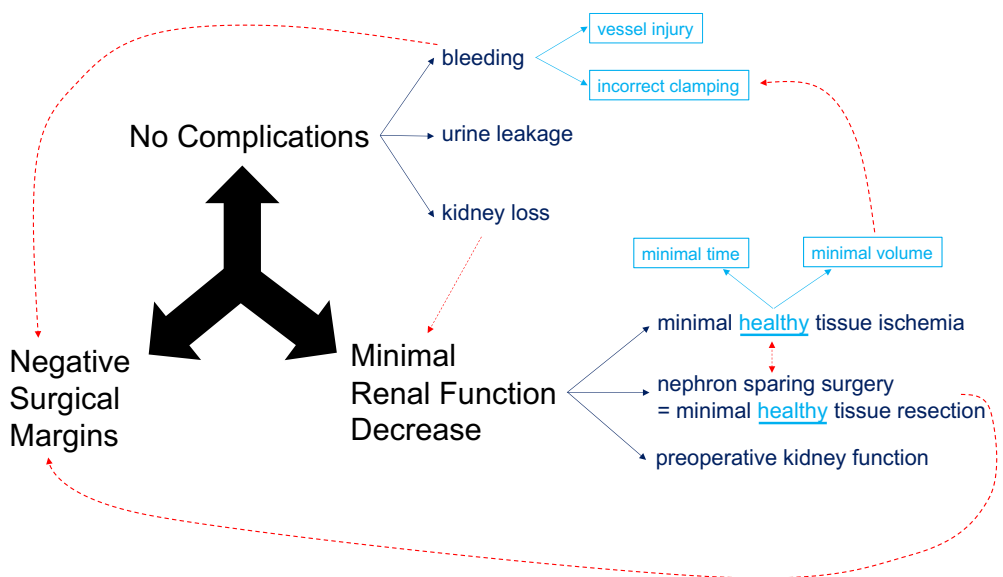


Figure 2.9: Trifecta in partial nephrectomy (in black) with factors influencing successful achievement of the trifecta and their relative influences and relationships.

2.5.3. Radiologic Assessment and Preoperative 3D Planning

Knowing the nuances which make up a good RAPN, we first shed light on pre-operative planning before discussing surgical techniques. As highlighted before, 3D models are increasingly integrated into pre-operative RAPN planning. When assessing 2D imaging such as CT or MRI (Magnetic Resonance Imaging) for surgical planning, the renal angulation caused by the psoas muscle becomes very relevant. As the kidney rest on top of this conically shaped muscle, axial, coronal or sagittal CT/MRI slices are not aligned according to the orthographic renal axes and e.g. an upper pole tumor may occasionally appear on planar imaging as a mid-renal tumor [31]. Hence, appropriate ‘mental’ orientation of cross-sectional slices by the surgeon is required when determining surgical strategy.

CT/MRI imaging advancements are consistently improving renal visualization due to thinner slices thickness and in-plane resolutions, special acquisition protocols and hardware changes such as multiple row detectors which allow for isotropic imaging. This implies that every part of the studied patient volume is now scanned and reconstructions in planes differing from the traditional reconstructed axial, coronal or sagittal planes are possible. This higher 3D spatial resolution in combination with increased computing power also allows for advanced 3D visualization, such as 3D rendering [67]. CT imaging has been a longstanding gold standard for renal tumor characterization[68] and while MRI is also proven useful[15], CT remains the most frequently used modality for both diagnosis and treatment up to now. Additionally, the possibility to acquire submillimeter slice thickness (and thus volume information) without excessive scanning times has further favored CT imaging as the basis for these 3D visualization capabilities in clinical practice.

Volumetric Rendering versus Segmented 3D Models

Volumetric rendering is the process in which every 3d pixel ('voxel') of a CT scan data is assigned a color and a transparency by a so-called transfer function. The chosen transfer function determines which structures are to be highlighted. When the transfer function's opacity is set to 100% for a certain Hounsfield Unit (HU) range, this part of the CT volume is visible [69].

Figure 2.10 depicts several volumetric renders with the according transfer functions underneath creating using 3D slicer [70]. It concerns a patient with a right sided hilar tumor and cyst located on top of the tumor. Figure 2.10.a depicts the axial and coronal slices on the arterial scanning phase with the tumor delineated in green. Figure 2.10.b-f are volumetric renders derived from this arterial phase, whilst Figure 2.10.g is derived from the blanco phase and Figure 2.10.h from the venous scanning phase. Figure 2.10.b shows the render for a commonly used preset transfer function to visualize bony structures. We note how the complete arterial tree, which is also hyperdense in the arterial scan phase is equally withheld due to its high Hounsfield units, when compared to the blanco phase scan with identical transfer function applied in Figure 2.10.g. For both, the lower HU range is set to transparent to only visualize high density parts. In the visualized HU range, certain colors can be attributed to certain HU ranges to create an artificial sense of distinction between tissues and organs with different densities/HU.

In Figure 2.10.c we see a render for a transfer function set to withhold more soft tissue. Note the discrete color shift inside the transfer function towards more yellow and reddish. Figure 2.10.d depicts a narrow transfer function which only withholds the density of skin and likewise tissues, in which we can even see the patient's t-shirt seams and some hyperdense decorations in this t-shirt. Figure 2.10.e shows a similar transfer function to Figure 2.10.b however this commonly used preset is referred to as an arterial preset given its red color pallet which is more designated towards depicting blood. Nevertheless, the hyperdense vertebral column is still depicted, although less of interest when purely assessing arterial structures. Figure 2.10.f is generated to further exemplify the possibility of adding or editing whichever color the user finds interesting, but in essence it is nothing but the visualization as in Figure 2.10.e with a different applied color coding. Figure 2.10.h finally uses the same transfer function of Figure 2.10.e (arterial imaging), but on the venous scanning phase, when the contrast is already heavily diluted and mainly circulating venously. Only the renal pyramids are withheld, which still retain contrast and are busy filtering it. It furthers stresses the impact of correct contrast

admission for volumetric rendering and its inability to easily differentiate between different tissues of interest which have identical HU densities.

More recently, cinematic rendering has improved the lifelikeness of volumetric rendering through addition of so-called path tracing methods and a global illumination model, resulting in highly realistic 3D images. Nevertheless, they require extensive hardware requirements to be run in real-time. Current research efforts [71] are also aimed at decreasing these computational requirements so that these 3D renders can be manipulated real-time on non-specialized computing resources and such be used for instant surgical planning [72].

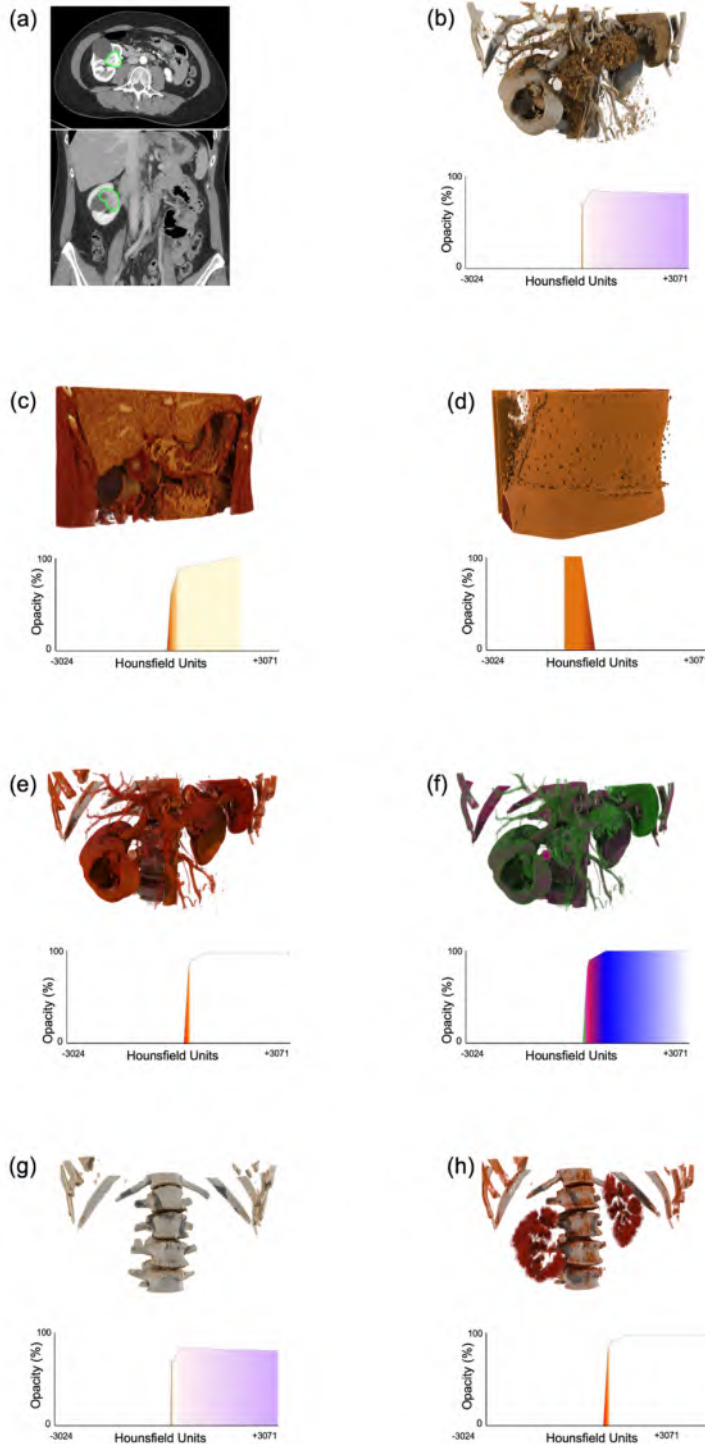


Figure 2.10: Volumetric rendering to 3D visualize anatomy. (a) axial and coronal slices, with the renal tumor delineated in green. (b)-(f) several transfer functions applied to the arterial scanning phase of Figure 2.(a). (g) and (h) identical transfer function as respectively (b) and (e), for the blanco and venous scanning phase. Generated using 3D Slicer [70]

As noted above, volumetric or cinematic rendering generally requires significant graphical processing power, not readily available on standard computers. As such, these renders are often performed inside the radiology department, screenshots are taken, and these are distributed towards other medical departments through the radiology viewer. This also implies that, after rendering, the transfer function, color, opacity and position cannot be altered by the surgeon and he/she is looking at a fixed set of images. As equally noted above, volumetric rendering does not allow a distinction between tissues of the same density, as both have identical HU in the transfer function. As an example, note how Figure 2.10.e also depicts the spleen next to the kidneys while it is of no significant interest in surgical planning for a right partial nephrectomy. Nevertheless, the spleen cannot be simply removed. Likewise, the renal tumor present in the kidney is not clearly visualized as its color and density is similar to the renal parenchymal density.

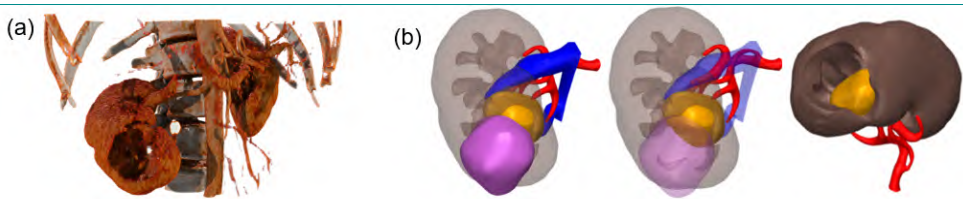


Figure 2.11: (a) volumetric rendering derived from the arterial scanning phase. (b) segmented kidney model derived from the same arterial scanning phase, which can be instantly manipulated and rotated.

Figure 2.11 shows another bottleneck of 3D rendering. In the case of Figure 2.10, a cyst was present on top of the tumor. However, due its watery consistency, volumetric rendering is unable to visualize the cyst as this would imply also visualizing all other watery structures. It now appears as a crater inside the right kidney. However, visualizing all watery structures would in turn obscure the tumoral region of interest. Furthermore, the surgeon needs to know the exact location of the tumoral mass whilst assessing Figure 2.11.a. and use this prior knowledge due to the tumor not being visualized as a separate entity. Figure 2.11.b shows the same anatomical model, derived through the process of segmentation using Mimics software (Materialise, Belgium). This segmented 3D model can be easily rotated and structures can be disabled for viewing or their transparency can be edited. Note how the tumor is more clearly visualized, and all structures can be easily toggled on or off. All of the above is not possible with volumetric rendering. This favours 3D segmented models for clinical integration as discussed below.

Segmentation

A 3D segmented model consists of separate structures of interest, which are predefined by delineation (or 'segmentation') in dedicated software packages. This delineation significantly compresses and simplifies the abundant information present in a CT scan to small entities.

Figure 2.12.a depicts how the operator manually needs to delineate organs of interest to instruct the software which regions of the CT scan belong together. The software conglomerates all parts belonging to arteries to a single group and likewise for venous structures, tumors, cysts, parenchyma, urinary excretory system etc. The generation of the 3D model (Figure 2.12.b) from the segmented structures typically requires computational power and results in a compressed format which can subsequently be easily handled without computational restraints. The segmentation process typically takes place hours or days before the surgery, using a dedicated hardware solution with

computational power. The resulting compressed information is often presented in the STL format (“Standard Triangle Language”) which basically consists of triangulated surfaces. This is an easy to use and lightweight format when used in the correct way.

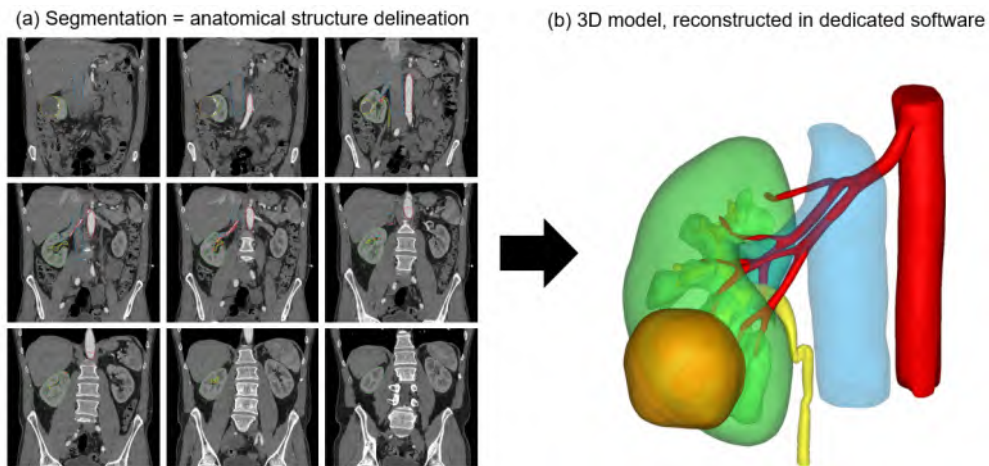


Figure 2.12: Generation of 3D segmented models by the process of segmentation (examples prepared using Mimics software (Materialise, Belgium)). (a) the operator manually or semi-automatically delineates all structures of interest in different CT slices. (b) the software package reconstructs a 3D volume from this sliced information which can be manipulated.

Due to this information compression, 3D segmentation models allow instant rotation, visualization and toggling of transparencies and colors, when compared to volume rendering, as depicted in Figure 2.11.b. As such, 3D segmented models do not require significant computational power for visualization once they have been segmented. This implies that they can be easily displayed in internet-browsers, mobile devices etc. Apart from 3D virtual visualization, they can integrally be used as an input for 3D Printing, Virtual Reality (V.R.) or Augmented Reality (A.R.) as shown in chapter 5.1. Lastly, they are also required as an input for patient-specific computer simulation techniques such as ischemia zone predictions (see chapter 3.1.).

However, segmented models have two major drawbacks. Firstly, the conversion from CT to STL files still requires minor computational resources during the preparation phase. Secondly and more important, as can be seen in Figure 2.12.a., the segmentation process remains a bothersome, time-consuming, and iterative task which can be prone to error. Here, novel A.I. methods can significantly reduce workloads due to automated segmentation.

We refer to Chapter 7 (section 7.1) for more information.

[Pre-operative 3D Model Based Planning](#)

Accurate surgical planning for renal cancer surgery is mandatory in order to achieve the best possible outcomes. A comprehensive evaluation of kidney tumors is non-trivial, as tumor size, localization and the relationship of the collecting system to the vascular system have to be taken into account. It is clear from section 2.4 that the renal anatomy is highly variable and an in depth per case understanding is important. In order to

facilitate this process, several nephrometry scores have been implemented in clinical practice over the last ten years, of which PADUA (Preoperative Aspects and Dimensions Used for Anatomical classification) and RENAL (Radius Endophytic/exophytic Nearness Anterior posterior Location) are the most widely used [73], [74]. All current nephrometry scores have been developed, validated and calculated using bidimensional imaging. As a consequence, the surgeon is once more required to create a three-dimensional mental image starting from the observation of two-dimensional images in the three spatial axes (axial, coronal and sagittal), with suboptimal results [75]. Especially when dealing with complex kidney tumors, where bidimensional imaging has been suggested to provide inadequate assessment [76].

Thanks to its ability to overcome some limitations of established 2D imaging techniques [77], the use of 3D technology has widely spread in the urological community since its first use in 2012 [78]. Moreover, 3D reconstructions have been proven to have a stronger correlation with excised renal tumor, in terms of both morphology and volume, when compared with conventional imaging [79].

In order to overcome the limits of conventional imaging in nephrometry scoring, Porpiglia et al. suggested the use of 3D reconstruction for the assessment of nephrometry scores [80]. Using three-dimensional models, all cases experienced a significant change in the score assigned to renal sinus involvement, urinary collecting system invasion and exophytic rate, while up to 50% of the cases had a downgrade in the PADUA and RENAL risk group.

A key aspect several other authors investigated, is the shift towards nephron sparing surgery (going from radical towards partial nephrectomy) by the use of virtual and printed 3D models. This is in concordance with the findings of downscaling PADUA and RENAL scores. Wake et al. reported a change of 30-50% after visualization of a 3D printed kidney model by the surgeon [81]. Bertolo et al, evaluated the role of 3D planning in highly complex renal tumors, either regarding the size of the tumor or other anatomical characteristics. Of the urologists involved, and regardless of their experience, 25% changed their indication after reviewing the 3D model in favor of partial nephrectomy [82]. However, most studies report on small patient series which remains a bottleneck in acquiring clear evidence. Specific factors attributing to the small patient counts, is the availability of in house knowledge for 3D model making, as well as the cost and logistics involved when deciding to purchase 3D models through commercial services.

In summary, current evidence does suggest that 3D models provide a more accurate overall perspective on renal cancer surgical planning, broadening the indication for nephron sparing surgery. Moreover, these findings may imply a shift in current research trends, moving the focus from “which is the most accurate nephrometry score” to “which is the best imaging tool for tumor complexity evaluation and 3D visualisation”.

Apart from informing the surgeon, 3D models can also be used to better inform patients on their pathology and the surgical strategy [83]. 3D printed models were found to be most useful for patient education when compared to virtual models. Virtual models in turn were also still considered superior to bidimensional imaging. Nevertheless, printed models imply a larger cost: apart from segmentation, they also require fabrication/3D Printing. As such, 3D virtual models are more common practice at present for both surgical planning and patient education.

2.5.4. Intra and Post-operative Outcomes Using 3D Models.

2.5.4.1. Intra-operative Application

While 3D models can help provide anatomical insights and broaden the candidate selection for nephron sparing surgery, early evidence shows they also have significant intra-operative advantages.

Clinical Outcomes

Up to present, the use of 3D models has been found to reduce estimated blood loss and enable smaller ischemia volumes. Through alteration of the arterial clamping strategy, 3D model use results in higher rates of selective and super-selective clamping (section 2.5.6.) [84]. 3D models also allow for more nephron sparing (more enucleation) and less frequent opening of the collecting system [84]. 3D models do not extend operative time, they might possible even reduce OR time [85]. The intra-operative complication rate (such as bleeding and conversion to radical nephrectomy) as well as the global ischemia time is found to be comparable with and without 3D model planning [84].

Intra-operative Fusion Through Augmented Reality

3D models are mostly visualized on separate screens by use of laptops or tablets. When integrated into robotic console, the Intuitive™ TilePro system (Intuitive, California, USA) is often used as it is up to present one of the few console systems which allows other data inputs. In recent years, a shift has taken place in how the 3D models are visualized in the TilePro module. Originally, virtual 3D models were only visualized as a separate entity (Figure 2.13.a). This is also called Virtual Reality, as the space in which 3D models are visualized is completely virtual. Recent studies have used the TilePro system to combine the live operative stream with overlaid 3D models to produce an Augmented Reality overview (Figure 2.13.b). During Augmented Reality, the space in which 3D models are visualized is no longer purely virtual, but the real world is augmented and interacts with these 3D models. Apart from the general 3D model benefits as described above, preliminary evidence shows that A.R. 3D models are found to reduce operative time [84]. A.R. might also have a role in being complementary to endoscopic ultrasound as 3D models can also provide subsurface information which can be useful in complex lesions [86]. Nevertheless, the integration is still logistically bothersome and has important pitfalls such as manual alignment, lacking soft tissue deformation and instrument occlusion. We refer to section 2.6.1 for a more technical in-depth discussion.

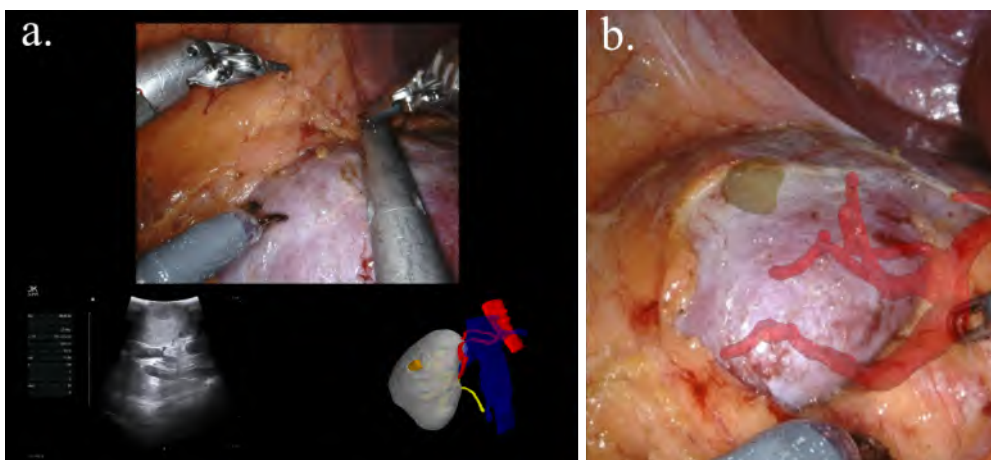


Figure 2.13: a. Robotic Console View during usage of the TilePro system: Right lower corner visualizes a virtual 3D model (Virtual Reality), while the left lower corner visualizes the incoming live echography image. b. Zoomed in TilePro view showing Augmented Reality view of the same renal mass and arterial tree. The live surgical view is now augmented with information of the 3D model rather than displayed in a different screen or environment.

2.5.4.2. Post-operative Findings

3D models in renal surgery were found to significantly reduce post-operative transfusion rates. No significant differences in post-operative complications, change in renal function (glomerular filtration rate) or surgical margins were found [84].

2.5.5. RAPN Surgical Steps

Before diving into the surgical technique, we provide a global overview of the surgical steps which make up a “traditional” transperitoneal RAPN. Transperitoneal refers to the surgical access, which is performed through the peritoneal cavity (in contrast to the retroperitoneal approach in which the peritoneum is not opened). We briefly highlight the surgical importance per step and indicate the relevance to the ensuing paragraphs. We refer to Chapter 6.2. for typical durations of these phases.

2.5.5.1. Development of Pneumoperitoneum, Trocar Placement and docking

During this phase, the virtual space of the peritoneum is insufflated with CO₂ gas in order to create working space for smooth manipulation of the robotic instruments. The trocars are placed and subsequently docked, after which the robotic instruments are advanced.

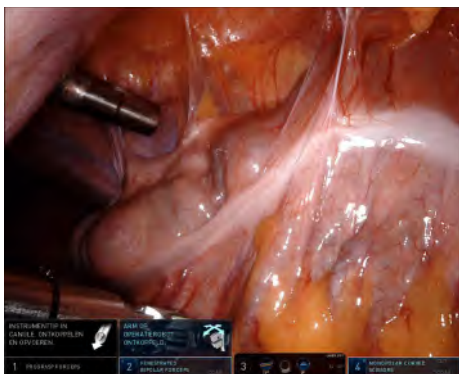


Figure 2.14: Robotic docking to inserted trocars and advancements of robotic instruments into the abdominal cavity

2.5.5.2. Retroperitoneal Access

Reflecting of the ascending colon and duodenum and mobilization of the liver for right-sided tumors; reflecting of the colon descendens and mobilization of pancreas tail and spleen for left-sided tumors. We move towards the target organ, which is located in the retroperitoneal space. This step is not present in the retroperitoneal approach.

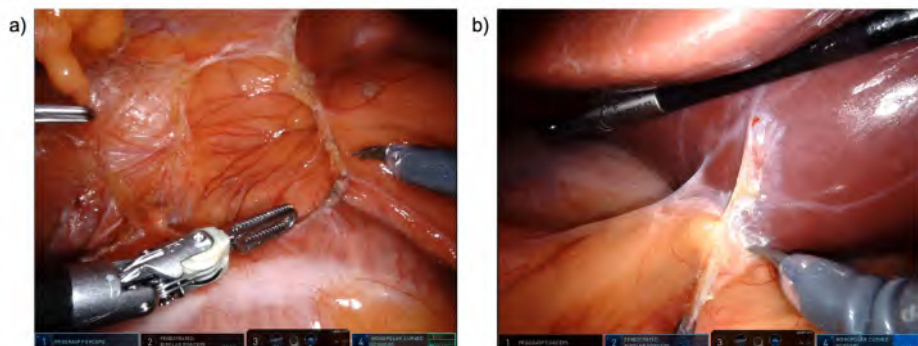


Figure 2.15: a) lowering of the ascending colon. b) Liver mobilization and tilting through extra laparoscopic forceps

2.5.5.3. Hilar Dissection

We dissect the renal artery and vein to allow manipulation of the vessels in case of bleeding or complications. In traditional RAPN, the renal artery and vein are encircled with vessels loops for fast/easy retrieval. Detection of small arteries which only perfuse the tumor region becomes equally relevant here. This step is relevant for minimizing healthy tissue ischemia volume (section 2.5.6.).

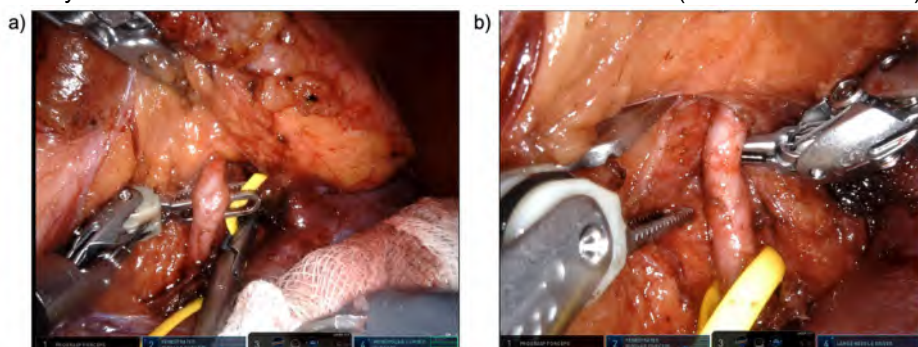


Figure 2.16: a) insertion of vessel loop to identify target artery for clamping. b) dissection and manipulation alongside renal arterial branch.

2.5.5.4. Tumor Delineation and Renal Capsula Incision

The tumor is delineated and a minor rim of renal capsula is already incised, until bleeding becomes bothersome.

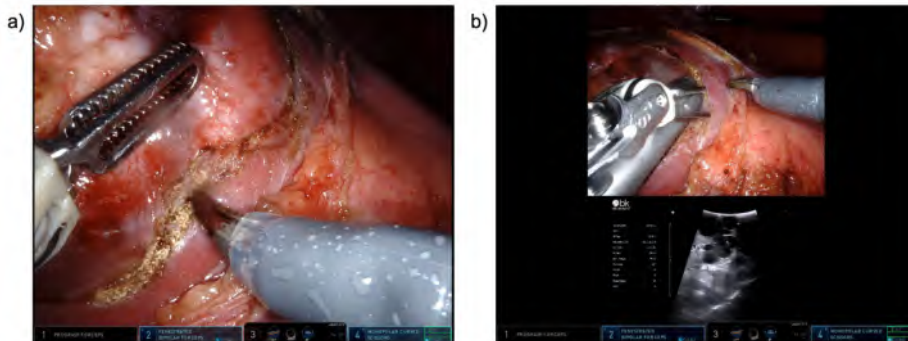


Figure 2.17: a) tumor delineation by incision of peritumoral tissue. b) endoscopic ultrasound can help guide identification of endophytic tumoral portions.

2.5.5.5. Renal Artery Clamping (Warm Ischemia)

The renal artery or the selected renal artery branch from step 3 is easily retrieved using the vessel loop. A reversible clamp is placed and from this point in time, the kidney volume perfused by this artery is deprived from oxygen rich blood. If this warm ischemia time takes too long, the clamped renal volume might become irreversibly damaged. This step is once more relevant for minimizing healthy tissue ischemia volume (section 2.5.6.)



Figure 2.18: Application of bulldog clamp on the renal artery

2.5.5.6. Tumor Resection

Whilst being on a tight temporal window, the tumor can now be removed with minimal risk of arterial bleeding thanks to the clamping. This step is relevant for maximizing nephron sparing surgery (section 2.5.7)

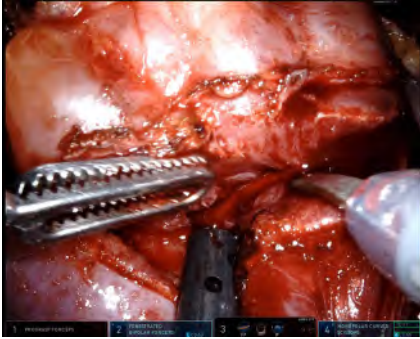


Figure 2.19: Tumor excision under continuous aspiration for remaining venous bleeding during fully clamped procedures.

2.5.5.7. Renorrhaphy

Classically a separate inner and outer renorrhaphy is performed. Here, the parenchymal defect which result from the removal of the tumor is reconstructed and closed. First, selective sutures are used to close very prominent arterial, venous or pyelocaliceal defects. Next, the inner renorrhaphy consist of a running suture in which possible remaining small venous or pyelocaliceal defects are closed. Finally, the outer renorrhaphy is performed to avoid too much traction on the inner renorrhaphy running suture. The timing of this step is also relevant in order to minimize healthy tissue ischemia time (section 2.5.6.)

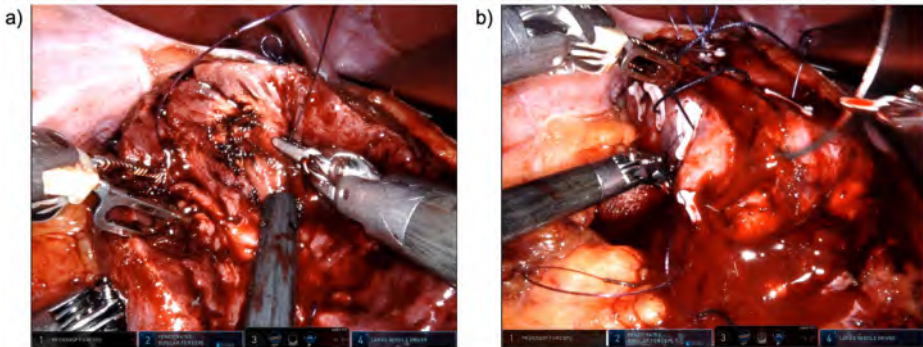


Figure 2.20: a) inner renorrhaphy. b) outer renorrhaphy

2.5.5.8. Unclamping and Hemostatis

Next, the renal artery is unclamped, which ends the warm ischemia time. The ischemic volume is now again perfused. This is also the point in which possible bleeding in the resection bed can be noticed and fixed if needed.

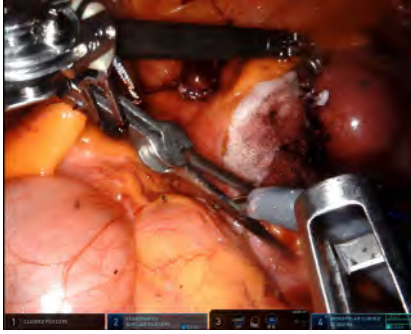


Figure 2.21: Bulldog clamp removal

2.5.5.9. Renal Fascia Closure, Specimen Extraction, Trocar Wound Closure

The retroperitoneum is again closed. The tumor and all foreign material are removed from the abdominal cavity. The cutaneous incisions are closed. The operation is terminated.

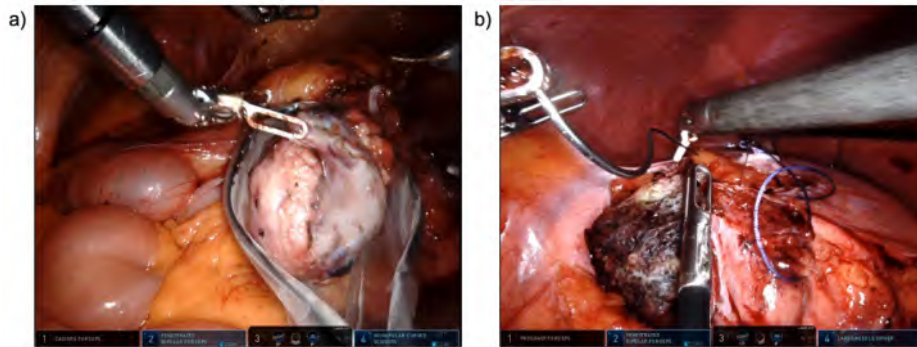


Figure 2.22: a) tumor bagging; b) retroperitonealisation of the kidney, on which previously a hemostatic sealant was applied after outer renoraphy (brown patch).

2.5.6. Hilar control – Minimizing Healthy Tissue Ischemia

Renal artery clamping is part of the “traditional” partial nephrectomy as it allows a bloodless and precise tumor resection (less risk of complications and positive surgical margins).

As already highlighted in section 2.5.1 and 2.5.2., the impact of renal ischemia has lesser impact on kidney function than originally considered. Nevertheless, both renal ischemia time and volume are amongst the factors that are surgically modifiable. Therefore, a lot of effort has been put in developing strategies which on one hand minimize healthy renal parenchyma ischemia volume (off-clamp resection, (super)selective clamping or on-clamp resection) and on the other hand minimize ischemia time (early unclamping or the application of cold ischemia). The improved ability to dissect and identify vessels in the robotic surgery setting, further add to this. This requires an in-depth knowledge of patient’s anatomy to optimize functional and oncological surgical outcome.

While historically, the full renal hilum (artery, vein and ureter) was clamped, nowadays most often only the artery is clamped, while renal vein and ureter are dissected for emergency situations but usually not clamped.

Figure 2.23 depicts the different steps that can be taken whilst attempting minimal ischemia volume[87]. On one end of the spectrum we find a fully clamped renal artery which entails the largest ischemic volume but the lowest risk of bleeding. On the other end, off-clamp resection does not entail any clamping or any ischemic volume however with possible higher risk of bleeding [88]. We discuss the different strategies below.

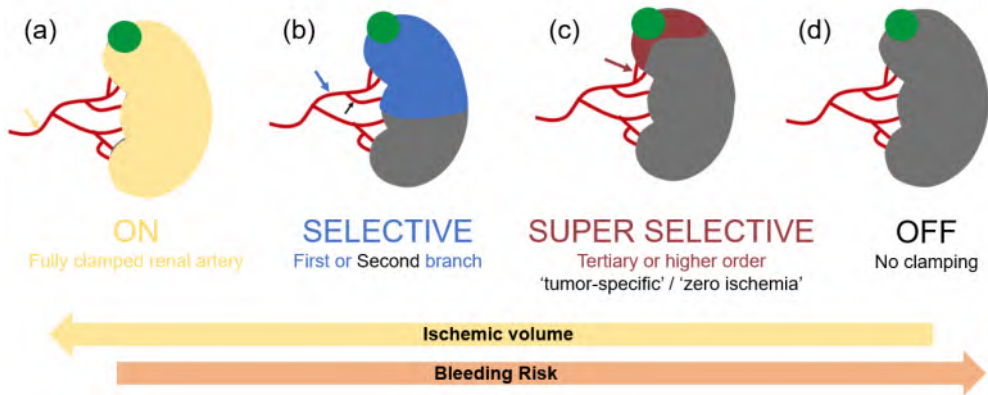


Figure 2.23: Selective arterial clamping and its terminology.

Minimizing Ischemic Volume

Off-clamp Resection

In an off-clamp resection, the renal artery is never clamped and all renal parenchyma (and hence also the tumor) remains vascularized throughout the procedure. For safety, the renal artery is however often dissected and isolated, so it can be clamped in case of excessive bleeding.

From a semantic point of view, it is not to be confused with the 'zero ischemia' technique. Whilst off-clamp resection is the only true technique in which the kidney does not experience ischemia, the 'zero ischemia' term was coined by Gill et al [87] in case tertiary or higher order arterial branches were clamped as can be seen in Figure 2.23.c. At that time, the authors were unaware that techniques would evolve towards off-clamp resections and super selective clamping was referred to as 'zero ischemia'. We choose super selective clamping as more sensible term here.

Two randomized controlled trials (RCTs) and one prospective propensity matched analysis have studied the effect of renal artery clamping versus off-clamp partial nephrectomy on renal function.

The recent CLOCK trial multicentrically randomized 324 patients with bilateral kidneys, normal baseline renal function (Glomerular Filtration Rate (GFR) >60) and a solitary kidney tumor with RENAL score ≤ 10 to receive either an on-clamp or an off-clamp RAPN [63]. In the "off-clamp" group, 34% of patients were crossed over to on-clamp because

of excessive bleeding and 9% because the surgeon desired ischemia 'due to high complexity of the tumor'. No significant differences were seen in terms of estimated blood loss, transfusion rates and postoperative complications [89]. Warm ischemia time (WIT) for the on-clamp group was limited (median 14 minutes, interquartile range (IQR) 11-18). No significant difference in postoperative kidney function at 6 months was seen (median -6.2 ml/min [IQR -18 – 0.5] on-clamp versus -5.1 ml/min [IQR -14 – 0.1] off-clamp), nor at 12, 18 and 24 months, both in the intention-to-treat analysis and the per protocol analysis [63].

Likewise, Anderson et al. randomized 71 patients in a single-surgeon RCT between on- and off-clamp RAPN and found no significant difference in 3-month postoperative GFR [90]. Sharma et al conducted a prospective propensity matched analysis of 205 patients (on vs off-clamp RAPN) and found no difference in post-operative renal function, intra- and postoperative complications. They did see a significant 2.9% increase for blood transfusion and a 9.2% increase in conversion to radical nephrectomy in the off-clamp group [88].

We can conclude that most patients undergoing RAPN with contralateral healthy kidney will experience little clinical impact on renal function as estimated by GFR when undergoing either an off- or on clamp RAPN as long as clamping times are limited. Nonetheless, subclinical impact as measured by renal scintigraphy is real when warm ischemia exceeds 10 minutes [65]. As such, current clinical evidence suggests on-clamp partial nephrectomy to be a valid and more conservative surgical approach, with accompanied lower bleeding risk. Similar renal function outcomes between off- or on clamp groups might not hold in case of complex tumors or multiple unilateral tumors, where long clamping time can be expected. Likewise, patients with a solitary kidney, bilateral tumors or pre-existing CKD [15] require special attention and further research on the effect of ischemia time and volume in this more vulnerable population is warranted [15].

Superselective Clamping = "Zero Ischemia"

As depicted in Figure 2.23.b and c, selective arterial clamping can balance the risks of bleeding with the avoidance of unnecessary healthy tissue ischemia. In superselective clamping, only the tumor-feeding renal vessels are temporarily clamped, to further minimize the healthy ischemic volume and approximate the off-clamp situation. In this technique dating back to 2011 [87], tertiary or higher order branches of the renal artery are dissected. However, the main enigma here remains how to determine up front which vessels need to be dissected/clamped and if this dissection is worth the accruing risks of bleeding and increased operative time. Gill et al. who originally proposed this technique have been using 3D models since 2012 to facilitate this decision [91]. Near-infrared imaging and indocyanine green (ICG) administration was also used in later studies to determine if the clamping was successful at the kidney surface level before starting resection. This showed that a purely cognitive clamping-position estimation does not always establish an avascular resection [92]. Indeed, the clamping strategy is solely based on the surgeon's assessment of which vessels are perfusing the tumor. In lateral rim tumors for instance, vessels are not always connected to the tumor region due to limits in CT imaging resolution. Thus, perfusion needed to be roughly estimated by a 3D 'cognitive region fusion' of nearby vessels. This in turn increased the interest in the development of techniques which could facilitate the estimated perfusion regions per artery.

The first simulation of perfusion regions in 3D renders can be traced back to 2018 [93]. However, no details on the perfusion algorithm or validation were provided. Different perfusion zones are separated by straight planes as can be seen in Figure 2.24.c and d. Each vessel was estimated to perfuse the same perfusion volume with a subsequent linear percentage split (Figure 2.24.a and b). This can also be seen as the way a surgeon would mentally reconstruct his clamping strategy while solely looking at the bidimensional images or 3D models without any functional information on perfusion. However, as tumors are not seldomly perfused by different arterial branches, this approach quickly proved to be overly simple and inaccurate. On one hand, it is incapable to estimate on one hand possible zones of bleeding as the cut-offs are just planar. On the other hand, these old perfusion models are inadequate in providing an informative decision on the amount of ischemic healthy tissue volume compared to tumor ischemia volume. In the same time window, commercial solutions started to provide “virtual clipping tools” for partial nephrectomy (e.g. Visible Patient (Strasbourg, France), FujiFilm Synapse (Tokyo, Japan),...). Nonetheless, these solutions had no clinical validation and use of these perfusion tools was mostly at the surgeon’s own risk. As such, this perfusion information was more an optional additional feature on top of the 3D patient specific anatomical model rather than an informative surgical decision tool.

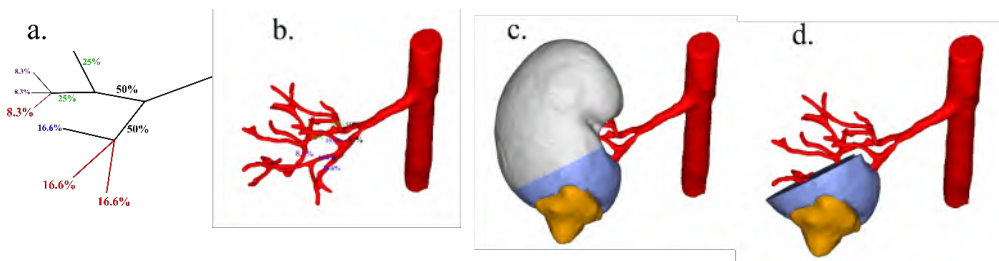


Figure 2.24: Exemplary sketch of first efforts in determining clamped volumes to maximize selective clamping. Per subsequent branch, equal splits of perfusion volumes were assumed.

These pitfalls, in combination with the zeitgeist of the importance of selective clamping, was one of the key drivers to develop and validate our own, patient-specific, perfusion zone predicting algorithm (see chapter 3.1). This algorithm is based on mathematical models which include 3D segmentations and several patient-specific arterial features to calculate volumes of the regions of interest in a completely different way than Figure 2.24. More specifically, our algorithm calculates geometrically which parenchyma is located closest to which vessels in three dimensions. From this, the algorithm deduces which vessel perfuses which kidney volumes. Apart from providing more precise volume information per arterial branch, preliminary results have also shown it holds potential in providing information where a surgeon might expect bleeding during tumor resection if the tumor volume is not completely ischemic. In parallel, Amparore et al have more recently published a similar track [94]. Whilst they also make use of a region growing approach which assigns voxels to the nearest vessels, they choose to assign parenchyma to the nearest vessel in the axial plane rather than considering the 3D vessel geometry. In the axial slice, a 3D voxel can only relate to arteries transecting this plane but not to arteries which cross in lower or higher axial slices. These arteries are not readily visualized in the current axial slice but their 3D distance can theoretically be shorter.

Minimizing Warm Ischemia Time

Early Unclamping

In early unclamping, perfusion is restored not after the outer renorrhaphy but already after internal renorrhaphy [95]. Some observational series demonstrated a 5.6 minutes median time reduction in WIT [96]. A meta-analysis of a handful observational series on laparoscopic and robotic PN calculated an increase in mean blood loss of only 37 mL after early unclamping with no difference in transfusion rates or complications. Hence, early unclamping is safe to use when technically possible and diminishes WIT. Furthermore, it provides the surgeon with feedback on hemostasis after internal renorrhaphy.

Cold Ischemia

When longer warm ischemia times (>25 minutes) are expected, reducing the kidney metabolism through cooling of the kidney may limit the parenchymal damage. Several techniques exist to apply this so-called 'cold ischemia'. Ice slush can be placed around the kidney, but this is more complex in minimal-invasive surgery and therefore has not been widely adopted [97]–[99]. In the laparoscopic setting, cold saline surface irrigation [100], retrograde cooling through the ureter [101] and intra-arterial cold perfusion [102] have been performed. However, no data is currently available comparing these different cooling techniques in terms of kidney temperature and postoperative renal function in minimal invasive surgery. Marberger et al in 1980 [103] compared topical ice slush to transarterial cold perfusion in 1980 during hypothermic nephrolithotomy. Postoperative kidney function decreased less in the perfused group (-19.4% at 2 weeks; -7.9% at 6 months) than in the topical group (-30.3% at 2 weeks; -29.8% at 6 months). As such, intra-arterial cold perfusion might deliver a more homogeneous renal parenchyma cooling compared to topical cooling. A more recent systematic review and meta-analysis found no significant difference between cold and warm ischemia in terms of blood loss, surgical margins and postoperative renal function in PN. However, the number of included studies and patients was low, as was the level of evidence (Oxford level of evidence 4) [104]. The above studies relate to laparoscopic PN and intra-arterial cooling had not yet been applied in the robotic setting. Given the low evidence above, the remaining enigma of long clamping times for highly complex lesions and the introduction of new robotic techniques such as renal auto-transplantation [105], we evaluated the feasibility and safety of intra-arterial cooling during RAPN for highly complex lesions which might otherwise result in radical nephrectomy. We refer to chapter 3.2. for a more in depth discussion.

In summary, currently no strong evidence exists which favors one ischemia technique over the other. The surgeon should balance acceptable ischemia time, limited ischemia zone, operative risks and surgical duration, while prioritizing maximal oncological control. 3D models including perfusion zone estimations can help facilitate this decision.

2.5.7. Tumor Resection – Minimal Healthy Tissue Resection

As discussed above, nephron sparing surgery or the maximization of healthy renal tissue is one of the strongest modifiable predictors for postoperative renal function, provided that extended ischemia time is avoided. NSS has expanded its application from an imperative indication in case of singular kidneys, CKD or hereditary tumours, towards the elective setting for both T1a and T1b/T2 tumors [106].

NSS can be performed to different extents as depicted in Figure 2.25. The Figure 2. depicts from bottom to top how NSS has evolved and how healthy tissue preservation has been maximized throughout the years. Originally, a 1-cm healthy tissue border resection was advised to achieve negative margins. This however implied increased risk of collecting system injury, longer WIT and damage to more healthy tissue [107].

Resection strategies have effectively been shown to impact the treatment of patients localized renal masses. A prospective multicentric study by Minervini et al [106] even found that the resection technique was the most significant predictor of positive surgical margins and one of the strongest predictors of complications such as acute kidney injury, surgical complications of grade ≥ 2 , and failure to achieve the trifecta.

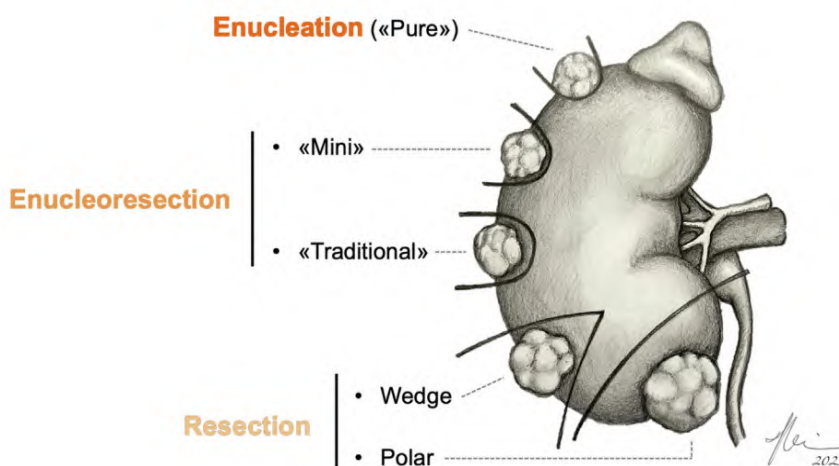


Figure 2.25: Different resection strategies for nephron sparing surgery. Derived from Bertolo et al. 2023, European Urology Open Science [59].

The maximisation of NSS culminates in so-called tumor enucleation (TE). From a pathological point of view, tumor enucleation leverages the presence of a fibrous pseudocapsule present in most renal tumors, together with histologic changes at the interface of the tumor-parenchyma [108]. The goal is to remove the tumor primarily through blunt dissection, following the natural cleavage plane between the peritumoral pseudocapsule and the renal parenchyma, without removing any visible healthy renal tissue. Positive surgical margins after tumor enucleation are consistently low, making it at least non-inferior to standard partial nephrectomy in this regard [109]. Robotic tumor enucleation is even considered safe in case of pseudocapsule infiltration by providing a "microscopic" layer of healthy renal tissue beyond the peritumoral pseudocapsule [110].

Surgeons in favour of TE also argue that it has several potential other advantages to "standard" partial nephrectomy (i.e. enucleoresection, wedge or polar resection) without

compromising oncologic safety [111]. It allows for optimal visualization of the tumor contours, enabling the resection of only a microscopic amount of healthy renal tissue which can reduce the risk of positive surgical margins [112]. Additionally, TE can minimize the risk of damage to the urinary collecting system and/or renal sinus, particularly for anatomically complex, hilar renal masses [111]. Apart from this, TE also supports nephron-sparing renorrhaphy, particularly during robotic-assisted partial nephrectomy (RAPN), as well as facilitates anatomical nephron-sparing renal reconstruction. This is important for highly complex and/or hilar tumors where reconstruction can be difficult (see chapter 3.2.).

Despite a possible contra-intuitive gut feeling, the evolution of going closer and closer to the tumour through TE instead of the classical resection has shown several benefits. A recent systematic review has shown that TE facilitates the dissection and reduces complication risks, operative time as well as the need for arterial clamping. TE is found to be equally oncologically safe with respect to surgical margins and positively impacts post-operative renal function [59].

Despite robust evidence in support of TE in open and robotic partial nephrectomy, some experts remain sceptical about its advantages, arguing that it may lead to insignificant differences in postoperative renal function and complications at the cost of a higher risk of tumour violation (95–97). Even in the era of accruing evidence for TE, intentionally taking a healthy tissue rim can be interesting in specific indications, such as tumours with an "infiltrative" growth pattern, which may indicate a more aggressive histology. Likewise, tumors without pseudocapsula such as papillary RCCs or complex cystic lesions, might not be most suitable for pure TE. Hence, decision-making for resection methods in patients undergoing RAPN should take into account both patient and tumour characteristics [113].

As the debate is ongoing, the various resection strategies including tumor enucleation, enucleoresection, and wedge resection as depicted in Figure 2.25, still coexist and are in active use. These techniques have often been used interchangeably which sometimes hampers a straightforward comparison of surgical series [59]. To address this issue, Minervini and colleagues [114] developed a standardized reporting system called the Surface-Intermediate-Base (SIB) margin score, which allows for a more meaningful comparison of PN series. Additional to the SIB margin score, the surgeon's intent should be taken into account. The unique features of the tumour's interface with the surrounding tissue provide a consistent and identifiable "anatomic dissection plane" as discussed earlier, regardless of whether a small amount of healthy tissue is planned to be removed or not. As such, apart from SIB margin score, the tumor removal can also be broadly classified as either anatomical (when it is the surgeon's intent to explicitly follow this plane and hence performs an enucleation) or non-anatomical (in which the surgeons dissect through healthy tissue and hence performs a "resection"). Nevertheless, a standardized definition of "anatomical resection" is lacking [59].

2.6. State-of-the-art in Augmented Reality Surgery

Despite a rather premature technologic state of Augmented Reality during RAPN, several research groups have achieved clinical RAPN A.R. integration [115]. The key technological challenge to be solved is the correct mapping or registration of a static pre-operative 3D model, to a continuously moving and deforming renal anatomy during surgery. This requires both a correct orientation of the 3D model, as well as a subsequent model deformation to the altered anatomy. The altered surgical anatomy finds its origin in the pneumoperitoneum induction [116], flank positioning [117] and tissue dissection (e.g. tumor removal) [118]. Figure 2.26 provides an overview of the three main approaches investigated to achieve successful A.R.. As discussed in section 2.5.4., preliminary clinical evidence is available on using A.R. during RAPN. It is however important to note that these in-patient trials have been performed with the least technologically advanced registration technique which is manual registration. Here, a human operator continuously adjusts and realigns the preoperative model to the moving intraoperative field using gestures (mouse, touch screen, hand tracking). The A.R. testing performed in this work also uses manual model registration. Manual registration is the most reliable method up to present. However, it is certainly not considered the most sustainable, given the dependency on an extra operator with technical and clinical knowledge for only a small procedural part.

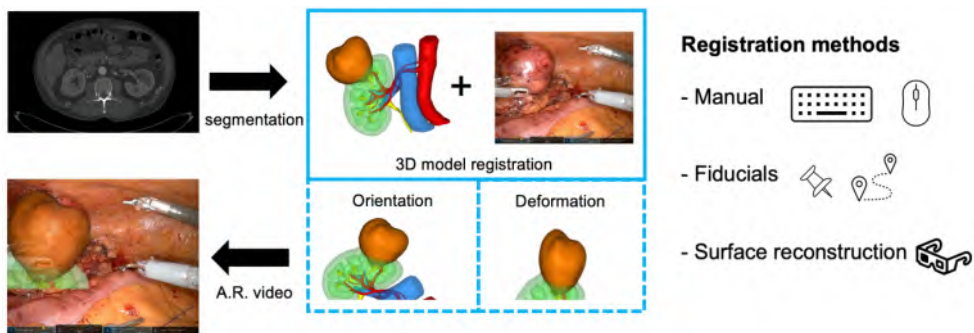


Figure 2.26 Registration techniques used during Augmented Reality RAPN

Methods using automated orientation and deformation are therefore the way forward. These can be broadly split up into the use of fiducials and the use of the anatomical surface. In fiducial-based registration, fiducials (e.g. charuco squares [119]) are inserted inside the abdominal cavity and these are subsequently tracked in an attempt to get a clear sight on how and where the anatomy is shifting and deforming [116]. Whilst these methods have proven to be robust, the extra steps add to the total operation duration and can be considered bothersome for clinical implementation [120].

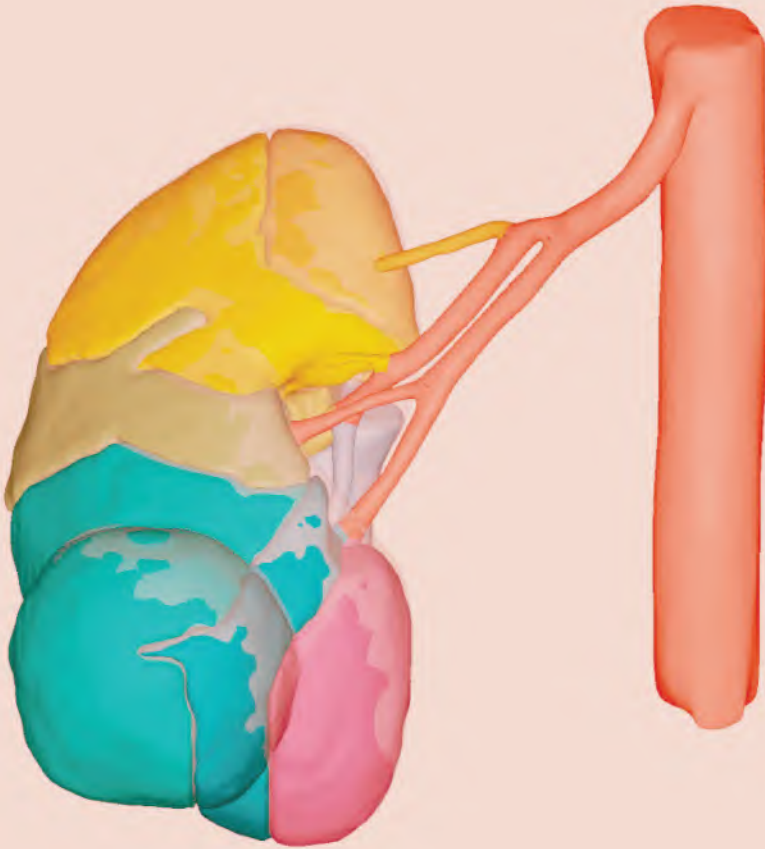
Surface reconstruction methods typically do not use any markers. These methods reconstruct a 3D map of the surgical surface after which they map the 3D models into this surface. This problem can be further broken down into three basic steps. Firstly, it is important to know which region is of interest inside the viewpoint, secondly the 3D map of this zone of interest should be created and thirdly the preoperative 3D model should be registered to exactly that anatomical surface, preferably in real-time. When creating the 3D map, 2 main methods have been applied. The first approach implies a manual contouring of the surface with an object, e.g. a stylus or instrument, to create a 3D point map. This however requires additional gestures and thus adds to the operative time. The

second approach reconstructs the 3D map from the stereoscopic vision inside the robotic surgery console and instantly creates a point cloud of the full surgical view.

A commonly known approach for surface reconstruction is the use of simultaneously localization and mapping (SLAM) techniques [121], [122]. SLAM leans most towards clinical integration but is also computationally the most intensive. Furthermore, it has other bottlenecks such as tool occlusion, where tissue which is behind the robotic instruments cannot be rendered as it is simply not visualized at that point. Neural radiance fields (NeRFs) however pose an interesting path forward and have furthermore been shown to cope well with the instrument occlusion problem during robotic surgery [123]. Nonetheless, NeRFs are not yet able to generate new viewpoints instantaneously. More recent work has demonstrated the potential of 3D Gaussian splatting, which allows for real-time synthesis of new, previously unseen 3D viewpoints and at an unseen high-definition resolution [124]. Despite being state-of-the-art in terms of resolution and real-time application, 3D Gaussian splatting still requires several minutes of network training after which it can be applied in real-time, making it less suitable at present to cope with continuously changing surgical scenes. Also non-SLAM methods hold potential and include the utilization of rectified stereo image key frames with key/feature points [118], point clouds from reconstructed depth maps and registration of pre-operative computed deformations to intra-operative meshes [125].

Even if perfect registration becomes achievable, A.R. is still not ready for primetime. As can be seen in Figure 2.13.b and Figure 2.26, the projection of the 3D anatomy induces instrument occlusion. This implies that the surgeon no longer visualizes his/her instruments during A.R. guided surgery, which is in essence a more hazardous situation than without A.R. An important contribution of this thesis has been solving the instrument occlusion problem during robotic surgery A.R. by means of A.I. We refer to chapter 5 for an in-depth discussion.

In conclusion of this chapter and in my opinion, the techniques discussed above, in combination with the new technologies introduced throughout this work, hold the potential to revolutionize surgical care. As we enter the era of personalized medicine, our surgical strategy should be adapted on a per patient basis. Novel techniques and tools are here to exactly serve the patients and their outcomes. We hope this work can provide insights into the future direction of surgical strategies and technologies in RAPN.



NEPHRON SPARING SURGERY

03

*« The digitization of human beings
will make a parody out of doctor knows best »*

- Eric Topol

This chapter has been adapted from:

- A Novel Three-dimensional Planning Tool for Selective Clamping During Partial Nephrectomy: Validation of a Perfusion Zone Algorithm
P De Backer*, S Vermijs*, C Van Praet, P De Visschere, S Vandenbulcke, A Mottaran, CA Bravi, C Berquin, E Lambert, S Dautricourt, W Goedertier, A Mottrie, C Debbaut, K Decaestecker - *shared first authors
European Urology 2023
- Robot Assisted Partial Nephrectomy using Intra-Arterial Renal Hypothermia for Highly Complex Endophytic or Hilar Tumors: Case series and Description of Surgical Technique
P De Backer, J Vangeneugden, C Berquin, S Vermijs, P Dekuyper, A Mottrie, C Debbaut, T Quackels, C Van Praet, K Decaestecker
European Urology Open Science 2023

3.1. Preoperative Prediction of Selective Arterial Clamping Strategy

3.1.1. Abstract

Background

Selective clamping during robot-assisted partial nephrectomy (RAPN) requires extensive knowledge on patient-specific renal vasculature, obtained through imaging.

Objective

Validate an in-house developed perfusion zone algorithm which provides patient-specific 3D renal perfusion information.

Design, Settings, and Participants

Between October 2020 - June 2022, 25 patients undergoing RAPN at Ghent University Hospital were included. 3D models, based on pre-operative CT scans, showed the clamped artery's ischemic zone, as calculated by the algorithm.

Surgical Procedure

All patients underwent SC during RAPN. Indocyanine green (ICG) was administered to visualize the true ischemic zone perioperatively. Surgery was recorded for postoperative analysis.

Measurements

The true ischemic zone of the clamped artery was compared with the predicted ischemic zone by the algorithm through two metrics (i) total ischemic zone overlap and (ii) tumor ischemic zone overlap. Six urologists assessed metric 1, metric 2 was objectively assessed by the authors.

Results and Limitations

In 92% of the cases, the algorithm was sufficiently accurate to plan a selective clamping strategy. Metric 1 showed an average score of 4.28 out of 5. Metric 2 showed an average score of 4.14 out of 5.

A first limitation is that ICG can only be evaluated at the kidney surface. A second limitation is that mainly patients with impaired renal function are expected to benefit from this technology but contrast-enhanced CT is required at present.

Conclusions

The proposed new tool demonstrated high accuracy when planning selective clamping for RAPN. A follow-up prospective study is needed to determine the tool's clinical added value.

3.1.2. Introduction

Currently, partial nephrectomy (PN) is considered the surgical treatment of choice for small renal masses. All T1 tumors and if technically feasible, T2 tumors associated with solitary kidney or chronic kidney disease should ideally be treated with a nephron-sparing approach [126]. Apart from an oncologic resection, RAPN balances minimal injury to the healthy renal parenchyma with the risk of complications such as bleeding [66]. The main origins of bleeding are twofold: direct vessel injury during hilar dissection and bleeding during tumor resection due to insufficiently clamped arterial perfusion.

The arterial clamping technique is suggested as one of several factors impacting healthy parenchyma injury during PN and influencing post-operative renal function [127]–[129].

Three main clamping techniques are currently used: (i) a full-clamp approach, imposing ischemia to the full kidney and tumor with minimal bleeding risk during tumorectomy, (ii) a selective-clamping (SC) approach which ideally induces maximal ischemia to the tumor and minimal ischemia to healthy parenchyma [91], [130], (iii) the off-clamp approach with no kidney or tumor ischemia but higher risk of uncontrollable bleeding.

Antonelli et al. [63] recently showed that off-clamp partial nephrectomy has no benefit on renal function when compared to on-clamp. Likewise, Long et al. [131] showed that SC does not provide better renal function preservation compared to an on-clamp approach with early unclamping.

Nevertheless, both studies assessed patients with a healthy contralateral kidney, which might mask the effect of tissue ischemia or act as a buffer during the ischemic event. Furthermore, the SC vessel selection in the latter study was pure expert opinion based on two-dimensional (2D) CT information. Although not statistically significant, 1 out of 16 cases was converted to radical nephrectomy due to bleeding during tumor resection, implying incorrect 'cognitive' selective clamping.

As more evidence accrues, SC can still be a good intermediate between tumorectomy bleeding risk and healthy tissue ischemia, with specific applications for cases of expected longer clamping times, impaired preoperative renal function and solitary kidneys.

Applying SC safely requires extensive knowledge on patient-specific renal vasculature for safe target vessel isolation, as well as reliable perfusion zone estimation. Previous studies confirm renal vasculature to be highly variable where one artery can perfuse multiple renal segments [8], [32].

Previous studies comparing 2D cross-sectional evaluation on CT/MRI versus three-dimensional (3D) reconstructions, suggested an improved tumor complexity understanding [80], [132], [133] and impact on the clamping approach, moving from initial full-clamp towards more SC approaches [134], [135]. Amparore et al. [136] even found improved post-operative renal function when using 3D models to plan PN. However, these models only provide 3D anatomical information whilst the clamping strategy estimation is still performed cognitively by the surgeon based on the 3D model. Other researchers tried tackling the latter problem by estimating perfusion zones using a Voronoi diagram approach [137], [138], but clear validation of this methodology is lacking. Wang et al. [139] recognized the inability to properly validate predicted perfusion zones in their study. The Voronoi diagram is also integrated in the Synapse 3D Kidney Analysis software (Fujifilm Medical Systems U.S.A., Inc.), where it is described as the approximation of vascular territories, however, again without reported validation [140].

Therefore, this study focuses on (i) adding perfusion information to the anatomical 3D information using an in-house developed perfusion zone algorithm (PZA) and (ii) validating this approach. The PZA calculates the perfusion zones of each renal arterial branch and visualizes these zones on the 3D model. Next, the ability of the proposed PZA to predict renal perfusion zones was validated through comparison with intraoperative indocyanine green (ICG) administration and imaging.

3.1.3. Materials and Methods

All patients treated for non-metastatic RCC through Robot-Assisted PN (RAPN) at Ghent University Hospital between October 2020 and June 2022 were consecutively enrolled. The study was approved by the ethical committee and participants signed a written informed consent allowing data collection.

Patient Inclusion

Patients were included in the study when a CT scan with early arterial phase was available with maximal slice thickness of 1.5 mm. Out of 69 patients eligible for RAPN, 61 received a preoperative CT scan according to an optimized study protocol consisting of a four-phase contrast-enhanced CT scan with a maximal slice thickness of 1.5 mm (range 0.6 - 1.5 mm) and a maximal pixel size of 0.94 mm (range 0.63 - 0.94 mm). If thoracic staging was not performed yet, this was combined with the 4-phase abdominal CT acquisition. The four phases were (i) blanco, (ii) arterial, (iii) venous and (iv) excretory. After a blanco phase acquisition, iodinated contrast was intravenously administered. Bolus tracking in the aorta at the level of the diaphragm triggered the start of the arterial phase. Subsequently, venous and excretory phases were acquired respectively 90 seconds and 4.5 minutes after bolus administration. Insufficient contrast filling of the renal calyces and ureter on this last scan required another acquisition after 15-30 minutes.

Study Design

The four-phase CT scan was used to create a 3D model by segmenting all relevant structures using Mimics Innovation Suite (Materialise, Belgium). The parenchyma and arteries were segmented using the arterial phase. The venous phase was used to segment the veins and delineate the tumor and cysts (if any). The excretory phase facilitated the segmentation of the pelvi-calyceal system (pelvi-calyceal system). All structures were aligned using the arterial phase and subsequently 3D reconstructed. This workflow is visualized in Figure 3.1.

CORONAL CROSS-SECTIONS ON THE ARTERIAL PHASE

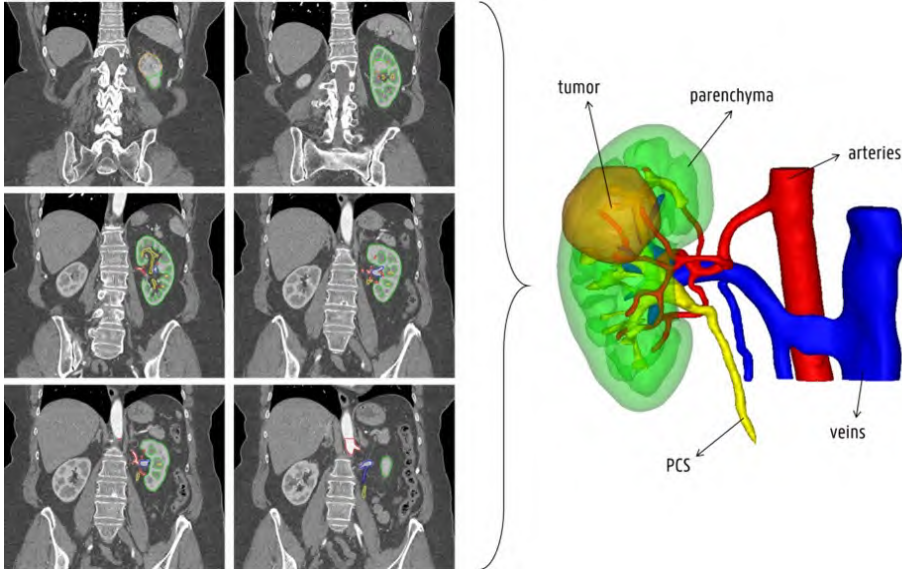


Figure 3.1: All structures (tumor, parenchyma, cysts (if any), arteries, veins and pelvi-calyceal system) are segmented in Mimics (Materialise, Belgium) using the four different phases of the CT-scan. Subsequently, all segmentations are aligned on the arterial phase (left) and 3D reconstructed (right). Identical colors are used on both panels.

Procedures were performed by a highly experienced RAPN surgeon (K.D. 346 RAPN and 1325 RA surgeries) and a beginning RAPN surgeon (C.V.P. 18 RAPN and 283 RA surgeries, trained and supervised by K.D.). Both surgeons used the anatomical 3D model without perfusion information to determine if a selective clamping strategy was feasible. RAPN was carried out according to reported surgical techniques [141], including multiport transperitoneal RAPN, hilar dissection, vessel loop marking of the main renal artery and required selective arterial branch(es), tumor enucleation or enucleo-resection, renorrhaphy with the sliding Hem-o-lok technique and early unclamping. Indocyanine green (ICG) was administered intravenously immediately after clamping to check the ischemic zone by means of near-infrared fluorescence light imaging (Firefly - Intuitive Surgical™, California, USA). Out of 69 included patients, 23 patients were excluded due to lacking video recording, 19 procedures were performed without selective clamping (11 full clamp procedures, 5 off clamp procedures, 3 procedures with arterial intra-corporeal cooling (Chapter 3.2.), and 2 procedures were performed without ICG administration. The inclusion protocol is described in Figure 3.2.

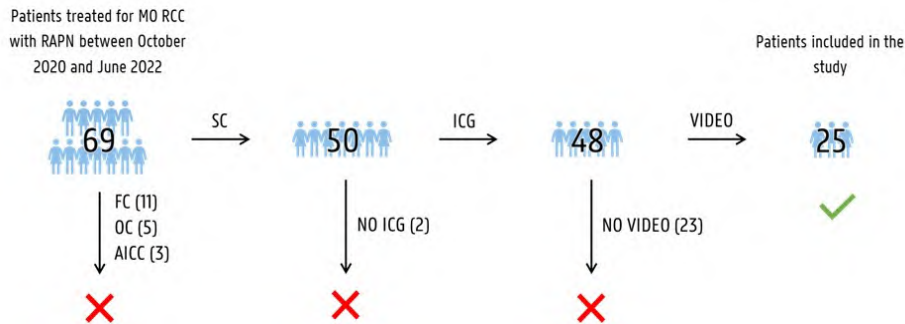


Figure 3.2: Patient inclusion. Between October 2020 and June 2022, 69 patients were treated at Ghent University Hospital for localized renal cell carcinoma (M0 RCC) with robot-assisted partial nephrectomy (RAPN). Patients were only included when they were treated with selective clamping (SC), when indocyanine green (ICG) was administered and when the surgical video was properly recorded. This led to the inclusion of 25 patients. (FC: full-clamp; OC: off-clamp; AICC: arterial intra-corporeal cooling)

After the surgery, the 3D model is used as an input to the in-house developed PZA, which adds the perfusion information to the 3D model. The algorithm assigns zones in the parenchyma and tumor to the closest artery by implementing our own region growing method. The workflow is visualized in Figure 3.3. The STL-files of the segmented structures were exported from Mimics and served as input for the automated python-based algorithm (Figure 3.3a). Arterial centerlines were subsequently digitally generated (VMTK - vmtk.org) and were used to uniquely label all renal arterial branches (Figure 3.3b). These labels were then used to initiate a region growing algorithm (Figure 3.3c). First, a 3D grid (100 x 100 x 100 voxels) was created around parenchyma and tumor. The 3D models of the structures in this grid were divided into voxels of equal size using a 3D mesh voxelizer [142], [143]. Then, the labeled arterial branches were introduced in the grid, by using the voxels circumscribing the centerline points as seeds. In iterative steps, the seeds grew in all six orthogonal directions (up/down, left/right, front/back) to assign all grid voxels of parenchyma and tumor to the closest labeled arterial branch. The output of the PZA was a 3D model of the patient-specific anatomy divided into perfusion zones (Figure 3.3d). Each perfusion zone corresponded to the tissue (healthy parenchyma and/or tumor) perfused by the corresponding arterial branch.

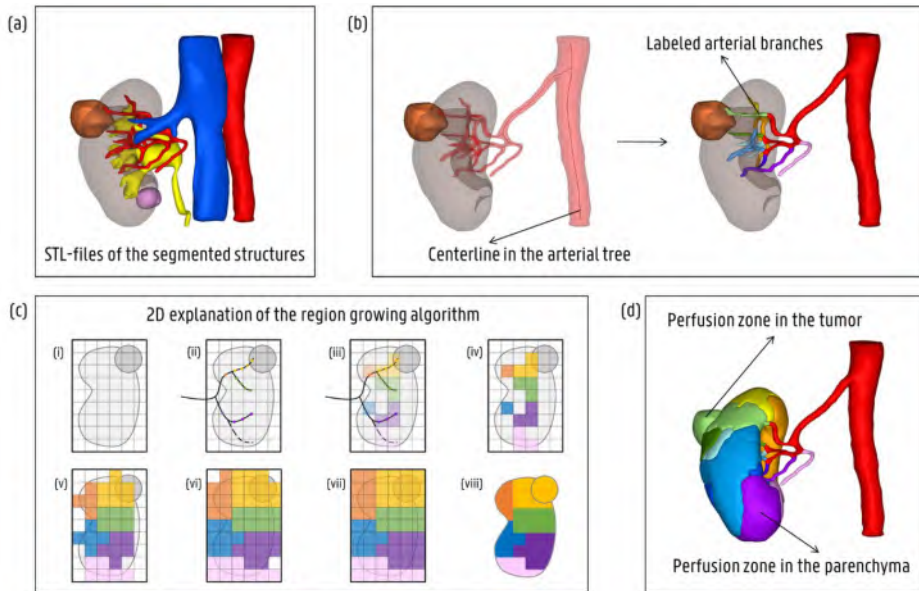


Figure 3.3: The different steps in the perfusion zone algorithm. (a) The 3D model is used as input. (b) Centerlines are constructed in the arteries to label the branches of the arterial tree. (c) The region growing algorithm is initiated in a voxelized grid around the parenchyma and tumor. The labeled centerline points of each branch are used as seeds. The seeds grow in all six orthogonal directions to divide the entire grid in perfusion zones. (d) The perfusion zones in the parenchyma and tumor are labeled in the same color as the corresponding perfusing branch.

The PZA was used for all included patients to determine the perfusion zones of the arteries that were clamped during SC.

Perfusion Zone Algorithmic Performance

Surgical videos were assessed post-operatively to compare the true ischemic zone, visible through ICG administration, with the predicted ischemic zone by the PZA. This comparison was graded using two different metrics. The first metric was the correctness of the total ischemic zone on both healthy parenchyma and tumor surface, assessed by six independent specialists (five urologists (C. A. Bravi, C. Berquin, E. Lambert, S. Dautricourt, W. Goedertier and one resident (A. Mottaran)), who had to rate the resemblance of the true ischemic zone with the predicted ischemic zone on a five-level Likert scale (1: very poor; 2: poor; 3: average; 4: good; 5: very good). They received the guidelines displayed in Figure 3.4 (left panel).

The second metric was the correctness of the ischemic zone at the tumor surface. The surgical video was used to detect the level of ischemia on the tumor's surface (100% ischemia; >50% ischemia; <50% ischemia; 0% ischemia). This was compared to the level of ischemia at the tumor surface predicted by the PZA and then translated into a score from 0 to 5. The better the predicted and true ischemic zone corresponded, the higher the score. Keeping in mind that it is better to underestimate tumor ischemia than to overestimate it (to avoid perioperative complications such as excessive bleeding), a scoring grid was developed to objectively grade the second metric, as shown in Figure 3.5 (left upper panel). The diagonal of the scoring grid (i.e. equal level of ischemia in both ICG video and 3D model) represents a score of 5. A minor deviation between the predicted and true level of ischemia led to a score of 4 (i.e. mild underestimation of the level of ischemia by the PZA) or 3 (i.e. mild overestimation of the level of ischemia by

the PZA). A major deviation led to a score of 2 (major level of ischemia underestimation) or 1 (major level of ischemia overestimation). A completely opposite prediction of the level of ischemia by the PZA resulted in a score of 0.

3.1.4. Results

Patients' characteristics are summarized in Table 3.1. All patients had singular renal masses for which SC was used. In two patients (8%) with multiple main renal arteries, a first generation blood vessel was clamped (i.e. one of the main renal arteries). In 10 patients (40%) a second generation and in 12 patients (48%) a third generation arterial vessel was clamped. In one patient (4%), superselective clamping of the fourth generation was performed. One case (4%) required conversion to full-clamp due to excessive blood loss during tumor enucleation. Total estimated blood loss (EBL) was 120 ml. We report one EBL outlier of 1900 ml, however with a postoperative 10.2% hematocrit drop without blood transfusion, implying a potential EBL overestimation. No perioperative instability was detected here, accordingly with no conversion from SC to full-clamp. The hilar and main renal artery dissection time was 16 minutes (range: 10 - 29), with a median additional selective artery dissection of 16 minutes (range: 2 - 24). The dissection time was only reported in 19 cases: in six cases, the dissection of the hilus and/or selective arteries was not recorded. The median warm ischemic time (WIT) was 18 minutes (range 10 - 36). No severe postoperative complications (Clavien-Dindo grade III-V) were reported. Median follow-up time is 7 months (range 1d – 19mo), while 11 patients have at least 1 year follow-up. Table 3.1 reports the pre- and postoperative levels of hemoglobin (Hb), serum creatinine (sCr) and estimated glomerular filtration rate (eGFR). No significant changes (Wilcoxon signed-rank test; p-value > 0.05) in renal function were measured postoperatively compared to preoperative. Some blood values are missing due to recent time of surgery. Two cases (8%) had focal positive surgical margins after tumor enucleation. No patient had disease recurrence.

Age (years)	median	67
	range	38 - 83
Gender	female	10 (40%)
	male	15 (60%)
Affected side	left	12 (48%)
	right	13 (52%)
Maximal lesion diameter (mm)	median	31
	range	15 - 84
PADUA score	low (6 - 7)	10 (40%)
	medium (8 - 9)	10 (40%)
	high (10 - 14)	5 (20%)
Clamping technique	selective	24 (96%)
	selective to full	1 (4%)
Clamped generation of the arterial tree First generation: main renal artery	first	2 (8%)
	second	10 (40%)
	third	12 (48%)
	fourth	1 (4%)
Warm ischemic time (min)	median	18
	range	10 - 36
Early unclamping	yes	20 (80%)
	no	5 (20%)
Tumor resection technique	enucleation	23 (92%)
	enucleo-resection	2 (8%)
	resection	0 (0%)
Estimated blood loss (ml) – 24/25*	median	137.5
	range	5 - 1900
Operative time in the robotic console (min) – 24/25*	median	150
	range	60 - 230
Dissection time hilus (min) – 19/25*	median	16

	range	10 - 29
Dissection time selective artery (min) – 19/25*	median	15
	range	2 - 24
Complications (Clavien-Dindo) Reported values: 30d – 25/25 90d post-op – 24/25*	no complications	22 (88%) - 24 (100%)
	grade I	2 (8%) - 0 (0%)
	grade II	1 (4%) - 0 (0%)
	grade III - V	0 (0%) - 0 (0%)
Surgical margin	negative	23 (92%)
	positive	2 (8%)
Blood values		
Hemoglobin (g/dl)		
Preop	median	14.5
	range	12.7 – 16.1
1-3d postop	median	12.3
	range	10.6 – 14.8
Change: 1-3d postop - preop	median	-1.6
	range	-4.2 – +0.1
Serum Creatinine (mg/dl)		
Preop	median	0.90
	range	0.62 – 1.51
1-3d postop	median	0.84
	range	0.55 – 1.57
Change: 1-3d postop - preop	median	-0.04
	range	-0.26 – +0.24
1mo postop – 20/25*	median	0.89
	range	0.61 – 1.60
Change: 1mo postop - preop – 20/25*	median	0.05
	range	-0.21 - +0.18
1yr postop – 11/25*	median	1.10

	range	0.66 – 1.58
Change: 1yr postop - preop – 11/25*	median	0.09
	range	-0.32 - +0.26
Estimated glomerular filtration rate (ml/min/1.73m ²)		
Preop	median	83
	range	45 - 90
1-3d postop	median	87
	range	44 - 90
Change: 1-3d postop - preop	median	0
	range	-12 - +23
1mo postop – 20/25*	median	79
	range	42 – 90
Change: 1mo postop - preop – 20/25*	median	-1
	range	-9 – +10
1yr postop – 11/25*	median	74
	range	42 – 90
Change: 1yr postop - preop – 11/25*	median	-3
	range	-22 – +25

* No data available of all 25 cases

Table 3.1: The pre-, peri- and postoperative characteristics of the 25 patients included in the study.

Metric 1, the visual inspection of the overlap of the ischemic zone of the clamped artery by the six independent specialists, resulted in an average score of 4.28 out of 5 (median: 5; range: 2-5; interquartile range: 4-5). This correlates with a score between good and very good on the proposed Likert scale. The score distribution over the 25 cases for all observers is visualized in Figure 3.4 (right panel). Four cases (16%) showed a consensus of 5 out of 5 among all six raters. Ten cases (40%) had a one-point range, eight cases (32%) had a two-point range and in three cases (12%), the observers disagreed with a range of three points. This large variability was detected in cases in which the predicted contour of the ischemic zone was situated on the tumor surface. A small deviation of the true ischemic zone was hence interpreted by some observers as very similar to the predicted ischemic zone (score of 5), but since this small deviation was on the tumor surface, some observers scored this as major deviations at tumor level (score of 2).

METRIC 1: VISUAL OVERLAP OF THE TOTAL ISCHEMIC ZONE

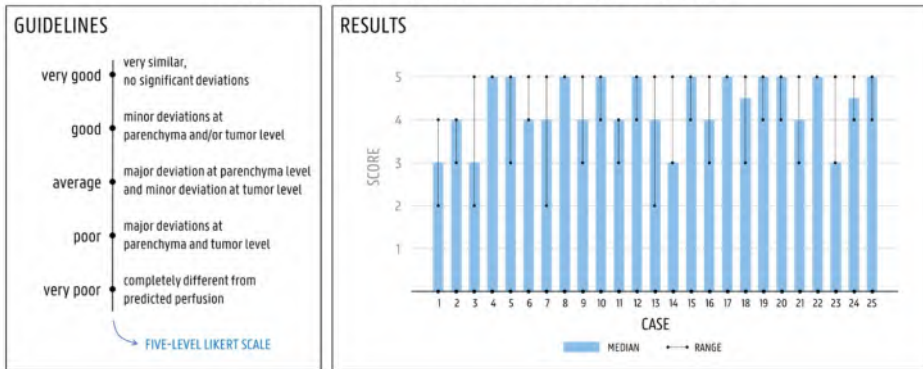


Figure 3.4: The first proposed metric to evaluate the performance of the perfusion zone algorithm. Six observers were asked to grade the visual overlap of the true and predicted total ischemic zone in the 25 cases on a five-level Likert scale. They received the guidelines seen in the left panel. In the right panel, the results (median and range) are visualized for each case.

Metric 2, the tumor surface ischemia parameter, resulted in an average score of 4.14 out of 5 (median: 5; range: 2-5; interquartile range: 3.5-5). Figure 3.5 presents the results (right upper panel) and provides four cases illustrating different scores (lower panel). This metric was used in 23 of the 25 cases, since two cases had endophytic tumors, making tumor surface ICG observations impossible. In two cases (8.70%), a score of 1 was obtained as the perfusion zone border was predicted close to the tumor area. Hence, a small deviation of this contour imposed a large shift on metric 2. In four cases (17.39%), a score of 3 was obtained. In three (13.04%) and fourteen (60.87%) cases, a respective score of 4 and 5 was obtained. No cases were found with a score of 0 or 2.

METRIC 2: TUMOR SURFACE ISCHEMIA

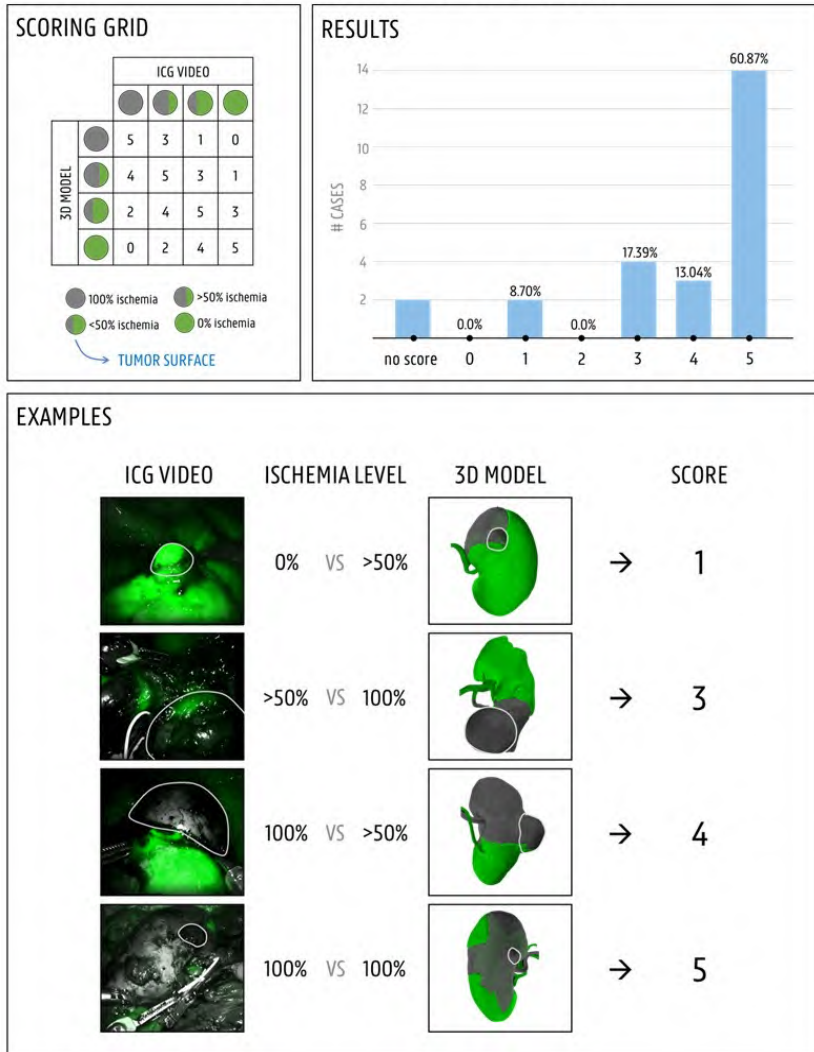


Figure 3.5: The second proposed metric to evaluate the performance of the perfusion zone algorithm. The scoring grid (left upper panel) was used to quantify this metric by comparing the predicted ischemic zone on the tumor surface with the true ischemic zone obtained from the surgical video with indocyanine green (ICG). If the ischemic zone was correctly predicted, a score of 5 was assigned. If the ischemic zone was wrongly predicted, a score between 0 (no overlap) and 4 (only minor deviation) was assigned, depending on the degree of deviation. The results are presented in the right upper panel. Two cases concerned an endophytic tumor, hence no score was given because ICG only shows surface perfusion. More than half (60.87%) of the cases got a score of 5. An example of each score is visualized in the lower panel. The tumor is delineated with a white contour.

When a score of 3 or higher is obtained on both metrics, the predicted perfusion zones are considered sufficiently accurate to plan a SC approach. This is achieved in 92% of the cases. A score of 4 or higher is considered highly accurate to plan a SC approach and is obtained in 68% of the cases.

3.1.5. Discussion

Preoperative knowledge of tumor arterial perfusion might facilitate SC decisions during RAPN. We report, to our knowledge, the first validation study of arterial clamping strategy prediction [137]–[139].

In this study, we developed a new perfusion zone algorithm based on our own region growing method and addressed the lack of validation by using ICG administration as a method to visualize the perfused areas. The performance metrics proposed in this study were defined to assess the predictions of the PZA. This demonstrated accurate prediction in 92% of the cases. Clinical outcome of the 25 patients also demonstrates that RAPN could be safely performed using SC.

As the aim of the study was investigation of the ability to correctly predict a selective clamping strategy rather than study functional outcomes, we did not focus solely on patients with solitary kidneys or impaired preoperative renal function, although these might benefit most from this technology. We also believe that patients with aberrant arterial anatomy such as polar arteries may benefit from this technology, provided that the algorithm can guarantee tumor ischemia based on the imaging in these selective cases and hence avoid hilar dissection.

This validation study shows that perfusion zone estimation is possible but has several limitations.

The PZA requires a contrast-enhanced CT scan with a good arterial phase as minimal requirement. In the targeted patient population, contrast nephrotoxicity can be an issue. Nevertheless, it is debatable to always have an arterial phase for adequate hilar dissection and detection of possible aberrant anatomy, as is performed in our center also outside the study protocol. In case of pre-operative eGFR <45 mL/min, pre- and post-scan intravenous hydration was administered to minimize nephrotoxicity. For these cases which might benefit most from selective clamping, initial tests with MRI imaging outside this study show potential technology transferability but need further validation.

No comparison was performed with an ICG-only arm. ICG can only provide surface perfusion information but provides no information on the 3D tumor resection bed. As such, we found our PZA approach to solve an unmet need, rather than duplicating the role of ICG. Nevertheless, a limitation is the lack of an objective parameter to assess tumor bed ischemia during resection. Due to venous circulation and blood spill, the tumor bed cannot longer be assessed with ICG after resection. Furthermore, the performance metrics could be improved if, during surgery, the entire kidney would be freed from the surrounding fat and captured from all angles with the endoscopic camera during ICG imaging. This would retrospectively allow an overlay with the predicted 3D model to evaluate the perfusion zones on the surface quantitatively instead of using the more subjective Likert scale (metric 1). However, entire kidney mobilization would unnecessarily increase surgical time and complexity. On top of this, capturing the entire kidney is not always feasible due to the limited field of view of the endoscopic camera. We also note that this is a proof-of-concept single center study with a small number of cases.

Despite the given limitations, this study shows that the proposed PZA based on a region growing approach is reliable and could provide support for the surgeon to decide whether SC is possible and determine the optimal SC strategy. As a next step, the added value of this preoperative information on the surgical strategy and clinical outcome should be investigated. A multicentric prospective randomized controlled trial, comparing 3D

models for selective clamping with and without perfusion information is underway to solve these pitfalls. Visual assessment of selective clamping efficiency should be performed by urologists with preferably no association to the center of development to avoid any form of confirmation bias.

3.1.6. Conclusions

This study illustrates that calculating and adding perfusion information to anatomical 3D models is sufficiently accurate to plan the SC strategy in 92% of the cases studied. Future studies should address optimization of the validation technique and further finetuning of the algorithm. A larger prospective study is needed to evaluate and confirm the added value of this new tool during surgical planning of RAPN procedures.

3.2. Maximization of Nephron Sparing Surgery through Intra-arterial Cooling

3.2.1. Abstract

Background

In partial nephrectomy for highly complex tumors with expected long ischemia time, renal hypothermia can be used to minimize ischemic parenchymal damage.

Objective

Describe our case series, surgical technique and early outcomes for robot-assisted partial nephrectomy (RAPN) using intra-arterial cold perfusion through arteriotomy.

Design, Settings, and Participants

Retrospective analysis of 10 patients with renal tumors (PADUA score 9-13) undergoing RAPN between March 2020 - March 2023 with intra-arterial cooling because of expected arterial clamping times longer than 25 minutes.

Surgical Procedure

Multiport transperitoneal RAPN with full renal mobilization and arterial, venous and ureteral clamping. After arteriotomy and venotomy, 4°C heparinized saline is administered intravascular through a Fogarty catheter to maintain renal hypothermia while performing RAPN.

Measurements

Demographic data, renal function, console and ischemia times, surgical margin status, hospital stay, estimated blood loss and complications were analyzed.

Results and Limitations

Median warm and cold ischemia time were 4 min (IQR 3 – 7) and 60 min (IQR 33 – 75) respectively. Median rewarming ischemia time was 10,5 min (IQR 6,5 – 23,75). Median pre- and postoperative eGFR values at least 1 month after surgery were 90 ml/min (IQR 78,35 – 90)) and 86,9 ml/min (IQR 62,08 – 90) respectively. Limitations include small cohort size and short median follow-up (13 months (IQR 9,1 - 32,4)).

Conclusions

We demonstrate the feasibility and first case series for RAPN using intra-arterial renal hypothermia through arteriotomy. This approach broadens the scope for minimal invasive nephron sparing surgery in highly complex renal masses.

3.2.2. Introduction

If technically feasible, nephron-sparing surgery through partial nephrectomy (PN) is the standard treatment for fit patients with T1-T2 renal masses [126]. The main goals of PN include complete tumor excision and minimal injury to the healthy renal parenchyma, whilst avoiding complications [66].

Robot-assisted PN (RAPN) has increasingly been adopted as it allows safe tumor resection and kidney reconstruction with similar oncological outcome and less morbidity for the patient compared to open surgery [54]. Main predictors for postoperative kidney function include the patients' pre-operative kidney function, the preserved renal parenchyma volume and warm ischemia time. Classically, maximal warm ischemia times of 20-25 minutes are targeted [97], [144]–[147]. Recent high-level evidence has also shown that the clinical impact of warm ischemia time is futile when staying below these thresholds [63]. However, Antonelli et al. did find statistically significant renal function impairment on renal scintigraphy at 6 months post-operative when clamping times exceeded 10 minutes [65]. This indicates that, at least in the first 6 months, warm ischemia does negatively influence renal metabolism and function. Nonetheless, the effect is subclinical and not noticeable when assessing global renal function with a healthy baseline renal function and normal contralateral kidney.

In highly complex cases such as completely endophytic, hilar or multiple unilateral tumors, clamping time during PN may easily exceed the 25-minute threshold, which may induce chronic kidney disease.

Several studies have investigated different renal hypothermia application methods. In open PN, ice slush can be positioned around the kidney. In minimal-invasive surgery (apart from kidney transplantation[148]), ice slush application is rather cumbersome and therefore not widely adopted [97]–[99], [149]. Alternative cooling techniques have been described for laparoscopic PN, including cold saline surface irrigation [100], ureteral retrograde cooling [101], and intra-arterial perfusion [102], [150]. Little evidence exists comparing different cooling techniques with no clear superior method [151]. Marberger et al. did report better postoperative GFR outcomes using intra-arterial cooling, compared to an ice slush technique [103]. Advantages of the intra-arterial approach for renal hypothermia include rapid, stable and homogenous decrease in kidney temperature, removal of any blood left in the kidney, prevention of intravascular coagulation and improvement of intraoperative visibility [152], [153].

Both Marberger [103] and Liu [150] used an endovascular femoral access with catheterization of the renal artery by an interventional radiologist. Femoral intra-arterial access before abdominal surgery is time consuming, logistically demanding and requires intra-renal administration of nephrotoxic contrast agents. Alternatively, the renal artery and vein can be incised and catheterized transperitoneally during surgery. This technique has been described by Gschwend et al. and Steffens et al. in open surgery [153], [154], by Simon et al. laparoscopically in a porcine model [155] and by Herrmann et al. laparoscopically in 2 patients [156]. Previously, we successfully used this technique for establishing cold ischemia in total intracorporeal robot-assisted kidney autotransplantation (tiRAKAT) [157], [158].

Here, we describe our initial experience applying transperitoneal intra-arterial renal cooling using arteriotomy during RAPN for highly complex small renal masses. We provide a step-by-step description of our technique. To our best knowledge, this is the first patient series of robotic transperitoneal intra-arterial cooling (IAC) for localized kidney cancer.

3.2.3. Design, Setting and Participants

This study focused on patients treated with intra-arterial renal hypothermia between March 2020 and March 2023 in 3 different tertiary setting hospitals.

10 patients were treated for complex renal tumors (PADUA 9-13) through RAPN. All cases were referred as second to fourth opinion and previously advised for radical nephrectomy as clamping times above 25 minutes were to be expected.

Apart from radical nephrectomy, the following other therapies were considered: active surveillance, radiofrequency ablation, open partial nephrectomy with cold ischemia, auto-transplantation with ex-vivo tumor resection [159].

None of the patients preferred active surveillance. Radiofrequency ablation was not pursued either due to risk of vascular injury given the hilar or endophytic tumor location, as well as the possible risk of a heat sink effect or due to too large tumor mass. Classical partial nephrectomy with full arterial clamping was discarded due to expected prolonged clamping times well exceeding 25 minutes [61].

Patients were deemed eligible for RAPN with IAC when they had a single renal artery, without early branching or abundant arterial calcifications on the anticipated position of the arteriotomy. Given the anatomical complexity, virtual 3D models were created by segmenting arteries, veins, parenchyma, tumor and possible cysts using Mimics Innovation Suite (Materialise, Leuven, Belgium) in a systematic 3D model making method as detailed in Chapter 3.1.

All surgeries were performed using the Intuitive Xi® platform (Intuitive Surgical, Sunnyvale, CA, USA). The technique was initiated and performed in eight cases by a highly experienced robotic and renal transplant surgeon (K.D., 843 robotic procedures, including 42 R(A)KAT and 297 RAPN) [105]. Subsequently, a second experienced robotic surgeon (T.Q., 1386 robotic procedures including 249 RAPN) performed one case while proctored by K.D., and a subsequent case independently.

3.2.4. Surgical Procedure

Patient Positioning

Patients were positioned in our standard setup for RAPN as depicted in Figure 3.6.a, with port placement as depicted in Figure 3.6.b. All procedures were performed under low pneumoperitoneum pressure at 8mmHg pressure, using AirSeal® (ConMed Corp, Utica, NY, USA)[160].

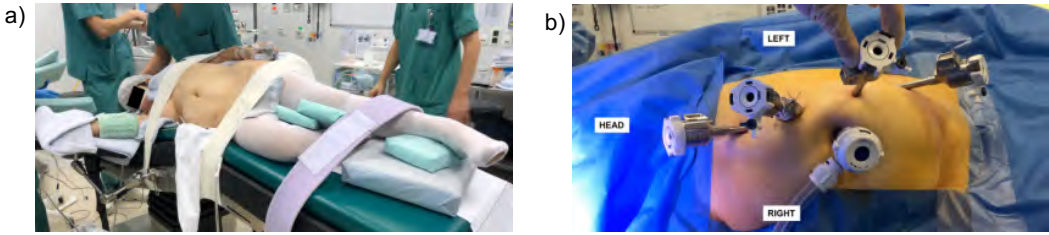


Figure 3.6: Patient positioning and trocar placement for RAPN with intra-arterial cooling. Figure 3.6.a. depicts the standard patient positioning for a left sided procedure, with the patient positioned in right lateral flank position, strapped to the operating table at the thoracic and ischial level. Extra posterior support is placed at the pelvic level and underneath the ipsilateral scapula. Special care is taken for head positioning as well as to avoid traction on the brachial plexus. Figure 3.6.b. indicates the trocar placement for the same left-sided procedure. Camera ports were inserted using the Hasson technique (Hasson et al. 1974, J. Reprod. Med. [161]). Other ports were inserted under direct vision.

Hilar Dissection

After reclining the descending colon (for left RAPN) or performing Kocher's maneuver (for right RAPN), Gerota's fascia is incised and the renal artery and vein are identified, mobilized, and wrapped with vessel loops. The kidney capsule is exposed and the kidney is entirely mobilized until it is only attached through the hilum. Incomplete mobilization may cause residual arterial or venous flow into the kidney through small collateral branches, compromising effective cooling and a bloodless tumor enucleation. Fatty tissue in the 'golden triangle' between the ureter, the lower pole of the kidney and the hilum is maintained to protect vascular supply to the proximal ureter (Figure 3.7.a.) [162]. The left gonadal vein and/or adrenal vein is clipped when necessary. In case of endophytic lesions, the tumor is delineated through robotic drop-in ultrasound assistance (BK Medical, Massachusetts, USA). For completely endophytic tumors, the course of renal vessels and the urinary collecting system is considered to identify the most practical and safest access. The 3D model is visualized through the TilePro™ window (Intuitive™, California, USA) to assist as depicted in Figure 3.7.b. or overlaid using the Augmented Reality of Chapter 5.

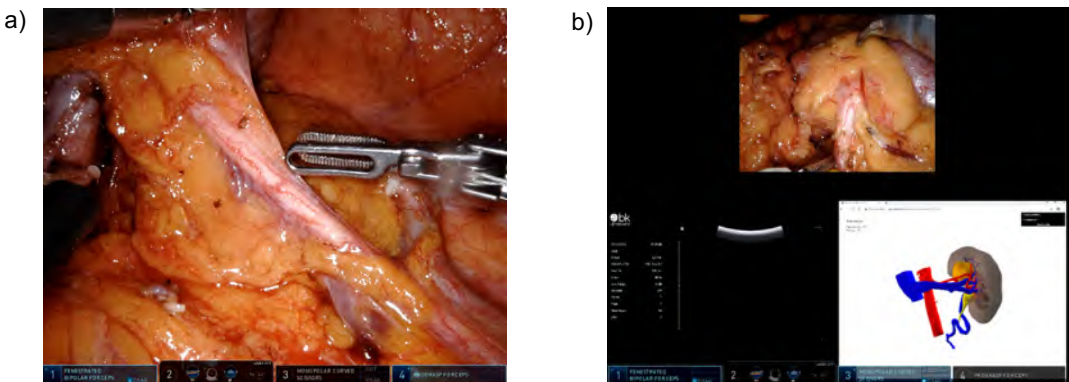


Figure 3.7: Complete kidney mobilization and tumor identification. Figure 3.7.a. depicts the retained fatty tissue to preserve ureteral perfusion, whilst Figure 3.7.b. shows the integration of the 3D model into the operative flow to help in tumor delineation and surgical approach.

Intra-arterial Cooling

A thru-lumen Fogarty catheter (Edwards Lifesciences, California, USA) is inserted transcutaneously into the abdominal cavity using the Seldinger technique [163]. Bulldog clamps and sutures for renorrhaphy are introduced intracorporeally to minimize ischemia times.

Bulldog clamps are placed on the renal artery, on the renal vein and on the proximal ureter and its vascular sheath. Renal arterial clamping initiates the warm ischemia time. Ureteral and venous clamping are performed to avoid venous backflow which also occurs through the ureteral golden triangle.

Renal artery and vein are incised using Pott's scissors. On the left, the gonadal vein can also be incised instead. Figure 3.8 depicts the testing of the Fogarty catheter before arteriotomy and subsequent arterial introduction. The 4-6 Fr Fogarty catheter is inserted into the renal artery and inflated with just enough saline (usually 0,1 or 0,2 mL) to block the catheter in the arterial lumen but avoiding intima rupture. Pulling the arterial vessel loop can further help to prevent backflow from the arteriotomy. A 4°C heparinized isotonic saline solution (10 I.U./ml) is injected, which initiates the cold ischemia time. The heparinized solution should prevent or dissolve possible intrarenal microthrombi. Following the cooling administration, the kidney usually rapidly decolors. Proper cold ischemia is achieved when observing clear effluent from the incised renal vein (Figure 3.9.a and 3.9.b). The effluent was continuously aspirated, and its temperature was measured at 20°C during the first cases [157].



Figure 3.8: Transcutaneous introduction and catheterization of 6Fr Fogarty thru-lumen catheter. The catheter is tested for functionality by flushing (Figure 3.8.a) and by inflation (Figure 3.8.b) before commencing the arteriotomy and inserting the catheter to administer heparinized sodium chloride (Figure 3.8.c).

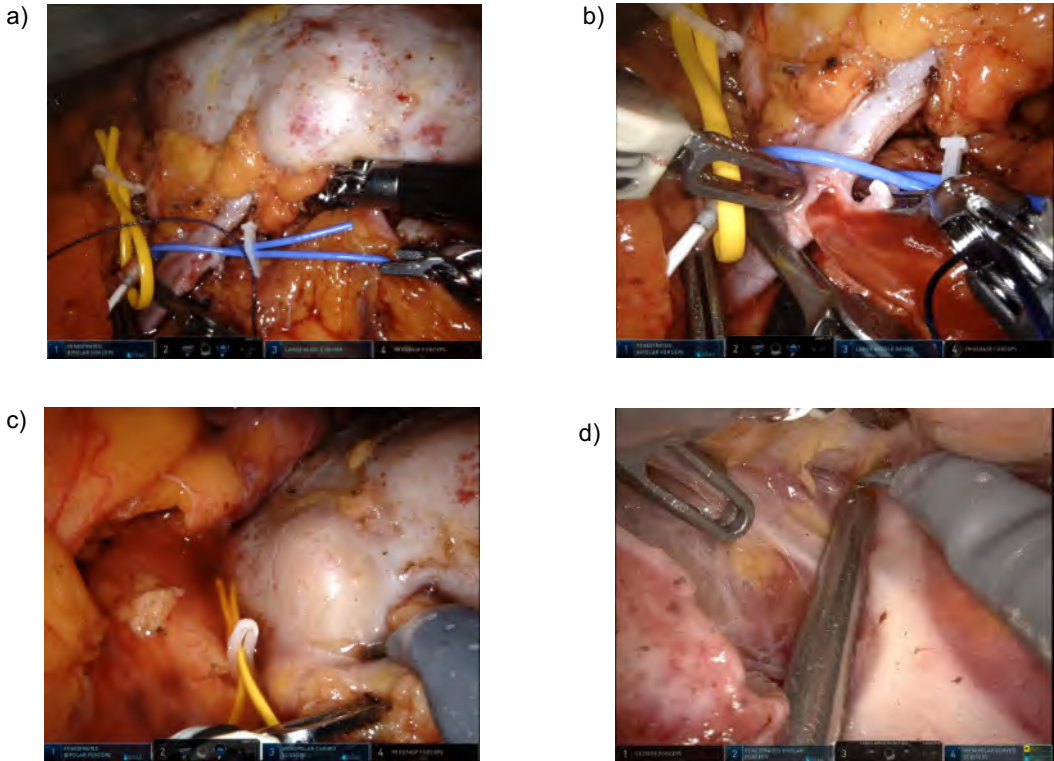


Figure 3.9: Application of intra-arterial cooling through arteriotomy. Figure 3.9.a shows the pale kidney after flushing with heparinized saline at 4°C. Figure 3.9.b shows the clear effluent from the renal venotomy which implies that switching to non-heparinized saline at 4°C is possible. Figure 3.9.c shows how the tumor gently delineates itself from the underlying tissue due to a more yellowish appearance. Figure 3.9.d demonstrates how ureteral clamping facilitates tumor dissection and enucleation. The temporarily hydronephrotic renal calyces are better objectifiable, as can be seen on the right side of the suction device. The tip of the suction is compressing a minor calyx on its left side.

Tumor Enucleation and Renorrhaphy

Once cold ischemia is in place, the cooling solution is switched to a non-heparinized 4° saline solution and tumor enucleation is started. Tumor enucleation is facilitated due to the color difference between healthy parenchyma and the lesion (Figure 3.9.c). Apart from backflow, ureteral clamping can also assist in tumor enucleation and recognition of the collecting system (injury) due to the temporary ensuing hydronephrosis (Figure 3.9.d).

After resection, the tumor specimen is inspected and placed in an endobag for removal. The tumor bed is inspected, and any significant leaking vessels are selectively sutured with a Prolene 5/0 suture. Opened urinary collecting system is closed with a running PDS 5/0 suture (both Ethicon Inc., Johnson & Johnson Corp, Cincinnati, OH, USA). This is followed by a classic internal renorrhaphy using Monocryl 3/0 suture and external renorrhaphy using Vicryl 1 suture with sliding hem-o-lok technique [164]. In hilar tumors, adjacent vessels may impede proper renorrhaphy. In these cases, the kidney defect is filled with a Surgifoam® absorbable gelatin sponge that is compressed and tied inside a Surgicel® absorbable hemostat (both Ethicon Inc., Johnson & Johnson Corp, Cincinnati, OH, USA). It is held in place by one or two overlying sutures in the kidney parenchyma.

Reperfusion

After renorrhaphy, the cooling perfusion is stopped, initiating rewarming ischemia time. The incisions on the renal artery and vein are closed using a running Gore-Tex 6-0 suture (W.L. Gore and Associates Inc., Flagstaff, AZ, USA). Before final closure, the vessels are vented with a heparinized saline solution. Bulldog clamps are removed from the ureter, vein and artery in this order. The kidney is reperfused and the resection zone is inspected once more for hemostasis. Additional external renorrhaphy sutures or hemostatic agent application may be performed. The global renal parenchymatic reperfusion and turgor is assessed and double-checked using intravenous indocyanine green (ICG) administration through near infra-red fluorescence technology (Firefly - Intuitive Surgical™, California, USA) and through the robotic drop-in ultrasound probe.

After specimen extraction and incision closure, a single abdominal drain is placed and removed on the first postoperative day if no urinary leakage or abundant bleeding is present.

Post-operative Evaluation

Postoperative renal monitoring was performed for the first cases through renal ultrasound. This ultrasound assessed proper revascularization and was performed in the post-anesthesia recovery unit. Thrombo-embolic prophylactic stockings are applied peri-operatively and continued until the patient is completely ambulatory. Low-molecular weight heparin is administered in prophylactic dosage starting 8 hours postoperatively and continued for 10-20 days depending on patient's risk for thrombo-embolic events. The patient is mobilized on the first postoperative day and is discharged when he or she is pain-free and self-reliant.

During follow-up, kidney function was assessed through estimated glomerular filtration rate (eGFR) and creatinine levels.

3.2.5. Results and Limitations

Figure 3.10 depicts the 3D models of all cases.

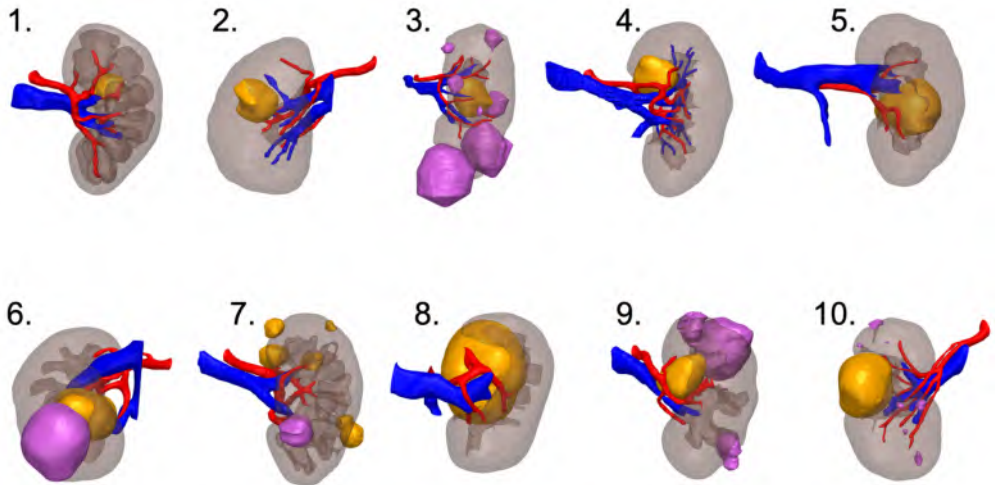


Figure 3.10: Overview of the different renal lesions with corresponding patient number (Table 3.2). Tumors are depicted in orange, renal cysts in purple, the arterial tree in red and the venous tree in blue. All arteries and veins were truncated at the respective levels of the aorta and vena cava. Case 10 depicts the anatomy after cytorreduction through neo-adjuvant therapy.

Table 3.2 depicts patient demographics and surgical outcomes. We generally note stable kidney function, with one significant drop for patient 8 who was converted to radical nephrectomy.

Median warm ischemia time (time between clamping and initiation of saline irrigation) was 4 min (IQR 3 – 7 min). Median cold ischemia time was 60 min (IQR 33 – 75 min). Median rewarming ischemia time was 10,5 min (IQR 6,5 – 23,75 min). Median hemoglobin drop on the 1st postoperative day was 2,7 g/dl (IQR 2,7 – 3,3 g/dl). Median length of stay was 4 days (IQR 4 - 4 days). Median pre-operative eGFR and serum creatinine levels were 90 ml/min (IQR 78,35 – 90 ml/min) and 0,79 mg/dl (IQR 0,69 – 1,00 mg/dl) respectively. Median postoperative eGFR and serum creatinine levels were 75,95 ml/min (IQR 54,7 – 87,2 ml/min) and 0,89 mg/dl (IQR 0,82 – 1,20 mg/dl) at postoperative day 1 and 86,8 ml/min (IQR 57,1 – 90 ml/min) and 0,81 mg/dl (IQR 0,71 – 1,06 mg/dl) during follow-up of at least one month after surgery. When pooling renal function (eGFR) of the 8 cases which had a contralateral healthy kidney in situ, mean eGFR decreased from 87.68 ml/min to 83.49 ml/min during follow-up of at least one month, where for the 2 single kidney cases, mean eGFR even increased from 42.0 to 45.65 ml/min.

Patient number	1	2	3	4	5	6	7	8	9	10
Gender	F	F	F	F	M	F	M	F	F	F
Age (y)	29	49	66	58	44	54	58	49	70	57
BMI (kg/m ²)	19.04	26.16	22.79	23.94	23.77	26	28.7	24.5	31.4	21.9
Indication	DE	DE	IH	IH	DE	DE	6 lesions, including 1 DE	DE + IH	IH + non-Part. funct. contralat.kidn solitary kidney	Part. Endoph. in kidney
Side	L	R	L	L	L	R	L	L	L	R
LS (mm)	15	26	35	31	51	67	T1=19;T2=13;T3=18;T4=13;T5=8;T6=14	80	41	43
PADUA score	12	11	12	10	13	13	T1=7;T2=7;T3=6;T4=6;T5=6;T6=9;AVG = 7	13	9	11
CT (min)	180	190	300	180	306	216	259	254	153	330
Warm ischemia time (min)	4	4	4	3	2	3	4	9	13	8
Cold ischemia time (min)	32	23	65	36	72	96	55	76	24	81
Rewarming ischemia time (min)	40	23	24	24	10	11	5	5	6	8
Number of calyces opened during UCS repair	1	2	None	None	2	2	1	3	1	3
Haemostatic agent	Hilar Surgicel	none	Surgifoam + Surgicel fibrillar	TachoSil	Hilar Spongostan + Surgicel	Floseal	Floseal	TachoSil	Floseal	none
EBL (ml)	150	130	600	100	300	200	400	1200	200	800
Hb drop postop day 1 (g/dl)	-2.2	-0.2	-4.0	-1.4	-3	-3.3	-2.7	-4.2	-2.4	-4.6
Histotype	reninoma	ccRCC	OCC	OCC	ccRCC	ccRCC	pRCC	chRCC	chRCC	ccRCC
pT	NA	pT1a	NA	NA	pT3a	pT1b	pT1a m R0	pT2a	pT1a R1	ypT0
Preop eGFR / creat	90 /0.83	90 /0.65	92 /0.7	82.4 /0.79	90 /0.64	90 /0.68	77 /1.05	90 /0.78	36 /1.43	48 /1.45
Postop day 1 eGFR / creat	78.5 /0.97	71.5 /0.94	73.4 /0.83	78.8 /0.82	90 /0.74	90 /0.73	96 /0.83	49.1 /1.28	26 /1.87	26.7 /2.01
Postop eGFR / creat	86.8 / 0.89 (3m)	90 / 0.72 (12m)	87 / 0.72 (12m)	77 / 0.64 (6m)	90 / 0.64 (6m)	90 / 0.71 (6m)	90 / 0.92 (6m)	57.1 / 1.13 (1m)	36 / 1.46 (12m)	55.3 / 1.1 (1m)
Length of stay (days)	4	4	4	4	4	4	4	5	3	6

TABLE 3.2: Patient Characteristics for intra-arterial RAPN cases. The last 2 columns in grey depict cases of unique kidneys.

BMI = Body Mass Index, DE = Deep Endopythical lesion, IH = Intra-Hilar lesion, LS = Lesion Size, CT = Console Time, EBL = Estimated Blood Loss, eGFR = estimated Glomerular Filtration Rate (ml/min), creat = creatinine (mg/dl), preop = preoperative, postop = postoperative, Hb = Hemoglobin, F = Female, M = Male, NA = Not Applicable, R = Right, L = Left, 1m = 1 month postoperative, 3m = 3 months postoperative, 6m = 6 months postoperative, 12m = 12 months postoperative, OCC= Oncocytoma, ccRCC = clear cell Renal Cell Carcinoma, chRCC = chromophobic Renal Cell Carcinoma, pRCC = papillary Renal Cell Carcinoma, UCS = Urinary Collecting System

Patient 7 had multiple bilateral tumors. First, left sided RAPN for 6 lesions including one endophytic lesion was performed using IAC.

Patient 8 required conversion to radical nephrectomy due to excessive bleeding from the resection bed during the reperfusion phase despite selective suturing and second renorrhaphy. Apart from patient 8, no intraoperative complications were withheld.

Patient 10 received neo-adjuvant axitinib-pembrolizumab treatment with radiologic tumor reduction from 80 to 43 mm for a biopsied clear cell Renal Cell Carcinoma (ccRCC) ISUP grade 2. This patient previously underwent contralateral radical nephrectomy for ccRCC. One mostly endophytic lesion was resected using IAC, 6 suspicious satellite lesions were subsequently resected off-clamp as cold ischemia time had attained 81 minutes and the intra-arterial cooling was thought to be suboptimal as the renal vein effluent still contained some blood, indicating remaining partial renal perfusion (arterial inflow or venous backflow) despite main artery occlusion. Final pathology did not withhold remaining tumor (all ypT0). The patient received a blood transfusion post-operatively (2 units packed cells).

All patients completed 90 days follow-up. Median follow-up was 13 months (IQR 9,1 - 32,4). Patient 2 experienced hematuria two weeks postoperatively: a pseudoaneurysm was diagnosed for which segmental embolization was performed (Clavien-Dindo grade 3b [165]). Patient 9 received empirical postoperative ciprofloxacin due to fever. No other complications were noted beyond 30 days for all patients.

We note one positive surgical margin (patient 9). No sign of recurrence was withheld up to 13 months of follow-up. All other surgical margins were negative.

We show that transperitoneal applied intra-arterial cooling has several advantages. First, it extends the scope of robot-assisted nephron sparing surgery in small but anatomically difficult located lesions or multiple tumors due to safe prolonged clamping times.

Second, due to flushing and cold ischemia, tumor visualization and enucleation becomes increasingly achievable, also for challenging tumor locations. In classical arterial clamped procedures, continuous blood loss may still hamper visualization and cause inadvertent damage to healthy parenchyma, blood vessels or the urinary collecting system. It may also lead to positive surgical margins. This oozing and blood loss can originate from aberrant unidentified arterial vessels, venous backflow from both venous and ureteral systems and intra/extrarenal venous anastomosis. One way to tackle the oozing is full renal mobilization in combination with arterial, venous and ureteral clamping. However, this would increase operative time to similar ranges as our proposed approach. A less invasive and more time efficient alternative might involve ICG administration after clamping. Similarly, complete kidney surface inspection for ICG necessitates complete mobilization, does not provide sub-surface information for deep endophytic tumors and does not adequately inform on venous backflow. Lastly, even under perfect fully clamped conditions, remnant blood can still be present inside the parenchyma as it is not flushed and can obscure initial enucleation.

Third, applying cold irrigation through arteriotomy has several advantages compared to the endovascular arterial cooling approach. Operative time was not reported by Liu et al [150] who used a transfemoral renal arterial access, but their approach did require patient transfer between two operative rooms and 2 subsequent procedures with patient movement and repositioning. Endovascular balloon dislocation [150] is very unlikely in our approach as catheters are positioned under direct endoscopic sight and thus can be easily repositioned. We note similar average kidney temperature during cooling (19.3°C

vs 20.0°C in our approach). We do note longer average cold ischemia times (56 minutes on average compared to 39.5 minutes) in our case series, however with higher nephrometry scores (PADUA 12 compared to PADUA 8-11) and in a smaller cohort. It might be advocated that the relative benefit for intra-arterial cooling due to prolonged clamping increases for highly complex lesions.

Our proposed operative strategy also has several limitations. First, the proposed technique requires expert robotic surgery skills in both oncology and vessel manipulation such as in renal transplantation. In all cases, bench surgery with auto-transplantation [159] or radical nephrectomy were considered as backup strategies.

Second, this technique is not eligible for every complex renal lesion due to constraints on the arterial tree. Renal arteriotomy requires a sufficiently long renal arterial trunk to insert the Fogarty catheter and deploy the balloon and hence would not be the proposed approach in case of early arterial branching. Using multiple Fogarty catheters for multiple arteries is also feasible as we already experienced in tiRAKAT, although not in this IAC RAPN series. Care should be taken with heavily calcified vessels as arteriotomy and intra-arterial manipulation might dislodge plaques or cause intima rupture with subsequent thrombosis. This should be considered a contra-indication for IAC.

Third, when compared to radical nephrectomy, the operative time and bleeding risk increase, due to the extensive arterial tree manipulation and the complexity of the lesions. In our cohort, we report one intra-operative bleeding requiring radical nephrectomy and one postoperative bleeding requiring interventional radiologic coiling. It should be noted that radical nephrectomy should always be considered as the safest alternative when expecting long ischemia times in complex masses, especially whilst a contralateral healthy kidney is in place with good baseline renal function. In comparison, the procedure we describe has a higher complication rate, which was illustrated by one patient who needed embolization for a postoperative pseudo-aneurysm. The benefit of saving the kidney should be weighed against the increased complication risk for each individual case.

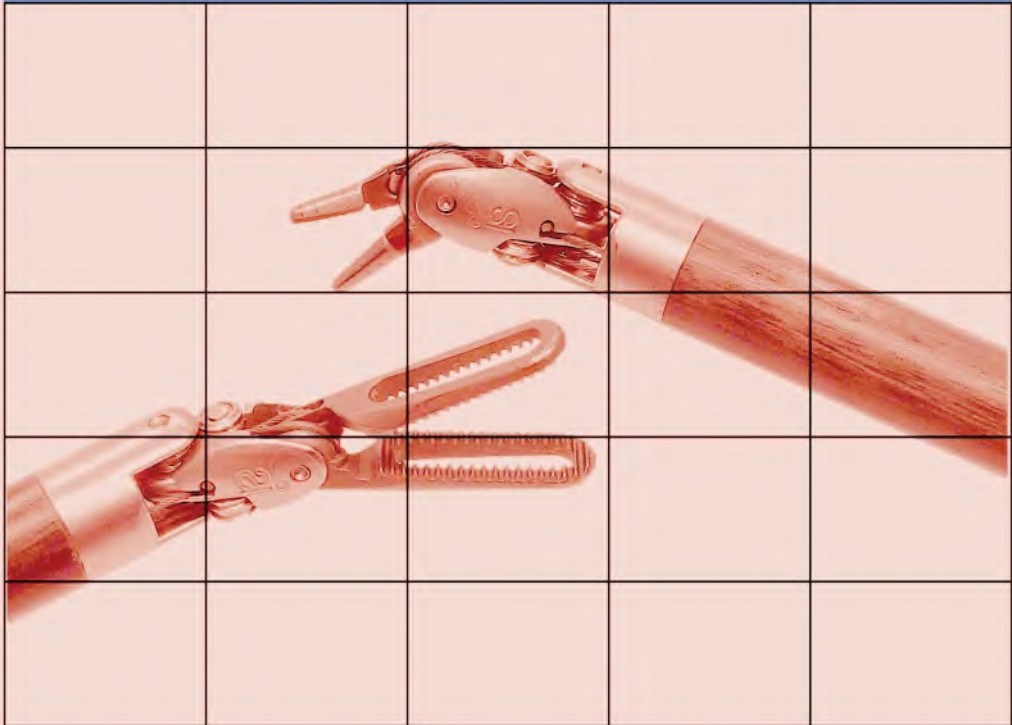
Fourth, we did not add a comparative arm to investigate the protective effect of cold ischemia when compared to standard warm ischemia. Identifying 10 matched cases proved to be impossible as such cases with expected long ischemia times were previously typically addressed with radical nephrectomy. Given the small sample size of 10 patients, a differential outcome in one single matched case could also easily alter the results.

3.2.6. Conclusions

In this patient series we demonstrated, to our best knowledge, the first feasibility study of RAPN using intra-arterial renal hypothermia with arteriotomy. In selected patients and when performed by expert robotic surgeons, this approach allows for more precise surgery in a bloodless field. The most clinically relevant setting for this technique might be patients with highly complex renal masses and comprised renal baseline function and/or a solitary kidney when prolonged ischemia times are expected.

Select all squares with a **needle driver**.

If there are none, click skip.



I'm not a robot



reCAPTCHA

[Privacy - Terms](#)

AI ASSISTED VIDEO ANALYSIS

04

*“Tussen droom en daad staan wetten in de weg
en praktische bezwaren”*

- Willem Elsschot

This chapter has been adapted from:

- Privacy-proof live surgery streaming: Development and validation of a low-cost, real-time robotic surgery anonymization algorithm
P De Backer, J Simoens, K Mestdagh, J Hofman, JA Eckhoff, M Jobczyk, E Van Eetvelde, M D'Hondt, MC Moschovas, V Patel, C Van Praet, HF Fuchs, C Debbaut, K Decaestecker, A Mottrie
Under revision – Annals of Surgery
- Multicentric Exploration of Tool Annotation in Robotic Surgery: Lessons learned when starting a Surgical Artificial Intelligence Project
P De Backer, JA Eckhoff, J Simoens, DT Müller, C Allaey, H Creemers, A Hallemeesch, K Mestdagh, C Van Praet, C Debbaut, K Decaestecker, CJ Bruns, O Meireles, A Mottrie, HF Fuchs
Surgical Endoscopy 2023
- Manuscript in preparation to release the instrument segmentation dataset created during this PhD

4.1. Privacy Proof Video Sharing

4.1.1. Introduction

In recent years, minimally invasive surgery (MIS) video has become central to enabling live streaming, telementoring, post hoc case evaluation, skill assessment, and novel technological advancements through artificial intelligence (A.I.), virtual reality, and robotic automation[6], [166]. On a legal or ethical basis, video anonymization is essential for sharing data across institutions[167], [168]. This anonymization is currently limited to manually removing patient metadata, including names and other identifiable information, such as data and recording locations from file names only. Nevertheless, sequences captured outside the body due to lens cleansing or other interruptions of intracorporeal video display the entire operating room (OR), the patient, and the operative team. These images can reveal the patient's identity (e.g., the patient's name displayed in the OR, on the pathology specimen, etc.) or the medical staff identity (scrub nurse, anesthesiologist, residents, etc.), neither of whom may have consented to be recorded. While previous research of full OR recordings has already focused on blurring faces alone [169], the requirements for endoscopic camera anonymization can be more stringent. Endoscopic cameras are indeed seldomly used to record video data other than the surgical field, in contrast to ceiling or wall-mounted cameras. As such, out-of-body data is of far less interest in endoscopy.

Figure 4.1 depicts a possible privacy breach in an image retrieved from a publicly shared 'anonymized' dataset of laparoscopic cholecystectomies[170]. It also shows how image blurring can solve this privacy issue. Despite extensive efforts in the standardization of the OR workflow and the use of surgical video data[171], no formal guidelines or consensus exists for the anonymization of MIS video data. This can be attributed to the lack of infrastructure or the lack of awareness of the methodology to perform such anonymization efficiently and safely.



Figure 4.1: The need for intraoperative video analysis and anonymization. The left image depicts a non-anonymous frame derived from a public dataset [170], captured when the endoscope is out-of-body. For privacy reasons, we have manually edited the frame by covering the faces with red rectangles. This image is subsequently pixelated to show how privacy can be conserved.

In addition to legal and ethical needs, there is a clear technical need for video anonymization. Previous work [172] has shown significant video size storage reduction by removing out-of-body segments. Furthermore, the advent of A.I. for surgical video analysis requires anonymized video sharing with technical people who have no role in the patient-physician relationship. From an A.I. engineering perspective, automated

anonymization is required, as it facilitates the creation of large and varied datasets, it is a preprocessing step for A.I.-assisted video analysis[166], [173] and it speeds up the labeling efforts for supervised A.I. techniques as discussed in Chapter 4.2.

Manual video processing, including out-of-body image reviews, is time consuming and prone to human error. Previous automated video anonymization research was predominantly limited to laparoscopic videos of single procedural types[172], [174]. Recent studies have expanded the scope across different laparoscopic procedures using deep learning techniques[168], [175] but none have investigated robotic surgeries[176].

Moreover, intraoperative MIS video anonymization in real-time has not yet been investigated. Real-time anonymization offers safe live video streaming as well as efficiency enhancements because the video can be distributed directly after completion of the procedure.

In this study, we developed and validated a real-time, low-cost, open-sourced anonymization algorithm for robotic surgery streaming. We assessed the algorithmic robustness across different procedures and new robotic soft tissue platforms, and we benchmarked our algorithm to existing solutions and laparoscopic procedures. We proved that our algorithm works in a real-time, intraoperative setting for surgical video streaming with minimal computational requirements. The algorithm is available online, democratizing laptop-based anonymized robotic live-case streaming.

4.1.2. Materials and Methods

Data Collection

Our multicentric global collaboration resulted in 63 full-length robotic surgery recordings, which were retrospectively collected under appropriate IRB approval.

Firstly, we analyzed 42 Intuitive Xi cases (Intuitive Surgical™, California, USA):

- 7 liver metastasectomies (RALM) - AZ Groeninge Hospital Kortrijk
- 7 partial nephrectomies (RAPN) - OLV Hospital Aalst, Ghent University Hospitals
- 7 radical prostatectomies (RARP) - OLV Hospital Aalst
- 7 radical cystectomies (RARC) - OLV Hospital Aalst, Ghent University Hospitals
- 7 minimal invasive esophagectomies (RAMIE) - University Hospital of Cologne
- 7 right hemicolectomies (RARHC) - University Hospital Brussels

Additionally, we included 21 robotic radical prostatectomy cases using three other robotic systems:

- 7 HUGO RAS (Medtronic, Minneapolis, MN, USA)[177], at OLV Hospital Aalst (Belgium)
- 7 Versius Surgical (CMR Surgical, Cambridge, UK)[178], at Salve Medica Hospital Lodz (Poland)
- 7 Intuitive Single Port (Intuitive™, California, USA)[179], at AdventHealth Global Robotics Institute (Florida, USA)

Finally, we selected the first five laparoscopic cholecystectomies from a public dataset[170] to validate and compare performance on this laparoscopic benchmark procedure.

Video Frame Annotation

All videos were shared without associated metadata (i.e., surgeon, patient, or institutional identifiers), and were manually annotated for out-of-body segments. These segments mainly include the pre- and postoperative periods, as well as lens cleaning and port hopping.

All out-of-body periods are either initiated or terminated by a trocar passage. Trocar transitions tend to happen fast, so defining a single video frame where the transition occurs is challenging. The endoscope can also be positioned at the edge of the trocar during more extended parts of the procedure, allowing the surgeon to have a larger field of view without the intention of endoscope removal. As previous work on automated anonymization has used different transition points, we firstly benchmark two previously used annotation methods.

Both methods require sampling every video frame during endoscopic trocar passage. The first method, referred to as the “Valve definition” (Figure 4.2.a), follows the most time-efficient annotation methodology as described by Lavanchy et al.[175] who defined the start of out-of-body sequences by the visual presence of a trocar valve. This work considered frames out-of-body once the trocar valve becomes visible. Consequently, the frame is defined as the back inside-body once the trocar valve is no longer visible. The second and more laborious method, referred to as the “50% definition” as depicted in Figure 4.2.b., similar to Schulze et al. [168], samples all video frames when the endoscope is at the edge of the trocar. All pixels are labeled as either trocar (in orange) or surgical scene (in green). If the trocar pixel proportion exceeds 50% of all image pixels, the image frame is considered out-of-body. As such, the out-of-body sequence is distinctly longer compared to the first method.

We identified the methodology by Lavanchy et al[175] as superior (see Supplemental Digital Content A.1.) and subsequently applied it throughout .

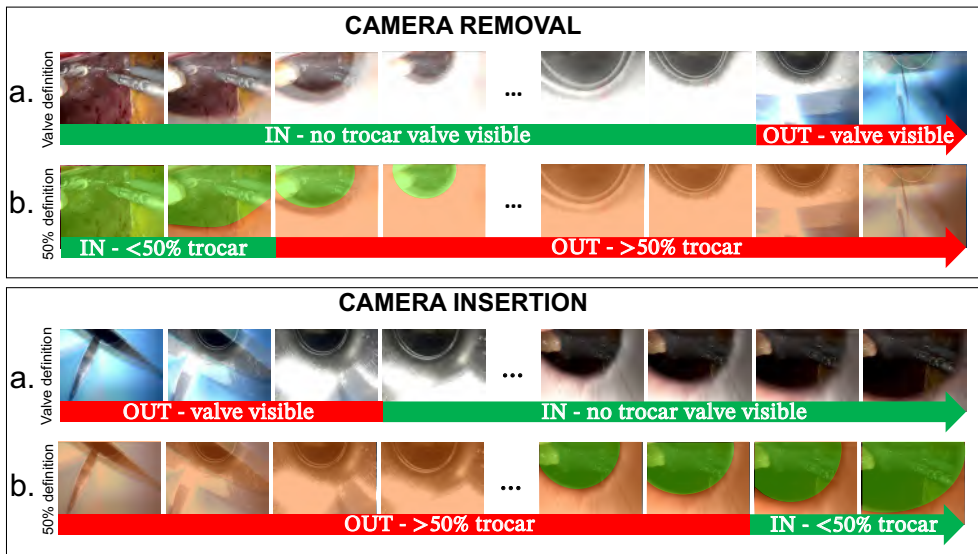


Figure 4.2: Video frame sequences when the camera is removed (top) or reinserted (bottom) into the abdominal cavity and the according definitions of out-of-body. (a) “Valve definition”: Annotation strategy when visualization of a trocar valve is used as a transition point as by Lavanchy et al. 2023, Sci. Rep. [175]. This methodology proved to be the most performant one and is used for ROBAN. (b) “50% definition”: Annotation strategy when pixel

proportions of trocar presence are used, with the annotations of surgical scene (green) and trocar (orange) overlaid as proposed by Schulze et al. 2023, Surg. Endosc. [168]. The horizontal arrows indicate the resulting definitions.

Dataset Creation

To create our deep learning network, we split the dataset into a training set for algorithmic training, validation set for parameter optimization, and test set for reporting the final performance on unseen videos. Each procedural type included seven cases, of which five videos were selected for training, one for validation, and one for testing. We automatically extracted one image frame from the video every second using a Python script (OpenCV). All sampled frames are labeled as inside or out-of-body based on the above definitions. Inside-body frames are considered negative labels, whereas out-of-body frames that require blurring are considered positive. A false-positive frame is an inside-of-body frame that is wrongly blurred as out-of-body. Figure 4.3 shows the confusion matrix principle used in this study for the analysis. Out-of-body frames are considered positive events that require anonymization. False-negative minimization is central to this study. Procedural parts containing image guided surgery techniques including TilePro (Intuitive™, California, USA) visualization of CT and 3D model information, as well as indo-cyanin-green (ICG) segments were kept inside the dataset. None of them had identifiable patient information.


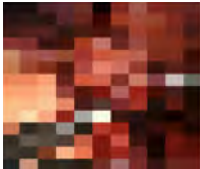


		Prediction	
		Negative = no blur	Positive = to blur
Actual value	Negative = inside body	<p>True Negative</p> 	<p>False Positive</p> 
	Positive = out-of-body	<p>False Negative</p> 	<p>True Positive</p> 

Figure 4.3: Confusion matrix for the binary classification problem of out-of-body anonymization. Positive labels are images that need anonymization. False negative minimization is the main goal for safe video sharing

Model Architecture and Neural Network Training

We developed a deep learning classification algorithm that learns to classify every frame as belonging to either inside-body or out-of-body. We trained a MobileNetV2 architecture followed by a fully connected classification layer, where the MobileNetV2 backbone was pre-trained on ImageNet. However, the gradients of the weights of the first three layers were not fixed and retrained, allowing a more specialized feature extraction dedicated to surgical images. We identified the MobileNetV2 architecture as the most suitable for anonymization tasks, given its previous SOTA classification performance[180] and low

computational demands, which are essential for real-time applications. The network training details can be retrieved in the Supplemental Digital Content A.2.

When training our deep learning system for this classification task (inside versus out-of-body), we face a class imbalance problem[181]. In our dataset, far more images are labeled inside-body than out-of-body, as out-of-body sequences are far less prevalent in surgery. This can bias the network towards inside-body classification and can be mitigated using weighted random sampling and the “receiver operating characteristic area under the curve” (ROC AUC) as a validation metric.

Other reported performance metrics include False Positive (FP), False Negatives (FN), accuracy, sensitivity, specificity, precision, Negative Predictive Value (NPV), and F1-score.

We trained three deep-learning neural networks to explore the influence of adding different robotic systems or procedural types.

Firstly, we trained a network that pools all Intuitive Xi procedures. We used 30 procedures for the network to learn (five videos per procedural type), and six other procedures (one video per procedural type) for validation (hyperparameter tuning).

Secondly, we train a ‘ORSI-RARP’ network that pools all 20 robot-assisted radical prostatectomies (RARP) performed on the different robotic systems (5 RARPs per system: Intuitive Xi, HUGO RAS, Versius CMR, Intuitive Single Port) with 4 RARPs (1 video per robot) for validation.

Third, we pool all the data above to a respective training and validation set to train and validate our ROBotic Anonymization Network ‘ROBAN’.

We report the final network performances on an identical test set for a fair comparison. In contrast to previous works, we evaluated this performance on complete test set videos, which implies assessing every single frame, as is performed in a real-time application, and which results in the most precise and reliable evaluation. Similar to the ROBAN validation set, this identical test set contained nine randomly selected procedures, each having exactly one of the following procedures: RALM, RAPN, RARC, RAMIE, RARHC, RARP-Xi, RARP-HUGO, RARP-CMR, and RARP-Single Port.

We compared ROBAN’s performance with that of two recently published SOTA algorithms (OoBNet[175] and IODA[168]) on this test set as well as on a frame-by-frame review of 5 randomly selected laparoscopic cholecystectomy procedures[170]. We also benchmark ROBAN’s framewise inference time against both works to assess the real-time potential.

[Postprocessing Predictions](#)

When analyzing the duration of automatically detected out-of-body sequences, some of the shortest automatically detected fragments were in the millisecond range. It is implausible for an endoscope to be extracted from and entered back into the body within milliseconds, as manual lens cleansing, for example, requires more time. Consequently, we use this assumption to post-process our single frame predictions for the offline/non-live streaming setting. We applied a morphological operator that attributes video snippets smaller than 2 seconds to the existing surrounding prediction (inside versus outside the body). The 2-second period was identified through an optimization study for fragment durations between 0.5 to 5 seconds. Schulze et al.[168] also proposed a 2-second postprocessing period as a potential algorithmic performance boost, but without

implementation. This postprocessing step cannot be performed in the real-time setting because it requires the context of the preceding and succeeding frames. We report the performance before and after the postprocessing step.

Real-time Application in the Operating Room

We deployed ROBAN during an Intuitive Xi radical nephrectomy (surgeon C.V.P., Ghent University Hospital). A low-resource setup was installed to assess the feasibility of real-time anonymization without a dedicated computer infrastructure (estimated cost of 2000€). A schematic illustration and the OR setup are shown in Figure 4.4.a. Surgical endoscopic video frames were extracted from the surgical tower using a frame grabber (USB3HDCAP, Startech, London, Ontario, Canada). The video stream was sent from the frame grabber to a laptop (equipped with an Intel i7 CPU, 32GB of RAM, and NVIDIA RTX A2000 GPU). The computer analyzes incoming video frames and blurs them directly when it detects an out-of-body frame; otherwise, the original frame is displayed. The anonymized videostream was sent to the HDMI port of the laptop. As such, this output can be streamed immediately for live surgeries. In our validation setup, the output was transferred to a secondary screen for visualization and to the surgical tower using an HDMI splitter (HDMI-splitter S312 UHD, MARMITEK, Eindhoven, The Netherlands). The image displayed on the secondary screen was never displayed to the operating surgeon as to not interfere with the surgery. Its sole purpose is to double-check the laptop's output. The anonymized live video was also inputted into the surgical tower using the Intuitive Xi TilePro functionality to prove its real-time application.

Second, we evaluated the highest achievable algorithmic performance with ultra-low latency using a high-cost setup (estimated cost 12,000€) as depicted in Figure 4.4.b. in a wet-lab setting. The wet lab consisted of a cadaveric porcine model, previously used during robot-assisted kidney transplantation teaching. Basic surgical manipulations (cutting, coagulation, suture cutting and grasping) were performed during the testing. The hardware setup consists of an integrated solution of both GPU device (NVIDIA Clara AGX processing power[182]) and capture card (Deltacast DELTA-12G-elp-key [183]), where we also immediately live streamed the anonymized cadaveric porcine surgery through Microsoft Teams to 45 live viewers.

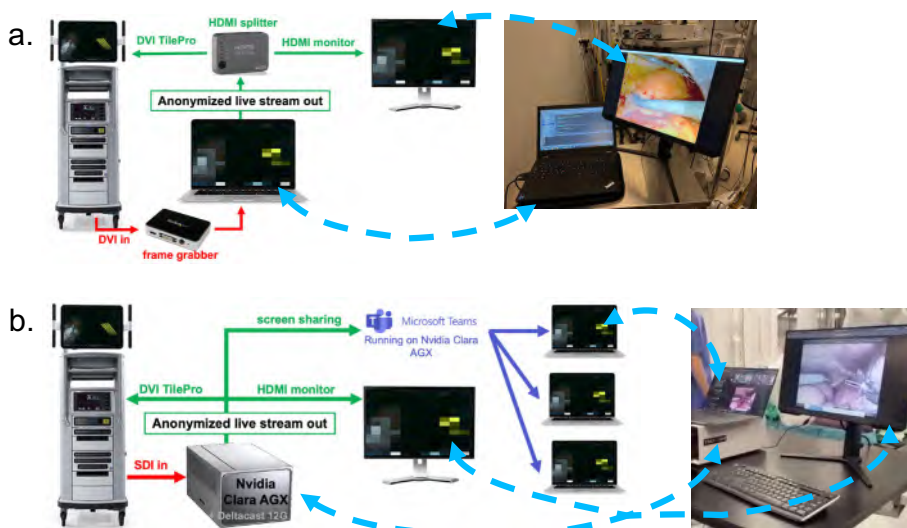


Figure 4.4: Setup for real-time live surgery anonymization. Left: connections schematic, right: intraoperative setup. The blue dotted arrows depict the corresponding components between the schematic and the real OR setup. a. Connection schematic for low-cost real-time anonymization. Surgical video is taken from the endoscopic tower with a frame grabber. The laptop anonymizes every outside body frame using the ROBAN-network. The video is sent back into the TilePro input for comparison, as well as to a secondary screen mimicking live broadcast. b. Connection schematic for dedicated computer infrastructure using a Nvidia Clara AGX device with ultra-low latency as demonstrated in a wet lab setting. The AGX device instantly streams the anonymized surgical stream to Microsoft Teams.

4.1.3. Results

[Dataset Description](#)

We refer to Table 4.1 for an overview of the training and validation dataset sampled at 1 frame per second (FPS). We analyzed 4,119,373 frames for the frame-by-frame test set evaluation, of which 149,650 out-of-body frames.

Table 4.1: Overview of the three datasets, including the video statistics, frame count and out-of-body statistics.

Train + validation	video count	Mean video duration	Total sampled frames	Out-of-body frames		Number out-of-body sequences	Mean out-of-body sequence duration
Dataset	(n)	± stand. dev. (min.)	(n)	(n)	(%)	(n)	± stand. dev. (s.)
Intuitive Xi	36	131.34±68.57	283,695	13,831	4.88	72	46.69±182.50
ORSI-RARP	24	115.11±28.44	165,763	5,940	3.58	48	34.99±81.36
ROBAN	54	125.24±58.91	405,784	18,568	4.58	108	47.47±166.96
Test set	9	168.60±73.04	4,119,373	149,650	3.63	18	35.39±70.14

Single Robot vs. Multiple Robots vs. ROBAN vs. SOTA

Table 4.2 depicts the results of the three networks (Intuitive Xi, ORSI-RARP and ROBAN) compared to IODA[168] and OoBNet[175]. Across all the evaluated metrics, ROBAN outperformed the other networks in classifying out-of-body frames. We refer the reader to the Supplemental Digital Content A.3. for confusion matrices and full-length procedural evaluations, which provides extra insight where misclassifications occur throughout the video.

Table 4.2: Performance metrics through framewise inference of the Xi Valve definition, ORSI-RARP network and ROBAN, compared to previous solutions IODA and OoBNet. The bottom row shows the performance metrics after postprocessing predicted labels using ROBAN.

	Accuracy (%)	Sensitivity (%)	Specificity (%)	Precision (%)	NPV (%)	F1-score (%)	ROC (%)	AUC (%)
Intuitive Xi	99.83	96.79	99.95	98.57	99.88	97.67	98.37	
ORSI-RARP	99.53	98.78	99.56	89.46	99.95	93.89	99.17	
ROBAN	99.91	98.96	99.95	98.66	99.96	98.81	99.46	
IODA⁴	99.41	92.40	99.68	91.49	99.71	91.95	96.04	
OoBNet[175]	98.46	97.64	98.49	70.94	99.91	82.18	98.07	
ROBAN post-proc	99.91	99.88	99.91	97.58	100.00	98.72	99.89	

At first sight, IODA seems to outperform OoBNet in most aspects. Nevertheless, the sensitivity of OoBNet is 4.45% higher than that of IODA. Decreasing false negatives (out-of-body sequences that are missed) should be the primary objective, and IODA's sensitivity is lower than that of OoBNet in robotic surgeries and laparoscopic cholecystectomies. Furthermore, the inherent class imbalance problem results in low numbers of positive counts compared with the total negative count. Hence, the precision and F1-score are very sensitive to even small increases in FP counts. As such, IODA's performance is considered inferior with respect to privacy preservation, despite OoBNet being overly sensitive and falsely anonymizing nearly five times more frames than IODA's. With 40 FP frames for ICG anonymization (1.98% of all ROBAN FP frames), ROBAN also clearly outperforms OoBNet (8673 FP frames during ICG, 14.49% of all OoBNet FP frames) and IODA (12854 FP frames during ICG, 49.20% of all IODA FP frames).

Postprocessing ROBAN predictions for non-real-time use with a 2 second window further boosted performance, with NPV 99.9953%. In absolute numbers, 185 frames out of 149,650 out-of-body frames were missed, which is a further reduction by factor 7.4 (confusion matrix in Supplemental Digital Content Figure A.3.). However, the number of

incorrectly anonymized inside-body frames increased by a 1.8 factor, negatively impacting the specificity, precision, and F1-score.

Average inference time per frame was 0.96 milliseconds for ROBAN, 2.2 milliseconds for OoBNet and 0.57 milliseconds for IODA on an RTX3090 GPU with 256GB RAM.

Per Procedure Performance

When assessing the test set results on a procedural level, we note that out of all procedures, RAMIE achieved the highest sensitivity for ROBAN and OoBNet (respectively 99.99% and 99.68%), and second to highest for IODA (98.56%), whilst also having the highest ROC AUC for all three methods (respectively 99.88%, 99.69% and 99.11%). We also note that IODA has 2 laparoscopic esophagectomies in the training data, whilst OoBNet has none. RARP on HUGO-RAS scored the poorest for ROBAN, OoBNet and IODA on both sensitivity (respectively 95.21%, 91.11% and 78.23%) and ROC AUC (respectively 97.59%, 95.55% and 89.11%). Per procedure test-set results can be retrieved in the Supplemental Digital Content A.3.

ROBAN evaluation on Laparoscopic Cholecystectomy

Table 4.3 shows the superior ROBAN performance on five laparoscopic cholecystectomies, compared to IODA and OoBNet which were, in contrast to ROBAN, both trained on laparoscopy data. We refer the reader to the Supplemental Digital Content A.5. for the confusion matrices and full-length procedural overviews. Postprocessing application again increased performance: a 2.7 times false negative count reduction at the expense of a 1.6 times false positive count increase.

Table 4.3: Performance metrics of framewise inference of 5 laparoscopic cholecystectomy procedures by ROBAN and comparison to state-of-the-art networks IODA and OoBNet. Bottom row contains the results of ROBAN after postprocessing.

	Accuracy (%)	Sensitivity (%)	Specificity (%)	Precision (%)	NPV (%)	F1-score (%)	ROC AUC (%)
ROBAN	99.66	93.43	99.79	90.84	99.86	92.12	96.61
IODA	99.06	66.37	99.78	86.64	99.27	75.16	83.08
OoBNet	99.64	90.42	99.85	92.71	99.79	91.55	95.13
ROBAN							
post-proc	99.63	97.54	99.68	86.77	99.95	91.84	98.61

Qualitative Results

A visual qualitative error analysis of misclassified frames by ROBAN shows that false negatives frames (out-of-body frames falsely predicted as inside-body, and thus insufficiently blurred) include images where the abdomen of the patient is in view, often with blood stains or where the image of the operating room is very blurry, possibly due to condensation (Figure 4.5.a-d). False positives (inside-body frames falsely anonymized as if they were out-of-body) included images where gauzes or hemostatic agents limited the endoscopic field of view, frames where the endoscope was located inside the trocar (Figure 4.5.e-h) or ICG segments. Very blurry, or overexposed images and images depicting bloody sequences are sometimes misclassified as false negatives (FN) or false positives (FP). It is important to note that no images compromising patient or healthcare provider identities were misclassified.

Real-time Application in the Operating Room with Low-Cost Setup

ROBAN was successfully deployed in both the real OR (low-cost setup) and the wet lab settings (high-cost, high-performance setup) as can be seen in the video in Figure 4.5.i.

Because of its less capable graphics card, the laptop used in the low-cost setup is limited to processing 15 FPS, which includes loading, inference, and display of the anonymized videos stream. However, the Intuitive Xi output frame rate is 30 FPS.

This problem was tackled by analyzing only one of every four frames and providing the same value to the three subsequent frames by interpolation. As discussed before, shifts between the inside and out-of-body below one second are impossible, making the impact of interpolating between four frames (133 milliseconds) for surgical video streaming negligible.

Theoretically, an inference period of two frames would be possible; however we chose a four-frame period to build in larger margins for potential slowing factors like other programs concurrently being executed on a laptop (e.g. a video conferencing application that shares the video stream and that is also using graphical processing power). The low-cost setup achieved a total delay of 300 ms when comparing the surgical video stream with the processed video stream from our laptop, as visualized in the TilePro window (Figure 4.5.i.). The objectified delay is not due to inference on the laptop but is the result of other serial video components that capture the video stream and input into the laptop, as well as carrying the signal back to the surgical console.

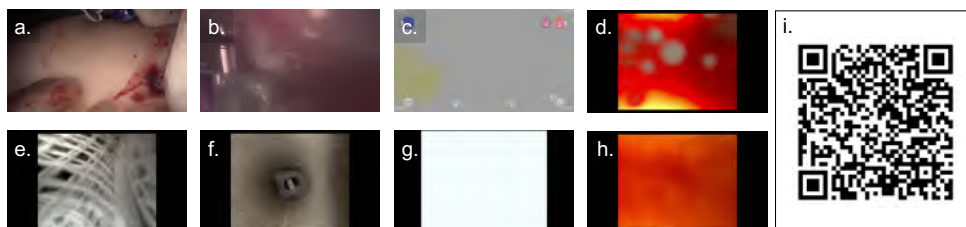


Figure 4.5: Examples of misclassified frames found in qualitative analysis. Top row shows false negatives implying too little anonymization, bottom row shows false positives, implying overly sensitive anonymization. (a) Abdomen of the patient in view, blood stains. (b) Blurry frame due to condensation. (c) Very bright frame due to reflection of the endoscope light. (d) Blood obstructing the endoscopic view. (e) Gauze obstructing the endoscopic field of view. (f) Endoscope inside the trocar, transition between out-of-body and inside body. (g) Very bright frame due to reflection of the endoscope light. (h) Blood obstructing the endoscopic view. (i) QR code link to video showcasing the real-time application, with troubleshooting of False Positive reduction.

Real-time Application in the Wet Lab Setting with High-Performance Setup

The measured delay in the low-cost setup was reduced from 300 to 13 ms when using the dedicated high-performance setup, which no longer required frame interpolation. Furthermore, direct streaming from the NVIDIA Clara AGX device to 45 external viewers using Microsoft Teams running on the device worked flawlessly. Porcine anatomy had no impact on the algorithmic performance, indicating that ROBAN learns to grasp general visual anatomical and robotic surgery cues. Real-time wet-lab video streaming testing did reveal two other causes of false positives. ROBAN is overly sensitive to abrupt manual camera movements that can occur during manual unstable endoscopic manipulation. These movements result in milliseconds of unsharp frames that are falsely detected by the algorithm as out-of-body. However, abrupt endoscopic movements are rare in laparoscopy, and for robotic surgery, they only happen during camera insertion or removal. During wet lab testing, ROBAN was also found to be overly sensitive to full-instrument occlusion: when the endoscopic vision is fully occluded with robotic instruments only, false positive frames can occur.

4.1.4. Discussion

In this work, we develop and validate a robust anonymization algorithm, which achieves adequate and reliable real-time surgical live streaming. The systematic approach provides insights how anonymization algorithms can be further optimized.

ROBAN outperforms SOTA on both robotic surgery as well as on laparoscopic cholecystectomy which it has never seen before. More specifically, OoBNet performs better than ROBAN on specificity and precision metrics, nevertheless these metrics depend on FP counts (falsely anonymizing inside-body frames), which as stated above, are less important when considering safe data sharing. SOTA also tends to anonymize robotic indo-cyanin-green (ICG) segments where it is outperformed by ROBAN. Although the SOTA datasets are not openly available, they might have little or no ICG application inside. One explanatory hypothesis might be that green surgical drapes outside the body could be confused with ICG segments. The increased performance on both unseen procedures and ICG segments further strengthen the hypothesis that exposing an algorithm to various procedures reduces FP count and helps avoid an overly sensitive system.

Comparing IODA and OoBNet, the first was trained on a larger dataset with a higher procedural variation, having more procedures in common with our ROBAN dataset than OoBNet which might explain the lower IODA FP count. OoBNet had some robotic procedures in the dataset, which might have helped reduce FN count. IODA was trained according to another annotation protocol but this is not the main cause of its poorer performance.

The above results suggest that the anonymization performance depends on the surgical platform (laparoscopy versus robotics) and procedural variation. Combining different robotic systems and procedures result in a more robust algorithm as seen in the ROBAN superiority. We indeed note a higher FN count in case of the single robotics algorithm (Intuitive Xi network). In comparison, the FP count is higher for ORSI-RARP (confusion matrices in Supplemental Digital Content Figure A.3.). Hence, scaling across robots makes the algorithm more sensitive to out-of-body portions, which could be explained by using different trocars which signal a visual cue for anonymization need.

As such, training ROBAN on laparoscopic data is also expected to remove the hypersensitivity to abruptly moving, blurry laparoscopic frames. Likewise, real-time instrument detection (Chapter 5.2 and 6.1) can further reduce FP counts, implying that the endoscope is most likely inside the body.

When assessing the results on a procedural level for the test set, no clear patterns were detected as the best (RAMIE) and worst (RARP on HUGO RAS) performing procedures were on average when assessing the number of frames used for training and analysis as well as their out-of-body proportion. Furthermore, as RARP was overrepresented as a procedure, albeit with different robotic systems, the poor performance cannot be attributed to lack of training data.

In the offline setting of post-procedural video sharing, extra postprocessing overall improves the overall results. Given our prioritization of FN minimalization, postprocessing positively affects the overall performance. To achieve 100% perfect anonymization at low-cost and minimal effort, surgeons can anonymize videos fully automatically after the procedure and rewatch only the anonymized segments to double check if no interesting surgical information is lost and undo these video snippets from anonymization.

We demonstrate that ROBAN can be used in real-time OR settings using a low-cost laptop setup, which is useful for live streaming without compromising identity clues. This democratizes the possibility of using surgical video data worldwide for teaching, research, and technological advancements. This, in turn, helps to add diversity to the abundance of video data. We objectify a 300-millisecond delay which is considered irrelevant for live streaming and teaching purposes. Nevertheless, using a dedicated high-cost computer infrastructure reduced this delay to 13 milliseconds. The algorithm was overly sensitive when only instruments and no tissue were in view. However, this happens rarely, as surgery is about tool tissue interaction and this flaw was only revealed through intentional instrument occlusion during wet lab testing. Furthermore, this instrument occlusion sensitivity can be addressed by real-time deep-learning surgical instruments detection, which can be performed on the same computer as will be detailed in Chapters 5.2 and 6.1. The high-performance, high-cost computer used is too heavy for the application at hand. Smaller dedicated on-edge computational devices are now entering the market and are expected to decrease costs four-fold. When considering the inference time, all tested algorithms work in the millisecond range, which should have a negligible impact on real-time implementation.

Future research should entail further dataset expansion, including the addition of other surgical procedures to reduce too strict anonymization and further increase precision, while combining laparoscopic and robotic datasets should help maintain high sensitivity. However, the dataset expansion should be performed thoughtfully, as more data does not necessarily result in better performance. Our dataset is 39% larger than OoBNet and 3700% smaller than IODA. Combining classical computer vision techniques such as windowing and filtering, together with newer (deep learning) computer vision techniques, can positively affect the performance. Building deep learning anonymization solutions requires large amounts of videos and images. Therefore, a pooling approach for anonymization through decentralized learning, such as federated learning, may provide a valuable route. Lastly, video streams retrieved from wall or ceiling mounted camera

recordings is not suited to be processed with this type of algorithm. It will require special attention to safely store and distribute these data streams.

In conclusion, the importance of video anonymization is only expected to increase. However, an international ethical and legal framework is lacking. In addition to teaching purposes, big data processing and surgical data science require dataset sharing to unlock surgical videos' full potential. This study facilitates such data exchange for robotic surgery owing to its open-sourced character, real-time applicability, and robustness, whilst minimizing or potentially eliminating harm to patient and healthcare workers through de-anonymization.

4.1.5. Data Availability

The ROBAN algorithm, its real-time application, and the postprocessing offline component are publicly available for non-commercial use under the Creative Commons Attribution CC-BY-NC-SA 4.0. This can be found at <https://github.com/orsiacademy/ROBAN/tree/main>. Due to privacy restrictions, the datasets used in the present work cannot be publicly shared. If readers want to use this algorithm for non-commercial surgical streaming, they must cite this article or acknowledge Orsi Academy and the primary author, Dr. Pieter De Backer.

4.1.6. Supplemental Digital Content

A.1. Video Frame Annotation

To evaluate which sampling method yields the ideal compromise between efficiency and accuracy, we annotated all 42 Intuitive Xi surgeries according to both methods, using the online annotation platform SuperAnnotate (Sunnyvale, CA, USA). The dataset generation pipeline is depicted in Figure A.1.

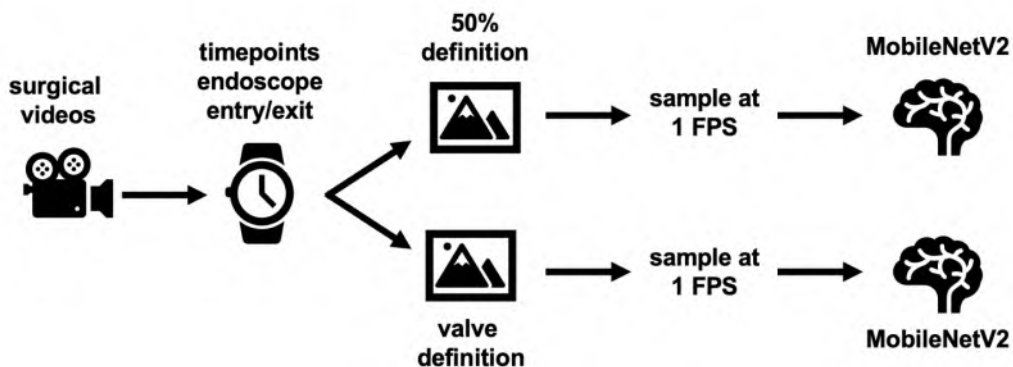


Figure A.1: (a) Image annotation and processing overview before the final dataset is fed into our network. Surgical videos are reviewed manually to indicate outside body fragments and framewise labels are constructed using either the “50% definition” or the “valve definition”. Subsequently, all videos are sampled at 1 frame per second (FPS) and the images are fed to the convolutional neural network for training (MobileNetV2).

The resulting annotation characteristics are summarized in Table A.1. Figure 1 (manuscript) shows that IODA out-of-body sequences are typically longer, and this is also reflected in the dataset characteristics as depicted in Table A.1., where more out-of-body frames are present.

Out of the 42 annotated procedures, we use 30 procedures for the network to learn (5 videos per procedural type) and six other procedures (1 video per procedural type) to optimize the learning process parameters (the so-called hyperparameter tuning). The network is trained twice: once with the 'Valve definition' and once with the '50% definition'. We perform a side-by-side benchmark to identify which annotation methods result in the best performance by evaluating the Intuitive Xi test set labeled for both definitions.

Table A.1: Overview of both datasets used for annotation definition exploration, including the video statistics, frame count and out-of-body statistics.

Dataset	video count (n)	Mean video duration \pm stand. dev. (min.)	Total sampled frames (n)	Out-of-body frames (n)	(%)	Number out-of-body sequences (n)	Mean out-of-body sequence duration \pm stand. dev. (s.)
Intuitive Valve	Xi 42	135,69 \pm 69,94	341.942	16.169	4,73	367	44,02 \pm 164,42
Intuitive 50%	Xi 42	135,69 \pm 69,94	341.942	18.066	5,28	376	48,03 \pm 162,37

Table A.2. depicts the performance metrics when comparing both definitions as assessed on the Intuitive Xi procedures. We found that the 'valve definition' outperforms the '50% definition' when trained with consistent training parameters. Additionally, the valve definition is easier to define and has lower annotation needs. As such, this definition is applied for our full cross-robotics comparison and real-time application.

Table A.2.: Performance metrics of the Valve and 50% definition networks on the Intuitive Xi test set.

	Accuracy (%)	Sensitivity (%)	Specificity (%)	Precision (%)	NPV (%)	F1-score (%)	ROC (%)	AUC (%)
Valve definition	99.91	99.13	99.94	98.54	99.96	98.83	99.53	
50% definition	99.87	98.93	99.92	98.25	99.95	98.59	99.42	

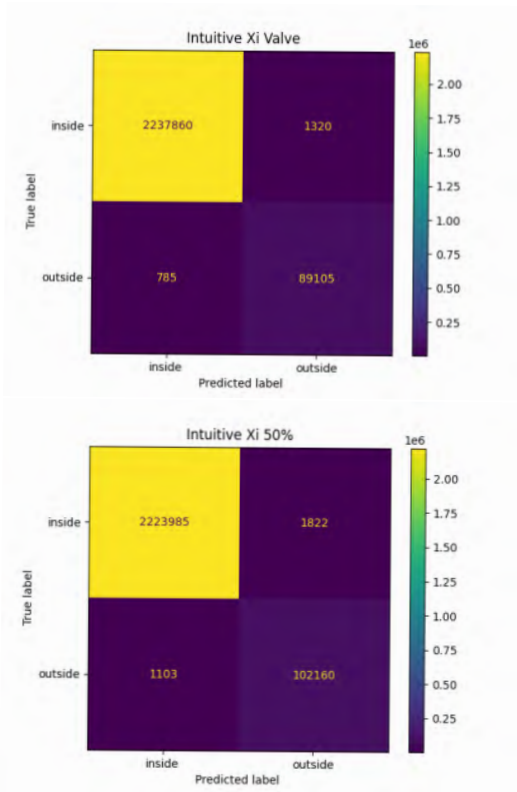


Figure A.2: The confusion matrices of the Intuitive Xi Valve network and the Intuitive Xi 50% network, resulting from running framewise inference on the Intuitive Xi test set.

[A.2. Deep Learning Network Training – Technical Details](#)

The model is trained for 50 epochs/iterations with a batch size of 256 images and an initial learning rate 0.0001. We used an Adam optimizer next to a ReduceLROnPlateau-scheduler with a factor of 0.5 and patience of 3. During training, early stopping is applied based on the “receiver operating characteristic area under the curve” (ROC AUC) of the validation set. The patience of the early stopping is set to 5. Each training image is preprocessed and augmented by applying random rotation, random contrast change, random horizontal flip, and a random resized crop, resulting in a 224x224 image normalized and fed to the network.

A.3. Single Robot vs. Multiple Robots vs. ROBAN vs. SOTA

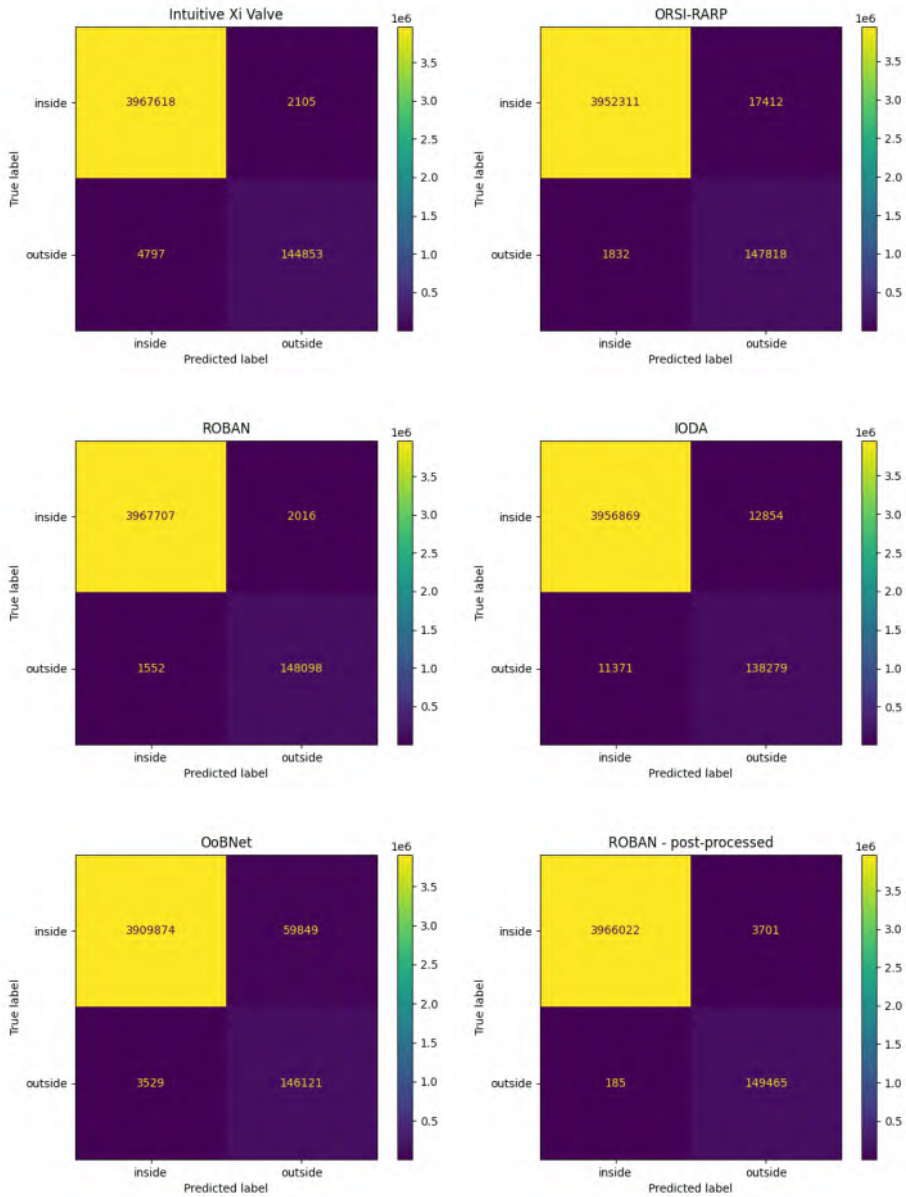
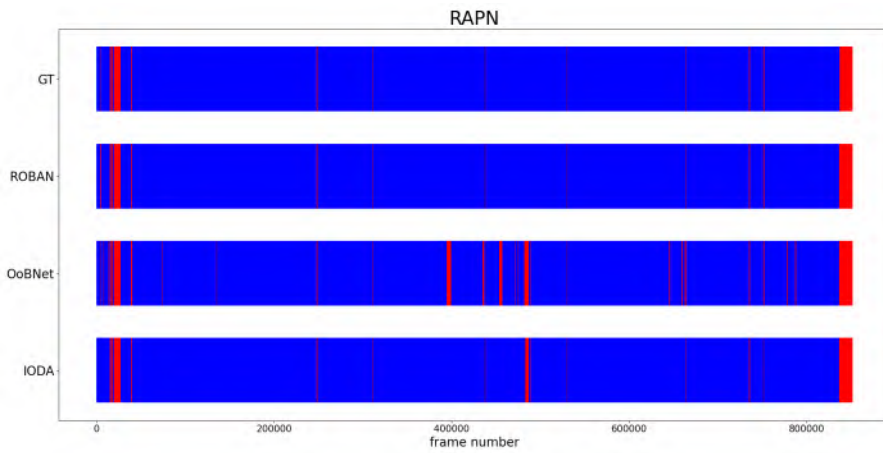
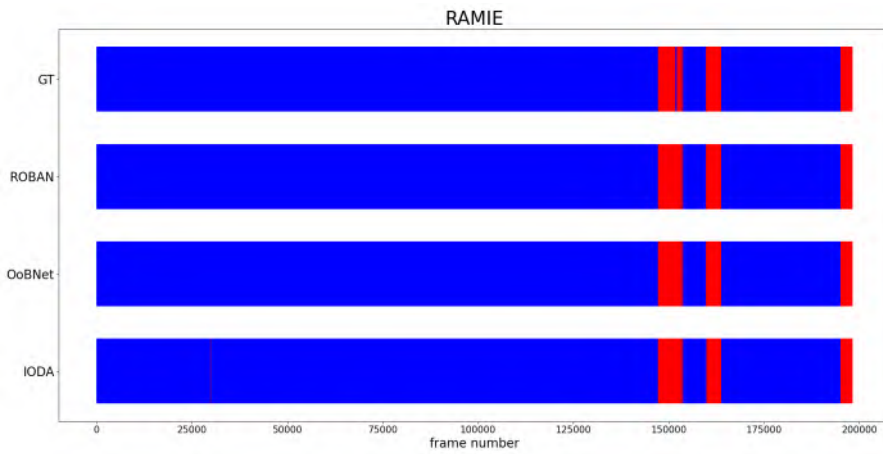
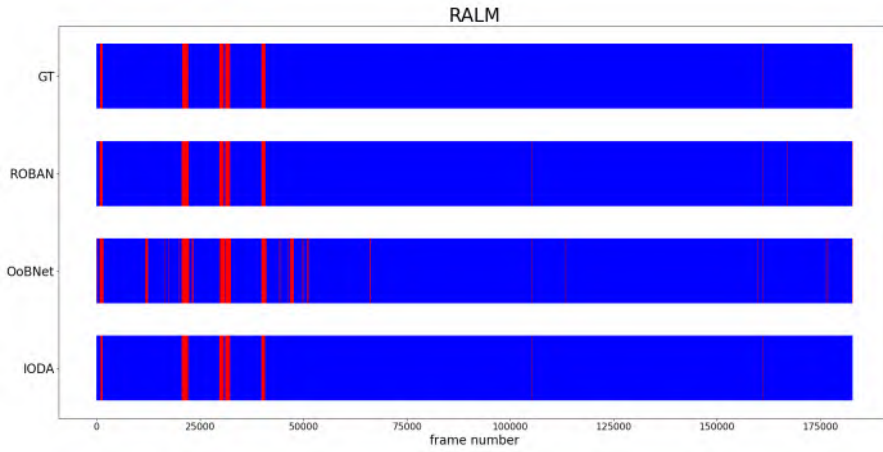
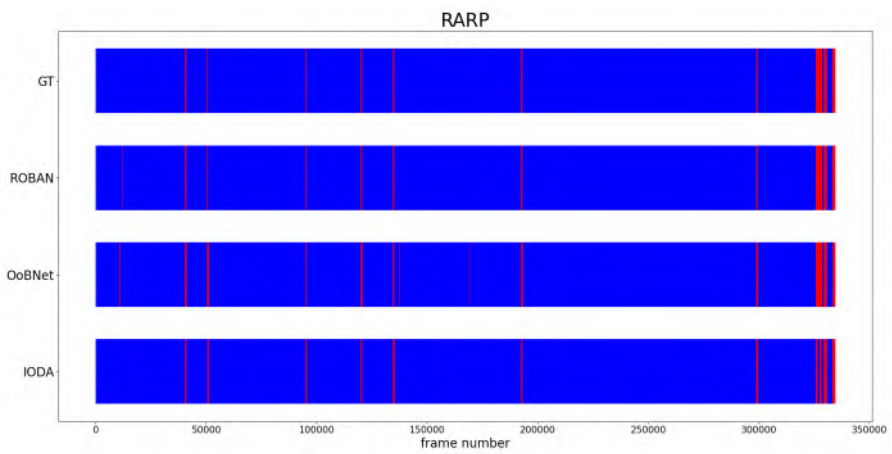
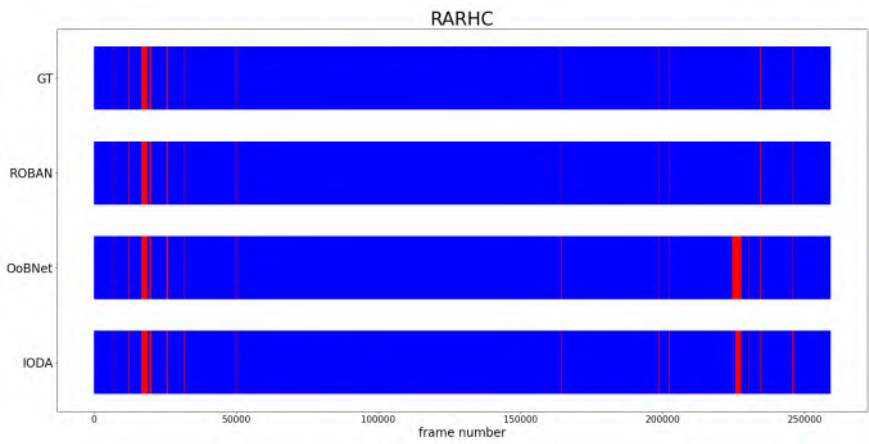
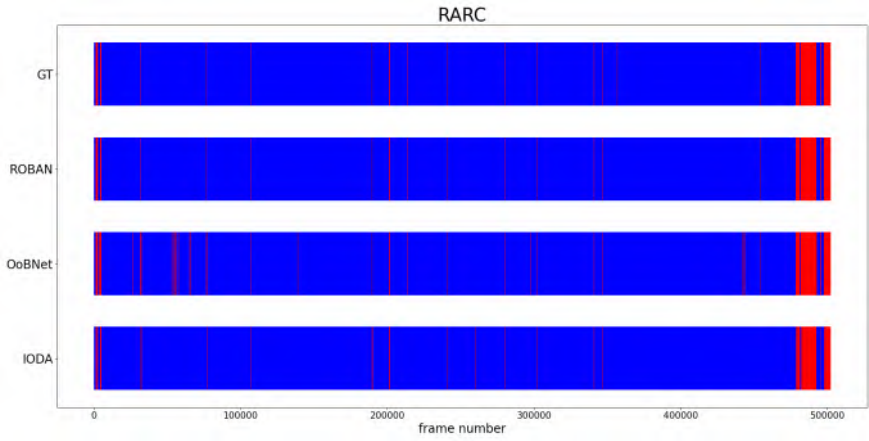


Figure A.3.: Confusion matrices of the Intuitive Xi Valve network, ORSI-RARP, ROBAN, IODA and OoBNet. The confusion matrices show the number of correctly and incorrectly classified images by comparing predicted label to the actual ground truth label (see Figure 3).





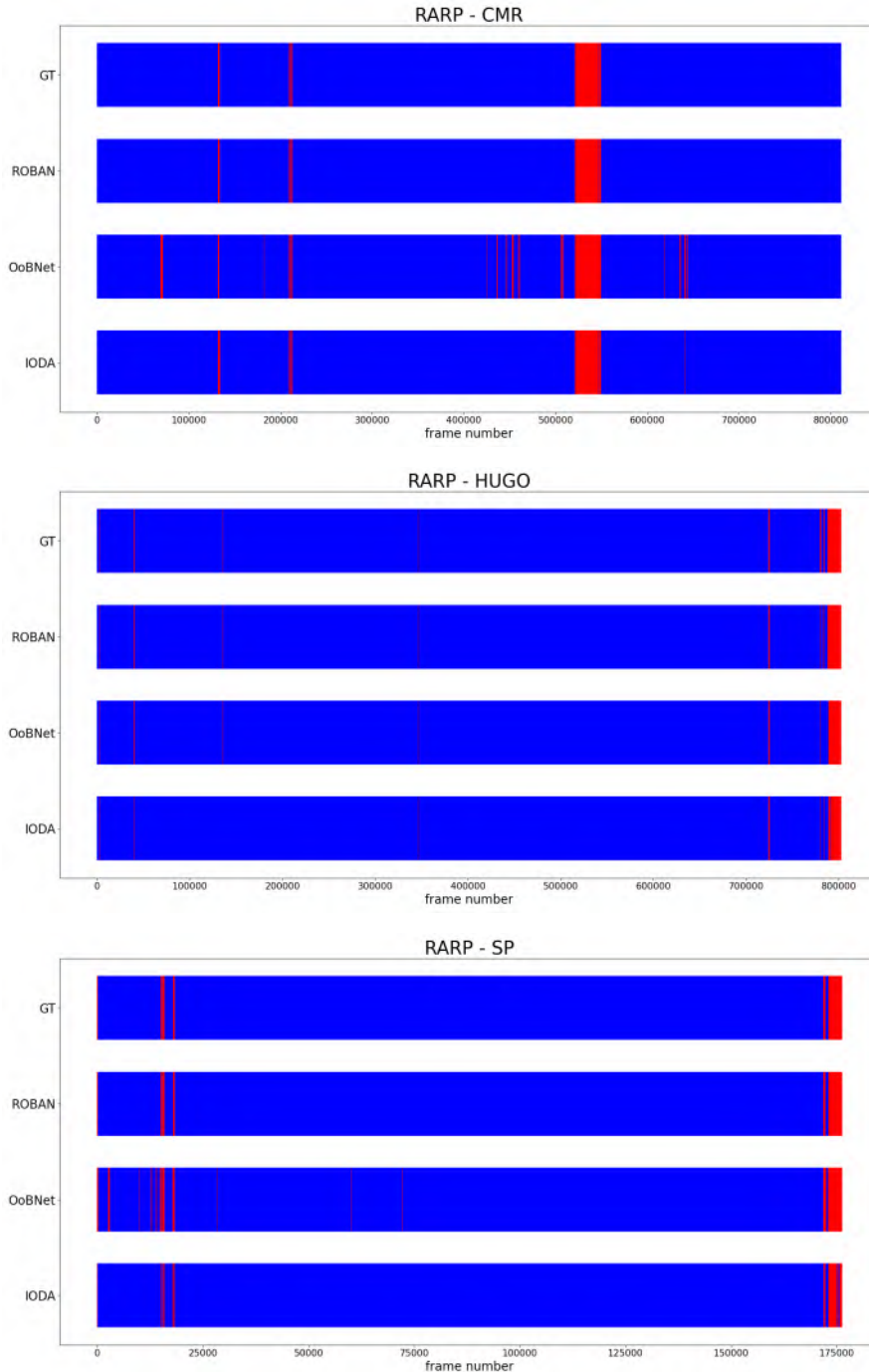


Figure A.4.: All 9 full length test-set videos, plotted by frame number in a side-by-side comparison. GT depicts the ground truth, as annotated manually, which is the correct solution. In red are out-of-body segments which should be detected, in blue are surgical segments. The 9 procedures are Robot-Assisted (RA) - liver metastasectomy (RALM), partial nephrectomy (RAPN), radical prostatectomy (RARP), radical cystectomy (RARC), minimal invasive esophagectomy (RAMIE), right hemicolectomy (RARHC). We compare ROBAN (Robotic Anonymization Network), OoBNet [175] and IODA [168].

algorithm	test set procedure	Accuracy (%)	Sensitivity (%)	Specificity (%)	Precision (%)	NPV (%)	F1-score (%)	ROC AUC (%)
ROBAN	RALM	99,87	99,74	99,87	96,13	99,99	97,90	99,80
	RAMIE	99,79	99,98	99,78	97,04	100,00	98,49	99,88
	RAPN	99,92	99,82	99,92	97,94	99,99	98,87	99,87
	RARC	99,91	99,48	99,93	98,71	99,97	99,10	99,71
	RARP - CMR	99,96	99,29	99,99	99,70	99,97	99,50	99,64
	RARP - HUGO	99,85	95,21	99,98	99,33	99,87	97,23	97,59
	RARP - Single Port	99,98	99,64	99,99	99,62	99,99	99,63	99,81
	RARP - Xi	99,97	99,63	99,98	99,48	99,99	99,55	99,81
	RARHC	99,96	99,64	99,96	98,17	99,99	98,90	99,80
OoBNet[175]	RALM	97,24	97,80	97,23	53,06	99,93	68,79	97,51
	RAMIE	99,70	99,68	99,70	96,01	99,98	97,81	99,69
	RAPN	96,98	99,05	96,90	55,01	99,96	70,74	97,98
	RARC	98,59	98,20	98,61	78,76	99,90	87,41	98,41
	RARP - CMR	98,11	98,74	98,08	68,46	99,95	80,86	98,41
	RARP - HUGO	99,76	91,11	100,00	99,85	99,75	95,28	95,55
	RARP - Single Port	98,82	99,52	98,80	71,76	99,99	83,39	99,16
	RARP - Xi	99,47	97,88	99,51	85,28	99,94	91,15	98,70
	RARHC	98,55	99,15	98,54	57,37	99,98	72,68	98,84
IODA[168]	RALM	48,46	86,15	99,96	98,41	99,56	91,87	93,05
	RAMIE	50,36	98,56	99,66	95,47	99,90	96,99	99,11
	RAPN	51,21	97,61	99,48	87,88	99,91	92,49	98,55
	RARC	49,70	91,77	99,70	94,19	99,57	92,96	95,74
	RARP - CMR	50,38	99,01	99,82	95,87	99,96	97,41	99,41
	RARP - HUGO	47,22	78,23	100,00	99,85	99,40	87,73	89,11
	RARP - Single Port	47,85	82,62	99,99	99,52	99,47	90,29	91,31
	RARP - Xi	49,82	85,07	99,62	86,44	99,57	85,75	92,34
	RARHC	55,49	95,86	98,50	55,99	99,92	70,70	97,18

Table A.3: Test set result metrics on a per procedure basis. In bold are the highest values per algorithm per metric. Underlined are the lowest values.

A.5. ROBAN Evaluation on Laparoscopic Cholecystectomy

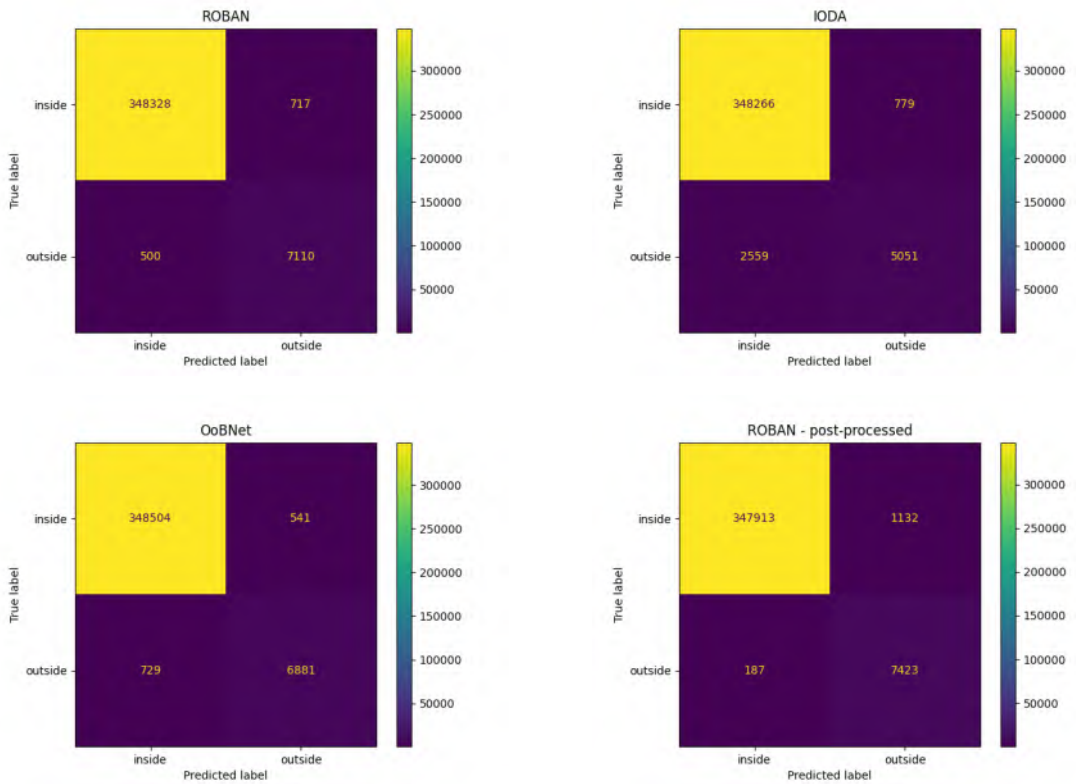
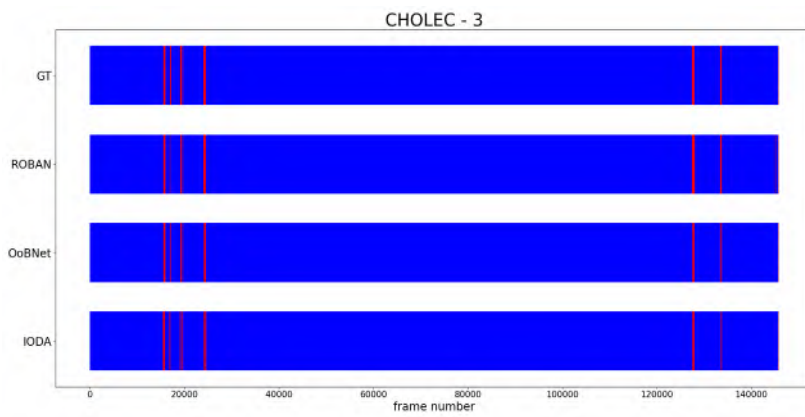
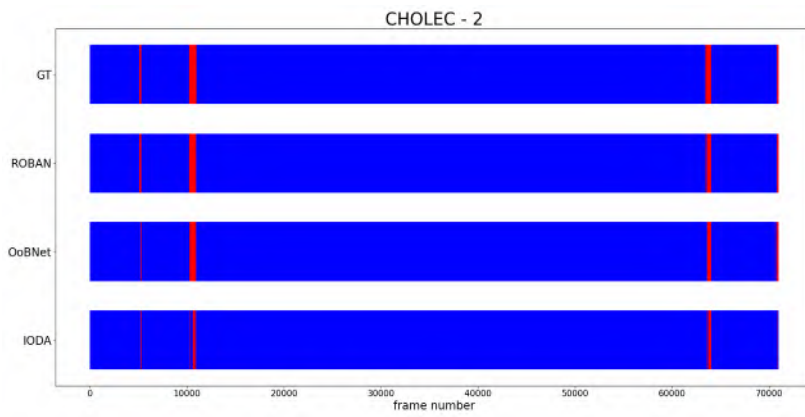


Figure A.5.: ROBAN, IODA and OoBNet Confusion matrices on the cholecystectomy test set. The confusion matrices show the number of correctly and incorrectly classified images by comparing predicted label to the actual ground truth label. In 367155 assessed frames, ROBAN found 500 false negatives and 717 false positives, reducing false negatives to 187 after postprocessing.



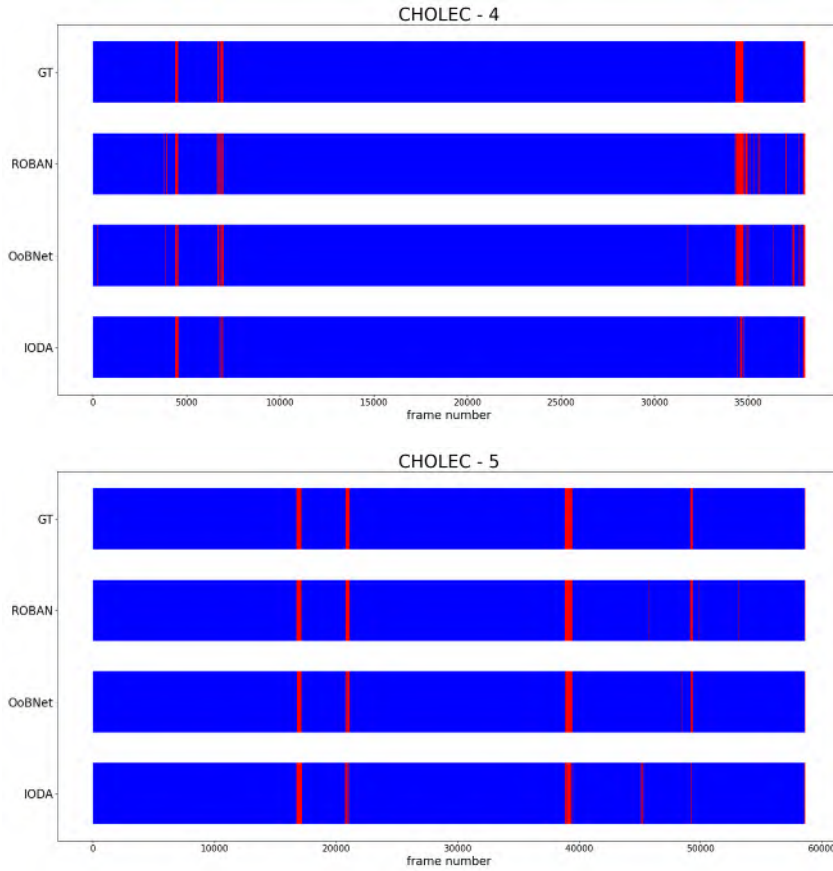


Figure A.6.: Evaluation on 5 cholecystectomy procedures[170]. All 5 full length test-set videos are plotted by frame number in a side-by-side comparison. GT depicts the ground truth, as annotated manually, which is the correct solution. In red are out-of-body segments which should be detected, in blue are surgical segments. We compare ROBAN (Robotic Anonymization Network), OoBNet[175] and IODA[168].

4.2. Data annotation

4.2.1. Abstract

Background

Artificial Intelligence (A.I.) holds tremendous potential to reduce surgical risks and improve surgical assessment. Machine Learning, a subfield of A.I., can be used to analyze surgical video and imaging data. Manual annotations provide veracity about the desired target features. Yet, methodological annotation explorations are limited to date. Here, we provide an exploratory analysis of the requirements and methods of instrument annotation in a multi-institutional team from two specialized A.I. centers and compile our lessons learned.

Methods

We developed a bottom-up approach for team annotation of robotic instruments in robot-assisted partial nephrectomy (RAPN), which was subsequently validated in robot-assisted minimally invasive esophagectomy (RAMIE). Furthermore, instrument annotation methods were evaluated for their use in Machine Learning algorithms. Overall, we evaluated the efficiency and transferability of the proposed team approach and quantified performance metrics (e.g. time per frame required for each annotation modality) between RAPN and RAMIE.

Results

We found a 0.05Hz image sampling frequency to be adequate for instrument annotation. The bottom-up approach in annotation training and management resulted in accurate annotations and demonstrated efficiency in annotating large datasets. The proposed annotation methodology was transferrable between both RAPN and RAMIE. The average annotation time for RAPN pixel annotation ranged from 4.49 to 12.6 minutes per image; for vector annotation we denote 2.92 minutes per image. Similar annotation times were found for RAMIE. Lastly, we elaborate on common pitfalls encountered throughout the annotation process.

Conclusions

We propose a successful bottom-up approach for annotator team composition, applicable to any surgical annotation project. Our results set the foundation to start A.I. projects for instrument detection, segmentation and pose estimation. Due to the immense annotation burden resulting from spatial instrumental annotation, further analysis into sampling frequency and annotation detail needs to be conducted.

4.2.2. Introduction

In recent years, the application of Artificial Intelligence (A.I.) techniques in the automated analysis of surgical video data has surged. More specifically, subfields of A.I. such as Computer Vision (CV) and Machine Learning (ML) are increasingly being applied to surgical videos. A systematic literature search for the key words “Computer Vision” and “Surgery” in Pubmed illustrates a continuous uprise in scientific publications in the field with a 50 fold increase between 2010 and 2021 (Figure 4.6). Real world applications of surgical computer vision include surgical workflow analysis, intra-operative guidance and objective action, error and risk assessment[184]. As such, these techniques might impact surgical outcomes and patient safety. One major building block for surgical video and image analysis through CV and ML is the detection and pose estimation of surgical instruments[185]. Knowing and foreseeing the position, orientation and action of an instrument provides a ML model with insights in the surgeon’s intent. Detecting instruments also allows for a more thorough comprehension of surgical workflow and potentially prevention of harmful tool-tissue interaction.

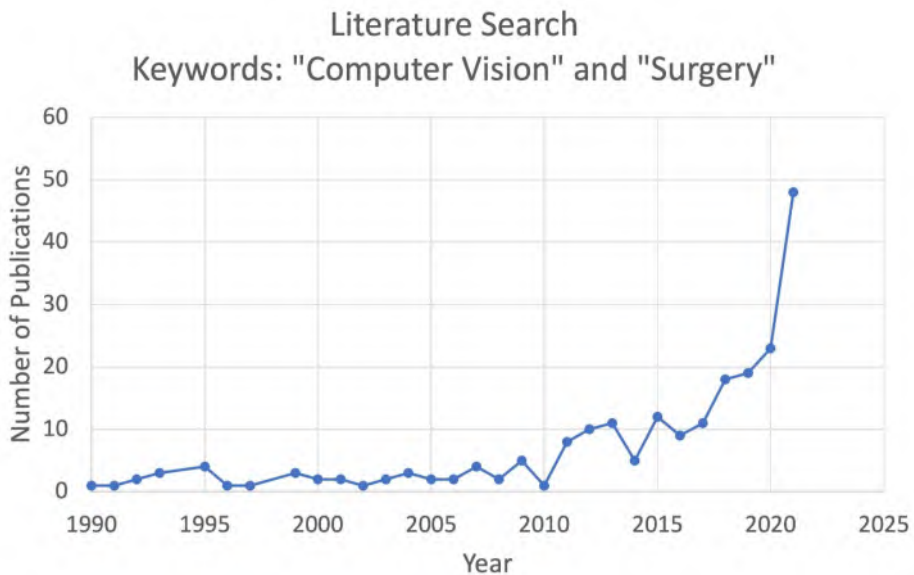


Figure 4.6: Literature search in Pubmed for the key words “Computer Vision” and “Surgery”

The spatial and temporal patterns, provided by moving instruments, are detected by ML models. State of the art ML and CV models rely largely on supervised learning[184], [186], meaning that the models learn to interpret video and imaging data on the basis of previously internalized, labeled data containing annotations of target features, such as instruments, organs, surgical phases or actions. Recent ML algorithms have even demonstrated good accuracy with respect to identification of operative steps and surgical tools in various procedures[187]. Besides providing visual information about current surgical actions, instrument segmentation also lends itself to CV analysis of surgical video data by giving clear boundaries and contrast compared to surrounding anatomical structures and tissue, which should also be interpreted. As such, labeling or annotating instruments is generally considered a good starting point for any new A.I. projects focused on surgical analysis and can serve as the basis for temporal as well as spatial analysis of surgical procedures.

Previous explorations of annotation requirements and proposals for annotation guidelines are quite coarse, lacking specific step-by-step information for A.I. laboratories or researchers new to the field. Clear guidelines proposing homogenous approaches to instrument annotation are missing. Previous work on the generation of standardized guidelines was initiated by the Society of American Gastrointestinal and Endoscopic Surgeons (SAGES) A.I. Taskforce[186]. In a Delphi Consensus, general questions around surgical video and imaging annotation, such as general characteristics of an annotation framework were addressed by an expert panel. While this presents a fundamental first step towards unified methodology, questions remain about what to annotate specifically, who the annotators should be, how to efficiently construct an annotation team and how to commence an A.I. project. Hence, this work sets out to address some of these questions in a “how to” manner. It demonstrates a feasible approach for instrument annotation along the SAGES consensus recommendations, aiming to assist surgical research groups novel in the field of A.I.. Regarding spatial annotations, the SAGES consensus recommends a hierarchical approach to increasing detail. For tool annotation this means increasing granularity ranging from the type of instrument, function, manufacturer and potentially functional subunits of the instrument (i.e. frontal edge of cautery hook rather than just hook). Therefore, we analyze the feasibility of instrument annotation in detail and describe encountered pitfalls to contribute to potential future refinements of this framework.

Ward et al pointed out that a major obstacle in time-consuming annotation, is the time spent by clinicians on annotations rather than designating that time to patient care and clinical work[188]. Additionally, annotator selection was pointed out to be one of the big challenges in surgical video annotation. The balance between clinical and annotation expertise is crucial for meaningful annotations[188]. Allan et al[189] also pointed out that a good rule of thumb for starting instrument annotation is to annotate all non-biological objects, as these are also easily identifiable by laymen, and leaving the more detailed discrimination of subunits of instruments and functional properties to medical students or clinicians.

Due to the previously observed low inter-annotator variability and good concordance between annotations of laymen and medical experts[190], instrument annotation is highly suitable for team annotations and multi-institutional collaborations. This facilitates the generation of large, annotated datasets, required for supervised ML, and eases the annotation burden for individuals. Nevertheless, currently available annotated laparoscopic and robotic surgical video datasets focused on tool segmentation remain rather small[184] and are limited to routine procedures, such as laparoscopic cholecystectomy[170], gastric bypass, sleeve gastrectomy and colectomy. This limits the diversity of annotated tools to the few examples present in these standard procedures and restricts transferability of annotations to other more complex procedures containing a wider range of instruments. Additionally, instrument annotation has been concentrating mainly on laparoscopic procedures, while robotic procedures are finding their way into surgical practice with equal or even superior outcomes. As such, robotic surgery is clearly gaining significance and prevalence regarding desired A.I. applications. However, up to date existing robotic datasets tend to be limited to ex-vivo experiments.

We suspect that the limited diversity of annotated datasets is not only due to shortage of qualified, medical annotators but that it is also related to missing guidelines governing annotation methods[188]. Furthermore, the limited clinical information and datasets openly accessible to most engineers regarding the target procedures results in repetitive

utilization of existing datasets rather than expanding the field towards novel approaches. This results in limited generalizability and transferability of the current CV techniques.

In this work, we present a comprehensive framework for robotic tool annotation, that may serve as groundwork for the start of any robotic surgical A.I. project on surgical workflow analysis evolving around instrument detection. This includes a detailed outline of a possible annotator team composition to decrease annotation burden for experienced surgeons. We demonstrate lessons learned from annotating >10.000 images manually by novel as well as expert annotators in two specialized A.I. centers and propose solutions to overcome said obstacles. To show generalizability, we apply the annotation methods developed during annotation of instruments in robot-assisted partial nephrectomy (RAPN) to robot-assisted minimally invasive esophagectomy (RAMIE). This may serve as a detailed guide for instrument annotation for any researcher interested in CV based automated tool detection.

4.2.3. Materials and Methods

Data Collection

We analyzed 82 videos of robotic-assisted partial nephrectomy videos (RAPN) from two Belgian tertiary referral centers (OLV Hospital Aalst and Ghent University Hospitals) collected between 05/2018 and 10/2021. Videos were collected from the Intuitive Si, X and Xi robots (Intuitive Surgical™, California, USA) using Hauppauge PVR Rocket recorders (Hauppauge Computer-Works GmbH - Mönchengladbach, Germany) and a MAQUET Tegriss system (Getinge Ag – Göteborg, Sweden). Videos were captured in 3 different resolutions: 720x576 pixels (p) resolution at 25.00 frames per second (fps) (VOB format), HD ready resolution (1280x720p) at 58.94 fps and Full HD resolution (1920x1080p) at 30.00fps (both mp4 format).

A multicentric collaboration was set up with the goal of exploring transferability of annotation methodology and adding to the diversity of the dataset. 94 videos of robot-assisted minimally invasive esophagectomy were collected in a German specialized upper GI Cancer center (University Hospital of Cologne, Department for General, Visceral, Tumor and Transplant Surgery) between 01/2020 and 07/2021. Videos were collected from the Intuitive Xi robots (Intuitive Surgical™, California, USA) using Mediacapture HD USB300 Recorders (MediCapture Inc.- Pennsylvania USA) in HD resolution (1280 x 1024p) at 29.97 fps (mp4 format). A subset of 15 standardized RAMIE videos was selected as a primary use case to demonstrate the transferability of the proposed annotation pipeline and evaluate methodological similarities and differences across procedures. To obtain a representable subset of videos we decided to exclude videos with quality issues (blurred images, incomplete video data), deviations from the standardized operative protocol resulting in use of different instruments and adverse events (minor bleeding, rupture of suture). These exclusion criteria ensure a standardized sample from the overall population to explore the general feasibility of our proposed methodology. Future investigations and establishment of annotation guidelines will take a larger variety of video characteristics and deviations from regular operative workflows into account. For this transfer feasibility study, the annotation focused on frames extracted from the anastomotic reconstruction phase, as defined by Fuchs et al[191], where the starting point of the operative phase is defined as when the hook touches the esophagus first and the endpoint when the needle is removed after suturing in of the circular stapler. This was decided due to the significance of the anastomotic phase in postoperative course and presence of various additional instruments throughout this reconstruction phase.

Data Preprocessing

Preprocessing of the videos included patient deidentification and removal of images containing patient clues inside the videos, as well as joining of multiple video segments to one consecutive video. Finally, for tool annotation purposes, video frames, meaning still images, were extracted at a framerate of 0.5 Hz for 5 videos, 0.1 Hz for 1 video and 0.05 Hz for 76 videos, meaning one still image was being captured every 2, 10 and 20 seconds of video respectively. The images were saved as uncompressed png-files resulting in a total count of 27597 RAPN images. Of these, 23598 images were completely annotated, resulting in 56 completely annotated procedures (16622 images). This slicing and video reformatting, as well as the frame sampling, was conducted using freely available open-source software ffmpeg (FFmpeg Developers (2016) - available from <http://ffmpeg.org/>). These images were subsequently uploaded to a professional annotation platform.

Annotation Methods

Spatial annotation of robotic instruments in RAPN and RAMIE were performed in the online annotation platform SuperAnnotate (Sunnyvale, CA, USA) by both ORSI Academy, Belgium and the Robotic Innovation Laboratory, University Hospital Cologne, Germany. Apart from SuperAnnotate, we also tested the freeware software Computer Vision Annotation Tool (CVAT) (<https://github.com/openvinotoolkit/cvat>).

In spatial analysis of surgical procedures, two major types of annotation methodologies need to be differentiated, namely pixel segmentation and vector annotation.

- Pixel Segmentation

In pixel segmentation, each pixel of the image is assigned to a certain class, or in this case instrument, by precise delineation of areas of interest[192]. Segmentation is one of the most popular image processing tasks[193], as it provides the most precise delineation of the surgical scene. However, it does not necessarily provide information on the position of the instrument and the ongoing action. During pixel segmentation the edges of each instrument are manually delineated and later assigned to corresponding classes. All pixel segmentations were performed using polygon tools. Tools facilitating segmentation like watershed algorithms[194] were explored and abandoned, as they were found to introduce impreciseness into the dataset due to less crisp side edges or imperfections at the instrument tips (see Figure A.13. in the Supplemental Digital Content Section Pitfalls). Figure 4.7 gives an overview of the explored necessary granularity of instrument segmentation for RAMIE.

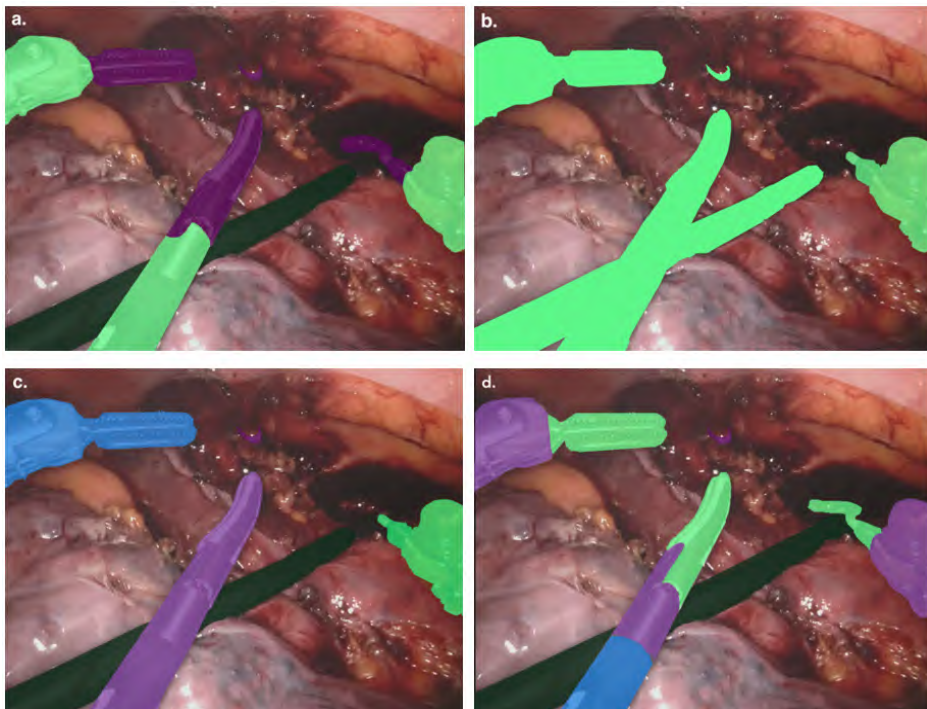


Figure 4.7: Pixel Annotation in RAMIE at different levels of granularity: (a) segmentation of tip and shaft (b) binary segmentation (instruments vs background) (c) instance segmentation of full instruments (d) segmentation of all articulations

- Vector Annotation

Vector Annotation specifies the orientation of instruments inside an image. This yields information such as instrument pose and interaction of individual parts. It is performed through denoting key points as a simplified version of the full instrument. These keypoints form wireframes indicating the relative position of the individual sub-elements of the robotic instruments. The points clearly differentiate the transition points between these sub-elements. This was considered particularly important for robotic instruments to account for the various angles and degrees of freedom.

Vector annotation was applied to the same surgical frames used for pixel annotation and also entails the indication of rectangular bounding boxes.

These bounding boxes were applied to frame the outer edges of each instrument, not accounting for the exact borders and subparts of the instruments. The bounding boxes could either include the entire visible part of the instrument or just the functional tip. An example of vector annotations for RAPN is given in Figure 4.8.

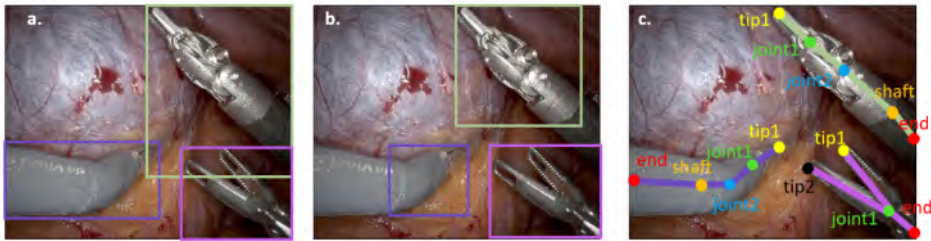


Figure 4.8: Bounding Box and Vector annotation of robotic instruments in RAPN. (a) bounding boxes delineating the whole instrument (b) Bounding boxes delineate the functional tip of the instruments (c) Vector Annotation for pose estimation: separate points indicate the entry point in the image ('end'), the start of the instrument tip ('shaft'), both joints of the robotic instrument ('joint1' and 'joint2'), as well as the instrument tips ('tip1' and 'tip2', or 'tip1' if the instrument is closed)

[Down Sampling of Frames for Annotation Purposes](#)

1 minute of a 60 fps video contains 3600 images. Hence it is impossible to annotate every single image and the annotation load should be balanced against the loss of detail. Taking into consideration that the ideal sampling frequency required for training of ML models is yet to be determined, we provide a quantitative analysis for instrument annotation by down sampling of video frames. We resampled RAPN frames, sampled at periods of 2 seconds to sampling periods of 4, 6, 8, 10, 20, 30 and 40 seconds. Per time interval, we calculate the intersection over union (IoU) for all RAPN procedures as a measure to quantify at which frequency the instruments are sufficiently differently positioned from the previous image or timepoint. Figure 4.9 shows a correlation between the extraction period and the position change of the instruments, it also shows the calculation of IoU[195].

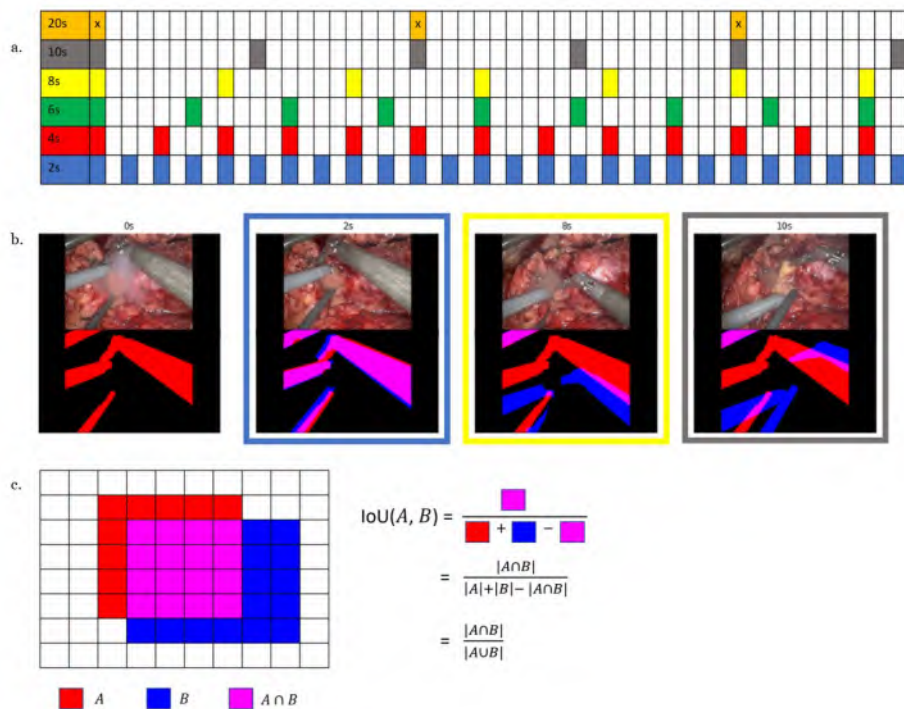


Figure 4.9: Correlation between (a) Sampling period and (b) position change of robotic instruments as compared to the initial position at time zero. In blue we see the new position as compared to the previous position in red. In magenta we see the overlap; (c) Intersection over Union calculation

Annotation Team Composition and RAPN Annotation

Due to the previously described low inter annotator variability in tool annotation and the large workload of two robotic datasets, we composed a hierarchical team structure (Figure 4.10). The team was led by one annotation-experienced supervisor, in our case a surgical resident, who served as the supervisor for a “Quality-Assessment (QA) Team” as well as an “Annotator (A) Team”. The supervisor took responsibility for data collection and data handling as well as close communication with an engineering team, concerning the requirements on annotations for ML purposes. Besides that, the supervisor’s roles were (1) conducting annotation training among the QA Team, (2) coordination of the annotation process including guidance of the individual annotators in the QA Team, and (3) ensuring the legal and ethical integrity of the data handling by coordinating with the involved ethical and regulatory committees.

Additionally, parts of the annotation workload were performed by professional annotation teams with no medical expertise (denoted as ‘laypeople’ in Figure 4.10). This served as measure to decrease annotation burden and helped to explore and assess the feasibility of our proposed hierarchical annotation team composition.

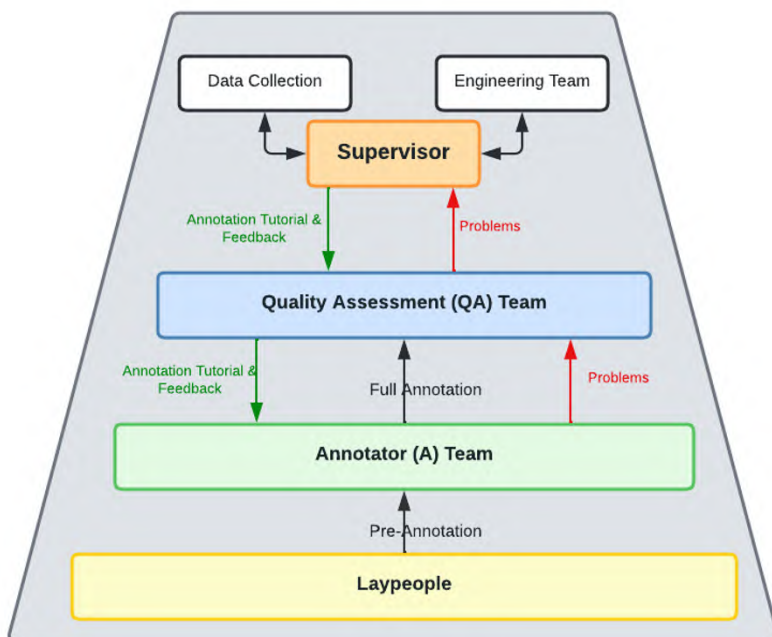


Figure 4.10: Overview of the proposed hierarchical team composition for scaling data annotation.

The QA Team consisted of 4 medical students with equivalent levels of annotation expertise who previously worked in different annotation packages. The QA Team’s role is to (1) pass on the annotation training and annotation guidance to the A-Team and (2) perform a quality check on every frame annotated by the A-Team. The A-Team in turn consists of a group of medical students (n=33), responsible for (1) performing spatial annotations of instruments and (2) overseeing and checking laymen workforce’s annotations. The laymen workforce is part of professional organization, and thus were already proficient in the software packages at hand, but they had no insight in the labeling

methods or requirements. Troubleshooting, questions or doubts concerning the annotation process and technical obstacles were handled in a layered “bottom up fashion” where the A-Team consults the QA team, which then consults the supervisor in turn. 10489 out of 16622 images were pre-annotated by the laymen workforce to investigate the impact of annotators with no medical experience on performing instrument annotation with regard to accuracy and time saving.

Both the laymen and A-Team were provided with a list of instruments required to annotate, and performed a test set annotation round on which they received feedback. The test set was composed by the supervisor with respect to adequate image variability and possible bottlenecks or questions that arise during annotation. Both groups were asked to do every annotation fully manually, (i.e. without the help of intelligent algorithms, e.g. watershed algorithms etc). All images were quality checked in SuperAnnotate (Sunnyvale, CA, USA). 10489 images were pre-annotated by laymen, 22% of these images were pre-annotated in CVAT (<https://github.com/openvinotoolkit/cvat>), while the remaining 78% was pre-annotated in SuperAnnotate.

For pre-annotation, 2 schemes were tested. In a first scheme, the laymen workforce only annotated instruments as binary segmentations, without indicating instrument names (see Figure 4.7.b). In a second experiment, laymen also added the instrument name, and the A-Team provided quality control on the annotated instruments, as well as added additional small items like needles, wires, gauzes, etc. Subsequently all annotations of both schemes were quality checked by the QA Team.

[Annotation Training](#)

For the A-Team, annotation training consisted of having every annotator in the A-Team annotate a predefined test set of sample frames to overcome the suspected learning curve during annotation of robotic instruments. The A-Team was immediately trained to discern the different instruments, clips, wires, hemostatic agents, etc. after a hands-on instrument training session combined with an introduction to the annotation software package. Laymen workforce also received a test set, with a focus on robotic and laparoscopic instruments. They were already proficient in the labeling software at hand and only received further feedback or instructions if the test set they delivered back was insufficiently precise.

[Annotation Process](#)

Every annotator within the A-Team was required to perform between 50 and 72h of accumulated annotation activity in the annotation platform over the course of 4 weeks, divided over pixel segmentation and vector annotation. There was no predefined split between the different annotation types per annotator. The A-Team was given new images dependent on the general progress of the annotation process. Every annotator in the A-Team received a fixed number of images which are submitted to the QA team when the annotator believes them to be finished. Incorrect images are sent back to the A-Team by the QA team, accompanied by feedback so that they can be adjusted properly. The A-Team annotators can view their performed working hours inside the software package, which allows for a sense of self-evaluation and benchmarking. The focus of the annotation process was primarily on pixel annotation, attaining a total of 11431 images. In this identical dataset, 3896 vector annotations were finished by the A-Team. After finishing the annotation work packages, all A-Team annotators filled in an online questionnaire about their annotation impressions.

[RAMIE Annotation](#)

The above described bottom up approach for annotation of robotic instruments was then transferred to a separate annotator group in the Robotic Innovation Laboratory for annotation of RAMIE. Annotation training was performed in the same manner as described above. The primary goals of this project extension was the assessment of transferability of the annotation methodology established throughout this instrument annotation project, the validation of the established annotator team structure and the quantification of the times needed by novel annotators to perform pixel and vector annotation of robotic instruments in RAMIE after implementation of a pre-established annotation guide. Within the RAMIE video dataset, 15 videos of the anastomotic phase were annotated. With a mean duration of 27.39 min of the anastomotic phase, an average of 82 frames per video were extracted at a sampling period of 20 seconds. This would result in a total of 1232 frames for all 15 videos. Pixel as well as vector annotations of 183 images were performed within the SuperAnnotate software. The Annotator Team consisted of 3 medical students, the QA Team of 2 surgical residents with little annotation experience and the supervisor was an attending for upper GI surgery.

4.2.4. Results

In the following section we describe the observations made throughout the spatial annotation of robotic instruments. We illustrate our findings regarding the ideal sampling frequency for instrument pose estimation. We evaluate the annotator team composition for our hierarchical bottom up approach. Furthermore, we display the average time spent on the spatial annotation of robotic instruments in each individual frame of RAPN and RAMIE.

[Dataset Instrument Distribution](#)

We accumulated a total of 41 different annotated classes throughout the whole RAPN dataset. We discern between robotic and laparoscopic instruments and other non-organic objects such as bulldog clamps or hem-o-lok clips. A list of all different instruments and objects for pixel and vector annotation can be found in the Supplemental Digital Content Table A.4. Figure 4.11.a gives an overview of the top 5 instruments present in the RAPN dataset.

[Sampling Frequency](#)

To determine sufficient change in instrument positioning for two consecutive frames, the intersection over union (IoU) was calculated. Figure 4.11b-d shows the correlation between IoU and sampling period. Expectedly, the IoU decreases as the sampling period increases. As the procedure progresses and the camera angle changes, the instruments indeed have higher chances of being positioned at completely different angles and locations. This results in a higher variety of diverse frames, leading to more varied training data available for ML models. However, sampling periods should not be too large as to not lose too much surgical detail. Figure 4.11.b shows the pattern of decreasing overlap (IoU) when all instruments are considered together as in a binary segmentation (Figure 4.7.b). When investigating single instruments (monopolar curved scissors and large needle driver) on a frame per frame basis, we denote similar trends. We see a decrease down to 8 seconds, after which the IoU slowly start to plateau. We choose a sampling period of 20 seconds (0.05 Hz) as for some instruments like the large needle

driver (Figure 4.11.d), the IoU still experiences quite a drop. After periods of 20 seconds, all curves tend to flatten, meaning the instruments are sufficiently differently positioned.

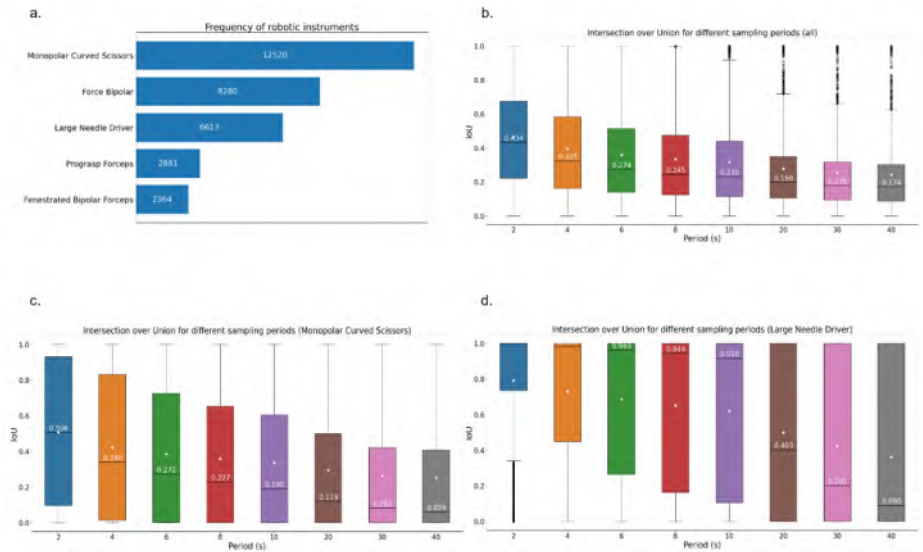


Figure 4.11: (a.) Distribution of top 5 annotated robotic instruments. (b.) Boxplot diagram of the IoU of all instruments compared between frames for different sampling frequencies, as in binary segmentation - Figure 4.7.b. (c.) Boxplot diagram of the IoU of monopolar curved scissors, the most prevalent class, for different sampling frequencies. (d.) Boxplot diagram of the IoU of large needle driver, the third most prevalent class, for different sampling frequencies. The white dots inside the boxplots denote the mean IoU for that period.

Annotator Team and Annotation Time

The deployed hierarchical, bottom-up approach for annotator team composition proved to be feasible and effective. Additionally, the pyramid-based approach proved to be a cost-effective way to scale-up annotation efforts. Figure 4.12 provides a flowchart of our different experiments for all completely annotated procedures.

Out of the 16622 annotated frames, 6025 images were annotated by medical students in the A-Team without any prior annotation, with a subsequent quality check, resulting in the overall longest annotation time of 12.6 minutes per image. 108 images without prior annotation were directly annotated by the QA Team, resulting in the overall second fastest annotation time of 5.17 minutes per complete image.

The fastest throughput time per image was achieved for the images which underwent pre-annotation by laymen and which were subsequently adjusted and checked by the QA Team, resulting in a total annotation time of 4.49 minutes per image.

The 10489 images which were pre-annotated by a professional workforce, showed that professional teams tend to work faster, however, a thorough quality check which corrects certain classes or adds certain details by the A or QA Team is required. We do note that, bringing in a professional workforce of laymen with no medical background, approximately halves the required time per annotation compared to annotation from scratch by students.

When looking at different types of pre-annotation by these laymen (not depicted in Figure 4.12), the setup in which pre-annotation consisted of binary segmentation as in Figure 4.7.b., subsequently took the QA Team 2.23 minutes per image on average to complete.

In the second setup, pre-annotation was performed as in Figure 4.7.c, in which annotators now also assign the instrument class. On average, the QA Team took 1.66 minute per image on average to complete.

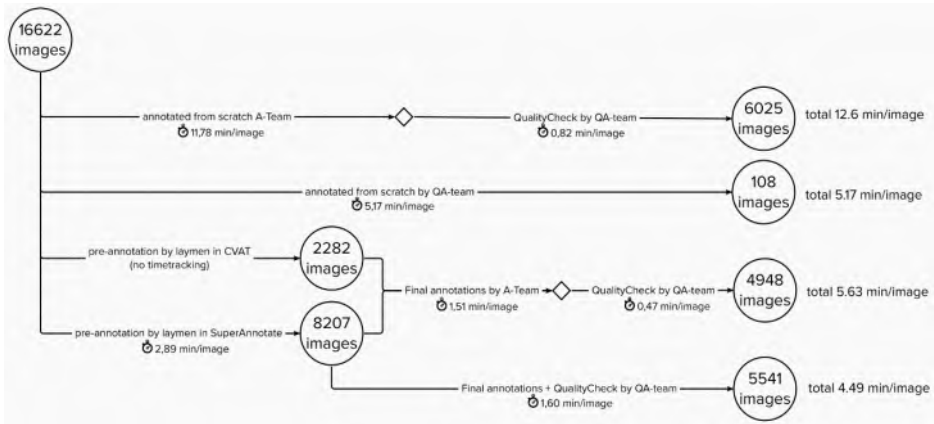


Figure 4.12: Flowchart of different annotation times for annotation pipelines.

Learning Curve for Annotation

Within the A-Team, 29 medical students completed their assigned working package, 4 students dropped out. All participating 33 medical students filled in a questionnaire afterwards.

21% (7 students) felt they needed 0-4 hours to master the instrument segmentation, 52% (17 students) estimated 4-8h would be necessary to master the instrument segmentation, and 27% (9 students) needed 8-12h of annotation before achieving a sense of mastery. No participants indicated needing more than 12 hours of annotation to achieve a sense of mastery.

A large variation was observed between annotation times of different A-Team members. Plotting average annotation times versus number of completed images indeed revealed a trend of decreasing annotation times as more images were annotated. Figure 4.13 shows average pixel segmentation times plotted against the number of completed images. We note a clear decrease with increasing numbers of completed images, which tends to plateau around 500 images. Even at the fastest annotation rate of 5.17 minutes per finished instrument segmentation, the annotation of 500 images corresponds to approximately 43 hours. As such, there is a clear discrepancy between the objective assessment and the subjective feeling of a novel annotator.

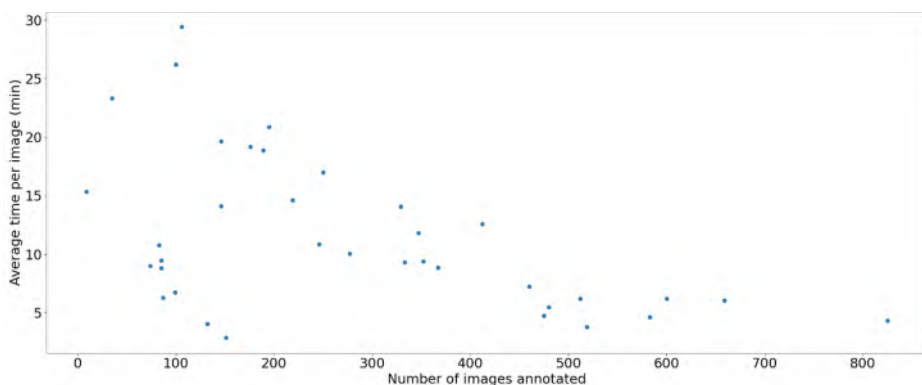


Figure 4.13: Annotation times per images versus number of annotated images. All images were annotated from scratch.

Pixel Annotation

Pixel Annotation was evaluated for different levels of granularity. Figure 4.7 already showed the different levels of detail deployed during semantic segmentation through pixel annotation. Each color represents a different part of the instrument. This means that figure 4.7.d has a visible total of 7 classes (each instrument consists of maximally 3 subunit classes) and figure 4.7.a consists of 6 visible classes (maximally 2 classes per instrument). Figure 4.14.b shows a binary segmentation, separating instruments from the background, and thus consists of only one class: “instruments”. Figure 4.7.c shows the most commonly used approach, where each instrument is assigned an individual class, which can be considered the most time efficient. We note that every form of pixel annotation can be derived from figure 4.7.d by simply merging the different classes per instrument. While this proved to be the most precise form of pixel annotation, the time investment is higher. Hence, we chose to perform the multiclass segmentation as depicted in Figure 4.7.c for the entire dataset.

On a pixel level, we chose a very precise delineation of all visible objects.

Figure 4.14 depicts the results of a real-world application for instrument segmentation. A computer vision model (more specifically a deep learning model named DeepLabV3+[196]) performs semantic segmentation on unseen images, trained on the RAPN dataset developed in this work. We denote the clear need of precise annotation: the model can detect the orifices inside the force bipolar grasper, something which would have been impossible if these orifices would have never been annotated.

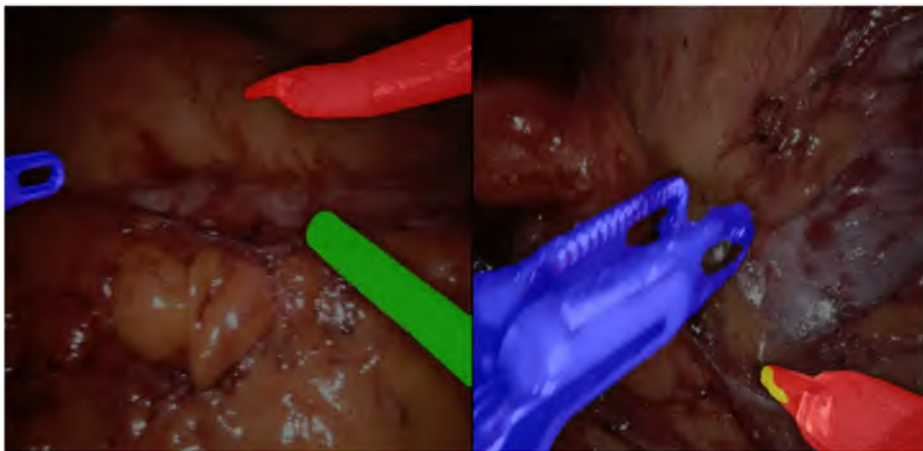


Figure 4.14: Results of DeepLabV3+ model doing semantic segmentation on new unseen images. We denote how the orifice of the force bipolar is correctly predicted, due to very precise input data of this model.

Another problem encountered was dealing with multiple instances of the same class, e.g. with hem-o-lok clips. Figure 4.15 shows a surgical scene after renorrhaphy with 12 hem-o-lok clips. When identical items are present in the image, we found it important to assign these to different classes. As can be seen in Figure 4.15.a, when all clips have the same class and therefore same color it is hard to distinguish the positioning of the clips. Applying different labels and colors for each individual clip, as seen in Figure 4.15.b, allows for easy differentiation. This is a good example of the difference between ‘semantic segmentation’ (Figure 4.15.a) and ‘instance segmentation’ (Figure 4.15.b). This might be important for algorithms evaluating the safety of clip placement but also in bleeding detection to differentiate individual objects from a bleeding vessel. The same applies to other surgical items that can be present multiple times, e.g. vessel loops, needles and sutures or bulldog clamps. A more in depth elaboration on pitfalls for pixel annotation is provided in the Supplemental Digital Content.

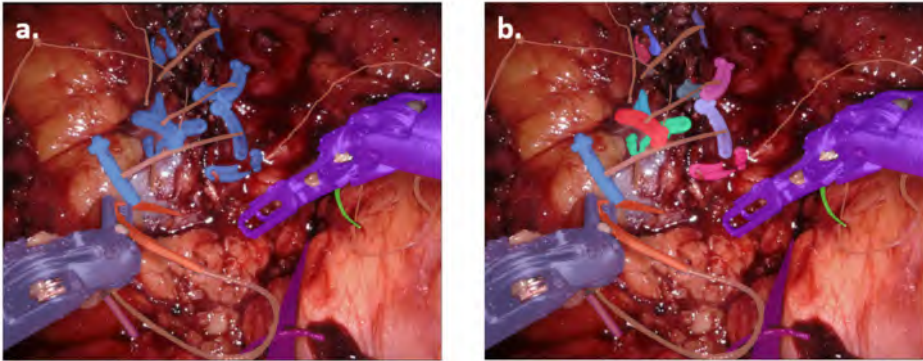


Figure 4.15: Results for pixel annotation for smaller objects (e.g. clips) (a) semantic segmentation (b) instance segmentation

Vector Annotation

In addition to various levels of detail in pixel annotation we evaluated different inclusion criteria for bounding boxes and vector annotation. In Figure 4.8.a, the entire visible part of the instrument is included in a bounding box assigned to an individual class.

Bounding boxes offer an easy way to locate an instrument inside the surgical scene and the annotation is very time efficient. However, it is also a very coarse annotation not allowing for conclusion on where the exact tip of the instrument is located within the operating field. If bounding boxes overlap, it is also difficult to interpret how instruments are interacting (Figure 4.8.a). We counteract this effect by focusing only on tip bounding boxes, as shown in Figure 4.8.b. We also denote that bounding boxes can be derived automatically from segmentations, which implies a significant time gain. We refer to the Supplemental Digital Content for a more elaborate discussion.

Figure 4.8.c shows the results of our final wireframe definition for vector annotation. During the process, we noted it was far more useful to indicate different points along the instruments rather than defining lines. Rather than gathering a collection of lines or vectors along the axis of the instrument without knowing what the start and ending point of the vector signifies, we started to denote the different hinges of the instruments, and derive the vectors as the simple lines between these points. As such Figure 4.8.c demonstrates how adding simple points or subdivisions of the instruments using vector annotation can derive a fully functional wireframe. For our final convention, the point where the instruments enter the frame was noted as 'end', the location of both 'joints' were indicated and the position of the 'tips' were separately annotated when they could be seen. The 'shaft' noted the transition between instrument the head of the instrument and the shaft.

4

This allows detailed differentiation of visible and occluded parts of the instrument and derivation of the exact functional subunits of the instrument interacting with tissue. This wireframe information can subsequently be combined with a segmentation mask to show if the occlusion is due to another instrument, arising from overlaying tissue or because parts of the instrument are located outside of the camera view. Wireframes also provide information on the instrument orientation and give more fine grained details such as opening or closing of graspers, certain instrument angulations etc.

Transferability of Annotation Workflow to RAMIE

The transfer of the previously established hierarchical annotation team approach was perceived well at the Robotic Innovation Laboratory at University Hospital Cologne by participating medical students as well as surgical residents. Even though the annotator team was significantly smaller (a total of 5 annotators compared to 38 annotators without a layman annotation workforce) the annotation framework was successfully transferred to the second annotation site and completed by novel as well as experienced annotators. To enhance the feedback structure, there was close collaboration with ORSI academy to address difficulties along the annotation process. Average annotation time for pixel annotation was 6 minutes per frame and average annotation time for vector annotation was 3 minutes per frame. With an average total duration of 196 minutes for the thoracic part of RAMIE the annotation of all frames at sampling periods of 20 seconds, the total estimated time for annotation would result in 14.7 annotation hours per procedure. Figure 4.16 shows the results of pixel segmentation for RAMIE. Annotators reported that the annotation accuracy was most likely affected by camera aspects, such as presence of smoke and additional annotation burden by delineating information irrelevant to future model detection, such as display information as seen in figure 4.16.c and 4.16.d and the bottom of the image and alongside the instruments. To increase efficacy in assessing the overall transferability of the annotation methodology, a standardized subset of 15 videos was annotated. Excluding videos with quality issues and deviations from routine workflow ensured a focus on commonly utilized instruments in RAMIE. Inclusion of videos displaying deviations from a routine workflow, which would result in the annotation of a variety of more infrequent instruments, as well as annotation of low quality videos would have resulted in a significant time delay. This subset served as a use case for annotation methodology rather than a complete dataset. Future explorations will focus on exploring more diverse and larger sets of videos.

Other general pitfalls and limitations encountered as well as a detailed description is provided in the Supplemental Digital Content.

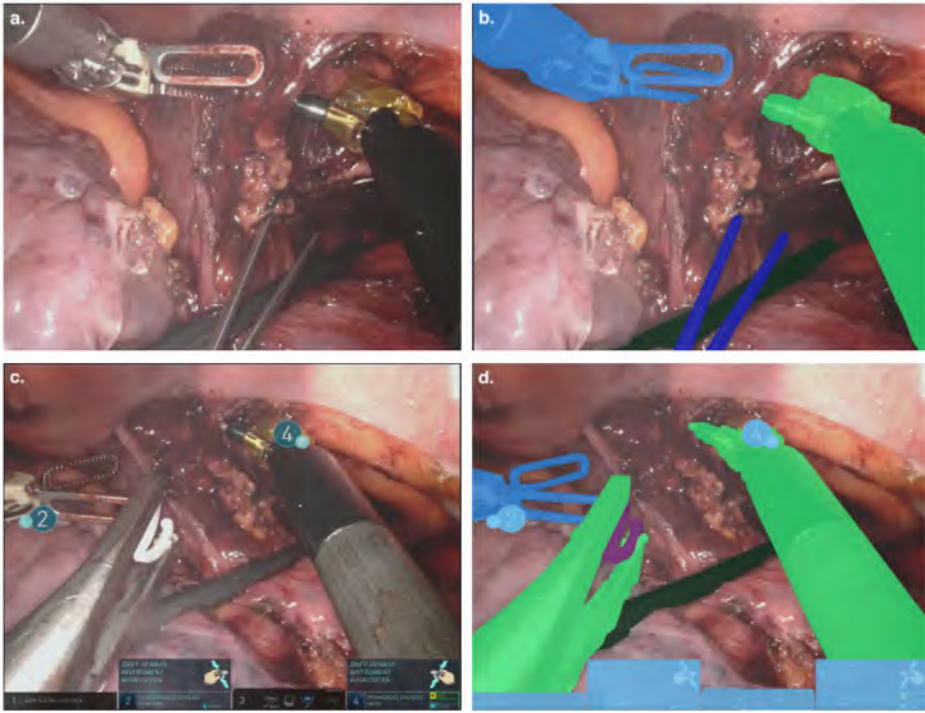


Figure 4.16: Results of pixel annotation in RAMIE (a + b) surgical scene without distraction (c+d) surgical scene requiring annotation of display

Figure 4.17 shows the results of combined bounding box and vector annotation in RAMIE. It is notable that the cautery hook was perceived the most difficult for vector annotation due to the changing angle effecting the orientation of the functional tip (Figure 4.17.c).

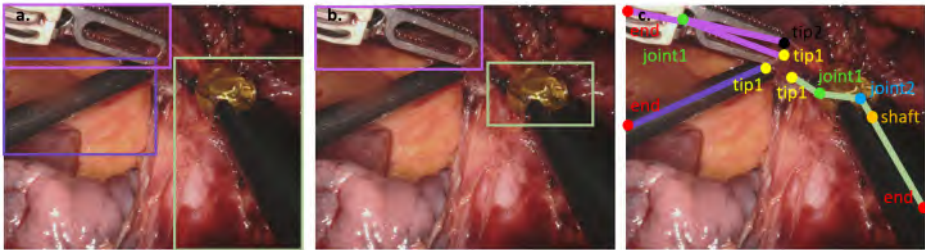


Figure 4.17: Results of bounding box and vector annotation in RAMIE contrasting the different angles of the cautery hook requiring alteration of annotation and resulting in higher diversity of frames. Note the absence of the tip bounding box for the suction, as there is no articulating or rotating end.

4.2.5. Discussion

Supervised machine learning comprises the majority of applications of artificial intelligence in surgery today. Arguably the performance of a model is just as good as the underlying information the model was trained on. As Meireles et al lay the ground stone for surgical video annotation in the SAGES consensus[186], a key message was that annotation, both spatial as well as temporal, should increase in granularity to ultimately account for all facts comprising the surgical field of view that are perceived by the

surgeon. This study is the first of its kind, exploring not only the required detail of spatial instrument annotation but also describing encountered pitfalls. Compared to previous datasets[197], [198], we perform a more detailed pixel annotation, annotating up to 41 different classes. We refer to the Supplemental Digital Content for elaborative images, tips and tricks. Besides passing on detailed information about first steps of instrument annotation, we demonstrate that our annotation methodology, annotation teaching and team composition is transferable across two highly complex robotic operations, RAPN and RAMIE, and across institutions.

The first key message when starting new projects is to think carefully about the level of detail in annotation. The main question arising from this exploration is the effectiveness of annotation and appropriateness of performed annotations for machine learning applications. Which annotation modality should be chosen for instrument detection algorithms is the first question every A.I. project should address. Combining pixel annotations at instruments level (without subunits) in combination with wireframes are expected to form a decent weigh of between exact delineation and functional instrument information on instrument pose and movement. Tip bounding boxes form an alternative to both vector and pixel annotation if annotation resources are limited or the focus is on mere instrument detection. When already performing pixel and vector annotation, there is no use in bounding box delineation as these can be derived automatically from the vector and pixel information.

In surgical procedures where small movements may cause huge damage, the detection of the full instruments through large bounding boxes does not appear to be helpful. The tip of the instrument provides most information about the position of the instrument, its differentiation towards others tools and the tool-tissue interaction.

Overall, we propose a combination of annotation methods depending on the surgical phase. In surgical scenes where wide range movements are dominant and a lower detection accuracy by machine learning models may be acceptable, bounding box annotation may be sufficient, whereas in fine-tuned dissection phases detailed pixel annotation and vector annotation is advisable.

The second key message of this work is that annotation efficiency can be significantly increased by a vertical hierarchical annotation team structure. The proposed bottom up approach requires a large workforce, however it also significantly decreases the annotation burden for clinicians.

In this approach, the need for a dedicated quality team is evident, as they provide high quality annotations, and have shown to be the fastest, both in annotation from scratch as in annotation and quality assurance of images pre-annotated by of laymen. With this comes the insight that there is a minimum number of annotations to be performed to achieve a decent performance. We found this to be more than 500 completed annotations in images from scratch.

Next to this, large variations in annotation times exist when working with novices to the use of annotation platforms. We suspect motivational factors to influence annotation times and note that assigning a predefined set of images works better than assigning working hours. Nevertheless, we found that for different robotic procedures, the expected time is around 4.5-6 minutes per pixel annotation per image and these times half when addressing vector annotations. This allows dedicated research teams to estimate the required workload to do these tasks.

An alternative successful team approach might be top-down. Here, a medical team, e.g. of medical students and surgical residents perform a very coarse indication of the instrument location and class, after which laymen perform a precise segmentation starting from this annotation[190]. Nonetheless, this requires experienced clinicians to check and adjust the laymen images, making the overall time saved questionable. We found annotation outsourcing to be very feasible and efficient. According to our first experiences, trained laymen are more efficient than novice medical students. However, the extent to which pre-annotations by laypeople speed up the process, and what qualifications annotators should possess, requires further in depth investigation.

The third key message constitutes several weigh-offs between annotation burden and accompanying costs when starting annotation projects. When analyzing complex and lengthy procedures, it is unfeasible to annotate every single frame. For example, annotating every frame of a one hour long video recorded at 30 fps, requires annotating 108.000 images. As such frames should only be sampled every few seconds in consideration of the balance between accounting for all relevant information throughout the procedure and avoiding annotation of identical scenes. Supervised computer vision models perform best when given a high variation of images, however very little is known on the sampling frequency required for detection and prediction of tool position. Another frequently addressed problem in data science, specifically medical datasets, is the class imbalance problem, that arises from low variability in surgical scenes, for example due to unchanged field of view and rare change in instruments[199]. This makes annotation projects focused on more than one procedure all the more relevant. For spatial instrument annotation, we propose sampling periods of 20 seconds. This balances the loss of details in the workflow with the cost of generating very large image datasets. Going beyond sampling periods of 20 seconds would imply losing other relevant temporal surgical tool information, which might be relevant for action detection or tool-tissue interaction. These aforementioned items are all considered next research steps in the field of surgical data science.

When aiming to achieve high quality annotations in the shortest period of time with smaller teams, we propose a combination of pre-annotation with class assignment by laymen. These images are subsequently checked by an experienced internally trained annotation team. When in lack of financial resources to hire a laymen team, we found that, having the annotations done entirely by the internally trained annotation team, seems to be most cost-effective alternative. Another way to cut costs is focusing on bounding box delineation, however with the drawback of loss of functional instrument information.

This work focused heavily on the annotation of instruments. Future work should focus on the annotation of soft tissues to study and quantify tool-tissue interactions. Soft tissue segmentation in combination with instrument segmentation is crucial to achieving successful augmented reality applications as 3D models should be registered correctly to the intraoperative view[200]. Tissue segmentation is also expected to help in the detection of critical anatomical structures. Initial demonstrations include the exposure of the critical view of safety in laparoscopic cholecystectomy[201].

Optimal sampling periods should however be investigated anew, as the soft tissues might be less prone to movements as compared to the instruments which are in constant movement.

To conclude, the validation of any annotation framework requires the exploration of other feasible, effective and well generalizable annotation methodologies. Consensus can only

be reached through diverse exchange of experience. Defining exact quantitative and qualitative benchmarks for spatial as well as temporal annotation is crucial to insure reliable applications of machine learning to surgery.

4.2.6. Supplemental Digital Content

Automated Derivation of Bounding Boxes from Pixel Segmentation Maps

When performing pixel segmentation in combination with vector annotation, there is little use in also delineating bounding boxes. We know exactly which pixel corresponds to each instrument, thus we also know the exact rectangle which will delineate all these pixels correctly. Figure A.7 below gives an overview how this automated derivation works in a step by step manner. Bounding boxes are frequently used in applications such as autonomous driving [202] where items move very fast and the main goal is instant detection of items. In contrast to surgery, it is often of less importance in autonomous driving what happens inside the bounding box. In surgery, you can only derive actions by looking what happens inside the bounding box. Therefore, we also explored a more precise way of delineating the instrument, by focusing our bounding box only on the tip of the instrument (Figure A.7.c and article Figure 4.8.b). While we performed an increase in granularity throughout pixel annotation (article Fig. 4.7.c), the decrease in bounding boxes appeared more effective for the vector annotation part.



Figure A.7. Results of automated deduction of bounding box position from instrument segmentation

Special Images

Below, we provide an overview of all types of images encountered when sampling at fixed framerate, and how to annotate them.

Out-of-body Images

Images captured out of body before, after or during the procedure are marked by a point or full rectangle. This allows for filtering out these images from the full dataset, as this is considered a classification problem (inside versus outside body) and not a segmentation problem (which part of the image shows something outside the body).

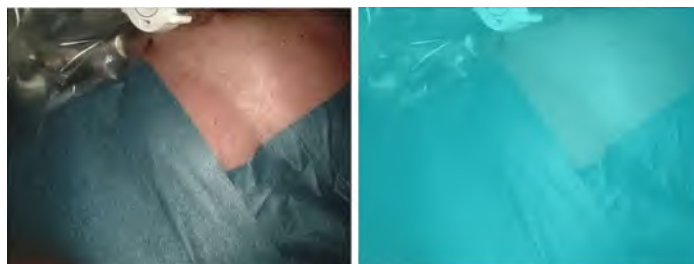


Figure A.8. Outside body images are labeled with a single label to be able to filter them out for classification

Lens Stains and Lens Cleaning

Lens stains caused by blood or other visceral fluids are annotated similarly as instruments by simple delineation. Lens stains are typically visible on plenty of subsequent images, until the endoscope is removed from the body for cleaning. We choose to annotate the stain on each image, however, as the stains are always in the same position, these annotations can be copied to subsequent images. Lens stains are not often clearly demarked, making this a rather delicate annotation with need for an explicit consensus when more evidence arises on the impact. The annotation of lens stains provides instrument detection algorithms with information to rule out false detection of such stains as relevant objects. This approach is also confirmed in previous large laparoscopic datasets[197], [198]. As lens stains are very frequent during any surgical procedure and have a high impact on visibility and edge detection of relevant instruments, we consider annotation of artefacts, like lens stains, to be equally important as delineating the target objects themselves.

Stains can sometimes also be confused with rapid movement of the robotic instruments, although these are primarily filtered out through blur detection. Once the camera leaves the body and the lens cleaning begins, the image is annotated as 'lens cleaning' in the same way as inside and outside body images (classification problem).

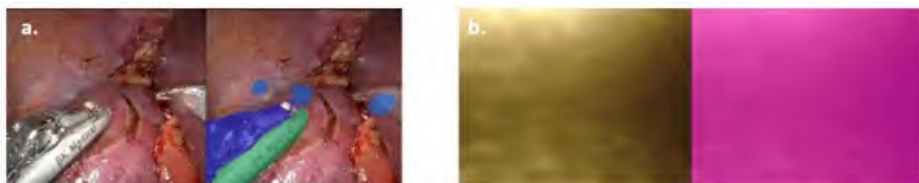


Figure A.9.a. Lens stains are delineated as a single class. Figure A.9.b. Lens cleaning is labeled with a single label to be able to filter them out for classification.

Trocar Presence

In some images, the insertion of the camera can be observed. When only the inside of the trocar is visible on the image it is annotated as 'inside trocar'. However, as soon as the inside of the body can be seen on the image, the visible part of the trocar is annotated in another class. Similarly, if other trocars can be seen on the images, they are annotated following the instance segmentation principle: 'trocar 1', 'trocar 2', 'trocar 3' and so on.



Figure A.10.a & b: Images of the endoscope inside the trocar or at the valve apparatus. Both have an identical label 'inside trocar'. Figure A.10.c: Abdominal cavity is present, and the yellow and blue trocar get labels 'trocar 1' and 'trocar 2'a.

Indocyanine Green

A particular phase during RAPN is the evaluation of the selective clamping strategy using indocyanine green (ICG). Here instruments are still visible and they should be annotated as such. The remaining part of the image can be fully delineated or just a small box or point can be placed as to also add the label 'ICG'. As mentioned earlier, it will be easier to distinguish the different classes by looking at the images before or after them.

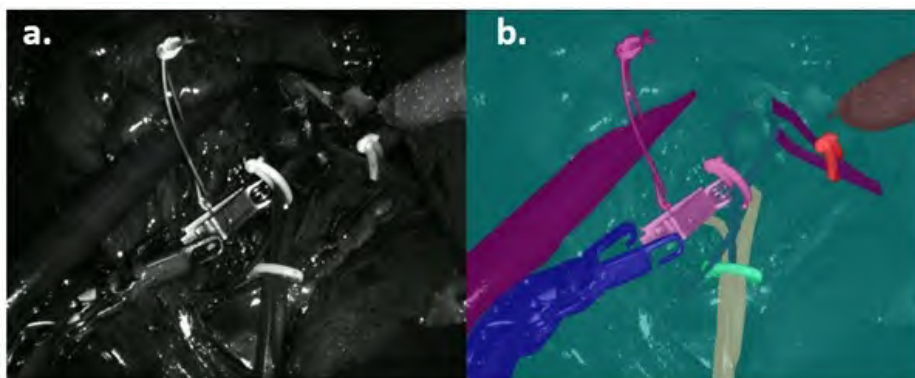


Figure A.11. Indocyanine Green Image, in which instruments are annotated classically and the rest of the background is segmented as ICG. An alternative strategy is placing a point label 'ICG', e.g. when moving on to organ annotation, as one pixel can only be assigned to a single pixel.

TilePro Information

While using the Da Vinci robotic system, it is possible to import other inputs into the surgeon console. During RAPN, such inputs are typically echography images, CT/MRI scans or patient-specific 3D models. We decided to label them in different classes using a classical bounding box approach as depicted in Figure A.12.

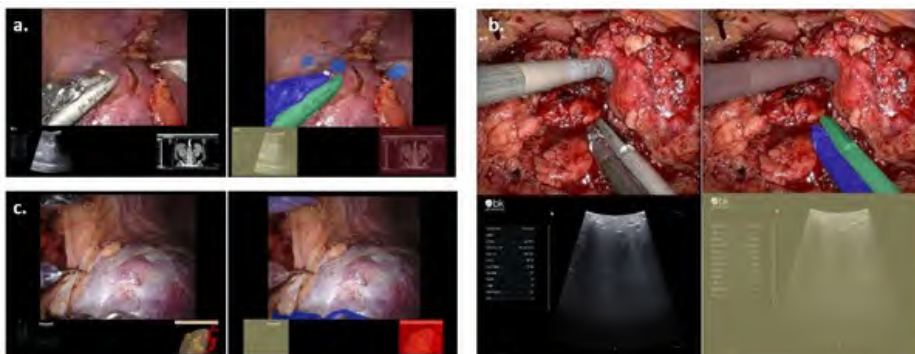


Figure A.12. Different TilePro inputs with corresponding labeling method.

Classes Overview

Pixel annotations				
Robotic instruments	Laparoscopic instruments	Foreign Objects	Peri-operative information	Situation
Monopolar curved scissors	Suction	Hemolock clip	CT	Outside body
Large needle driver	Laparoscopic clip applier	Echography image	3D	Lens cleaning
Da Vinci trocar	Laparoscopic scissors	Bulldog clamp	echo	Inside trocar
Force bipolar	Laparoscopic needle driver	Suture wire	ICG	Inside body
Prograsp forceps	Laparoscopic fenestrated forceps	Suture needle	Lens stain	
Cadiere forceps	Endobag specimen retriever	Da Vinci trocar		
Vessel sealer extend	Airseal trocar	Gauze		
Fenestrated bipolar forceps	Assistent trocar	Foam extruder		
	Echography	Vessel loop		
		Foam		
		Metal clip		
		Endobag		
		Drain		
		Bulldog wire		
		Veriset		

Table A.4. Overview of different classes and broad categories as segmented on a pixel basis

Point annotations		
Robotic instruments	Laparoscopic instruments	Objects
Monopolar curved scissors	Laparoscopic fenestrated forceps	Hemolock clip present in the laparoscopic clip applier
Cadiere forceps	Laparoscopic clip applier	Needle
Large needle driver	Laparoscopic needle driver	Bulldog clamp
Prograsp forceps	Suction	Metal clip present in the laparoscopic clip applier
Force bipolar	Echography	
Fenestrated bipolar forceps		

Table A.5. Overview of different classes and broad categories as annotated by wireframes and bounding boxes

As stated in the manuscript, a high level of annotation detail allows for a high level of precision by the developed algorithms. Here we elaborate further on encountered pitfalls and how to address them.

Common Pitfalls Specific to Segmentation

Segmentation Tools

Modern software packages have built-in tools to speed up segmentation. Figure A.13 shows common errors while using watershed techniques, in which images are preprocessed and an automated edge detection is plotted over the image. The first column shows the suggested delineation by automated edge detection (a, d) in an effort to speed up annotation. The corresponding segmentation by clicking these predefined ‘superpixels’ generated by watershed algorithms[194] are shown in the second column (b,e). The third column (c,f) shows the annotation when performed fully manual. We see that in figure c and f, the tip is immediately segmented correctly, and the stem is annotated much more precise by means of a straight line. We advise not to use such algorithms as to keep the annotation level at the highest possible quality.

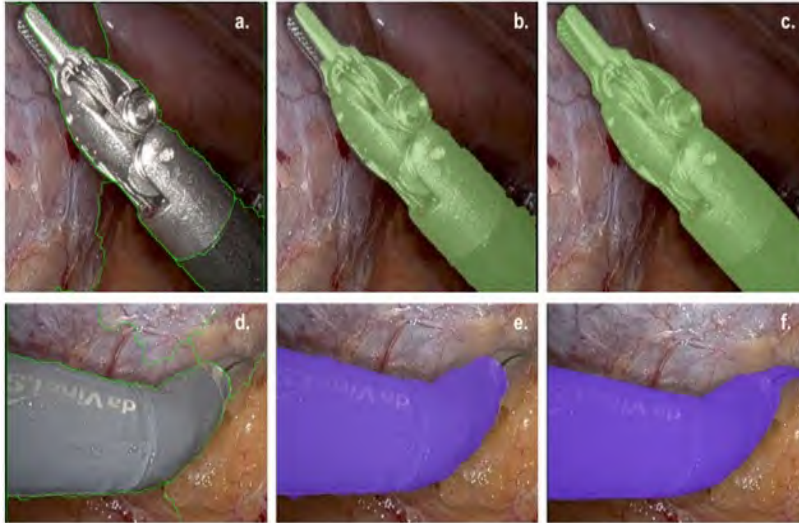


Figure A.13.: Decrease in annotation accuracy when using watershed techniques (a+d): Initial proposal of similar regions to speed up annotation by clicking them. (b+e): Pixel annotations resulting from the use of these regions (c+f) Correct segmentation, performed by annotating an image fully manual.

Common Errors

Common errors in pixel annotation include failure to respect the edges of the image, assigning wrong classes to instruments, forgetting to assign classes to instruments and inconsistent delineation of the edges of instruments. These errors show that image annotation is a delicate work that requires concentration and practice and may point towards annotation expertise and phenomena such as annotation fatigue.

To our experience, marking instruments outside the picture, forgetting to annotate objects or to assign classes were often the result of inattention and inaccuracy, whereas incorrectly assigning classes to instruments is mainly due to lack of knowledge with the various (robotic) instruments and objects. One solution we propose is to consult previous or following pictures for clarification, e.g. when an instrument is unrecognizable on a picture, because the full tip and joints are hidden behind tissue. An example is shown in Figure A.14 where the left upper instrument is in fact a large needle driver. Because their stem is dark grayish, it can be mistaken for a suction or another robotic instrument with the same stem.

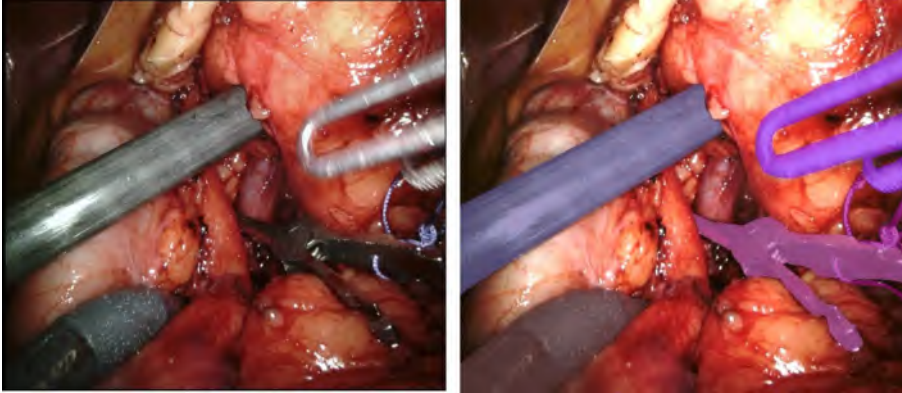


Figure A.14.: Example of incorrect identification of instruments, which may be solved by consulting chronologically later or earlier frames

One particular example of imprecise annotation is missing of the orifices inside instruments. The pixel annotation of graspers can be seen in Figure A.15.a. As shown in the manuscript, these details do indeed matter, as algorithms are able to discriminate between them, and correct instrument segmentation allows for more precise quantification of tool-tissue interaction. Another similar observation made throughout the pixel annotation was to focus annotation on what is seen, rather than annotation based on interpretation of previous frames. For example, graspers may be visible behind an endobag or inside a transparent trocar. Here, we choose to delineate the item closest to the camera, but speared out the others as the purpose for instrument detection is to comprehend surgical workflow and detect harmful tool tissue interaction. Figure A.15.b. shows the spearing out of fatty tissue at the tip of the bipolar grasper and Figure A.15.c shows the clear differentiation of tissue within the endobag in contrast to the surrounding bag. We also decided to annotate camera stains (Fig. 9b), as object detection models may falsely recognize them as instruments.

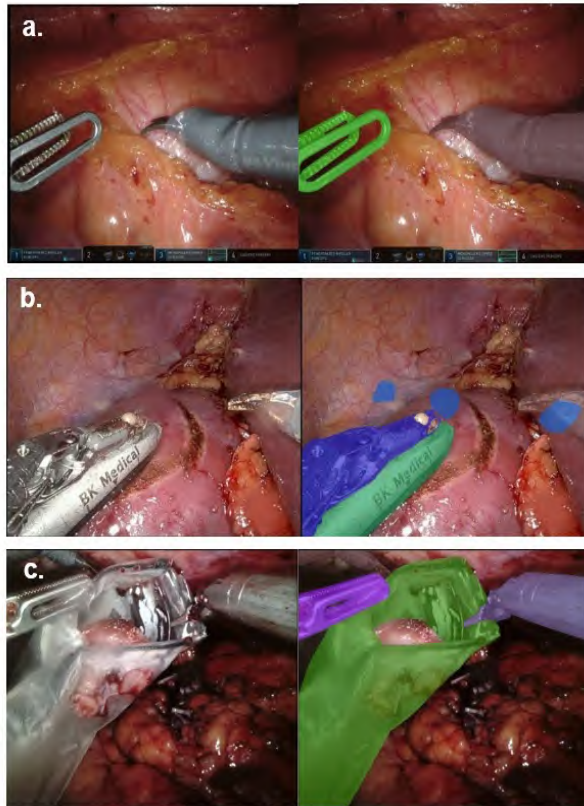


Figure A.15. Results of Pixel Annotation in RAPN (a) Semantic Segmentation of grasper (b) Spearing out of fatty tissue and camera stains (c) Differentiation between tissue and surrounding bag

The quality or sharpness of the image and how many visible elements present also impacts the difficulty in annotation. Figure A.16 shows a relatively simple image for annotation. Only two instruments are present in a sharp photo with no lens stains and blood. Figure A.17 shows difficult pictures to annotate; many instruments and other objects are present, some of which are difficult to see.

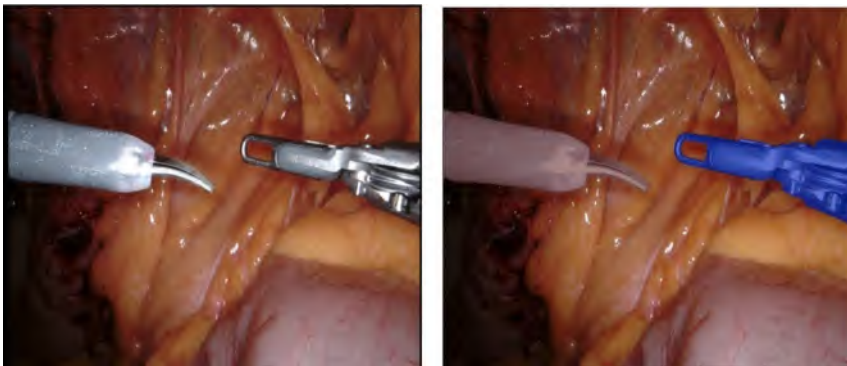


Figure A.16. Easy image to annotate

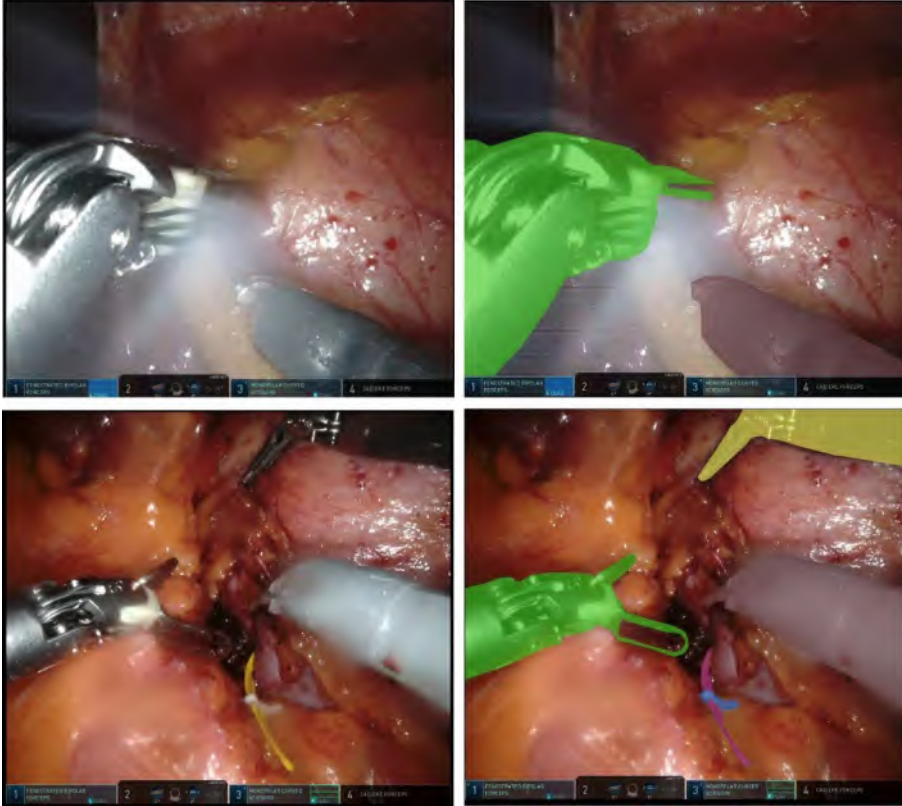


Figure A.17. The upper image is difficult because the monopolar curved scissor and fenestrated bipolar forceps are superposed by coagulation smoke. The lower image is difficult because there is a stain on the lens which makes the image blurry.

In addition, the photo is blurry and relatively bloody, which often makes annotation difficult. Thanks to several tools present in the annotation program, some of these difficulties can be partially overcome. By zooming in sufficiently, indistinct boundaries can be viewed and annotated in more detail. In addition, brightness, contrast and fill bar of the annotations can be played with to make darker parts of a picture more visible.

Common Pitfalls Specific to Pose Estimation

A second technique for mapping the instruments is pose estimation. Pose estimation is defined by placing points with a specific meaning. The purpose of these points is to indicate the direction of the instruments.

Each point represents a new part of the instrument. The rule of thumb is to start from the end towards the tip of the instrument to denote the different parts. Each point is placed as much as possible in the center of the instrument. If a point, such as a tip of the instrument, is not shown in the picture, it should not be marked. A maximum of six points can be placed on each instrument. A robotic instrument has the following parts (starting from the end to the tip of the instrument): end, joint 2, shaft, joint 1, tip 2 and tip 1. Laparoscopic instruments, on the other hand, have the same parts except for the shaft and joint 2, as laparoscopic instruments do not have 360° wrist movements like robotic instruments. Joint 1 differs from

joint 2 in that the second joint has a 360° robotic wrist reach while the first joint is where the blades of the instrument come together. It is obvious that joint 1 is different from joint 2.

Other instruments such as ultrasound and suction do not have joints and consequently only end and tip 1 is indicated there. Tip 1 is always the upper tip of the instrument on the image. If the instrument is closed (or holding tissue or a needle), only tip 1 has to be annotated. See the large needle driver on the right part of Figure A.18 and the fenestrated bipolar in Figure A.19.

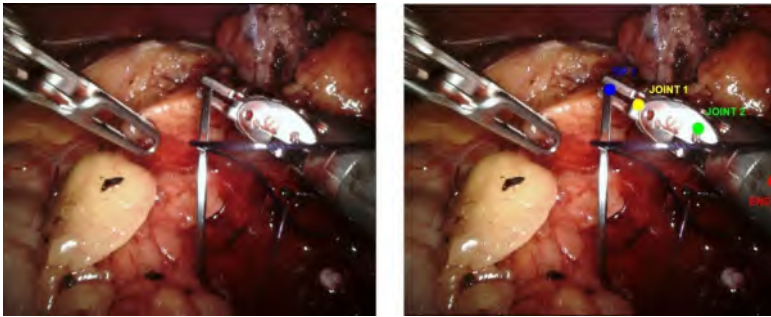


Figure A.18. Large needle driver holding a suture needle on the right side of the image. Point-annotated large needle driver on the right side of the image.

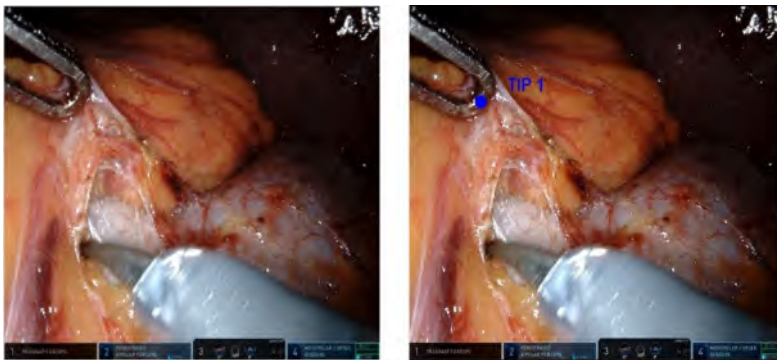


Figure A.19. Tip indication for fenestrated bipolar forceps

It is important that the point 'end' is always set. This way there is always the notion that an instrument is present. As shown in figure A.20, only the stem of the instrument is visible. No point but 'end' must be marked on it. If only the tip of an instrument is visible but contains a fenestration, the point 'end' may be marked on one of the two sides. (Figure A.21.)

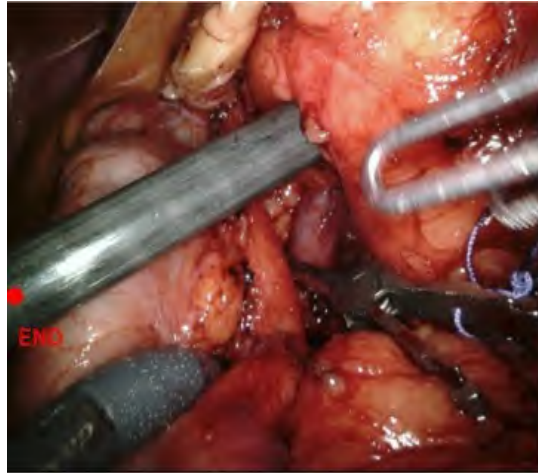


Figure A.20. The stem of the large needle driver is seen and 'end' should always be annotated.



Figure A.21. Only one leg of the fenestrated bipolar should be annotated as 'end' if only the tip is visible and contains a fenestration.

The point where the shaft is placed is more sophisticated to place than the others. As shown in the first paragraph, it allows for automated cropping of the large segmentation mask to a smaller tip bounding box. This point, as described earlier, is indicated only for robotic instruments. Assuming a bounding box is pulled both over the tip of the instrument and over joint 2, this point must be set on the vertical line, in the middle of the instrument, as seen in Figure A.20. The only robotic instrument where the learning curve is longer, is the monopolar curved scissors, as seen in Figure A.22. Since this instrument wears a blue-grayish cover, the joint 2 on this is harder to see. We determined to put it where there was a ridge visible, placed in front of the words "Da Vinci Surgery". The image below shows a bounding box on a robotic instrument and a bounding box on monopolar curved scissors. As with the pixel, the same rule will apply to the points regarding the information bar at the bottom: annotate on the blue bar, not on the black bar.

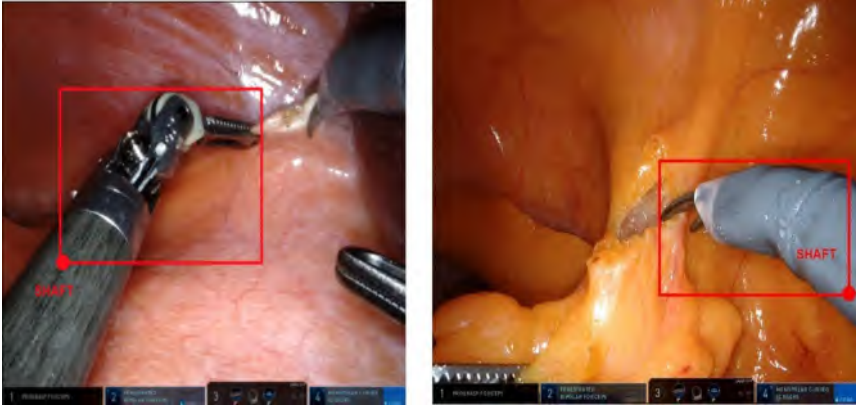


Figure A.22. Shaft annotated on a fenestrated bipolar forceps (left) and on a monopolar curved scissor (right)

[Addressing Annotation Errors](#)

Inaccurate annotation of the instrument edges by new annotators was quickly addressable through guidance from the QA-team and practice. This feedback loop and guidance does not only increase the precision of the annotations but also increases the efficiency of the annotator. The errors mentioned above improve as the annotators become more experienced with annotating, further confirming our hypothesis on a clear learning curve effect on the different tools and the annotation program. The QA-team provides feedback on a per image basis, by returning the images to the annotator with accompanying feedback on how to solve the error and avoid it in the future. This active feedback speeds up the learning process of the annotators which results in smoother and more qualitative annotations. After this, the annotator addresses the feedback, resubmits the image for quality check and if correctly annotated, the QA-team changes the image status to completed. If only minor edits are necessary, the QA-team can make these adjustments themselves.

4.3. Dataset Description and Open Sourcing

4.3.1. Abstract

As computer vision and artificial intelligence find their way into surgical practice, so does the need for large and annotated datasets. Computer vision in surgery could pave the way for a myriad of clinical applications, such as skill assessment, workflow optimization, automation and many others. One of the primary objectives in surgical data science is obtaining information on the instruments used, before advancing towards tissue and action interpretation. Nevertheless, currently available open source datasets are limited to rudimentary bounding boxes, large instrument segmentations, or entail only short snippets of longer procedures. The Orsi-RAPNI dataset consists of 31.868 images, sampled across 100 full length Robot-Assisted Partial Nephrectomies (RAPN), with all instruments segmented. Instruments include robotic and laparoscopic instruments, as well as every other non-organic intra-abdominal object. This dataset could significantly boost surgical data science applications as it allows for evaluation of multiple tool interactions across 100 different surgeries. The Orsi-RAPNI dataset is, to our best knowledge the largest publicly made available dataset for robotic surgery instrument segmentation.

4.3.2. Background & Summary

Despite the availability of community challenge datasets, data paucity remains a bottleneck to unlock the true potential of surgical data science [187], [203]. As discussed in Chapter 4.2., instrument segmentation is considered a major first enabler whilst tackling surgical computer vision tasks, as it often considered to provide the most precise instrument information [204]. Apart from being a building block for many related tasks like surgical phase detection, skill assessment, workflow optimization, automation etc., instrument segmentation has already proven to be useful in clinical proof-of-concept implementations such as real-time instrument delineation as a means to improve augmented reality in robotic surgery, detailed in Chapter 5.

Dataset building requires extensive time amongst others due to costly and labor-intensive annotations (Chapter 4.2) and the need for domain specific knowledge [205]. In parallel, the surgical progress is ever changing with a strong focus on becoming less invasive and more precise. One of these progressive factors is the current shift from classical laparoscopy towards robotic surgery, with an exponentially rising market share for robotic surgery [206]. This shift however has not yet translated to the surgical data science community, where the most extensive computer vision datasets mainly entail laparoscopy [203], [204]. Currently available human in-vivo robotic surgery instrument segmentation datasets are limited to certain surgical segments [207] or have rather limited classes of segmented instruments [203]. Instruments are often either segmented as being present or not (binary segmentation [198], [208], [209]) or the segmentation does not focus on small and fast moving items such as needles, clips and wires [197]. When considering robotic surgeries, the community only has access to porcine data [189], [210] or in-vivo human procedural parts [207]. Recent major efforts in laparoscopic dataset building have resulted in soft tissue segmentation datasets [211] but still leave the full instrument segmentation issue on the table. Several projects try to rely on synthetic datasets [212]. These synthetic datasets, despite being easier to create, can have a low adherence to real scenarios. With

this work, we open-source the Orsi-Robot-Assisted Partial Nephrectomy Instruments (Orsi-RAPNI) dataset. The Orsi-RAPNI dataset is, to our best knowledge, the largest robotic instrument segmentation dataset of full-length clinical robotic procedures to date [208]. The procedure under investigation is Robot-Assisted Partial Nephrectomy (RAPN), which is considered a standard treatment for small renal masses [140]. During RAPN, the surgeon only removes the tumoral part of the kidney, leaving the remaining healthy kidney parenchyma intact. RAPN is considered a complex urological procedure in which other inputs like 3D models and echography are often incorporated into the surgical view. We share our lessons learned how to preprocess clinical robotic surgery datasets from 2 hospitals and retain only informative parts for surgical instrument segmentation, whilst respecting privacy and General Data Protection Regulation (GDPR) policies. Figure 4.18 provides an overview of the acquired raw data and the evolution to the final dataset.

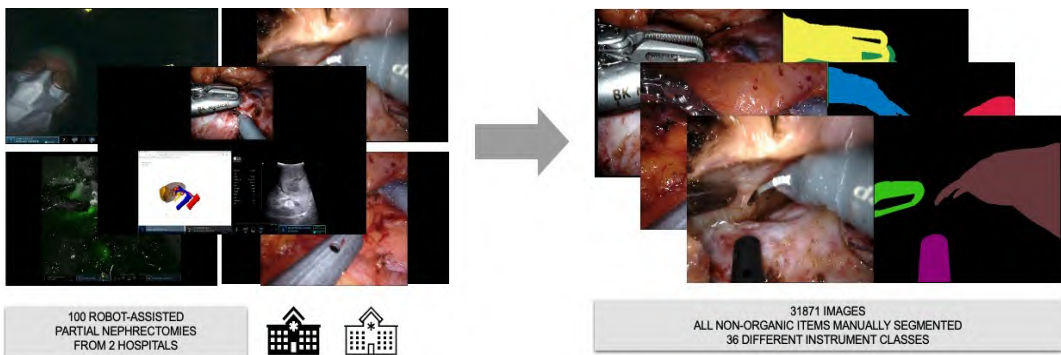


Figure 4.18. Summary of the data generation process. 100 full length video recordings are collected from 2 hospitals. Subsequently, all non relevant information for surgical instrument segmentation is removed, and all non-organic items in the surgical scene are manually annotated. This results in 31.868 images and 36 different instrument classes.

Our Orsi-RAPNI dataset contains 31.868 images in which all surgical items are segmented per image. This includes all robotic instruments, as well as fast all other non-organic items including needles, wires, clips, hemostatic agents, etc... The images are sampled equidistantly across 100 full length RAPN procedures. As such, we end up with a total of 33 different instrument classes and total count of 114.424 labeled instruments.

4.3.3. Methods

Figure 4.19 provides a schematic overview of the dataset generation process:

3. Videos are recorded
4. All videos are sampled temporally each 20 seconds
5. All out-of-body images are removed for privacy reasons
6. All IndoCyanine Green (ICG) images are removed
7. Images are manually segmented
8. The full surgical image is cropped automatically to the endoscopic part
9. The final dataset consists of the endoscopic image with a corresponding equal sized mask

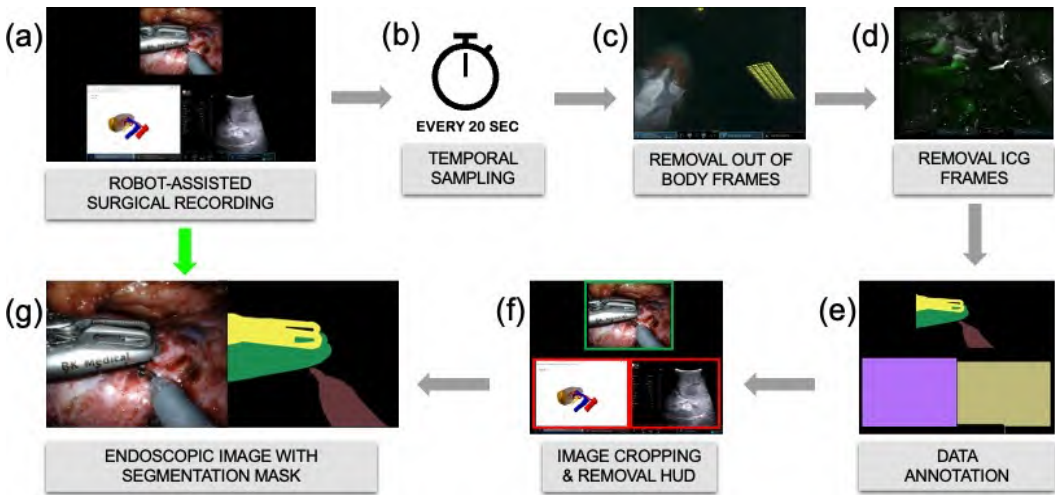


Figure 4.19. Overview of the applied pipeline for dataset generation. Full length RAPN recordings (a) are sampled every 20 seconds (b). (c) All samples containing out of body pictures are removed for privacy reasons. (d) IndoCyanineGreen (ICG) segments are removed to keep the data distribution homogenous and facilitate instrument annotation. (e) All non-organic items are annotated according to a pre-defined protocol. (f) Finally, the additional TilePro™ inputs which can again contain patient-specific details, are also removed. (g) Final input image and corresponding mask for computer vision applications

Each step is elaborated upon in more detail below.

[Video Recording](#)

100 procedures were recorded and collected under IRB approval in the period January 2018 - June 2022 from 2 tertiary referral hospitals. 80 procedures were recorded at OLV Aalst Hospital Belgium, the remaining 20 procedures were recorded at Ghent University Hospital. All procedures were performed on the Intuitive Xi robotic system (Intuitive™, California, USA). Recording was performed through Hauppauge PVR Rocket recorders (Hauppauge Computer-Works GmbH-Mönchengladbach, Germany) and a MAQUET Tegriss system (Getinge Ag - Göteborg, Sweden). Videos were captured in three different resolutions: 720 × 576 pixels (p) resolution at 25.00 frames per second (fps) (VOB format), HD ready resolution (1280 × 720 p) at 58.94 fps, and full HD resolution (1920 × 1080 p) at 30.00 fps (both mp4 format). Whenever possible, the robotic surgical console screen was captured, which includes possible third party inputs, as enabled by the TilePro™ system (Intuitive™, California, USA). An example of the most exhaustive surgical console image with multimodality input streams can be seen in Figure 4.19 (a). We refer to section on image resizing for more details.

We refer to Chapter 6.2 for more patient details of these 100 procedures.

[Temporal Sampling](#)

All 100 procedures were sampled equidistant in time after the temporal sampling exploration as elaborated upon in Chapter 4.2. This analysis showed that a 20 seconds is a decent trade-off between temporal proximity and sufficient visual heterogeneity for robotic instrument movements. One specific concern was the annotation of unsharp, fast moving instruments, which can also arise with rapid endoscopic camera motion. In

order to further ease the annotation process, we explored the possibility to skip partially blurred images. To this aim, we computed the Laplacian of the image, which is a measure used to highlight regions of rapid intensity change, as typically exploited for edge detection [213]. We considered high Laplacian variance to be representative of in-focus images. On the other hand, a low variance of the Laplacian was considered representative for blurred frames.

Figure 4.20 (a) and (b) show an example of images with low and high variance of the Laplacian, representative of blurred and sharp images. When sampling and finding a low Laplacian variance for an image, we initially moved to the next frame until a sufficiently high Laplacian variance was reached and thus would entail an in-focus image. Figure 4.20 (c) depicts the Laplacian variance over the course of a procedure.

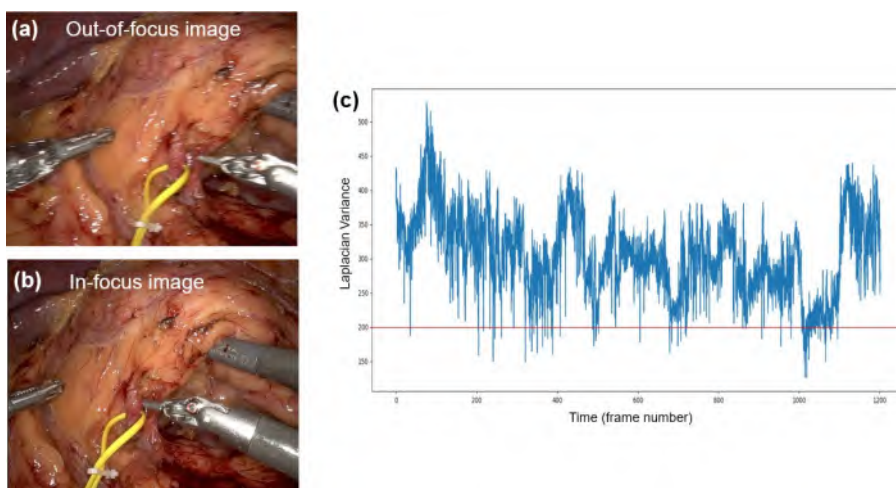


Figure 4.20: Impact of Laplacian variance on image sharpness in endoscopic images and comparison to endoscopic images outside of the body. Figure (a) shows a blurred image with Laplacian variance of 148.13, whilst (b) depicts the same videoframes later with a Laplacian variance of 224.01. Figure (c) depicts the laplacian variance over the course of a procedure.

As the empirical threshold of 200 proved to be insufficiently robust across different recordings, we decided to discard this approach and prioritize equidistant sampling over the relevance of crisp image quality. As such, final sampling at 20 seconds was withheld and blurred edges were annotated to our best means (Figure 4.19.b). Images were extracted in PNG format (lossless). After sampling, our dataset consisted out of 34.362 images.

[Endoscopic Out-of-body Frames and Indo-Cyanine Green Application](#)

4

During robotic surgery, the endoscope is typically removed from the body at the beginning and end of the procedure or when the endoscopic lens needs cleaning. During this removal period, the recording is still ongoing and patient's face, particular skin or body marks like tattoos, healthcare workers, ... inside the operating room could be captured and recognized without their consent. Figure 4.19.c. depicts the corresponding author's face as bedside assistant as an example of how identities might involuntary be disclosed. In order to protect patient and operating room staff privacy, removal or anonymization of these intra-operative out of body images is required. In order to anonymize the dataset, we manually removed all sampled frames in which the endoscope

is outside of the body or in transition through the trocar. Likewise all parts where the endoscopic camera was not turned on yet and provided a test image were removed. Apart from data privacy principles, these images can also confuse the instrument segmentation algorithms and are deemed less useful in this aspect. In a similar reasoning, images in which IndoCyanineGreen (ICG) is used to assess perfusion during the procedure, were considered out of scope for instrument segmentation as they are fundamentally different. Figure 4.19.d. depicts an ICG image.

As touched upon in Chapter 4.1., manual removal of out-of-body sequences by automated detection of these fragments are considered a promising tool which can enable easier sharing and dataset building.

[Semantic Segmentation](#)

In the remaining 31.868 images, all non-organic items were manually delineated on a per class basis in the online pixel annotator package SuperAnnotate™ (Sunnyvale, CA, USA). If multiple instances of the same class were present (e.g. several hem-o-lok clips were visible), these were programmatically grouped under one single denominator (e.g. "clip"). The annotations were performed as elaborated upon in Chapter 4.2. according to the pyramid scheme where laymen firstly annotated all items. They were given an annotation instruction guide, written and approved by a surgical resident (P.D.B) who acts as a supervisor. The laymen firstly performed test batches with feedback. These annotations are subsequently checked by a trained in-house team of 6 medical students, who referred to the supervisor as well as a consultant urologist in case of doubt or problems. The supervisor and urologist perform a final annotation check. All annotations are performed online in web-browsers. We refer to Chapter 4.2. for a more extensive description of the labeling instructions and workflow.

[Image Resizing](#)

A remaining anonymization issue when recording the robotic console view entails TilePro™ inputs. These inputs can contain other patient specific images and patient identity clues through visualization of MRI, CT, echography, or 3D models. Figure 4.19.f. depicts these inputs in red. It entails both a 3D model visualized side-by-side with the echography image, underneath the endoscopic image of interest. This TilePro information contains clues which could be relevant, e.g. for phase detection, but are irrelevant for surgical instrument detection. For this, we implemented an automated cropping algorithm, which uses binary thresholding to detect all three inputs (depicted in the green and red rectangles in Figure 4.19.f. Next, the algorithm only retains the green rectangle which has annotated instruments inside and performs cropping to these coordinates on the annotated mask (Figure 4.19.e). As such, this algorithm also instantly removes irrelevant black side borders, which are present in every recording.

These borders can also be appreciated on the original images in Figure 4.18. These manipulations, together with different original video recording resolutions, results in an annotated dataset with pixel sizes ranging from 311x390 pixels to 1080x1347 pixels. This implies that all recordings have undergone cropping of black side borders.

[Class Overview](#)

The dataset contains a total of 34 classes, hereby listed in descending order of number of occurrences: Monopolar Curved Scissors, Force Bipolar, Large Needle Driver, Suction, Suture wire, Hemolock Clip, Fenestrated Bipolar Forceps, Suture needle, Prograsp Forceps, Vessel Loop, Cadiere Forceps, Hemostatic Agens, Bulldog clamp,

Echography, Laparoscopic Fenestrated, Forceps, Bulldog wire, Endoscope Trocar, Endobag, Hemlock Clip Applier, Laparoscopic Needle Driver, Airseal trocar, Da Vinci trocar, Endobag wire, Drain, Endobag specimen retriever, Laparoscopic Clip Applier, Foam, Metal clip, Surgical Glove Tip, Foam extruder, Laparoscopic Scissors, Assistant trocar, Da Vinci Obturator and Tachoseal introducer which are differentiated from the tissue. Figure 4.21 shows the class distribution over the complete dataset in terms of number of occurrences.

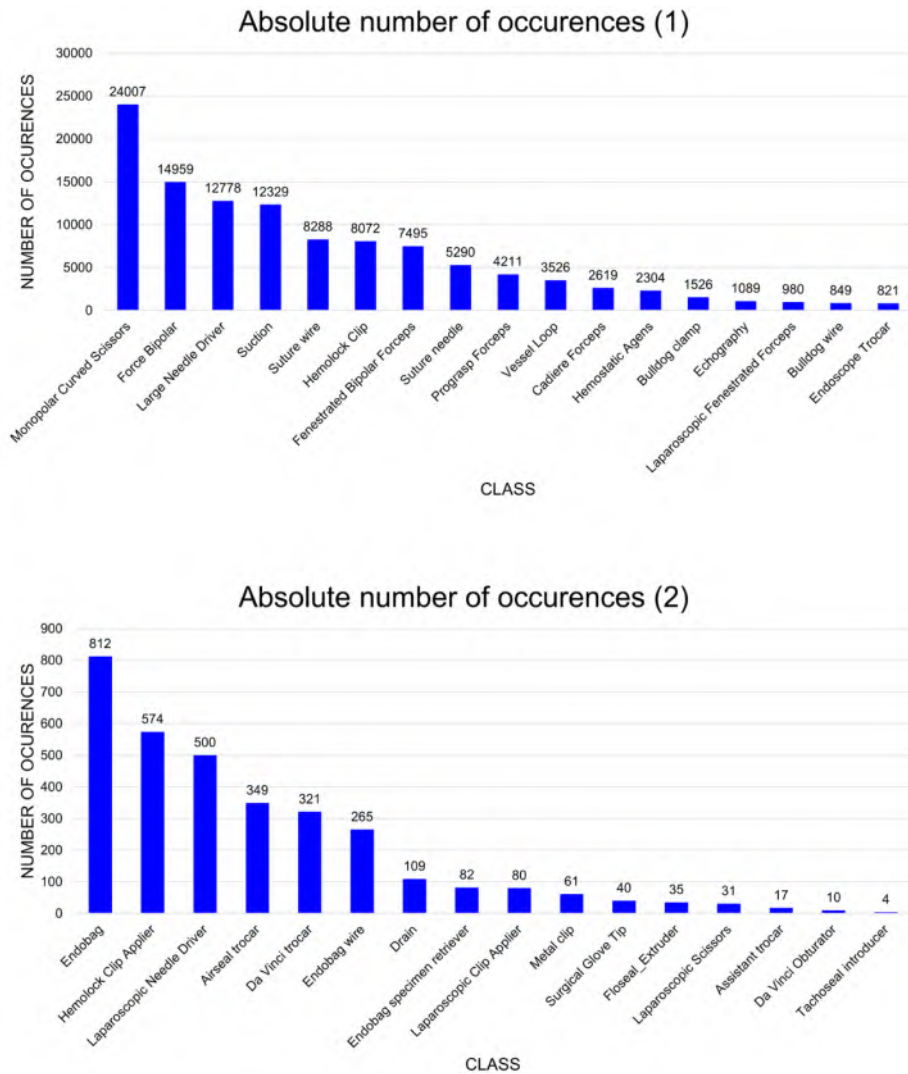


Figure 4.21. Class distribution in the complete dataset in terms of absolute number of occurrences of each class. The upper graph contains the 18 most prevalent classes and the lower graph contains the 18 other classes (divided for visualization purposes).

Balanced Dataset Split

Given the high imbalance of our dataset, we propose the following homogenous data split across procedures:

- validation set (13 procedures – 4.498 images): RAPN16, RAPN19, RAPN20, RAPN45, RAPN79, RAPN81, RAPN89, RAPN92, RAPN96, RAPN98, RAPN102, RAPN108 and RAPN115.
- test set (8 procedures – 2.902 images): RAPN7, RAPN41, RAPN47, RAPN48, RAPN50, RAPN66, RAPN74 and RAPN91.
- training set (79 procedures – 24.468 images): all other procedures

Figure 4.22 shows the class distribution of the training, validation and test split, as well as the distribution across the complete dataset. This split will also be used later on in Chapter 6.1. to evaluate segmentation algorithms.

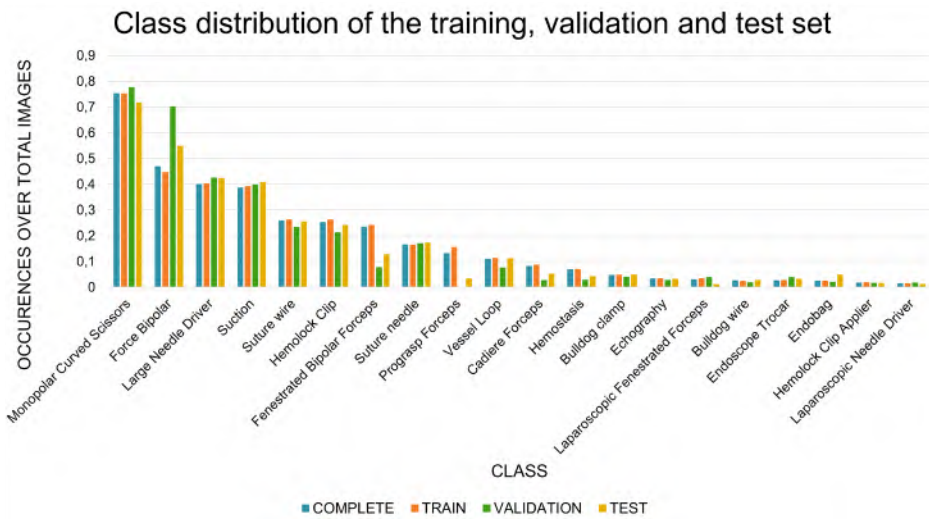


Figure 4.22. Class distribution in training, validation, and test set, as well as the class distribution in the complete dataset. Thematic plotted is the ratio of occurrences of the classes to the total number of images in the respective sets. Note: for visualization purposes, only the 20 most prevalent classes are shown here, as the remaining classes distribution of the other classes is negligible.

Proposed Sub-analysis

Given the myriad of surgical instruments and foreign bodies present in the dataset, we propose a grouping of classes. We refer to Chapter 6.1 for further details.

4.3.4. Data Records

The data will be publicly released at synapse.org/#!/Synapse:syn51664244. The patient population is described in Chapter 6.2.

4.3.5. Technical Validation

In all included procedures, the images are sampled and named in a chronological manner. This allows for time-dependent analysis where the presence of instruments can be tracked from one image to another. Using this information, irregularities could be

identified and if necessary corrected. These included, but were not limited to, unanticipated instrument appearances, for example an instrument appearing only in one frame, and improbable coexistence of multiple instruments within a single image frame. Images manifesting these aberrations were flagged as potentially erroneous, reassessed by the team of experts and corrected if necessary, thereby ensuring the veracity of instrument presence and configurations within the dataset. Additionally, an active learning approach was taken to make further corrections in the dataset. As described in Chapter 6.1., binary segmentation of non-organic material is considered a reference first step for quality assessment of the final dataset. This first model was used to identify frames with a large discrepancy between the predication and the ground truth, such as completely missed annotations.

4.3.6. Usage Notes

The Orsi-RAPNI dataset is publicly available for non-commercial usage under the Creative Commons Attribution CC-BY-NC-SA-4.0. If researchers wish to use or reference this dataset, they should do so by citing this paper and Orsi Academy. For commercial usage, companies should contact Orsi Academy through Pieter De Backer. This dataset can be used for various purposes. It can be used to push the field of surgical data science because of the addition of new classes previously unstudied for instrument segmentation and detection. To this end, it can also be joined with other datasets. The instrument segmentation itself can serve as a basis for plenty of other machine learning projects in surgical artificial intelligence such as phase and action detection as well as research concerning surgical skill assessment or surgical automation.

4.3.7. Code Availability

As the dataset is distributed as images and related masks, no frame extraction or other processing is necessary. Consequently, there is no code relevant to share.



3D & AI INTEGRATION

05

*« As soon as it works,
no one calls it AI anymore »
- John McCarthy*

This chapter has been adapted from:

Improving Augmented Reality through Deep Learning: Realtime Robotic Renal Surgery Instrument Delineation

P De Backer, C Van Praet, J Simoens, MP Lores, H Creemers, K Mestdagh, C Allaey, S Vermijs, P Piazza, A Mottaran, CA Bravi, M Paciotti, L Sarchi, R Farinha, S Puliatti, F Cisternino, F Ferraguti, C Debbaut, G De Naeyer, K Decaestecker, A Mottrie
European Urology 2023

First-in-human Realtime AI-assisted Instrument Deocclusion during Augmented Reality Robotic Surgery

J Hofman*, **P De Backer***, I Manghi, J Simoens, R De Groot, H Van Den Bossche, M D'Hondt, T Oosterlinck, J Lippens, C Van Praet, F Ferraguti, C Debbaut, Z Li, O Kutter, A Mottrie, K Decaestecker
*Shared first author

Wiley's Healthcare Technology Letters (MICCAI 2023 AE-CAI workshop)

5.1. Feasibility of Instrument De-occlusion in A.R. Guided Robotic Surgery

5.1.1. Abstract

Several bottlenecks prevent the integration and adoption of Augmented Reality (A.R.) in robotic renal surgery despite the increased availability of virtual 3D models. Apart from correct model alignment and deformation, all instruments are not clearly visible during A.R. This is attributed to the 3D model, which is superimposed on top of the surgical stream, including the instruments, resulting in a potential hazardous surgical situation. We demonstrate real-time instrument detection during A.R.-guided robot-assisted partial nephrectomy and show the generalization of our algorithm to A.R.-guided robot-assisted kidney transplantation. We developed an algorithm using deep learning networks to detect all non-organic items. This algorithm learned to extract this information through 65.927 manually labeled instruments on 15.100 frames. Our setup was deployed in 3 different hospitals, used by 4 different surgeons and runs on a standalone laptop. Hence, instrument detection is a simple and feasible way forward to enhance the safety of A.R. guided surgery. Future investigations should strive to optimize efficient video processing which can minimize the 0.5 second delay as currently experienced. General A.R. applications also need further optimization including organ deformation and tracking to achieve full clinical implementation.

5.1.2. Case Series

In recent years, patient-specific 3D models have entered the field of renal surgery as a tool to better define surgical strategies [84]. The adoption of robotic surgery has accelerated intra-operative integration as 3D models are now easily visualized inside the robotic console. One step beyond is the integration of the model into the live endoscopic surgical view through Augmented Reality. During A.R., preoperative images (in this case the 3D model) are superimposed on top of the surgical field to provide additional information such as important anatomical landmarks. Although the evidence is still preliminary, A.R. technologies show potential to further improve outcomes in renal surgery [214].

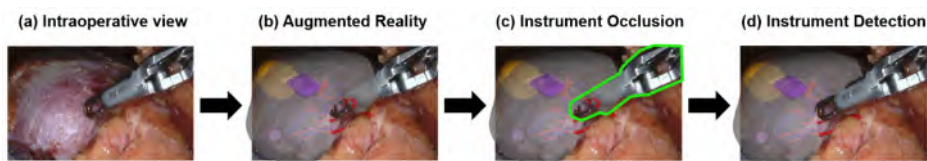


Figure 5.1: State of the Art in Augmented Reality (A.R.) for RAPN. (A) Original intraoperative view; (B) Overlay of the preoperatively made 3D model; (C) Green delineation depicts how the force bipolar forceps' view is occluded by the 3D model; (D) Automated instrument detection during A.R. solves this problem.

Figure 5.1.a depicts an endoscopic image next to its A.R. enhanced equivalent during robot-assisted partial nephrectomy (RAPN) in Figure 5.1.b This state-of-the-art A.R.-visualization for RAPN highlights two major bottlenecks for current A.R. implementations. One major bottleneck is the lack of automated precise 3D model alignment throughout the surgery [115], [215]. Figure 5.1.b. indeed shows a slightly misaligned 3D model when compared to the underlying kidney, due to the underlying manual alignment process, the lack of adequate elastic deformation of models as well as motion artifacts such as breathing. Nevertheless, promising initial attempts are underway to tackle this through artificial intelligence, 3D modeling, 3D scene reconstruction and computer vision algorithms[86], [115], [216].

A second major bottleneck for the implementation of safe A.R. guided surgery, is the occlusion of surgical instruments by the 3D model, as accentuated in green in Figure 5.1.c This study is, to our best knowledge, the first one to tackle the latter problem by enabling real time automated instrument delineation as depicted in Figure 5.1.d We present a proof-of-concept study which applies the “Augmented Reality Instrument Detection” (AR-ID) technology in RAPN for tumor dissection [86] and subsequently transfer it to robot-assisted kidney transplantation (RAKT) for iliac vessel projection and atherosclerotic plaque visualization [217].

Our real time instrument delineation or “binary segmentation” algorithm detects all instruments in the surgical scene as depicted in Figure 5.2.a. The algorithm was solely trained on instruments of RAPN videos. The algorithm architecture is a deep learning convolutional neural network with U-Net architecture, as depicted in Figure 5.2.b.

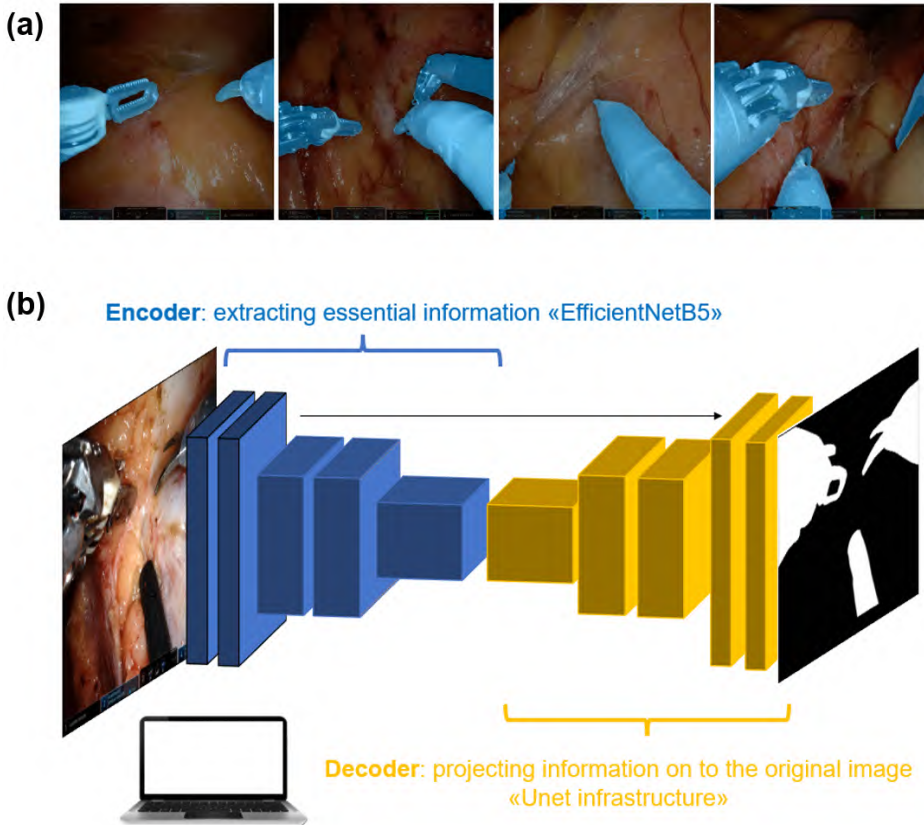


Figure 5.2: Real time instrument segmentation by means of Convolutional Neural Networks (A) Results of our segmentation algorithm. All non-organic items in the abdominal cavity are instantly detected by the algorithm as depicted here in blue. This segmentation is called binary as it differentiates between two classes: non-organic items and soft tissue. (B) Deep Learning convolutional neural network architecture. The enabling architecture to achieve the segmentation as depicted in Fig 5.2.a. is a classical architecture for deep learning. It consists of an encoder in blue (called EfficientNetB5) which has learnt how to extract the meaningful information for the task of instrument segmentation. The encoder is followed by a decoder in yellow (Unet) which learns how to project this condensed meaningful information back onto the original surgical image it was presented with. This architecture is able to run on a laptop with dedicated video graphics card and is written in PyTorch (<https://pytorch.org/>).

15.100 surgical video frames were obtained by sampling 57 recorded RAPN videos every 20 seconds, as detailed in Chapter 4.1. 65.927 non-organic items were manually delineated in the annotation platform SuperAnnotate™ (Sunnyvale, CA, USA), resulting in 33 different instrument classes including all robotic/laparoscopic instruments, needles, wires, and many others. The labeling effort duration was estimated at 1.258 hours. The original images and the corresponding instrument delineation information were fed to the deep learning network.

The labeled dataset of 15.100 images was subsequently split in 3 subsets. 10.573 images (40 procedures) were used to train the network, 3.019 images (12 procedures) were used for network optimization/validation and 1508 images (5 procedures) were used for testing and reporting the final performance on unseen images. The 3 datasets contain different RAPN procedures so the algorithm has never seen these images on beforehand during the training or optimization phase and hence cannot be biased. The

algorithm is trained on a standalone computer with dedicated computer graphics card (Nvidia RTX3090).

We quantify our results on the test set by reporting 2 commonly used technical metrics in the field of computer vision:

$$2. \text{ Intersection over Union (IoU)} = \frac{TP}{TP + FP + FN}$$

and

$$3. \text{ Dice score} = \frac{2 * TP}{2 * TP + FP + FN}$$

Where TP = True Positive pixels, FP = False Positive pixels, FN = False Negative pixels.

Figure 5.3 presents the calculation of both scores visually. Our algorithm achieves state of the art accuracy through a 94.4% Intersection-over-Union score and 97.10% Dice score.

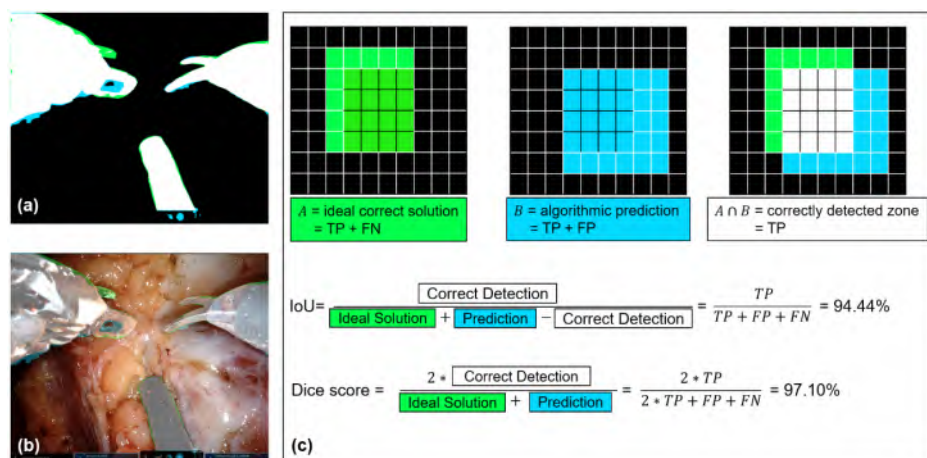


Figure 5.3: Quantification of algorithmic performance. IoU = Intersection Over Union, TP = True Positive pixels, FN = False Negative pixels, FP = False Positive pixels. (A) Simplified schematic for quantification of the algorithmic performance. Presented in white are all pixels that were correctly predicted as instruments (TP). In green, we see what the algorithm has still missed but was manually annotated by the authors as the perfect solution (FN). The blue pixels depict regions where the algorithm thinks instruments are present where they are not (FP). (B) Corresponding image of (a) in which the white, green and blue colours are overlaid for clear error visualisation. We see that the inside of the bipolar forceps is not correctly left out and the algorithm was not able to detect the top part of the forceps. (C) Schematic explaining the color coding of image (a) and (b). We see how the ideal solution in green (TP + FN) and the full prediction in blue (TP + FP) are weighed against the part that was correctly predicted in white (TP) by means of the Intersection over Union and Dice parameters. We also display our achieved scores for both parameters.

Once the training and optimization are finished, the algorithm is deployed intra-operatively. Figure 5.4 depicts our workflow, inspired by Schiavina et al [218]. A laptop with dedicated graphics-card pulls in the endoscopic view by means of a video capture card (Fig 5.4.1.). The neural network, deployed on the laptop delineates the instruments in real time (Fig 5.4.2.). The patient-specific 3D model is made preoperatively using

Mimics™ (Materialise, Leuven, Belgium) (Fig 5.4.3.). The 3D model is manually aligned and overlaid with the endoscopic view by a biomedical engineer (J.S.) (Fig 5.4.4.) using a Javascript 3D viewer (K3D Javascript, <https://k3d.ivank.net/>). Next, the laptop merges the classical A.R. video with the instrument detection (Fig 5.4.5.) using vMix software (StudioCoast PTY LTD, Robina, Australia), generating the AR-ID video which is displayed in the robotic console.

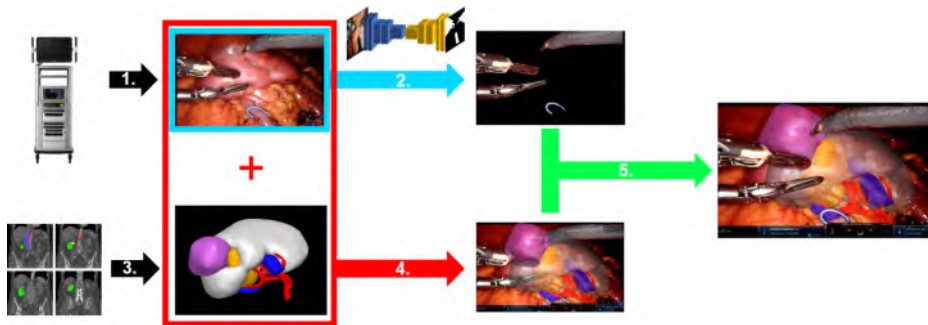


Figure 5.4: Workflow in the operating room enabling real time instrument segmentation during Augmented Reality. A laptop with dedicated graphics-card (NVIDIA RTX A2000) pulls in the endoscopic view by means of a video capture card (Fig 5.4.1.). The instrument segmentation neural network runs on the laptop and extracts the instruments from the incoming video in real time (Fig 5.4.2.). The patient-specific 3D model is made preoperatively using Mimics™ (Materialise, Leuven, Belgium) (Fig 5.4.3.). The 3D model is manually aligned and overlaid with the endoscopic view on the laptop (Fig 5.4.4.). 3D model rotation and alignment is performed in Javascript (<https://k3d.ivank.net/>). Next, the laptop merges the classical A.R. video with the realtime instrument detection (Fig 5.4.5.) using vMix software (StudioCoast PTY LTD, Robina, Australia). This generates the “instrument-detection A.R. video” which is displayed in the robotic console through the Intuitive TilePro™ input.

The workflow was set up successfully in 3 tertiary referral centres (Ghent University Hospital, OLV Aalst and AZ Maria Middelaeres) with 4 surgeons (respectively C.V.P., A.M. & G.D.N, K.D.). In all cases, we overlay a 3D renal model with its vasculature. For oncologic cases, the tumor and possible cysts are included, whilst for transplantation cases, iliac arteries were projected to demonstrate feasibility in case of atherosclerotic plaques.

Between May and October 2022, 10 patients undergoing robotic renal surgery were enrolled in this study and signed informed consent. To be eligible for enrolment, an arterial CT scan with maximal slice thickness of 1mm was required for adequate 3D model development.

Table 5.1 summarizes the individual patient characteristics. We performed 8 transperitoneal RAPN for localized renal cell carcinoma (including one case with intra-arterial cooling for a highly complex renal lesion), 1 RAKT with living donation for end stage renal disease and 1 Robot-Assisted Kidney Auto-Transplantation (RAKAT) for persistent loin pain hematuria after previous surgery. Median estimated blood loss was 200 ml (IQR: 143.75-275) for all surgeries. No intra-operative complications were recorded.

	RAPN 1	RAPN 2	RAPN 3	RAPN 4	RAPN 5	RAPN 6	RAPN 7	RAPN 8 ^Ω	RAKAT	RAKT
Gender	F	M	F	F	M	F	M	F	F	M
Age (y)	44	67	56	61	60	76	77	54	30	61
BMI (kg/m²)	36	23.5	22.5	27.7	31.5	21	33.9	26	20.5	27.9
Side	R	L	R	R	R	L	L	R	L	R
lesion size (mm)	19	24	16	55	35	19	24	67	NA	NA
Padua score	7	8	3	9	6	6	6	13	NA	NA
WIT (min)	0	19	16	0	16.5	11.5	12.85	96*/3	60*/3	123*/48
Histotype	OCC	ccRCC	chRCC	ccRCC	ccRCC	ccRCC	OCC	ccRCC	NA	NA
Surgical Margins	Free	Free	Free	Free	Free	Free	Free	Free	NA	NA
preop eGFR (ml/min)	82	63.1	85	83	88	80	72	90	90	14.7
preop creat (mg/dl)	0.86	1.18	0.77	0.77	0.94	0.73	0.96	0.68	0.55	4.09
postop eGFR (ml/min)	90	78	90	81	90	63	73	90	90	34
postop creat (mg/dl)	0.68	0.99	0.64	0.79	0.83	0.9	0.99	0.6	0.59	2.04
Console time (min)	150	150	120	70	180	75	80	216	260	207
Post-op Complic.	None	None	None	None	None	C1: hypoglycemia	C2: Cardial decomp	None	None	C2: RTI

Table 5.1: Patient Characteristics Overview of patients in which A.R. instrument detection was applied. * = cold ischemia time, Ω = with Intra-corporeal cooling, BMI = Body Mass Index, WIT = warm ischemia time, eGFR = estimated Glomerular Filtration Rate, creat = creatinine, preop = preoperative, postop = postoperative, RAPN = Robot-Assisted Partial Nephrectomy, RAKAT = Robot-Assisted Kidney Auto Transplantation, RAKT = Robot-Assisted Kidney Transplantation, F = Female, M = Male, NA = Not Applicable, R = Right, L = Left, OCC= Oncocytoma, ccRCC = clear cell Renal Cell Carcinoma, chRCC = chromophobic Renal Cell Carcinoma, Post-op Complic. = Postoperative Complications as rated by Clavien-Dindo [165], C1 = Class 1 postoperative complication, C2 = Class 2 postoperative complication, RTI = Respiratory Tract Infection, Cardial decomp. = Cardial decompensation.

Qualitative visual assessment of our real-time binary segmentation algorithm shows a precise real time delineation of all instruments during both RAPN and RAK(A)T. We did measure a 0.5 second delay when comparing the direct endoscopic view with the TilePro™ window (Intuitive™, California, USA). This is due to the serial infrastructure of both capture card and laptop, where each video frame is reprocessed multiple times.

Figure 5.5.a shows the setup as visualized inside the robotic console during echographic tumor demarcation. Figure 5.5.b depicts different examples of the current state of the art in the left column ('Detection off') and the improvement through AR-ID on the right ('Detection on'). We note that A.R.-guidance facilitates tumor demarcation in RAPN, whilst visualization of the iliac vessels is enhanced during RAKT. Figure 5.5.c provides a QR video link to view the difference between A.R. with and without instrument detection.

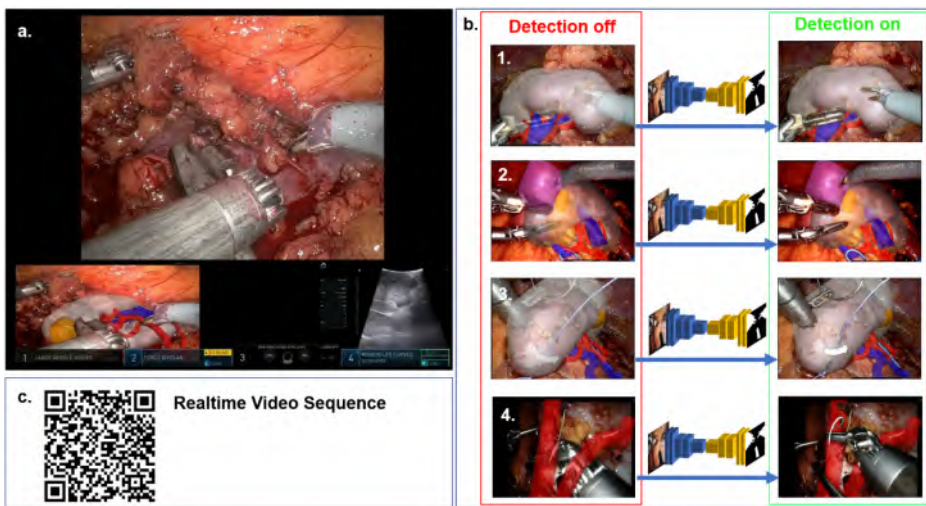


Figure 5.5: Real-time examples of Augmented Reality Instrument Detection. (A) Depicts the robotic console view as seen during surgery. Here we see the delineation of the monopolar curved scissors, force bipolar and ultrasound probe on top of the 3D model projection in the left TilePro™ window, while the right TilePro™ window depicts the echography image during ultrasound scanning across the tumor. (B) Shows 4 different cases of the increased visualization while the detection is being toggled on. Fig 5.5(b.1) shows the preciseness of instrument detection in RAPN. Fig 5.5(b.2) shows how palpation of cysts and visualization of underlying tumor in A.R. is improved, whilst also detecting the vessel loop. Fig 5.5(b.3) shows how wires, needles, hem-o-lok clips and vessel loops are detected, Fig 5.5(b.4) shows how the technology integrally transfers to RAKT during arterial anastomosis, where the robotic instruments, suture and applied bulldog clamps are detected. (C) Provides a QR code and video link to view the on-off toggling of the AR-ID technology in different cases.

5.1.3. Discussion

In this study, we show that it is feasible to remove the safety hazard of not visualizing instruments during A.R. surgery and we add a sense of depth to the 3D model interaction. We show that our real-time instrument detection is robust and transfers well from RAPN to RAK(A)T. Our setup requires a laptop with graphics card (1000-1500€), a capture card (100-400€) and an additional basic pc monitor (100-200€). It is easily applicable in different operating rooms and hospitals. Nevertheless, this setup also has a 0,5 second delay, which makes it at present unacceptable to perform surgery solely based on the TilePro™ window. As such, future research is focused on further time delay reduction through parallel integration of all components in a single computing device, which is expected to increase hardware costs at least 7 times. Secondly, the current application detects all instruments at once without a quantitative comparison on the individual instrument detection level. This requires a complete refactoring and retraining of the developed system. It might however enhance the comprehension of our proposed solution when the detection is imprecise. Thirdly, manual alignment of static 3D models to a constantly changing operative view remains bothersome. The implementation of A.R. guided surgery requires assurances on perfect alignment. Here, deep learning might help solve the localization problem [115], whilst numerical methods could help in realistic deformation of the models. All three bottlenecks above require dedicated and interconnected computational resources which present a future challenge for successful and smooth clinical integration.

5.2. Realtime Implementation of Instrument De-occlusion through Dedicated Hardware Setup

5.2.1. Abstract

The integration of Augmented Reality (A.R.) into daily surgical practice is withheld by the correct registration of pre-operative data. This includes intelligent 3D model superposition whilst simultaneously handling real and virtual occlusions caused by the A.R. overlay. Occlusions can negatively impact surgical safety and as such deteriorate rather than improve surgical care. Robotic surgery is particularly suited to tackle these integration challenges in a stepwise approach as the robotic console allows for different inputs to be displayed in parallel to the surgeon. Nevertheless, real-time de-occlusion requires extensive computational resources which further complicates clinical integration. This work tackles the problem of instrument occlusion and presents, to our best knowledge, the first-in-human on edge deployment of a real-time binary segmentation pipeline during three robot-assisted surgeries: partial nephrectomy, migrated endovascular stent removal and liver metastasectomy. To this end, a state-of-the-art real-time segmentation and 3D model pipeline was implemented and presented to the surgeon during live surgery. The pipeline allows real-time binary segmentation of 33 non-organic surgical items, which are never occluded during A.R. The application features real-time manual 3D model manipulation for correct soft tissue alignment. The proposed pipeline holds potential in improving surgical safety and ergonomics and paves the way towards acceptance of A.R. in minimally invasive surgery.

5.2.2. Introduction

Over the last decade, 3D models have entered oncologic surgery as a means to achieve better outcomes in renal and hepatic surgery [84], [219]. Nevertheless, the integration of 3D models into the operative field has been lacking due to three main reasons. Firstly, proper model alignment with the intraoperative anatomy has proven to be a major challenge due to shifting of organs during surgery and different patient positioning in surgery versus during computed tomography [115], [219]. Secondly, automated organ registration in a continuously moving surgical video has been another major challenge for many years [200]. Thirdly, 3D model overlay obscures the surgical field, including sharp surgical instruments which are manipulated, hence creating a possible hazardous situation rather than facilitating surgery. The latter occlusion problem has been a longstanding study topic [220] which, if solved, would further advance various surgical domains and applications [221]. Already in 2004, Fischer et al [222] proposed handling instrument occlusion in medical augmented reality (A.R.) through identification of occlusion zones by creating a virtual map of the existing environment upfront. Four years later, Kutter et al. [223] explored the design and implementation of a high-quality hardware system to enable real-time volume rendering in A.R. applications. However, to ensure that depth perception was not compromised, the authors needed to apply video color filtering to handle occlusion, as such limiting its robustness due to the color prior. Other approaches [224] for occlusion management relied on tracking and 3D positioning of the instrument within the A.R. environment, which in turn made it prone to certain instruments' directions. As such, previous de-occlusion attempts were unsuccessful in detecting all surgical items with sufficient robustness, whilst at the same time having no prior knowledge of the objects' orientations or positions inside the real-time surgical environment. The work in Chapter 5.1. showed the potential of deep learning binary instrument segmentation for robust de-occlusion during A.R. surgery. However, the

reported latency reached up to 0.5 seconds and was considered unfeasible for real-time surgical use.

In this work, a robust real-time binary segmentation pipeline for non-organic items was developed and deployed during three live robot-assisted surgeries: partial nephrectomy (RAPN), migrated endovascular stent removal and liver metastasectomy. Using a state-of-the-art binary segmentation method, as well as software and hardware level acceleration, the pipeline efficiently tackles instrument occlusion caused by the augmented reality 3D model overlay in real-time and reduces delay to a frame-by-frame latency of 13ms. Qualitative surgical feedback stated the resulting perceived end-to-end latency is acceptable for real-time surgery.

5.2.3. Materials and Methods

Non-organic Binary Segmentation

The binary segmentation data set of Chapter 5.1. was expanded to the full dataset of Chapter 4.3, containing 31.812 images on which all non-organic items were manually delineated in the annotation platform SuperAnnotate (Sunnyvale, CA, USA) according to the annotation strategy of Chapter 4.2. The 33 different non-organic instrument classes include robotic and laparoscopic instruments, needles, wires, clips, vessel loops, bulldogs, gauzes, etc... The images were sampled uniformly across 100 full-length RAPN procedures. The data set was split on a procedural base into 24087 images for training, 4545 images for validation, and 3180 images for testing. Different encoder-decoder deep learning architectures were evaluated for performance. Both Feature Pyramid Network (FPN) [225] and DeepLabV3+[196] architectures in combination with an EfficientNetV2 encoder [226] were identified as having good performance for binary segmentation in a separate optimization study (see Chapter 6.2). The model was trained over 50 epochs with batch size 16 and image size 512 x 512 pixels, using Adam optimizer with a learning rate of 2.25×10^{-4} and a combination of focal and dice loss. The learning rate was reduced on plateau over 5 epochs with a factor 0.7 and an early stopping criterion was evaluated on the mean IoU with a patience of 15 epochs. The performance is measured in terms of mean Intersection over Union (IoU) and processing time. Inference in the application pipeline requires conversion to ONNX and subsequent TensorRT optimization [227]. This optimization allows for smaller precision, reduced latency and model size, simplified network topology, reduced read and write operations, and dynamic memory allocation to reduce memory footprint. This type of optimization is necessary to meet the real-time needs during surgery. A side-by-side performance comparison of both architectures is performed for both the original Pytorch model as well as the final implemented TensorRT model. Both are evaluated for Floating Point(FP) 16 and FP32 precision.

Pipeline Deployment

Hardware Framework

This integration addresses delays imposed by different serial components whilst enabling the implementation of more accurate but also heavier deep learning networks for image segmentation. The Nvidia Clara AGX developer kit [182] (Nvidia, Santa Clara, California, USA) was identified as embedded computing architecture for highly demanding video processing applications. Live video capture was enabled through a Deltacast DELTA-12G-elp-key capture card [183] (Deltacast, Liege, Belgium). The card provides performance and efficient I/O, as well as a passive bypass, which safeguards original video throughput in case of real-time software malfunctioning.

Software Framework

The intra-operative A.I. & A.R. application was developed using the NVIDIA Holoscan SDK, an extensible open-source framework for implementing real-time, low-latency medical A.I. applications. The pipeline was implemented through a combination of existing Holoscan operators, extended with use case tailored ones. Figure 5.6 displays a schematic overview of the pipeline and corresponding operators. The pipeline can be divided into four main blocks: pre-processing, inference, post-processing, and visualization. The 1920x1080p captured frames are reformatted to serve as input to the segmentation model. For every frame, the alpha-channel information is dropped, black borders are removed, and the frame is resized to 512x512 pixels. The color channels are normalized with means and standard deviations derived from the binary segmentation model training set.

After inference, a sigmoid activation is applied to the 512x512x2 output, yielding a 512x512 pixels binary mask indicating whether the corresponding pixels make up non-organic items or soft tissue. The 512x512 pixels segmentation mask is subsequently resized to match the original input resolution. The 3D model is rendered through Visualization Toolkit (VTK - <https://vtk.org/>) and composited with the live full-quality surgical video and segmentation mask to create the final image. The 3D models are manually segmented pre-operatively using Mimics (Materialise, Leuven, Belgium) from a 4-phasic CT scan sequence, identical to that of Chapter 3.1 and consist of separate STL files for parenchyma, tumors, stents, arteries, veins, and other anatomical entities relevant to the procedure. All STL files can be toggled with hot keys during overlay and the transparency can be edited in real-time.

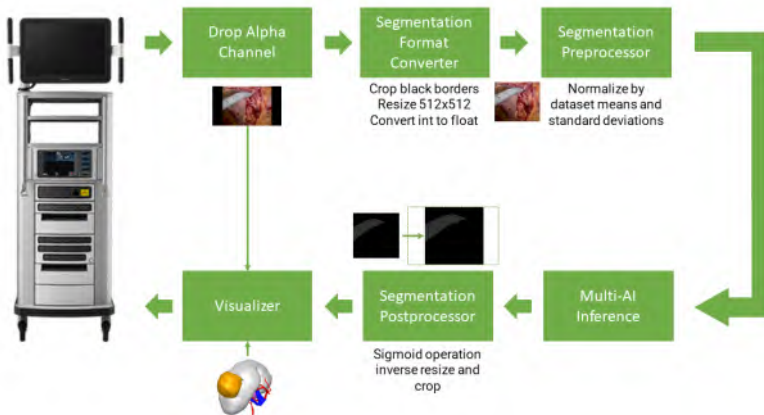


Figure 5.6: Schematic overview of the different steps and GXF-extensions in the segmentation application.

Live Surgeries

The study was performed with patient consent under institutional review board approval (B6702020000442). Figure 5.7.a displays the operating room setup during the live procedures: the 3D model requires manual alignment with the surgical scene. Figure 5.7.b provides a link to video footage of the live cases.

Figure 5.7.c demonstrates the connection scheme. The Clara AGX developer kit and other hardware were installed next to the surgical tower, allowing continuous model alignment during the procedure and direct communication between the user performing the alignment and the operating surgeon whenever needed. The DELTA-12G-elp-key capture card, which is integrated into the Holoscan box, receives the live video feed through Serial Digital Interface (SDI). The patient-specific 3D model was preloaded onto the Clara AGX developer kit for rendering inside the Holoscan application. The processed frames were sent over DisplayPort-out into an active HDMI-splitter. One of both HDMI-out signals was sent to a monitor through which the users could continuously interact with the application. The other signal was fed back with an HDMI-DVI cable into the Intuitive Xi robotic system (Intuitive, California, USA) by means of the DVI-TilePro input. Furthermore, a keyboard and mouse were connected to the Clara AGX developer kit to be able to manipulate and interact with the 3D model as discussed above. Thanks to constant manual alignment, the 3D model is perfectly aligned whenever the surgeon enables the TilePro feature.

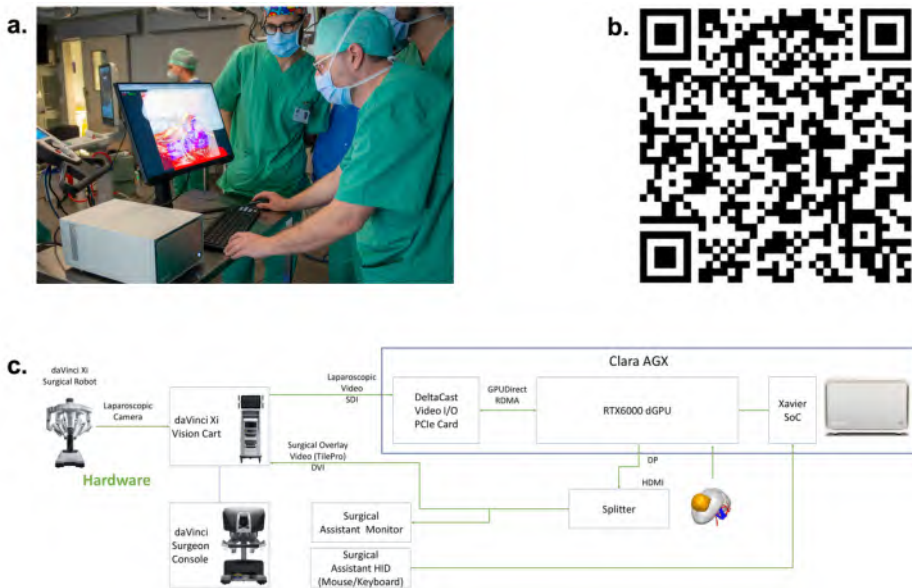


Figure 5.7: Experiment setup overview. Figure 5.7.a shows the physical setup of the Clara AGX developer kit next to the surgical tower, where the non-operating urologist performs the real-time model alignment in dialog with the operating urologist. Figure 5.7.b provides a QR code to video footage showing the setup in work. Figure 5.7.c depicts a schematic overview of the hardware setup and connection types.

5.2.4. Results

Non-organic Binary Segmentation

Table 5.2: Performance comparison of (TensorRT optimized) DeepLabV3+ (DV3+) and Feature Pyramid Networks (FPN) segmentation model architectures evaluated on Pytorch container.

Model	Precision	mean IoU		Inference time (ms)		Δ IoU		Δ inference time (ms)	
		Pytorch	TensorRT	Pytorch	TensorRT	Pytorch	TensorRT	Pytorch	TensorRT
DV3+	FP32	0.90318	0.90318	48.6	20.4	N/A	0	N/A	-28.2
DV3+	FP16	0.90317	0.90316	52.6	8.5	-0.00001	-0.00002	4	-40.1
FPN	FP32	0.94621	0.94621	36	14.2	0.04303	0.04303	-12.6	-34.4
FPN	FP16	0.94621	0.94623	40.5	5.1	0.04303	0.04305	-8.1	-43.5

Table 5.2 summarizes the comparison of evaluation metrics of the FPN model versus the DeepLabV3+ model, used in Chapter 5.1. on an identical test set of 1345 images derived from 4 distinct RAPN procedures. The baseline model for the reported side-by-side improvements is the DeepLabV3+ with FP32 precision, implemented in Pytorch. The Δ mean IoU and Δ inference time reflect stepwise improvements in segmentation quality and inference time, with respect to this baseline. Changing the model architecture to FPN resulted in increased mean IoU whilst TensorRT optimization significantly reduced inference times, with the largest time reduction for FP16 precision. Figure 5.8 provides an example of the improvement in segmentation quality in TensorRT. When compared to DeepLabV3+, the FPN model reduced both false positive and false negative pixel regions (respectively represented by red and green regions). Switching to FP16 has no effect on segmentation performance for both FPN and DeepLabV3+ architectures. The TensorRT FPN model with FP16 precision was identified as the most promising network for the live experiment. To profile the application pipeline, the Nvidia Nsight Systems profiling tool [228] was used. The profiling experiments were run over 20 seconds at an input frame rate of 80 frames per second. The resulting median processing time for the application pipeline was less than 13ms with an average GPU utilization of 42%. As such, the device still has GPU bandwidth for additional workloads such as real-time anonymization (Chapter 4.2). When assessing the different pipeline components of Figure 5.6, inference was the slowest component and took on average 6.8 ms.



Figure 5.8: Segmentation performance of DeepLabV3+ and FPN models (TensorRT optimized). The yellow regions indicate true positive pixels, the red regions indicate false positive pixels and the green regions indicate false negative pixels.

Live Demonstration and User Feedback

Figure 5.7.b holds a QR code with a link to a video containing highlighted segments during surgery. During the RAPN, the application was first enabled after the identification and isolation of the renal artery. The 3D model overlay confirmed the orientation of the kidney and tumor with respect to the artery, providing initial support for navigation, as well as confirmation of clamping level with respect to possible earlier bifurcations of the vessel. During this phase both the initial solution of Chapter 5.1 and the current solution were simultaneously visually compared through separate Tile Pro inputs inside the console. The surgeon (Dr. Ruben De Groote) stated a significant improvement in perceived latency, where the latency of the current solution was subjectively experienced small enough for surgical adoption. Thereafter, the A.R. application was enabled during tumor demarcation. Figure 5.9 displays the surgeon's console view for the 3 live cases, where the application is used in parallel with the ultrasound probe. For RAPN and robotic liver resection (respectively Figure 5.9.a and b), the resection margins and tumor depth estimation are augmented by the 3D model overlay with the segmented endoscopic ultrasound probe on top and as confirmed by the ultrasound imagery. Figure 5.9 also illustrates that the application solely served as support next to the endoscopic vision as not to impair or alter the surgeon's original vision or decision. In case of RAPN, the application was not used during the time-critical surgical phases for renal artery clamping and tumor resection. After tumor resection and arterial unclamping, the application was once more enabled during renorrhaphy.

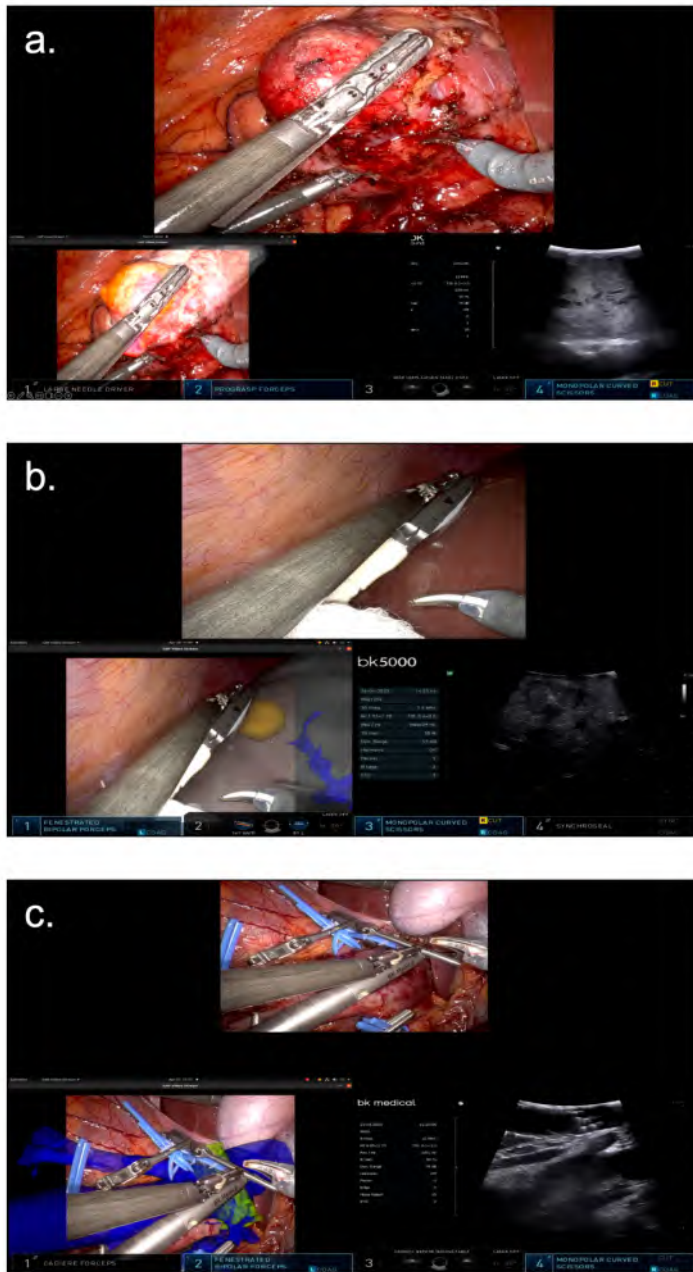


Figure 5.9: Robotic console view during all 3 live cases. The A.R. stream with instrument segmentation is presented in the lower left TilePro™ window, the lower right window depicts the echography image depicting respectively the renal tumor (a), the liver metastasis (b) and the hyperechogenic vascular stent (c). a) Tumor identification during RAPN. b) Ultrasound detection of an endophytic colorectal liver metastasis during robotic liver resection. c) Robotic migrated endovascular stent removal, placed for nutcracker syndrome.

Figure 5.10 illustrates the capability of the model to detect all non-organic items during RAPN. Figure 5.10.c illustrates the model's segmentation performance on suturing needles, wires, and hem-o-lok clips as other non-organic materials. Figure 5.10.e

illustrates the performance for gauze segmentation during hemostasis. The 3D setup was experienced as easy to manipulate without prior knowledge by the first clinician performing the alignment during RAPN (Dr. H. Van Den Bossche). For the liver and vascular case, alignments were performed by engineers. The ability to align the 3D overlay and toggle the tumor visibility added insights regarding localization of the tumor bed, while the segmentation effectively provided a sense of depth while suturing the renal capsule. Automatic model alignment was reported to be the major next clinical improvement.

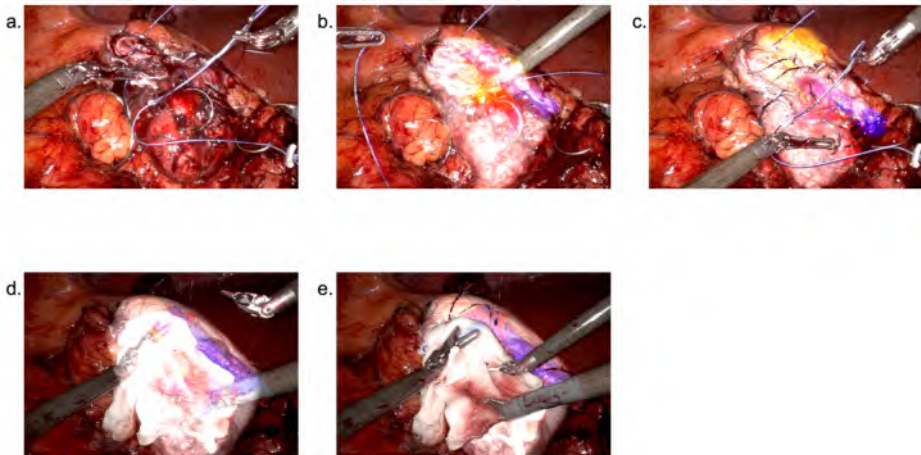


Figure 5.10: Detection of all non-organic surgical items during A.R. overlay. a) Renorrhaphy phase during RAPN. b) 3D model overlay without instrument segmentation to depict the location of vessels and calyces. c) Activation of real-time segmentation: detection of clips, needle, suture wires and instruments. d) 3D model overlay during hemostasis without instrument segmentation. e) Activation of real-time segmentation: successful detection of gauze, instruments, suture wires.

As stated above, the A.R. pipeline was also applied during a robotic liver metastasectomy. Figure 5.9.b shows the surgeon's console view where tumor demarcation and 3D model alignment are again validated using ultrasound. The surgeon (Dr. M. D'Hondt) stated that, although this setup solves the delay and de-occlusion problem, the application is not yet applicable in liver surgery due to the organ's deformative nature which complicates 3D model alignment. As for the first case, automatic model alignment with extension to deformable registration was reported to be the next major clinical improvement.

The third live case entailed a robotic removal of a migrated endovascular stent, placed for a nutcracker syndrome. This stent had migrated into the vena cava inferior causing relapsing symptoms and danger of further migration towards the right atrium. The stent was removed and vena cava reconstruction with left renal vein transposition was performed to treat the primary nutcracker syndrome. Figure 5.9.c. displays the surgeon's console view, with the endoscopic ultrasound depicted in the right lower TilePro window. We note the validation of the stent location, represented by the oval hyperreflective structure in the top of the ultrasound image. The surgeon (Dr. K. Decaestecker) confirmed that the delay was negligible and acceptable for surgery, and that the A.R. Tile Pro input was sufficiently informative and responsive to even be used as the main screen during this phase of the surgery. Figure 5.11 depicts all 3 A.R. views side-by-side to show the perceived benefit as compared to prior state of the art without instrument segmentation. All patients experienced a normal postoperative course and recovery.

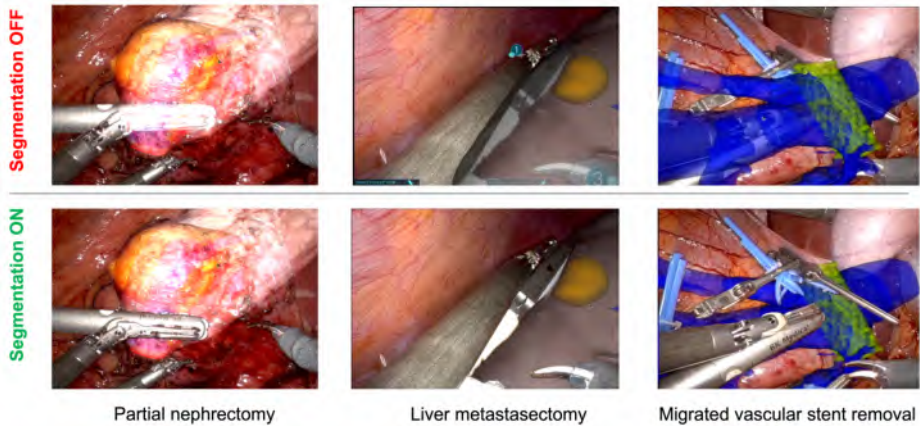


Figure 5.11: Benefit of real-time instrument segmentation during A.R. overlay. For the 3 cases, live instrument segmentation was toggled on/off. Instrument segmentation allows a more intuitive interaction with the A.R. overlay as surgical instruments are per definition not part of the 3D model.

5.2.5. Conclusion and Future Work

This work presents the implementation of a robust novel real-time approach for occlusion handling in surgical A.R. scenarios. It shows that A.R.-induced instrument occlusion is a resolvable issue when integrating software directly in a dedicated hardware pipeline. Our segmentation algorithm is shown to transfer smoothly across 3 different robot-assisted renal surgeries and the setup is applicable across Intuitive Xi systems, as shown in three different testing hospitals. Despite being trained only on robot-assisted partial nephrectomy instrument segmentation, the algorithm seems to generalize well across other surgeries using similar instruments. This could facilitate towards a broader A.R. adoption in robotic surgery. The subjective surgical feedback indicated that the application could bring clinical value to several parts of the procedure and that the delay is acceptable for real-time surgery. Specific perceived surgical benefits include better insights into tumor localization below the renal surface and corresponding arterial tree, together with improved tumor delineation due to de-occlusion. The pipeline is built on top of extensible open-source technologies, allowing to replicate and translate the work to other challenges in computer-assisted intervention (CAI) and surgical data science (SDS) for real-time adoption in surgery. By solving the long-standing problem of real-time instrument occlusion, the work is a demonstrator for translational research from lab to operating room. Furthermore, by optimizing compute resources, a frame latency of less than 13ms and average GPU utilization of 42% was achieved. These results reflect room for the integration of additional workloads such as parallel deep learning inference pipelines. Shifting towards a MobileNetV2 encoder can potentially further decrease computational loads if necessary (see Chapter 6.1). Future work resides in the implementation of a parallel soft tissue segmentation pipeline for automatic 3D model alignment, and by extension non-rigid body registration. The system should be further evaluated for user experience in a more formalized manner, by e.g. constructing a formal questionnaire, having the A.R. usefulness assessed by independent viewers, pipeline application in a greater number of surgeries and comparing them to similar cases without A.R.. Other future minor hardware improvements include the use of the capture card SDI-out to further reduce delays and enable continuous passive bypass for surgical safety.

5.2.6. Data Availability

The segmentation algorithm, and the real-time holoscan application are publicly available for non-commercial use under the Creative Commons Attribution CC-BY-NC-SA 4.0 at <https://github.com/nvidia-holoscan/holohub>. Due to privacy restrictions, the datasets used in the present work cannot be publicly shared. If readers want to use this algorithm, they must cite this article or acknowledge Orsi Academy and the primary authors, Jasper Hofman and Pieter De Backer. For commercial use interest, Orsi Academy can be contacted through Pieter De Backer.



BEYOND 3D MODELS: SURGICAL DATA SCIENCE

06

*« We are moving slowly into an era
where big data is the starting point, not the end »*

- Pearl Zhu

Adapted from:

- Manuscript in preparation which benchmarks encoder decoder architectures for real-time segmentation, applied on the novel dataset of Chapter 4.3.
- Surgical Phase Duration in Robot-Assisted Partial Nephrectomy: A surgical data science exploration for clinical relevance
P De Backer, M Péraire Lores, M Demuynck, F Piramide, J Simoens, T Oosterlinck, W Bogaert, CV Shan, K Van Regemorter, A Wastyn, E Checcucci, C Debbaut, C Van Praet, R Farinha, R De Groote, A Gallagher, K Decaestecker, A Mottrie
Diagnostics, 2023

6.1. Instrument Segmentation as an Enabler for Surgical Data Science

6.1.1. Introduction

Surgical Data Science is a relatively new field of science that aims to enhance surgical quality by collecting, organizing, analyzing, and modeling data related to various interventional medical disciplines like surgery, interventional radiology, radiotherapy, and endoscopy [205]. This data can come from different stages of patient care and can include information about the patient, surgeon, anesthesiology, operating room staff, and the technology used for treatment. The goal is to use this data to improve processes, predict outcomes, assist in decision-making, optimize systems, and advance prevention and training. Surgical Data Science integrates principles and methods from computer science, engineering, information theory, statistics, mathematics, and epidemiology. It works in conjunction with other advanced technologies like surgical robotics, smart operating rooms, and electronic patient records to optimize and streamline healthcare delivery.

Robotic surgery or robot-assisted surgery (RAS) is considered an enabler for surgical data science given the possibility to extract all sensor and mechatronic data used to perform surgery. RAS has become widely incorporated into the current surgical practice and enables the surgeon to exploit computer, vision and software technologies to control and move surgical instruments more efficiently and with higher precision. Hence, RAS also facilitates the integration of computer-assisted surgical techniques and image-guided surgery. For this integration, real-time knowledge of the surgical instrument position and underlying anatomy is of paramount importance. However, due to most surgical robotic instruments being cable-driven, determining instrument location through kinematics alone is challenging because of cable-related effects such as cable stretching and hysteresis [229]. As such, computer vision algorithms for surgical tool detection and segmentation are of great interest. Accurate tool segmentation can lead to accurate tool localization and tracking, which is an essential step in the roadmap to surgical automation. Likewise, instrument usage and movement form another data source can help propel the field of Surgical Data Science.

Up to present, real-time surgical tool segmentation has proven clinically beneficial in improving augmented reality applications (Chapter 5), whilst it also has been facilitating surgical workflow, surgical skill assessment and even general operative room logistics [187], [204]. Surgical tool and scene segmentation are however particularly challenging due to the changing illumination, shadows, reflections, visual occlusions (e.g. blood and camera lens fogging), and the complex and dynamic nature of human tissue. In addition, segmentation is typically performed on surgical video frames, which can be partially or totally blurred due to the instrument or camera motion.

Traditional methods for surgical image analysis have relied on color information and image gradients, as well as classifications based on semantic labeling using Support Vector Machines or tree-based algorithms [230]. However, these approaches present major limitations since color and gradient based methods can be vulnerable to noise and illumination changes and fail to capture higher level features. As for many other computer vision tasks, the advent of convolutional neural networks and subsequently transformers boosted semantic segmentation performance. ToolNet [231] was one of the first deep neural networks for real time binary segmentation of surgical tools (i.e. differentiating surgical tools from the tissue). In the same period, Bodenstedt et al [232] showed that

CNN based methods outperformed all other methods in a comparative evaluation of segmentation methods for both ex-vivo robotic and in-vivo conventional laparoscopic surgery images. Tanzi et al [233] more recently proposed a comparison of three different architectures with a variety of encoders for a three-classes segmentation problem (background, tool and catheter) to evaluate real-time intra-operative segmentation.

The investigated datasets and best results often originate from community challenges such as the MICCAI endoscopic vision challenges [210] which hold specific instruments segmentation challenges. These challenges tend to focus on getting good segmentation results but less on the real time application and computational load.

In this chapter, we aim at evaluating state-of-the-art CNN architectures for both performance and real-time segmentation potential on the newly created ORSI-RAPNI dataset (Chapter 4.3). This study is performed with increased complexity, moving from binary segmentation to multiclass tool segmentation.

6.1.2. Materials and Methods

Dataset Subsplit

As discussed in Chapter 4.3., the ORSI-RAPNI dataset adds several new challenges to the instrument segmentation. In effect, every non-organic item is now segmented (annotation process as detailed in Chapter 4.2.), resulting in an increased complexity for computer vision algorithms. To investigate the effect of this increased granularity, we have derived three different datasets from all 31.868 segmented images.

We assess both segmentation performance and computational loads for the following subset which increase in complexity:

- Binary Segmentation dataset, in which we differentiate all surgical tools and related materials from the background tissue (Fig. 6.1.b).
- Main Surgical Tools dataset, in which we differentiate between the 7 main robotic/laparoscopic tools and the tissue. The 7 surgical tools are monopolar curved scissors, force bipolar, suction, large needle driver, prograsp forceps, fenestrated bipolar forceps and echography (Fig. 6.1.c).
- Extended Surgical Tools dataset (Fig. 6.1.d), in which we differentiate between all 33 classes as detailed in Chapter 4 – Figure 4.21 and background. The Extended Surgical Tools segmentation can be considered the most extensive and thus most challenging segmentation task.

Figure 6.1. provides an overview of this granularity for an image sampled at the end of the renorraphy phase, containing robotic instruments, a suction device, gauze, hem-o-lok clips and suture wires.

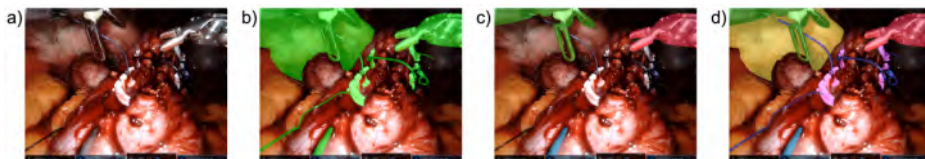


Figure 6.1. Increased granularity in segmentation. For a single image, from left to right, we depict the increased precision but also complexity for segmentation algorithms to cope with as presented by our 3 datasets. a) original image; b) binary segmentation; c) Main Surgical Tools dataset; d) Extended Surgical Tools dataset.

Investigated Computer Vision Architectures

CNNs have become the predominant tool to address semantic segmentation. Due to the nature of image processing, Fully Convolutional Networks (FCNs) are most often used with an encoder-decoder architecture. Whilst keeping in mind the weigh-off between computational cost and performance, Feature Pyramid Networks (FPN) [225], DeepLabV3+ (DV3+) [196] were evaluated as main architectures.

For feature extraction, we compared the performance of the above networks with different encoders or backbones based on a public benchmark [234]. In this benchmark, we selected eligible architectures with expected limited computation burden based on the total number of model parameters and the amount of GFlops. We identified EfficientNetV2-S (EV2) and MixNet-M (MNM) as the most promising ones, where EfficientNetV2-S was estimated to have better parameter efficiency than EfficientNet-B5, used in Chapter 5.1. MobileNet-V2 (MV2) was also tested for binary segmentation given its very low computational demands, with acceptable performance, whilst at that time, we were still aiming for a laptop based binary segmentation module as used in Chapter 5.1. The optimization of MV2 as an encoder for multiclass segmentation was not further pursued after initial results showed poor performance, possible due to lacking complexity of the model (low parameter count).

Training, Validation and Testing

The dataset was split on a per-procedural basis and balanced to have classes equally represented as discussed in Chapter 4.3, Figure 4.22. The final count attained 24.468 images for training, 4.498 images for validation, and 2.902 images for testing. Images and mask were resized to 512x512 pixels.

Data augmentation was performed by applying horizontal flipping, rotation up to 35 degrees, gaussian and multiplicative noise, median and motion blurring, random brightness and contrast, and hue, saturation, and value adjustments. Only one of these augmentation techniques was applied with 30% probability, implying that only 30% of the images were augmented.

The tuned hyperparameters impact both the network structure (number of hidden layers, dropout, weights initialization and activation function) and the training process (learning rate scheduling, optimizer, number of epochs and batch size).

Hyperparameter tuning was performed through Optuna [235] with the following categorical hyperparameters:

- Activation functions: Sigmoid – Softmax2d - Tanh
- Loss function: Focal – Dice – Focal + Dice
- Optimizer: Adam – AdamW – RMSprop - SGD

The evaluated integer and float parameters were:

- Encoder depth: 3 - 5
- Learning rate: 10^{-3} - 10^{-5}
- Batch size: 4 - 64
- Dropout: 0,2 - 0,5

Model training was performed on a Nvidia RTX3090 GPU with 256GB of RAM.

Real-time Inference, Computational Load and Performance

For real-time segmentation, we quantify memory footprint through comparison of the number of model parameters. For throughput, we measure the number of images the trained network can process per second when a test set image batch is sent to the model.

Mean Intersection over Union (IoU) was identified as an evaluation metric for quantifying accuracy [236].

6.1.3. Results

Hyperparameter Tuning

Binary Segmentation

Through Optuna, encoder depth and activation function were found to have little impact on performance and were not further optimized. The encoder depth was fixed at 5 layers, with a 2D softmax activation function. The other hyperparameters were extensively optimized retrieving the hyperparameter settings as depicted in table 6.1.

Architecture & Encoder	Learning rate	Optimizer	Loss	Dropout	Batch size
FPN & EV2	2.25×10^{-4}	Adam	Focal + dice	0.476	16
FPN & MV2	9.5×10^{-3}	AdamW	Focal	0.392	16
FPN & MNM	4.0×10^{-4}	AdamW	Focal + dice	0.370	16
DV3+ & EV2	2.1×10^{-4}	Adam	Focal + dice	0.432	8
DV3+ & MV2	1.15×10^{-4}	AdamW	Focal	0.429	16
DV3+ & MNM	3.0×10^{-4}	AdamW	Focal + dice	0.370	16

Table 6.1: Hyperparameter settings as identified through Optuna for binary segmentation. FPN = Feature Pyramid Network, DV3+ = DeepLabV3+, EV2 = EfficientNetV2-S, MV2 = MobileNet-V2, MNM = MixNet-M

Multiclass segmentation

For reasons of time-efficiency, batch size was varied between 8 and 16 instead of performing a full parameter sweep, and only architectures were tested, independent of the encoder combination. Table 6.2. shows the identified hyperparameters for multiclass segmentation.

Architecture & Encoder	Learning rate	Optimizer	Loss	Dropout
FPN	6.8×10^{-4}	AdamW	Focal + dice	0.399
DV3+	3.1×10^{-4}	RMSprop	Focal + dice	0.430

Table 6.2: Hyperparameter settings as identified through Optuna for multiclass segmentation. FPN = Feature Pyramid Network, DV3+ = DeepLabV3+

Network Performance

Binary Segmentation

Table 6.3 depicts the results of the binary segmentation algorithm. When aiming for the best computation-performance weigh-off, the MobileNet-V2 encoder with a DeepLabv3+ architecture is the optimal choice. EfficientNetV2-S attained the highest segmentation performance, however with severe penalty on computational loads.

Encoder	Mean IoU (%)		Parameters (M)		Throughput (Images/s)	
	DV3+	FPN	DV3+	FPN	DV3+	FPN
<i>EfficientNetV2-S</i>	94.4	94.4	22.5	23.4	38.6	34.3
<i>MixNet-M</i>	93.9	94.2	3.9	4.9	51.0	48.6
<i>MobileNet-V2</i>	93.8	91.8	4.4	4.2	64.6	63.6

Table 6.3. Binary segmentation metrics for explored architectures and encoders. DV3+ = DeepLabV3+, FPN = Feature Pyramid Network.

Multiclass Segmentation

Table 6.4. depicts the performance metrics for multiclass segmentation on both 8 and 34 classes (tissue included).

Encoder	Mean IoU (%)				Parameters (M)		Throughput (Images/s)			
	DV3+		FPN		DV3+	FPN	DV3+		FPN	
	Main	Ext	Main	Ext	Main/Ext		Main	Ext	Main	Ext
<i>EfficientNetV2-S</i>	83.4	74.3	81.0	73.8	22.5	23.5	30.7	19.1	29.6	16.9
<i>MixNet-M</i>	81.9	73.6	80.2	74.0	3.9	4.9	41.5	23.2	40.9	23.1

Table 6.4. Multiclass segmentation metrics for explored architectures and encoders. DV3+ = DeepLabV3+, FPN = Feature Pyramid Network, Main = Main Surgical Tools dataset (8 classes), Ext = Extended Surgical Tools Dataset (34 classes)

We found that DeepLabV3+ architecture mostly outperforms FPN. The efficientnetV2-S encoder was most performant. However, at one fifth of the memory footprint, MixNet-M achieves at least 30% more throughput for a relatively small penalty in mean IoU.

6.1.4. Conclusion

We provide an initial exploration of semantic segmentation frameworks keeping in mind real-time computation. We identified MobileNet-V2 encoding as highly performing encoder for low computational resource settings when performing binary segmentation. When solely focusing on best binary segmentation performance without considering computational loads, EfficientNetV2-S encoding is a good choice.

When reflecting on the edge optimization of Chapter 5.2., we note that network optimization towards edge applications requires a dedicated performance study. Here, we identified DV3+ in combination with EfficientNetV2-S to have slightly lower computational loads at equal performance, while Chapter 5.2. identified FPN + EfficientNetV2S as the best performing combination for real-time use. The main reason for this discrepancy is an evolution in the dataset throughout model testing in Chapter 5.2. There, during DLV3+ evaluation, we identified more imperfect data labels, despite

our best data quality assurance due temporal sampling error. These annotations were only corrected after the pipeline optimization of Chapter 5.2 was completed. The on-edge performance of Chapter 5.2. was thus only benchmarked on the 1345 images from 4 RAPN procedures of which the annotation quality was perfect. In this chapter, we evaluate on the fully corrected dataset of Chapter 4.3 with the test set of 2.902 images. This also means that possibly upon repetition of all on-edge optimization experiments of Chapter 5.2., DLV3+ might now come out on top and might further reduce the delay below 13ms. Nevertheless, the impact on real-time clinical usability is expected to be negligible.

The benchmarking and deployment in Chapter 5.2 was performed on a different GPU with dedicated PyTorch environment (Holoscan NGC Container on Clara AGX Nvidia RTX6000 GPU). This environment has a different inference operator which leverages C++ cuda programming to maximize the GPU capabilities, but this is not expected to be of any influence.

When assessing multiclass segmentation performed here, we notice that shifting from 2 (binary segmentation) to 8 classes incurs a 10% performance drop in mean IoU while throughput remains acceptable around 30 fps. Further increasing complexity towards the Extended Surgical Tool dataset with 34 classes once more incurs a 10% drop in mean IoU and a 50% drop in throughput compared to the Main Surgical Tool dataset. While at first sight, this could be problematic for real-time use, optimization for on edge deployment is expected to significantly increase throughput as was the case for binary segmentation. A mitigation plan here, is the use of MixNet-M or other encoders, which better balance computational loads with performance.

Future work should also investigate how the explored networks perform on other public datasets when considering computational constraints. Likewise, novel methods like transformer based on-edge deployments form an interesting research track [237], [238]. While we have performed a separate optimization for binary and multiclass optimization, novel research shows that this optimization might be overshooting and it could be wise to use one single model which learns from the panoptically segmented image [239]. At present, these methods are however not ready for real-time usage.

Computational efficient models segmenting all surgical items form a key step towards clinical integration of instrument segmentation models. Such segmentation is expected to further facilitate real-time surgical workflow estimation, instrument tracking for automation and tool-tissue interaction interpretation which in turn can help to objectify surgical skill.

6.2. Clinical value exploration of phase durations in RAPN

6.2.1. Abstract

Background

Surgical phases form the basic building blocks for surgical skill assessment, feedback and teaching. Phase duration itself and its correlation to clinical parameters at diagnosis has not yet been investigated. Novel commercial platforms provide phase indications but have not been assessed for accuracy yet.

Methods

We assess 100 robot-assisted partial nephrectomy videos for phase duration based on previously defined proficiency metrics. We develop an annotation framework and subsequently compare our annotations to an existing commercial solution (Touch Surgery, Medtronic™). We subsequently explore clinical correlations between phase durations and parameters derived from diagnosis and treatment.

Results

Objective and uniform phase assessment requires precise definitions derived from an iterative revision process. Comparison to a commercial solution shows large differences in definitions across phases. BMI and duration of renal tumor identification correlate positively, as well as tumor complexity and both tumor excision and renorrhaphy duration.

Conclusions

Surgical phase duration can be correlated with certain clinical outcomes. Further research should investigate if retrieved correlations are also clinically meaningful. This requires increasing dataset sizes and facilitation through intelligent computer vision algorithms. Commercial platforms can facilitate this dataset expansion and help unlock the full potential, provided the disclosure of phase annotation details.

6.2.2. Introduction

Surgical video recordings have become an indispensable tool in surgery and its use can be categorized into 3 main groups [6]:

1. **Surgical Education and Training:** Video recordings provide a valuable resource for trainees to observe and learn surgical procedures from experts [240], [241]. By capturing critical moments during surgery, videos also allow for retrospective analysis and discussions among surgical teams and aid in complex decision-making. Literature reports have documented the utility of surgical video review in assessing anatomical landmarks [242], identifying surgical errors, refining surgical techniques [243], and the development [244] and assessment [245] of objective surgical skill metrics which can be used for training. Additionally, video-based platforms [246] and telemedicine applications have enabled remote surgical education and mentorship [247], further expanding access [248] to surgical training opportunities.
2. **Patient Outcomes Assessment:** Surgical video recordings provide objective documentation of surgical procedures, enabling detailed analysis of surgical techniques, complications, and their impact on patient outcomes. Retrospective video analysis has been utilized in several studies to investigate patient outcomes [249].
3. **Quality Improvement Initiatives:** By reviewing surgical videos, surgical teams can identify areas for improvement, refine surgical approaches, evaluate adherence to established protocols, and enhance patient safety [250]. Furthermore, video-based quality assurance programs have been implemented to monitor surgical performance, benchmark outcomes, and ensure standardized practices across institutions [251].

Uniform surgical phase definition and assessment is an enabling factor in many of the applications above. Surgical phase assessment allows for consistent and standardized indexing across procedures which facilitates video review, analysis and sharing. As video analysis, computer vision, artificial intelligence, and data-analytics (so called "surgical data science") enter surgical theaters, the importance of correct and uniformly defined surgical phases increases [171]. This is especially true for complex surgeries which require a decomposition into simpler phase blocks for objective assessment and review [205]. Previous work has also shown that phase definitions, even for non-complex procedures, are often not uniformly defined [252] and there is a clear need for common ontologies to unlock the full potential of surgical data science [253].

Up to now, researchers have been focusing on shorter and often linear procedures such as laparoscopic cholecystectomy[254], whilst more varying and complex procedures, which might benefit most from new data science insights, remain poorly investigated.

One such longer procedure with more inherent variation is robot assisted partial nephrectomy (RAPN). Partial nephrectomy itself is the gold standard treatment for patients with T1 renal cell carcinoma [15]. RAPN has become increasingly popular, amongst others because of its low morbidity and early convalescence when compared to open surgery [51] and its shorter learning curve when compared to laparoscopy [52].

Apart from the usefulness of surgical phase indexing for video manipulation and case revision, surgical errors are often related with, and dependent on, specific surgical phases [255]. As such, surgical phases form an initial and crucial step towards achieving automated and objective surgical skill assessment. A skill assessment system should first identify the phase it is in, before focusing on the errors inherent to that phase. Error reduction and skill enhancement through proficiency based progression as compared to

classical training has proven to be beneficial for surgical skill acquisition and quantification [256]. Surgical phase duration has not yet been shown to correlate with surgical skill. When assessing clinical outcomes, full surgical duration has been investigated for correlations [257]–[259]. Apart from outcomes, retrieving correlations between diagnostic parameters and phase durations also has logistic benefits, as they could for instance enable a more precise OR time planning estimation at diagnosis. To our best knowledge, specific surgical phase duration and possible correlations with patient-specific clinical parameters at diagnosis or after treatment has not been performed.

In this work, we firstly propose a vision-based framework for objective, uniform, and precise surgical phase definition during RAPN. The definition is based on previously developed and clinically validated metrics for a proficiency-based curriculum[245].

Secondly, we manually analyze 100 RAPN procedures to refine and optimize the previously defined visual cues. We compare our annotations to a commercially available online platform (Touch Surgery™ – Medtronic, Minneapolis, USA) which provides phase information when uploading videos to its online library without user input. We evaluate its correctness by comparing manually performed in-house annotations.

Finally, we perform the first statistical exploration of phase durations and patient characteristics/clinical outcomes in RAPN.

6.2.3. Materials and Methods

Data Collection and Visual Cue Definition

During January 2018 - June 2022, 100 transperitoneal RAPN procedures were retrospectively and randomly collected from an existing video database in OLV Aalst Hospital (80 procedures) and Ghent University Hospital (20 procedures) after IRB approval. All procedures were performed on Intuitive Xi robotic systems (Intuitive™, California, USA). All procedures were either partially or completely performed by expert urologists, implying that procedural parts could have been performed by urologists in training, but always under expert supervision. Recordings were discarded if they did not contain a full-length procedure. Table 6.5 displays patient characteristics of the 100 procedures included in the dataset.

Table 6.5. Patient characteristics. Mean and standard deviation are displayed for age, PADUA score, pathology size and renal function. Other numbers are absolute counts as well as percentages as 100 patients were included. Side refers to the kidney which was affected and operated. Abbreviations: RCC = Renal Cell Carcinoma, TCC = Transitional Cell Cancer, eGFR = estimated Glomerular Filtration Rate

Age (years)	64.63 (+- 11.13)
Sex	
male	71
female	29
PADUA score	8.05 (+- 1.79)
RENAL score	8.47 (+- 2.77)
Side	
right	53

left	47
Pathology size (mm)	34.32 (+- 24.96)
Final Pathology Stage	
T0	25
T1a	49
T1b	18
T2a	5
T2b	2
T3a	1
Histology	
clear cell RCC	52
papillary RCC	17
oncocytoma	17
angiomyolipoma	6
chromophobic RCC	4
cyst	2
sarcoma	1
TCC	1
Preoperative renal function	
eGFR (ml/min)	75.48 (+- 16.26)
creatinin (mg/dl)	1.03 (+- 0.39)
Postoperative renal function	
eGFR (ml/min)	71.70 (+- 19.19)
creatinine (mg/dl)	1.07 (+- 0.55)

We derive 16 visually distinctive phases from the validated RAPN metrics framework as developed by Farinha et al [244], [245]. We define exact visual cues as starting points for surgical phases. Table A.6. (Supplemental Digital Content) depicts the exhaustive phase list and corresponding visual cues. We adapt the existing framework, defined for left-sided RAPN, for common phases as present in both left and right-sided RAPN. We refer to this annotation framework as the Orsi-framework.

An in-house developed manual annotation tool is used, consisting of an in-browser viewer which allows to load a video, precisely define starting points of selected phases and export the timepoints with millisecond precision afterwards. An example of the manual annotation tool can be found in the Supplementary Digital Content (Figure A.23.). All videos were assessed by three medical students (MD, CVS, TO) after consensus on the visual definitions with a consultant urologist (RDG). The final manual student annotations were subsequently double-checked by a second consultant urologist (MPL).

Comparison to Commercial Software

The precise and more nuanced Orsi definitions are concatenated in 13 phases to be consistent with the Touch Surgery (TS) phase definitions for a one-to-one comparison. The phases consistency can be found in Table 6.6. Two medical students (KVR, AW) reviewed all videos for correctness after automated, rule-based concatenation.

All uploaded videos were automatically anonymized with removal of all possible identity clues, which include removal of out-of-body segments, as well as removal of segments with TilePro™ function (Intuitive™, California, USA) while they display patient-specific information such as CT, MRI or 3D model data (e.g. Chapter 3). The anonymization did not alter the case duration as these parts were blacked out, rather than cropped. Subsequently, videos were uploaded to the TS platform (software version February 2023). The Orsi-analysis was performed on full non-anonymized videos, under IRB approval.

After upload and processing, TS timepoints were manually extracted from the online commercial platform.

Table 6.6. Congruence with phases derived from ERUS and definition by Touch Surgery.

Orsi definitions	Touch Surgery definitions
(1) Port Insertion and Surgical Access	(1) Port Insertion and Surgical Access
(2) Colon (and Spleen) Mobilization	(2) Colon Mobilization (3) Identification of Anatomical Landmarks
(3) Hilar Control General	(4) Hilar Dissection
(4) Selective Hilar Control	(5) Kidney Mobilization
(5) Kidney Mobilization	(6) Tumor Identification
(6) Tumor Identification	(7) Hilar Clamping
(7) Hilar Clamping	(8) Tumor Excision
(8) Tumor Excision	(9) Specimen Retrieval
(9) Specimen Retrieval	(10) Renorrhaphy
(10) Inner Renorrhaphy	(11) Hilar Unclamping
(11) Hilar Unclamping	(10) Renorrhaphy
(12) Outer Renorrhaphy	(12) Specimen Removal and Closure
(13) Specimen Removal and Closing	(12) Specimen Removal and Closure
(14) Instrument Removal	(12) Specimen Removal and Closure
(15) Retroperitalisation of the Kidney	(12) Specimen Removal and Closure
(16) End of Operation	(13) Operation Finished

The Touch Surgery platform does not provide details on the phase definition rules. The videos underwent automated similarity analysis in which the manual Orsi annotations are compared to Touch Surgery annotations by use of a predefined loss function. This function objectifies how differently phases were annotated and detects procedures who have least similarity.

We base the loss function on a commonly used metric called Intersection-over-Union (IoU). For each phase, a binary vector is created which indicates 1 for seconds that belonged to that phase for the given annotation method and 0 elsewhere. The total sum of all phase vectors equals the total procedure time in seconds. The concept is visualized in Figure 6.2. The IOU per phase is then calculated as follows:

$$IoU(\text{phase } X) = \frac{\text{sum}(v_1 \text{ AND } v_2)}{\text{sum}(v_1 \text{ OR } v_2)}$$

Where v_1 is the vector with the number of seconds spent in a certain phase X in the manual annotation and v_2 is the vector with the amount seconds spent in phase X according to the Touch Surgery annotation. Both are linked in a one-to-one temporal fashion as depicted in Figure 6.2.

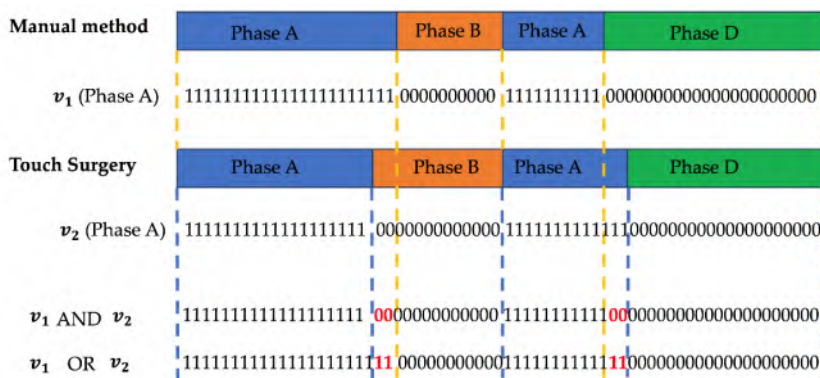


Figure 6.2: Example of the IoU calculation method. Depicted in red are the differences as picked up by the nominator and denominator in the IoU formula to better quantify the overlap or difference in recurring phases.

As such, the numerator holds the number of seconds where both procedures “agree” on the investigated phase for the full procedural. The overlaps are summed as phases can reoccur. The denominator counts the number of seconds where the phase was indicated by at least one of both annotation methods. A perfect correspondence between both annotation approaches results in an IoU(phase) of 100%. To determine the final loss, we multiply all IoU(phases) and take the negative logarithm.

The loss function is described below:

$$Loss = -\ln\left(\prod_{\text{phases}} IoU(\text{phase})\right)$$

Clinical Analysis

We explored correlations between phase durations and the following clinical parameters: age, gender, tumor complexity (PADUA score), tumor size, prior abdominal surgery, BMI, pT stage, histology, preoperative and postoperative renal function as measured by eGFR and creatinine. We also examined postoperative complications. Durations are assessed for both TS and manual (M) definitions. Correlation examination was performed by use of the Spearman's, Kendall's tau tests, as appropriate. In case of statistically significant correlation, a linear regression model was then built to analyze the relationship between the identified variables. All the analysis were performed by using Jamovi software v2.3.

6.2.4. Results

General Phase Data Analysis and Comparison

Touch Surgery does not provide phase assessment in case of cystic renal lesions, despite it being a similar technical approach. As such, the resulting final dataset for the side-by-side comparison was diluted to a total of 86 RAPN procedures. Table 6.7 shows the descriptive statistics for our concatenated manual (M) phase analysis and the TS analysis for 86 analyzed procedures.

Table 6.7. RAPN Phase Duration results for one-to-one comparison between manual annotations 'M(86)' and Touch Surgery 'TS(86)' on the 86 analyzed procedures by Touch Surgery, as well as the values for all 100 procedures as the manually assessed 'M(100)', which includes the 'M(86)'. Mean, median, standard deviation (SD) and interquartile distance (IQD) duration in minutes are depicted in normal black font. The number of occurrences of an annotated phase, this is whether it was annotated in of both methods or not, is depicted in italic and highlighted grey.

RAPN Phase	mean (+SD) [minutes]			median (IQD) [minutes]		
	number of instances			number of instances		
	M(86)	TS(86)	M (100)	M(86)	TS(86)	M(100)
Port Insertion and Surgical Access	5,8 (+- 5,6) 65	8,9 (+- 7,4) 34	6,2 (+- 5,6) 77	3,7 (8,3) 65	6,7 (7,6) 34	5,2 (9,7) 77
Colon Mobilization	5,6 (+- 7,6) 61	11,6 (+- 7,9) 71	5,7 (+- 7,7) 70	2,7 (7,4) 61	10,0 (11,3) 71	2,7 (7,6) 70
Identification of Anatomical Landmarks	13,1 (+- 8,7) 49	4,6 (+- 3,7) 50	12,0 (+- 8,5) 58	11,9 (14,5) 49	4,0 (5,5) 50	9,8 (12,3) 58
Hilar Dissection	16,0 (+- 11,5) 76	14,3 (+- 10,6) 74	16,3 (+- 12,3) 88	14,0 (19,6) 76	11,0 (16,0) 74	14,4 (19,3) 88
Kidney Mobilization	20,4 (+- 15,0) 84	27,5 (+- 17,7) 84	20,4 (+-14,6) 98	18,4 (20,5) 84	24,6 (27,1) 84	17,8 (19,2) 98
Tumor Identification	15,6 (+- 15,5) 85	9,4 (+- 6,8) 80	15,2 (+- 14,6) 99	11,3 (11,3) 85	8,6 (6,8) 80	11,6 (12,4) 99
Hilar Clamping	2,9 (+-3,6) 67	1,2 (+- 1) 65	3,2 (+- 4,1) 77	1,6 (2,5) 67	0,8 (1,2) 65	1,8 (2,6) 77
Tumor Excision	6,3 (+- 3,6) 86	8,7 (+- 4,9) 84	6,5 (+- 4,1) 100	5,3 (4,2) 86	7,8 (5,9) 84	5,3 (4,1) 100
Specimen Retrieval	1,5 (+- 2,5) 85	1,7 (+- 3,5) 83	1,7 (+- 2,8) 99	0,8 (1,0) 85	0,6 (1,0) 83	0,8 (1,0) 99
Renorrhaphy	14,9 (+- 9,9) 82	20,9 (+-12,3) 77	15,8 (+- 11,6) 93	12,9 (11,7) 82	19,1 (15,2) 77	13,5 (12,7) 93
Hilar Unclamping	4,5 (+- 6,1) 65	2,7 (+- 6,4) 67	5,0 (+- 6,9) 75	2,2 (3,5) 65	1,1 (1,6) 67	2,9 (4,0) 75
Specimen Removal and Closure	8,2 (+- 6,0) 82	9,3 (+-8,1) 71	8,5 (+- 6,3) 94	6,9 (6,1) 82	7,1 (8,5) 71	7,4 (6,5) 94
Operation Finished	5,9 (+- 5,8) 81	0,0 (+- 0,0) 85	6,0 (+- 5,7) 92	3,7 (5,7) 81	0 (0,0) 85	4,1 (5,8) 92

At first sight, phase duration in both platforms is quite different. When looking at similarity between phase definitions on the full dataset, the 20 RAPN procedures with the least similarity (consistent with a loss higher than 70) were analyzed in depth for phase assessment differences. Figure 6.3. shows the loss for all procedures.

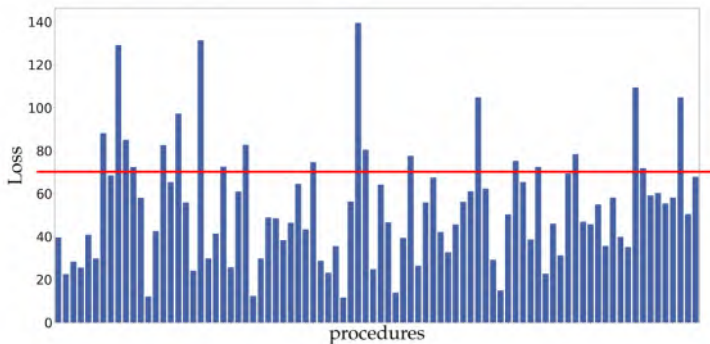


Figure 6.3: Loss for all 86 analyzed procedures. 20 procedures score above the empirically set threshold of 70, and were analyzed for discrepancies in definition and labeling.

The following recurring discrepancies were withheld in poorly corresponding videos. The 'Identification of Anatomical Landmarks' phase mainly shows overlap with the 'Colon Mobilization' phase, i.e. 'Identification of Anatomical Landmarks' is defined by one annotation method whereas 'Colon Mobilization' is defined by the other annotation method at this timepoint. This occurs in both ways, and is perhaps due to the fact that this phase is poorly defined and allows for multiple interpretations. Furthermore, although port insertion and surgical access was not always recorded, it was not annotated in TS in half of the cases, leading to a longer duration of 'Colon Mobilization'. From 'Colon Mobilization' onwards, we do note that in general the same number of phases are annotated. A clearly differing visual definition is present in 'Kidney mobilization' and 'Tumor identification'. Ultrasound use and guided demarcation forms an important part of tumor identification and in certain procedures, ultrasound (US) is initiated before opening of Gerota's fascia. In the Manual phase analysis, this US usage is considered a subphase of 'Tumor identification' and thus marks the beginning of this phase. Touch Surgery does not always recognize US usage as part of 'Tumor identification' yet, resulting in a missed phase initiation. Touch Surgery recognizes the start of the 'Tumor identification' phase when the US is used for the second time when the renal parenchyma with tumor zone is already freed from peri-renal fat. This also results in longer 'Tumor Identification' phases in the manual assessment. As the manual assessment is more nuanced and the definition is different, a side-by-side comparison on accuracy is irrelevant. This differing definition impacts all phase durations before the onset of hilar clamping and tumor excision, which makes phase duration comparison for other phases before 'Hilar Clamping' unreliable.

We do note that combining all surgical manipulations before 'Hilar Clamping', this is the combination of 'Port Insertion and Surgical Access', 'Colon Mobilization', 'Identification of Anatomical Landmarks', 'Hilar Dissection' and 'Kidney Mobilization', does have very similar mean and median durations (means are 76,5 and 76,3 minutes, medians are 62 and 64,9 minutes for respectively M and TS assessment).

The next important surgical landmark entails tumor excision, which is most often performed after hilar clamping. We see here that of all 100 procedures, 77 procedures

were performed off-clamp. The decision for off-clamp tumor excision is made by the expert surgeon on a case-by-case basis and was no criteria for video case selection. Touch Surgery did not indicate tumor excision and tumor retrieval in 2 cases due to our anonymization protocol. Both cases had patient-specific CT scan or 3D model info in the console view which was anonymized before upload. Despite being a clear drawback for comparison, these phases should not impact median times, where we note similar trends. The combined duration of 'Hilar clamping' and 'Tumor Excision' is very similar. We find mean and median combined values of respectively 9,2 and 6,9 minutes for manual assessment; 9,9 and 8,6 minutes for TS assessment. The main factors attributing to longer 'Tumor Excision' times in TS are twofold. TS includes application of hemostatic agents, which is excluded in our manual assessment and the TS 'Tumor Excision' phase starts as soon as the kidney is manipulated after clamping, where in our assessment it only starts when the blunt dissection takes place. This also results in a longer manual 'Hilar Clamping' duration.

After tumor excision, we enter the last procedural part in which the kidney is reconstructed after specimen retrieval. 'Specimen Retrieval' has very similar durations, nonetheless we note that, despite our best efforts, both our manual assessment and TS missed to annotate one specimen retrieval, albeit in different procedures. Similar to 'Hilar Clamping', the 'Hilar Unclamping' phase is once more shorter in TS. The main attributing factor is the rennoraphy starting point definition. In TS, this phase starts when needles are brought closeby the parenchyma and thus this ends the unclamping. In our assessment, this phase only starts at the first parenchymal suture. This is also reflected in shorter renorrhaphy times for our assessment and confirms the narrower definition. 'Specimen retrieval and Closure' has a similar time range and includes the renal retroperitonealisation. The 'Operation Finished' definition is more precise in our assessment and marks when the camera is removed from the abdomen for the last time, whilst for Touch Surgery this is simply the end of the video, resulting in an empty phase duration.

Clinical Data Correlation Exploration

Prior abdominal surgery did not significantly impact any of the phases' duration, independent of the phase assessment methodology (TS or M). Likewise, no significant impact was found for age, gender, pT stage, histology type or pre/post-operative renal function. The post-operative complication rate was too low to find any correlations.

Spearman's test showed a significant correlation ($p=0.011$) between patients' BMI and the 'Tumor Identification' duration for manually assessed cases only. Figure 6.4 shows the linear regression model. Increased BMI results in increased 'Tumor Identification' periods ($p=0.011$).

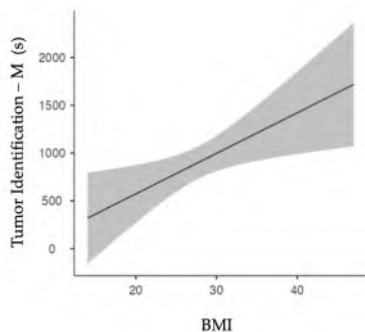


Figure 6.4: Linear regression model for BMI and surgical phase duration of manual tumor identification. Increasing BMI correlates with increasing tumor identification duration.

When assessing tumor complexity according to the PADUA scores, we see that 'Renorrhaphy' duration has a significant positive correlation with PADUA score ($p<0.001$ for both Touch Surgery and manual assessment). Likewise, 'Tumor Excision' was significantly correlated with PADUA scores, nevertheless only in manual assessment ($p<0.001$). At linear regression, PADUA score confirmed a positive correlation with 'Renorrhaphy' duration ($p<0.001$ for both TS and M assessment, Figure 6.5.a. and 6.5.b. respectively). Figure 6.5.c. depicts the positive correlation between manual assessment of 'Tumor Excision' and Padua score ($p<0.001$).

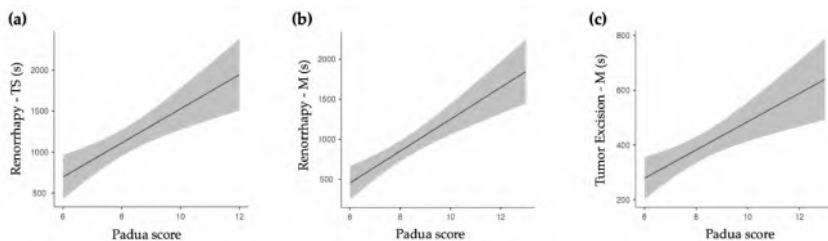


Figure 6.5: Linear regression model for PADUA scores. (a) Positive correlation with 'Renorrhaphy' as assessed by Touch Surgery (TS). (b) Positive correlation with 'Renorrhaphy' as assessed manually (M). (c) Positive correlation with 'Tumor Excision' duration when assessed manually (M).

6.2.5. Discussion

Data Quality and Visual Clue Definition

The retrospective datacollection poses a drawback on data quality. As both hospitals have a residency and fellowship programme, procedural parts have been performed by non-experts which might bias the results. Previous work has also shown that console time significantly decreases whilst going through the learning curve for off-clamp RAPN [260]. Nonetheless, these non-expert procedural parts were not documented at the time of surgery.

Defining visual clues for phase analysis is a repetitive process in which the multicentric approach allowed for a more robust and precise definition. Several iterations were required before agreeing on a final template as provided in Table A.6. (Supplemental Digital Content), which was then used for full dataset investigation. Despite our best efforts in checking all procedures fivefold, post-hoc data analysis revealed we still missed annotating one phase. As such, phase annotation is a time-intensive effort which reveals the clinical need for intelligent systems which can support this automatically and consistently.

Platform Comparison

When comparing our manual platform and the Touch Surgery platform for RAPN phase assessment, we identify three key items:

Firstly, the lack of analyzing renal cysts in Touch Surgery is an apparent drawback as it immediately discards 14% of the cases, despite having identical surgical technique and approach.

Secondly, when analyzing both platforms for the remaining 86 procedures, we identify the lack of uniform and transparent definition as the main inhibitor for in depth side-by-side comparison. Touch Surgery does not provide details on the phase analysis process. It is unknown whether the assessment happens fully autonomous, semi-autonomous or fully manually. In the latter case, nothing is known about the expertise level of annotators, their training, or their interrater reliability. The platform provides no information on the used visual phase cues. On the other hand, no public consensus exists for objectively defined visual phase cues. Despite having based our definition on a published consensus for phase metrics, defining visual cues requires more details and as such there is a clear mismatch between both definitions.

Thirdly, assessment of the most differing procedures as identified by the loss function, shows that phase combinations and evaluation of specific subphases results in greater similarity. As such, large surgical entities are annotated in a similar fashion. When assessing the full procedure, 3 major operative parts (preparation for tumor excision, tumor excision and the hemostasis and closure) were found to be similar. Nevertheless, they are insufficiently granular for immediate outcome correlation research.

Clinical Outcomes

BMI and 'Tumor Identification' duration correlate positively, which can be suspected as higher BMI often involves more intraabdominal fatty tissue. As the kidney is surrounded by perinephric fat, tumor identification on the renal surface can indeed be more tedious. This correlation was not withheld in the TS definitions. This can be attributed to the apparent TS definitions of only annotating 'Tumor Identification' when the kidney is already fully exposed. Another attributing factor is our removal of our echography TilePro™ segments in the TS group for anonymization purposes. Nevertheless, these

segments were often correctly picked-up inside the TS platform, starting when ultrasound entered the body and ending upon ultrasound removal.

When tumor complexity rises, e.g. because of larger size or endophytic nature, as expected tumor excision duration also increases. Likewise, 'Renorrhaphy' duration increases with tumor complexity. Big or deep tumor can indeed leave large or difficult to reach renal resection beds, which can effectively be more difficult to reconstruct or obtain adequate hemostasis. Nonetheless, it is noteworthy that these correlations are only withheld in manual assessment. The missing correlation for TS might be attributed to the broader 'Tumor Excision' definition which includes hemostatic agent applications. Touch Surgery retrieved statistical significance with renorrhaphy duration only. We do note that 2 out of 86 cases were irrelevant for tumor excision comparison, given the pre-upload anonymization. Furthermore, the manual data analysis was performed on 14 cases more.

6.2.6. Conclusions

Assessing surgical phase duration for clinical relevance requires nuanced and granular phase descriptions and definitions, which can be derived from metrics-based training curricula. We note that the nature of this work is hypothesis generating, without implying causation. Nevertheless, we found initial objective insights into how factors like BMI and tumor complexity, assessed at diagnosis, correlate with surgical phase duration.

Metrics-based definitions effectively resulted in more clinical correlations when compared to a commercial platform, where the main drawback in the latter was missing phase definition information. As such, this manuscript might act as a guide towards better standardization for future phase analysis projects in RAPN.

Lastly, this work can serve as the basis for automated phase detection in RAPN, where deep learning computer vision algorithms automatically define surgical phases [252]. This then enables larger patient cohort investigations, without the need for time-intensive manual annotations [30]. Furthermore, automated phase detection acts as an enabler towards fully automated surgical scene understanding [261] which in turn unlocks a myriad of other possible clinical applications [262].

6.2.7. Supplemental Digital Content

Table A.6: RAPN Phase list with the according visual cues .

	RAPN phase	Starting point	Visual starting cue	Phase characteristics
1	Port Insertion and Surgical Access	Inside abdomen	When the video starts in the abdominal space or when the camera is inserted into the abdominal space and there is no visual of the trocar	Port placement Instrument insertion Adhesion removal
2	Colon (and Spleen) Mobilization	Identification of the mesenteric line A*: spleen mobilization	Right kidney: when the camera points between the liver and the right paracolic gutter Left kidney: when the camera points between the paracolic gutter and the kidney contour can be seen A* when instruments mobilize the spleen	Opening of peritoneum Adhesion removal
3	Hilar Control General	Identification of gonadal vein A*: start dissection of renal vein	Identification of gonadal vein: when the gonadal vein can be partially seen A* when the renal vein can be partially seen	Dissection of main renal artery Start isolation of main renal artery** Vessel loop on main renal artery Hemolock clip on vessel loop
4	Selective Hilar Control	Start dissection of other than main renal artery	When the artery can be partially seen	Dissection of selective renal artery Start isolation of selective renal artery** Vessel loop on selective renal artery

				Hemolock clip on vessel loop
5	Kidney Mobilization	Start opening Gerota's fascia	When a new incision in the perirenal fat, representing the surrounding renal fascia (Gerota's fascia), is made	Dissection of kidney surface
6	Tumor Identification	Start demarcation of tumor A*: ultrasound start	When the monopolar curved scissors uses coagulation to delineate tumor position, whilst remaining on the kidney surface A* when the ultrasound probe is pressed against the parenchyma and the ultrasound image can be seen	Use of ultrasound probe Tumor demarcation
7	Hilar Clamping	Bulldog clamp on main artery A*: bulldog clamp on selective artery	When the bulldog clamp is positioned on the renal artery When the bulldog clamp is positioned on a first or higher order renal artery	Use of bulldog clamp Use of ICG
8	Tumor Excision	Start blunt dissection	When the monopolar curved scissors cut function is used to cleave open the renal parenchyma, or the tumor is being separated from the renal parenchyma whilst the scissor blades are closed	Resection of tumor
9	Specimen Retrieval	Free tumor base	When the tumor base is completely free from tumor	Specimen retrieval

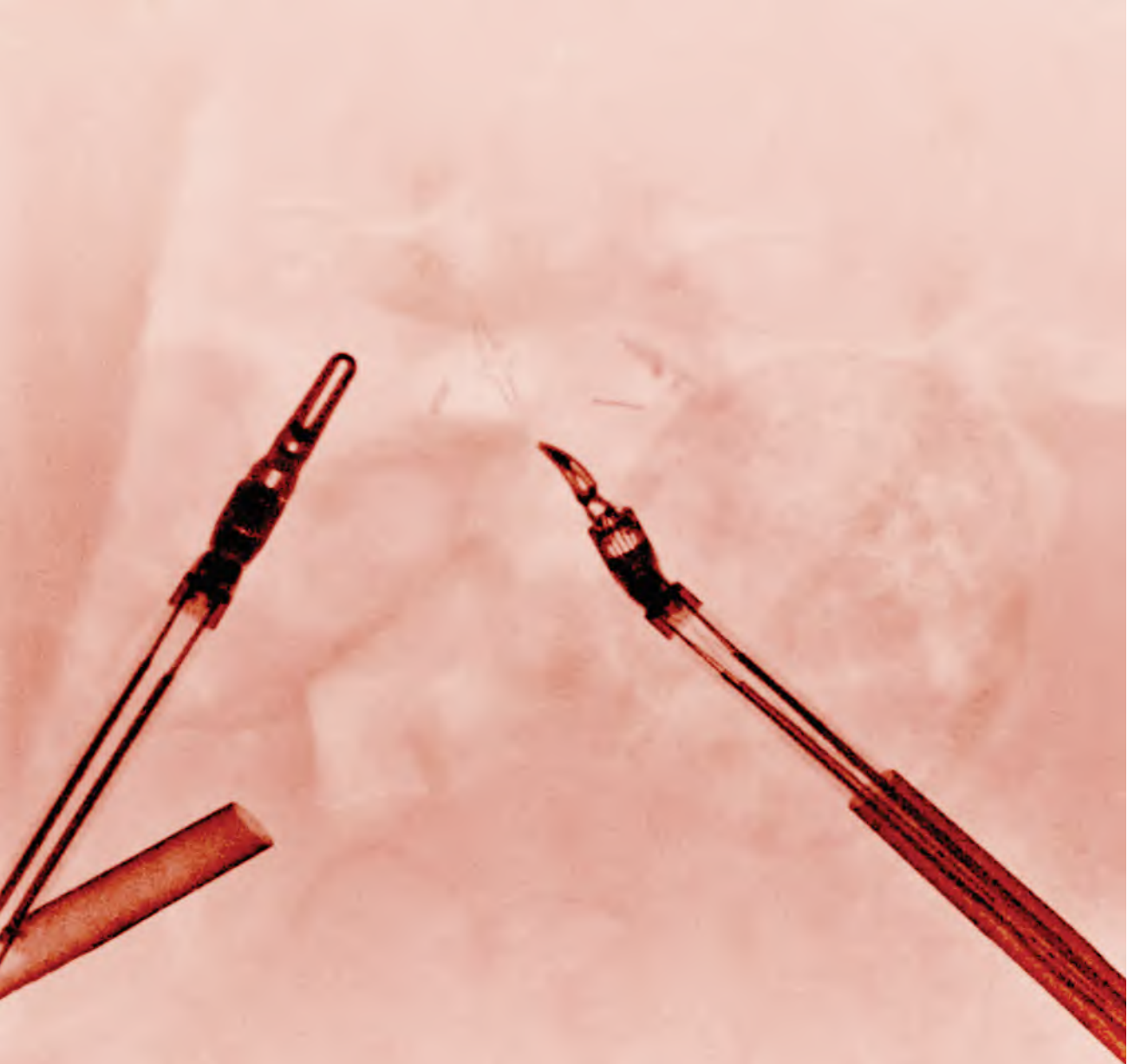
10	Inner Renorrhaphy	First inner renorrhaphy stitch	When the needle (not the needle wire) has fully exited the parenchyma after its first bite	Inner renorrhaphy
11	Hilar Unclamping	Bulldog clamp off main artery A*: bulldog clamp off selective artery	When the bulldog clamp is opened on the main renal artery A* when the bulldog clamp is opened on the selective artery	Hilar unclamping
12	Outer Renorrhaphy	First outer renorrhaphy stitch	When the needle (not the needle wire) has fully exited the parenchyma after its first bite	Outer renorrhaphy Use of hemostatic agent
13	Specimen Removal and Closing	Tumor bagging	When the tumor falls halfway into the endobag	Tumor bagging Use of hemostatic agent
14	Instrument Removal	Vessel loop removal A*: bulldog clamp removal	When the assistant fully grasps the already cut vessel loop using a laparoscopic instrument When the assistant fully grasps the bulldog clamp using a laparoscopic instrument	Instrument removal
15	Retroperitonealisation of the Kidney	Passing first stitch in parietal peritoneum	When the needle (not the needle wire) has fully exited the fatty tissue after its first bite.	Suturing parietal peritoneum
16	End of Operation	Tension hem-o-lok retroperitonealisation	When the non-absorbable clip is pressed against the peritoneum while the	Removal of robotic instruments** Drain placement

			<p>needle wire is still under tension</p> <p>A* When the last clip is fully applied on the suture wire</p>	<p>Camera out of body</p> <p>Camera stop</p>
		<p>A*: secure suture retroperitonealisation**</p>		

*A: alternative starting point: when an alternative starting point occurs first, this will be the starting point of the phase
 **alternative starting point only annotated when the typical starting point does not occur (also describes the beginning of the phase).

Selective hilar control	Start dissection of other artery than main renal	Start isolation of selective renal artery	Entering selective renal artery with vessel loop	Hemobok clip or vessel loop [selective]
	0:21.01	0:23.09	0:26.37	
	<input type="button" value="clear"/>	<input type="button" value="clear"/>	<input type="button" value="clear"/>	
<input type="button" value="event skipped"/>	<input type="button" value="event skipped"/>	<input type="button" value="event skipped"/>	<input type="button" value="event skipped"/>	

Figure A.23: Screenshot of the in-house developed HTML file for phase analysis.



DISCUSSION AND FUTURE PERSPECTIVES

07

*« The future of surgery is not about blood and guts,
it is about bytes and bits »*

- Richard Satava

Throughout the efforts of this PhD work to further digitalize robot-assisted partial nephrectomy, some obstacles were successfully tackled whilst revealing new research challenges for future work. Despite our best efforts, large building blocks of work in progress and remaining challenges lie ahead, as also depicted in the outline of Chapter 1 and Figure 1.1. Below, we resume the key messages and bottlenecks identified throughout this work, and list for each of them the first steps taken. We also provide possible directions to guide future efforts in the field.

As an overview, Figure 7.1 summarizes a detailed pipeline of how pre- and intraoperative planning using selective clamping and augmented reality can be productized. It also highlights key aspects for future improvements (to do's) per building block as discussed below.

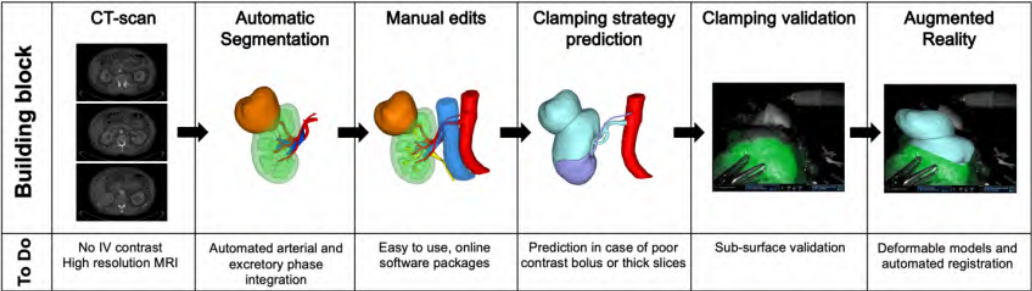


Figure 7.1: Productized pipeline for the clinical integration of 3D models for RAPN. The top row depicts necessary steps to facilitate the process, the bottom row shows current bottlenecks for easy clinical integration and areas for future improvement.

7.1. Pre-operative Virtual 3D Models

7.1.1. Steps Taken

This work entails the first validation of virtual selective clamping as predicted by a perfusion zone algorithm. Such validation has, to our best knowledge, not happened for available software packages that have been around for many years, despite using similar algorithms.

Despite their availability, 3D virtual models, even without perfusion information, still have not found their way into routine clinical practice. One main driver here is the time it takes to manually segment all structures of interest to obtain a 3D model [263]–[266]. As an alternative, 3D digital models can be purchased as such through existing commercial services [267]–[270], but these services are rarely reimbursed given the current lack of clinical evidence in reducing surgical morbidity. Furthermore, not all standard cases might require dedicated 3D planning.

An enabler for simultaneously obtaining clinical evidence whilst reducing costs, is automated 3D contouring and model generation through A.I. assisted segmentation [263]–[266]. CT and MRI data can be segmented automatically by neural networks which can learn to automatically extract the delineation and volumes of organs or other soft tissues and features of interest. As such, we also constructed a database of 219 retrospective CT scans with their respective 3D reconstructions and trained a nnU-Net [271] to perform a pre-segmentation. The latter is promising work in progress, as our current approach can segment renal parenchyma, arteries, veins, and tumor concurrently, with only a minimal need for manual editing afterwards.

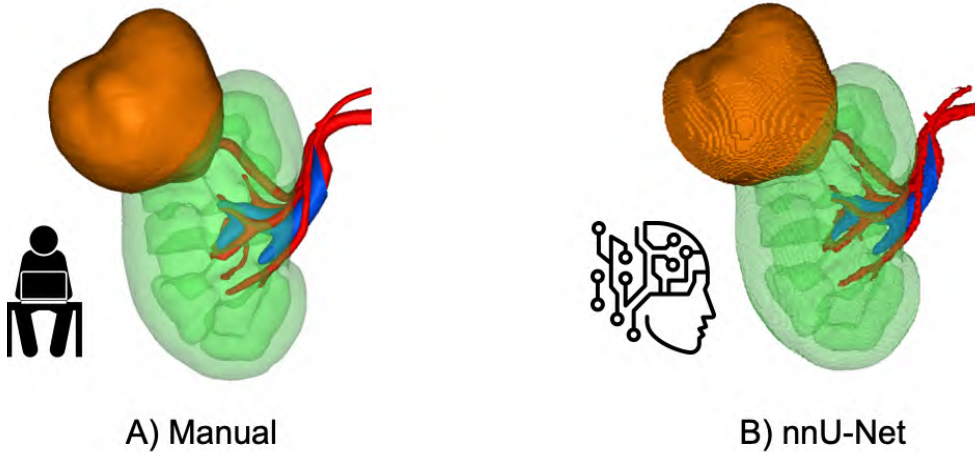


Figure 7.2: Deep learning segmentation speeds up 3D model generation. A) Result of manual delineation of structures of interest. B) Automatically generated 3D model by our deep learning algorithm.

Figure 7.2 demonstrates our fully automated deep learning segmentation (Fig 7.2.B), from which clinicians and engineers can subsequently delineate or correct certain missed structures to end up with a final model (Fig 7.2.A). As such, 3D model fabrication time was reduced with at least 70% to an estimated 15 minutes per case.

7.1.2. Future Work

3D Model Fabrication Automation

Further research and quantification is needed on how far automation can be pushed, using hybrid models or ensemble methods which concomitantly segment the pyelo-caliceal system on the excretory phase, while correctly aligning and registering these anatomical components. Likewise, dataset expansion will further add to the algorithmic robustness.

When aspiring to build own 3D model datasets, it is no longer required to start from scratch. Several powerful open-sourced automated segmentation algorithms exist [272], [273], often built on existing open-sourced datasets which are equally accessible [274]. Decreased 3D model fabrication time and empowering clinicians to independently create their own 3D models is expected to increase adoption and to decrease costs. Easy access to 3D segmentation software is another prerequisite here. Online modules rather than offline software installations should facilitate this integration. This could enable large prospective trials showing the benefit of 3D planning when compared to 2D imaging for surgical planning, which could be an enabler for reimbursement.

Alternative Imaging Modalities and Algorithms

Another relevant point is expansion towards MRI imaging as a 3D model input source. Given the absence of radiation exposure during imaging, this forms a promising path to investigate. However, MRI imaging protocols may be time-consuming when compared to CT and thin slices to obtain the highest possible spatial resolution are challenging to obtain. Furthermore, foreign materials (hip prosthesis, spinal screws, ...) can deteriorate image quality. Depending on the imaging protocol used, both MRI and CT may bear a concern of contrast nephrotoxicity to obtain precise arterial and venous anatomy when planning surgery. Patients who most desperately need nephron sparing surgery (i.e. patients with pre-existing poor renal function) are also the ones who are most sensitive to contrast toxicity. Novel MRI applications such as

arterial spin labeling which require no contrast administration might prove to be a powerful solution when successfully implemented in clinical practice [275], [276].

Increasing Evidence for Virtual Selective Clamping

Likewise, as for virtual 3D models which solely display anatomical information, large prospective trials should be setup for 3D models displaying functional information such as perfusion zones. This could further explore the potential benefit and/or relevance of such functional information. This impact can be situated both on the patient side (better renal function, less complications or adverse surgical events, lower induction of cardiovascular comorbidities on the long term, ...) as well as on a hospital level (length of stay, surgical duration, ...). Current studies are often retrospective, have rather short follow-up or small sample sizes. Therefore, high level evidence studies are needed to further shape the specific domains where functional 3D models are most useful.

Apart from the clinical validation, algorithmic optimization and validation are other key focusses. This includes perfusion validation not only at the renal surface (as was done in chapter 3.1 using ICG injections and imaging) but also inside the parenchymal volume. While we focused on quantifying the correctness of the predicted perfusion zones using questionnaires, more specific and objective methods should be developed.

Once more, novel functional imaging protocols, such as arterial spin labeling in MRI, could also improve functional information for volumetric perfusion validation [275], [276]. Nonetheless, further dedicated research is needed for these techniques to mature and be brought into clinical practice.

The clinical cost-benefit of selective arterial clamping is still under research. However, the techniques discussed in chapter 2, in combination with other new technologies introduced throughout this work, can be seen as the Swiss army knife for experienced surgeons who encounter patients with a risk of progression towards CKD. As we enter the era of personalized medicine, our surgical strategy should be adapted likewise.

7.2. Augmented Reality

7.2.1. Steps Taken

This work was to our-best-knowledge the first to solve instrument de-occlusion in robot-assisted Augmented Reality guided surgery through deep learning segmentation. Despite solving the occlusion problem, A.R. is still not ready for primetime. This implies that, even if the 3D models mentioned above are generated instantly and cost-efficiently, this information will at present not seamlessly integrate into the surgical field.

Hence, to achieve realistic A.R. and pure image guided surgery, the automated model alignment issue should be fixed. This is an active research topic and several options presented themselves as being helpful to this end in Chapter 2.6. For seamless clinical integration, tracker-less alignment strategies seem most suitable. A prior towards tracker-less alignment is automated tissue recognition. This tissue recognition could in turn allow a 3D model to get a coarse but automated anatomically correct sense of orientation. A subsequent finer alignment would be possible if the surface contours of the organ of interest as identified through segmentation are stereo-reconstructed and matched. This concept is visualized in Figure 7.3., in which we depict the first preliminary results of our automated surgical scene interpretation. In a preliminary attempt, we trained an EfficientNetB4 encoder [277] with

DeeplabV3+ backbone [196] on a dataset of 15.519 panoptic segmented images, with 97% specificity, 59.9% sensitivity and 66.1% precision on pixel level.

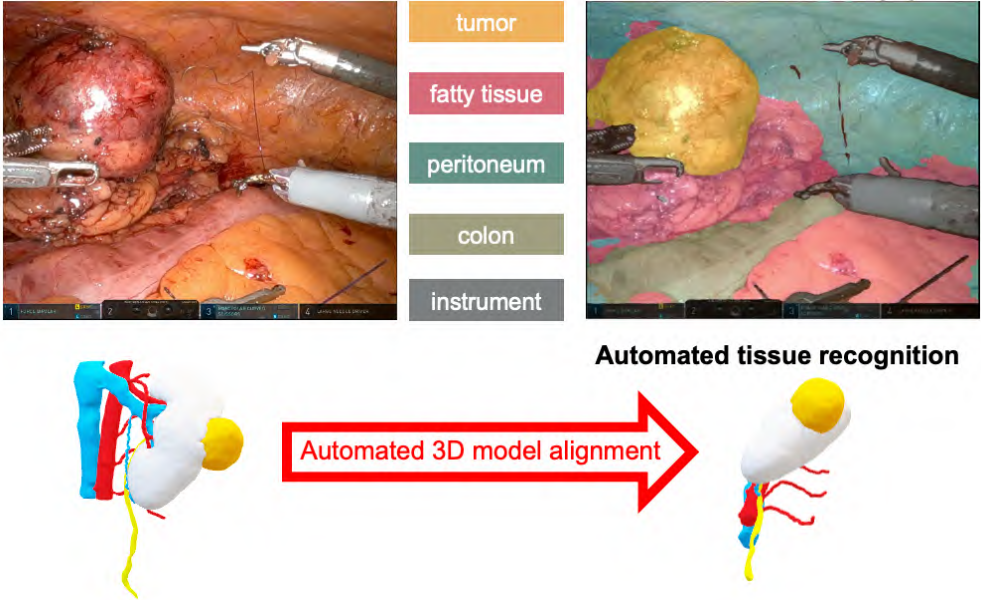


Figure 7.3: Automated surgical scene interpretation as an enabler for 3D model alignment during A.R. surgery. Left side: surgical scene as inputted into the segmentation algorithm. Right side: automated tissue recognition identifying the renal tumor. This allows the 3D model to already be partially aligned if stereo-reconstruction is performed on the pixels of interest.

7.2.2. Future Work

An anatomically correct alignment would subsequently also require the 3D models to deform and adjust to the corresponding and changing intraoperative anatomy as discussed in chapter 2. Both stereo reconstruction and deformable 3D meshes require significant graphical processing power. To this end, future work should investigate how dedicated hardware solutions like in Chapter 5.2. could be leveraged to perform these tasks in parallel. Other interesting research avenues, equally requiring extensive computational resources, include novel techniques that provide intra-operative generated sensor data and 3D information. Using intra-operative data automatically results in fewer registration errors when compared to preoperative meshes. This benefit increases as surgery progresses due to more extensive tissue deformations. Such novel techniques include on one hand the use of freehand ultrasound[278]. Ultrasound is often used during RAPN for endophytic lesions and A.R. is considered at present most promising for exactly these lesions. On the other hand, multi -or hyperspectral cameras are finding their way into the operating room and will provide additional sensor information, once more without additional tracking[279], [280].

Next to renal surgery, other soft tissue surgery can benefit from predictive 3D modeling and augmented reality. As such, we performed a first A.R. case for liver surgery (Chapter 5.2.), showing that the instrument de-occlusion technology transfers very well (Figure 7.4.A), but the floppiness of the liver poses new challenges for A.R., complementary to renal surgery [118]. Similarly, we performed first tests in lung segmentectomy planning to predict vascular domains in case of oncologic lung surgery (Figure 7.4.B) [281], where we note that the prediction is not yet physiologically correct and a more in depth exploration will be needed.

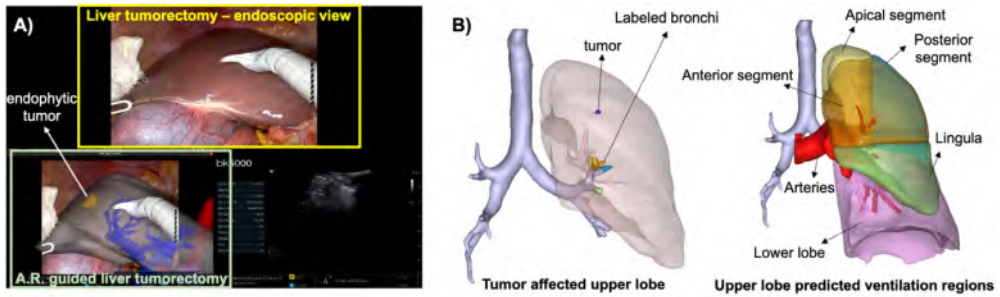


Figure 7.4: Technology transfer of 3D technology to other solid organs. A) Application of A.R. with instrument delineation during robotic liver surgery. B) Lung segmentectomy planning through allocation of ventilation volumes to bronchi.

Testing for Augmented Reality in lung surgery has the additional challenge that the lung is deflated during surgery which further increases complexity. To this extent, two proof-of-concept first-in-human A.R.-guided lung segmentectomies have been performed leveraging the A.R. technology developed in this thesis in conjunction with deformable lung models, developed outside this work. Figure 7.5. depicts the surgical console with a deflated lung in the top, where two segments are opened in a book-wise fashion. The bottom image shows the live TilePro input as provided to the console surgeon (A. Sadeghi – S. Siregar). The 3D model (in this case the arterial and vascular tree) deforms accordingly under manual digital stretching in a gaming engine (PulmoVR, Nieuw-Venep, The Netherlands).

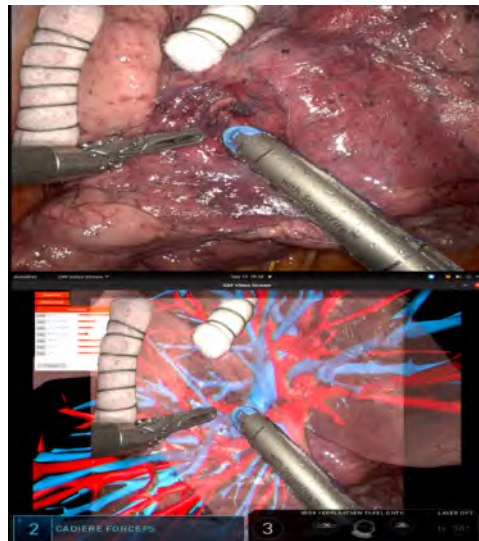


Figure 7.5: First-in-human A.R. guided lung segmentectomy, using real-time instrument segmentation in combination with deformable 3D lung models.

7.3. Surgical Phase Recognition

7.3.1. Steps Taken

When striving towards full A.R. automation, the system should be intelligent enough to know when to overlay which 3D model information. This is possible through automated surgical phase recognition. Compared to the longer timeline of achieving full A.R. automation, more imminent applications of automated surgical phase detection were provided in Chapter 6.2. These first steps include the facilitation of surgical video indexing, video revision and workflow optimization.

We performed a first exploration on offline automated phase detection during RAPN. To do so, we used 79 RAPN videos, annotated according to the 13 phases from Chapter 6.2. We trained a Resnet50 encoder followed by a Long Short Term Memory (LSTM) component, obtaining a 74% accuracy, 77.4% precision, 58.8% sensitivity and 97.7% specificity. Figure 7.6. depicts 2 procedures showing the annotated phases (ground truth) and the predictions.

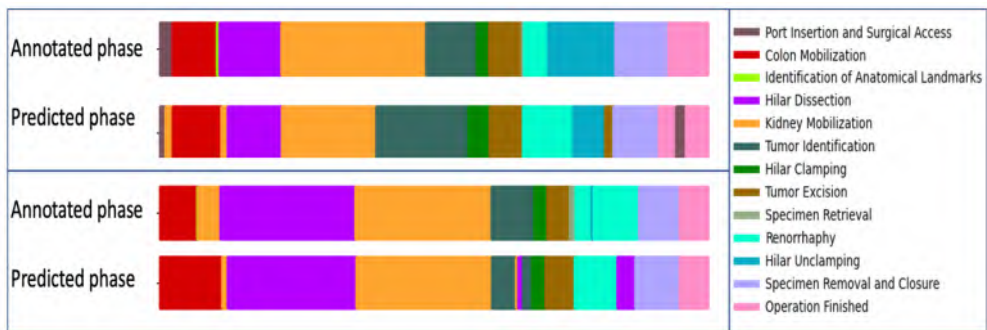


Figure 7.6: Automated surgical phase detection for RAPN. First result of a Resnet50 encoder + LSTM component, trained on the dataset as constructed in Chapter 6.2. Two procedures in the test set are depicted here, showing the ground truth data ('Annotated phase') as well as the predicted phase by the algorithm.

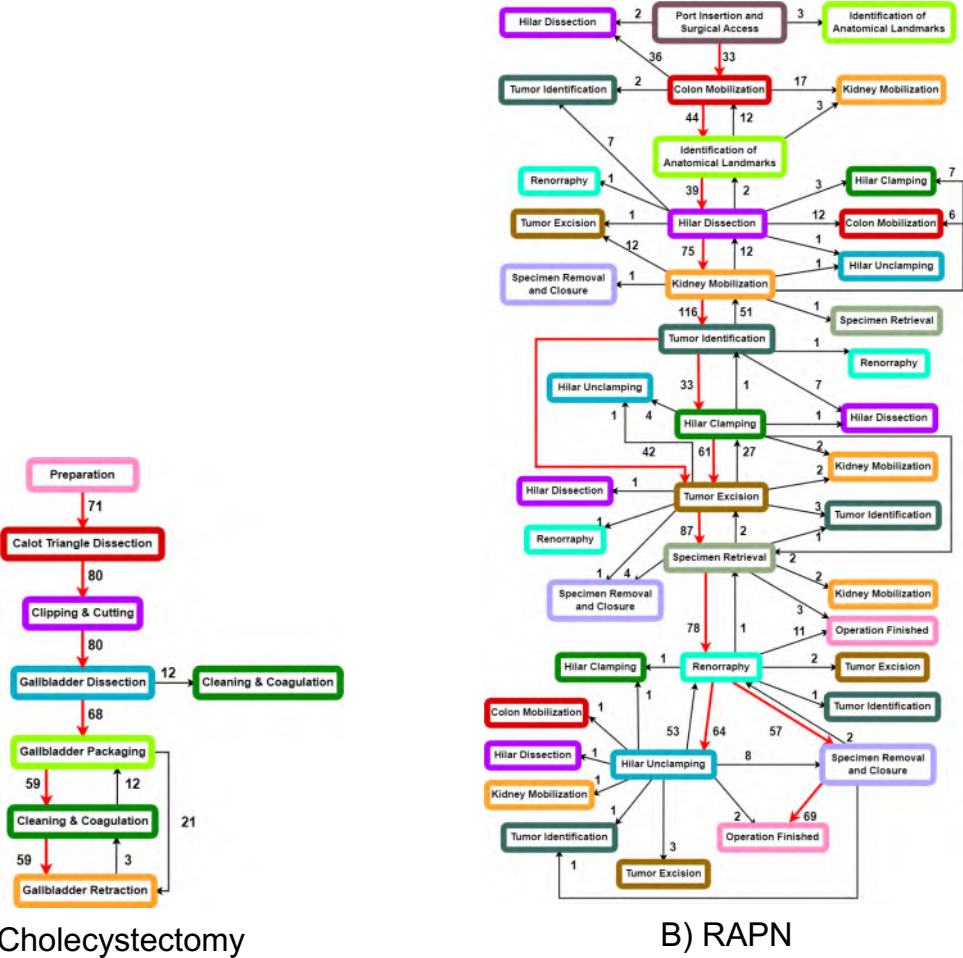
7.3.2. Future Work

While these results show that the system is able to grasp the broad surgical phase context in RAPN, there is clearly room for further improvement. This could for instance be achieved by adding tissue and instrument recognition in a multi-A.I. pipeline. This first exploratory approach above was aimed at keeping the computational demands low for possible real-time applications. The performance is also expected to be boosted by investigation of transformer-based architectures [282], which are increasingly being deployed or adapted for edge applications [283].

Another impactful way to improve performance is the expansion of labeled datasets. Collaborative video database expansion allows to gather data of rare events such as complications (bleeding, tumor lacerations,...). It also allows assessment of algorithmic robustness when different surgical techniques are used, which also adds to the explainability of these A.I. systems. Efficient anonymization as detailed in Chapter 4.1. can help in this data sharing.

We have already shown that instrument and phase detection are bothersome and time-consuming steps respectively in sections 4.2. and 6.2. When assessing purely temporal information, more complex procedures like RAPN require dedicated thought experiments to perform the labeling in a thoughtful but sufficiently granular approach. Figure 7.7 depicts a

side-by-side track of the opensource cholec80 dataset [170] with accompanying phase transitions, next to our 100 assessed RAPNs. The complexity and non-linearity of RAPN indeed requires the more granular annotations to be regrouped into larger blocks. It also shows that it is probably unsensible to compare algorithmic performances across procedures. Some procedures are simply too complex to aim for stellar classification results and a practical approach to detect the most clinically relevant steps might be the most practical way forward. Gathering insights into which steps are most clinically relevant requires further outcome based research which should primarily include surgical performance assessment, on a per phase basis [245].



video visualization when annotating phases on the device. We conducted a user survey across 3 robotic surgery fellows who each scored 6 identical 30 minutes snippets for surgical phase and error annotation, where 3 videos were scored on the html webpage whilst 3 videos were scored in the Stream Deck application. These preliminary results showed a non-inferiority on annotation quality, with an overall increased user satisfaction when using a dedicated annotation system. Figure 7.8.B demonstrates the results of the Satisfaction Survey.

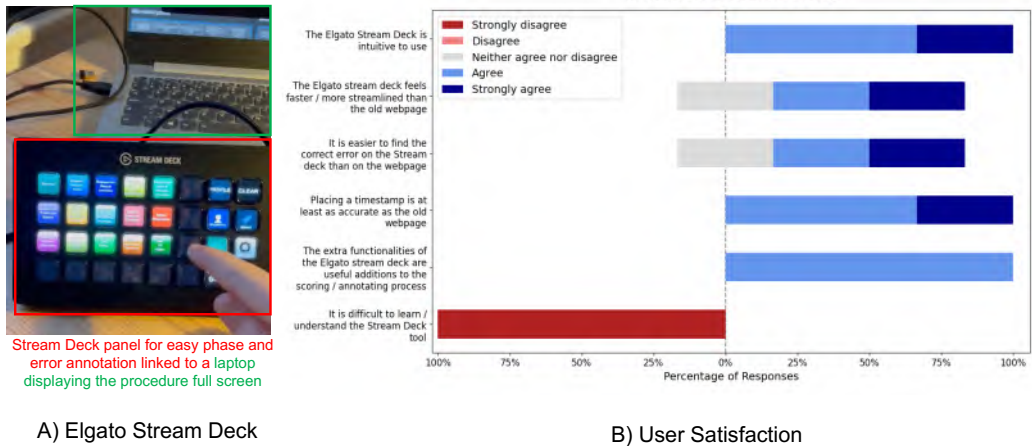


Figure 7.8: Facilitating temporal annotation through addition of an Elgato Stream Deck application. A) Setup with preprogrammed buttons for surgical error annotations. B) User satisfaction survey results.

7.4. Surgical Data Science & Surgical Fingerprints

7.4.1. Steps Taken

Phase information is crucial for holistic procedural understanding, and it is often considered a part of surgical data science. In contrast, surgical instrument usage provides insights during smaller temporal window than the durations. As such, the available datapoints per procedure are higher when compared to phase information alone. Surgical instrument detection has been shown to improve surgical phase recognition and helps in unravelling surgical action detection [262]. Integrating both to look for correlations in the long- and short-time window might likewise deliver new insights.

Figure 7.9. depicts an annotated RAPN procedure where both phase information and instrument usage are merged. Both information sources are ground truth data, obtained through manual labeling as elaborated upon in Chapter 4.2. Vertical blue lines depict the start of new surgical phases, as defined in Chapter 6.2. Some patterns are visible at first glance, e.g. hem-o-lok clips are omnipresent during the renorrhaphy phase. Purely visually, one can estimate the start and end of this phase. Likewise, vessel loops appear for the first time when handling the renal hilum. They are typically manipulated at the start of phases with vessel manipulations such as the hilar control or arterial clamping. This intuitively confirms that instrument usage can help in surgical phase detection, and the symbiosis is probably highest in lengthy complex procedures with plenty of instruments and variation. As a comparison, laparoscopic cholecystectomy is a short procedure generally using only 3 or 4 laparoscopic

instruments. This implies less instrument variation but even then, instrument recognition has still been instrumental for improvements in phase and action detection [262].

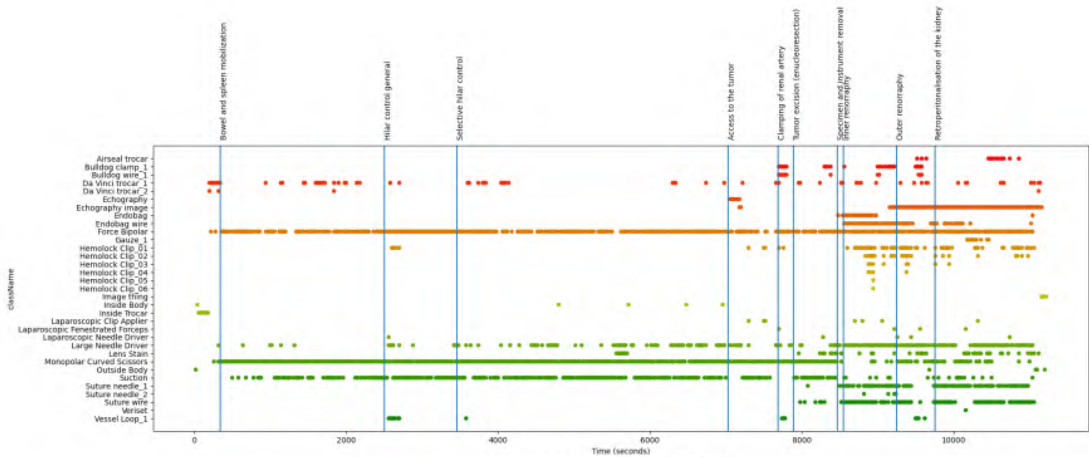


Figure 7.9: Surgical Fingerprint of a single RAPN procedure. Vertical lines show the different phases, whilst the points are annotations every 20 frames.

Up to present, automated instrument detection using deep learning systems has been successful for mainly large instruments. This work expands the scope to all non-organic items in the surgical field by providing lessons learned on the annotation process, hinting towards more efficient labeling practices, showing scalability across different robotic surgery domains as well as preparing a dataset release to help the community push the field forward. Preparing and annotating datasets is an iterative and time-intensive process which requires due diligence. Even with the best intentions, multiple layers of quality control and the use of active learning [285], handling the data for engineering purposes and assessing test set performances can still reveal data imperfections which might require resampling or annotation corrections. As such, the attentive reader might have noticed a slightly different dataset in Chapter 5.2 as compared to Chapters 4.3. and 6.1. These are due to small annotation errors retrieved whilst assessing test set performance during the engineering of Chapter 5.2. These errors were subsequently addressed. The dataset as investigated in Chapters 4.3. and 6.1. is the final dataset which will be publicly released. As such, this discrepancy is reflective of what is sometimes a seemingly never-ending process of perfecting annotations and should be kept in mind whilst building datasets.

7.4.2. Future Work

The aforementioned interaction and iteration between modeling and data preparation is a well-known phenomenon in data science and was already described over 20 years ago by Shearer [286]. Figure 7.10. depicts the CRoss-Industry Standard Process for Data Mining model (CRISP-DM) for best practices in data management and mining. Although developed by industry leaders, it translates well to surgical data science. We note the back and forth iteration between data preparation and modeling. When further assessing the model for surgical data science, the need for interdisciplinarity is apparent. Surgical experts should most probably take on a central role in the “Business Understanding” and “Data Understanding” part of the CRISP-

DM model. Subsequently, in collaboration with surgeons but led by engineers, “Data Preparation” and “Modeling” should take place. Finally, engineers and surgeons should jointly evaluate and deploy the technologies. This is also precisely how this PhD arose. The business and data understanding of Chapter 4 was mainly performed with collaborating clinicians, whilst the modeling in Chapters 5 and 6 were primarily engineering challenges. The subsequent evaluation and deployment of the technology were performed by clinicians in close collaboration with engineers.



Figure 7.10: CRoss-Industry Standard Process for Data Mining model (CRISP-DM) by Shearer, *Journal of Data Warehousing*, 2000 [286]

In contemplating the next pivotal future step for surgical A.I., perhaps the closest and potentially most transformative endeavor lies in the real-time identification and even prevention of surgical errors. Errors often include wrongly manipulated tissue, which is where full surgical scene assessments (both surgical scene and instrument understanding) again come in as enablers. While surgical error assessment for surgical training can be a bothersome and time-consuming job for busy clinicians, intelligent systems are expected to detect at least automatically some of the most basic surgical errors. As such, they can reduce the surgeon-assessor’s workload, while keeping the clinician in the loop as central coordinator. Furthermore, as alluded upon in Chapter 6.2., surgical errors are often dependent on surgical phases, which further highlights the need for a multimodal and comprehensive approach which combines temporal (phase detection) and spatial (scene understanding) information. If automated soft tissue surgical error detection can be achieved real-time, the next big leap might be surgical error prevention. Here, intelligent systems caution or prompt warnings of any experience level in real-time. Once we arrive at this level, automated robotic surgical assistance is expected to be just around the corner.

7.5. Closure

This work reveals several links integrating Virtual 3D models, Augmented Reality and Artificial Intelligence in one specific domain of surgical practice which is robot-assisted partial nephrectomy. Nonetheless, it shows that we are standing at the tipping point of a groundbreaking era where data-driven innovations will lead the way how surgical procedures can be optimized. After mastering anatomy, the introduction of artificial organs & prostheses and the shift towards minimal invasiveness, the fourth surgical revolution will be about digitization.

The integration of cutting-edge digitalization technologies such as robotics, artificial intelligence, and virtual reality is reshaping the surgical landscape. From a clinical point-of-view, we still await profound clinical evidence to be generated across surgical domains. Nonetheless, the first signs are hopeful, and the advancements and applications of surgical digitization are only expected to increase. As such, I firmly believe these transformative technologies are here to stay. Given the interlinking between domains, these technologies will show to have multiplicative rather than additive benefits, as was also clear throughout this work. As surgeons, we strive for objectivity to treat patients in the best possible way whilst navigating a healthcare system under financial pressure. The amalgamation of data analytics and surgical expertise should empower medical professionals to make data-driven, explainable decisions which enhance patient selection and surgical planning, reduce risks and improve patient safety. As engineers, we use the best available technologies to tackle these complex challenges and if technology is not available, we design it ourselves. Nonetheless, we should not forget that technology should serve a clinical need, rather than the other way around.

With continued research and development, surgical digitization will undoubtedly become an integral part of modern healthcare, paving the way for a more advanced and patient-centered care. As such, digitization and a more human surgical touch go hand in hand. It was exactly this human surgical touch which made me pursue a medical career. As we embark on this journey into the future, I am profoundly convinced that the key to unlocking further progress lies in the spirit of collaboration, much like the transformative partnerships that fueled the success of this PhD. It is through the collective exchanges of ideas, the synergy of diverse perspectives, and the unwavering support of mentors, colleagues, and stakeholders that we can continue to push boundaries and create meaningful impact in surgical digitization. As I move forward, I am committed to fostering collaboration and nurturing an environment where innovation thrives, recognizing that together, we can achieve far more than what is possible in isolation.

8. Summary

Partial nephrectomy is the gold standard treatment for small renal masses. This nephron sparing approach to renal cancer should be considered independent of the proposed surgical approach. Nonetheless, in recent years robotic surgery has taken on a dominant role because of both surgical technical useability as well as improved patient outcomes. Nephron-sparing surgery can be maximized amongst others using tumor enucleation or through the application of novel surgical techniques such as intra-arterial cooling. We described the first case series of robotic transcatheter applied intra-arterial cooling by arteriotomy and show that the technique is feasible in imperative indications. Bleeding risk remains a relevant issue during with nephron-sparing techniques with selective arterial clamping. Selective arterial clamping should be considered in difficult renal masses with long expected ischemia times, certainly in case of pre-existing renal function decline and in case of singular kidneys.

Novel technologies such as prediction of ischemic zones through patient-specific 3D models developed here might help mitigate this bleeding risk and inform surgeons on renal anatomy and function. Nevertheless, thorough algorithmic validation which include assessment of subsurface, intra-parenchymal predictions is required.

Augmented reality allows the integration of this 3D model information into the operative field and might guide the surgeon throughout the surgery without distractions. The current state of the art is however premature and main bottlenecks include instrument occlusion and correct 3D model alignment. We showed instrument occlusion to be solvable using real time deep learning based instrument segmentation. For this, we developed and deployed a dedicated combined hardware and software pipeline. The model alignment problem requires future work but first steps include proper surgical scene understanding which can likewise be facilitated through the use of artificial intelligence.

Automated surgical scene understanding entails a global temporal understanding which phase a procedure is in, as well as local frame by frame interpretation of visualized tissues, tools and actions. High quality and sufficiently large datasets are a prerequisite when building such deep learning based pipelines. Throughout this work, we share our lessons learned whilst building datasets for both instrument segmentation and surgical phase detection. We firstly demonstrate the surgical videos can be shared safely and anonymously. Secondly, we also show that surgical phase detection in itself can reveal possible clinical correlations and might even influence outcomes. Nonetheless, tapping into the real surgical data potential will require a true big data approach with large procedural numbers.

Automated surgical scene interpretation can also facilitate surgical guidance and teaching as it forms the basis for surgical error detection and possible even error prediction. Nonetheless, further research is required on building blocks such as phase detection, tool tissue interaction and action detection.

Lastly, we focused strongly on partial nephrectomy as a benchmark procedure. Plenty of other surgical domains can benefit from these technologies. As such, we performed first translational tests towards liver and lung surgery. Each surgery showed its own intricacies which require in depth optimization. As such, there is no one-size-fits-all formula for surgical digitalization. Nevertheless, the research opportunities are ample and the current optimism towards artificial intelligence developments might prove to be an important accelerator in bringing true clinical values in coming years.

9. Samenvatting

Partiële nefrectomie is de meest voorkomende niersparende heekkundige behandeling bij kleine niertumoren. Deze ingreep kan op diverse heekkundige manieren worden uitgevoerd, waarbij de laatste jaren robotchirurgie een dominante rol is gaan spelen omwille van minimaal invasieve aanpak waarbij de chirurg maximale vrijheid behoudt waarbij bovendien het herstel van de patiënt wordt bespoedigd.

Het niersparende aspect kan gemaximaliseerd worden door zogenaamde tumor enucleatie alsook door de toepassing van nieuwe chirurgische technieken zoals intra-arteriële koeling waarbij het metabolisme van de nier wordt gereduceerd door spoeling met ijswater. Zo beschrijft dit werk de techniek die transcutable intra-arteriële koeling via incisie in de arteria renalis mogelijk maakt. We tonen aan dat deze techniek maximale niersparing toestaat bij patiënten waar de nier anders volledig verloren kan gaan.

Bloedingsrisico blijft een inherent probleem bij niersparende heekkunde van complexe tumoren.

Complete arteria renalis afklemming is daar niet steeds mogelijk omdat lange klemmingstijd kan resulteren in permanente nierschade door langdurige deprivatatie van zuurstofrijk bloed (infarcering). Bij dergelijke grote of moeilijk gelegen tumoren, kan het aldus interessant zijn om slechts het deel van de nierperfusie af te sluiten die richting tumor gaat, de zogenaamde selectieve klemming. Bij patiënten met voorafbestaande chronische nierziekte of een unieke nier, vormt dergelijke selectieve arteriële klemming dan een gunstig alternatief. Dit werk ontwikkelde een nieuwe technologie die deze selectieve klemming op voorhand moet voorspellen op basis van patiënt-specifieke 3D modellen, afgeleid uit CT-scans. Zo moet het bloedingsrisico worden beperkt en wordt de chirurg maximaal geïnformeerd over de nieranatomie. Een grondige algoritmische validatie in een prospectieve studie is vereist om deze technologie verder te valideren en naar waarde te schatten.

Augmented reality staat toe om dergelijke 3D-modelinformatie instant in het operatieveld te projecteren en zo de chirurg tijdens de operatie te helpen. De huidige technologische stand van zaken techniek is echter prematuur waarbij de belangrijkste knelpunten de occlusie van instrumenten door de geprojecteerde informatie zijn, alsook de correcte uitlijning van 3D-modellen t.o.v. de anatomie tijdens de ingreep. Dit werk toont aan dat de instrument occlusie op te lossen valt met behulp van automatische instrumentherkenning d.m.v. artificiële intelligentie. Hiervoor werd een geïntegreerde software en hardware opstelling op punt gesteld die real-time instrument segmentatie uitvoert. In de correcte 3D-model uitlijning dienen nog grote stappen te worden gezet, doch een automatisch begrip van de chirurgische scène lijkt een goede eerste piste, dewelke eveneens kan worden gefaciliteerd d.m.v. artificiële intelligentie.

Het automatisch begrip van chirurgische scènes omvat zowel een globaal inzicht in welke fase de ingreep zich bevindt, evenals een lokale frame-per-frame interpretatie van gevisualiseerde weefsels, instrumenten en handelingen. Hoogwaardige en voldoende grote datasets zijn een nodige voorwaarde bij de ontwikkeling van dergelijke artificieel intelligente systemen. Zodoende bundelt dit werk ook onze inzichten m.b.t. het bouwen van datasets voor zowel instrument aflijning als chirurgische fasedetectie. We beschrijven eerst hoe chirurgische video's veilig en anoniem kunnen worden gedeeld. Vervolgens onderzoeken we hoe chirurgische fasedetectie op zich mogelijke klinische correlaties kan onthullen en zelfs de uitkomsten kan beïnvloeden. Doch, om het volwaardige chirurgische data potentieel te benutten, is een echte big data aanpak met waarschijnlijk duizenden procedures nodig.

Geautomatiseerde chirurgische scène interpretatie kan verder ook intra-operatieve ondersteuning faciliteren en vormt tevens de basis voor het opsporen en op lange termijn mogelijk zelfs voorkomen van chirurgische fouten. Huidige onderzoeksinspanningen dienen zich echter eerst nog te focussen op essentiële bouwstenen zoals fase-detectie en actieherkenning die video-interpretatie betrouwbaarder en robuuster moeten maken.

Tot slot richtte dit werk zich op partiële nefrectomie als centrale procedure. De concepten uit dit werk zijn uiteraard toepasbaar overheen chirurgische domeinen en zodoende werden ook de eerste translationele tests uitgevoerd voor lever- en longchirurgie. Elke chirurgische ingreep heeft echter zijn eigen bijzonderheden die een gerichte optimalisatie vereisen en er is op heden geen standaardformule voor chirurgische digitalisering.

Desalniettemin kan het huidige optimisme ten aanzien van artificiële intelligentie een gunstig klimaat vormen zodat deze technologie in de komende jaren een belangrijke katalysator vormt die translatie naar de klinische praktijk kan realiseren.

10. References

- [1] “ChatGPT,” *Openai.com*. [Online]. Available: <https://openai.com/blog/chatgpt>. [Accessed: 30-Oct-2023].
- [2] “DALL-E,” *Openai.com*. [Online]. Available: <https://openai.com/product/dall-e-2>. [Accessed: 30-Oct-2023].
- [3] “EU AI Act.” [Online]. Available: <https://www.europarl.europa.eu/news/en/headlines/society/20230601STO93804/eu-ai-act-first-regulation-on-artificial-intelligence>. [Accessed: 30-Oct-2023].
- [4] R. Schwendimann, C. Blatter, S. Dhaini, M. Simon, and D. Ausserhofer, “The occurrence, types, consequences and preventability of in-hospital adverse events - a scoping review,” *BMC Health Serv. Res.*, vol. 18, no. 1, p. 521, Jul. 2018.
- [5] J. W. Suliburk *et al.*, “Analysis of Human Performance Deficiencies Associated With Surgical Adverse Events,” *JAMA Netw Open*, vol. 2, no. 7, p. e198067, Jul. 2019.
- [6] S. Cheikh Youssef *et al.*, “Evolution of the digital operating room: the place of video technology in surgery,” *Langenbecks. Arch. Surg.*, vol. 408, no. 1, p. 95, Feb. 2023.
- [7] G. P. Mishra, S. Bhatnagar, and B. Singh, “Anatomical Variations of Upper Segmental Renal Artery and Clinical Significance,” *J. Clin. Diagn. Res.*, vol. 9, no. 8, pp. AC01-3, Aug. 2015.
- [8] S. Borojeni *et al.*, “Study of Renal and Kidney Tumor Vascularization Using Data from Preoperative Three-dimensional Arteriography Prior to Partial Nephrectomy,” *Eur Urol Focus*, vol. 6, no. 1, pp. 112–121, Jan. 2020.
- [9] J. Hyrtl, *Handbuch Der Topographischen Anatomie*. Sligo, Ireland: HardPress, 2019.
- [10] Brödel, *The Intrinsic Blood-Vessels of The Kidney and Their Significance In Nephrotomy*. Bull Johns Hopkins Hosp, 1901.
- [11] F. T. Graves, “The anatomy of the intrarenal arteries and its application to segmental resection of the kidney,” *Br. J. Surg.*, vol. 42, no. 172, pp. 132–139, Sep. 1954.
- [12] K. J. Weld, S. B. Bhayani, J. Belani, C. D. Ames, G. Hruby, and J. Landman, “Extrarenal vascular anatomy of kidney: Assessment of variations and their relevance to partial nephrectomy,” *Urology*, vol. 66, no. 5, pp. 985–989, Nov. 2005.
- [13] F. J. B. Sampaio and M. A. R. F. Passos, “Renal arteries: anatomic study for surgical and radiological practice,” *Surg. Radiol. Anat.*, vol. 14, no. 2, pp. 113–117, 1992.
- [14] F. J. B. Sampaio, “Renal anatomy: Endourologic Considerations,” in *Minimally Invasive Surgery Of The Kidney: A problem-oriented approach.*, vol. 27, 2000, pp. 585–607.
- [15] *EAU Guidelines. Edn. presented at the EAU Annual Congress Milan 2023. ISBN 978-94-92671-19-6.* EAU Guidelines Office, Arnhem, The Netherlands. <http://uroweb.org/guidelines/compilations-of-all-guidelines/>, 2023.
- [16] B. A. Urban, L. E. Ratner, and E. K. Fishman, “Three-dimensional Volume-rendered CT Angiography of the Renal Arteries and Veins: Normal Anatomy, Variants, and Clinical Applications 1 LEARNING OBJECTIVES FOR TEST 2 CME FEATURE,” *Radiographics*, vol. 21, pp. 373–386, 2001.

- [17] S. B. A. Koeppen BM, *Berne & Levy Physiology, Chapter 32 (Elements of Renal Function)*. Elsevier Health Sciences, 2009.
- [18] E. J. Johns and A. F. Ahmeda, "Renal Circulation."
- [19] M. A. Breshears and A. W. Confer, "The Urinary System," *Pathologic Basis of Veterinary Disease*, p. 617, 2017.
- [20] K. K. Upadhyay and D. M. Silverstein, "Renal development: a complex process dependent on inductive interaction," *Curr. Pediatr. Rev.*, vol. 10, no. 2, pp. 107–114, 2014.
- [21] E. Shapiro, D. A. Goldfarb, and M. L. Ritchey, "The congenital and acquired solitary kidney," *Rev. Urol.*, vol. 5, no. 1, pp. 2–8, 2003.
- [22] M. F. Schreuder and J. Nauta, "Prenatal programming of nephron number and blood pressure," *Kidney Int.*, vol. 72, pp. 265–268, 2007.
- [23] J. Smith, S. Howards, G. Preminger, and R. Dmochowski, Eds., *Hinman's Atlas of Urologic Surgery*, 4th Editio., vol. 49. 2019, p. 1008.
- [24] J. Furst and S. Kurra, "Adrenal Physiology," in *Surgical Endocrinopathies*, 2015, pp. 187–195.
- [25] I. M. Karam, A. Oliver, and J. Hubert, "Surgical Anatomy of Kidneys and Adrenals," in *Robotic Urology*, H. John and P. Wiklund, Eds. Cham: Springer International Publishing, 2018, pp. 63–70.
- [26] N. Horesh *et al.*, "Management of Pancreatic Injuries Following Nephrectomy," *Isr. Med. Assoc. J.*, vol. 22, no. 4, pp. 244–248, Apr. 2020.
- [27] J. K. Wang *et al.*, "Iatrogenic splenectomy during nephrectomy for renal tumors," *Int. J. Urol.*, vol. 20, no. 9, pp. 896–902, Sep. 2013.
- [28] K. Tan *et al.*, "Iatrogenic splenectomy during left nephrectomy: a single-institution experience of eight years," *Urol. Int.*, vol. 87, no. 1, pp. 59–63, 2011.
- [29] H. Fonouni *et al.*, "Hemostatic efficiency of modern topical sealants: Comparative evaluation after liver resection and splenic laceration in a swine model," *J. Biomed. Mater. Res. B Appl. Biomater.*, vol. 106, no. 3, pp. 1307–1316, Apr. 2018.
- [30] S. Jacob, *Human Anatomy*, 1st ed. Elsevier, 2007.
- [31] T. Klätte *et al.*, "A Literature Review of Renal Surgical Anatomy and Surgical Strategies for Partial Nephrectomy," *Eur. Urol.*, vol. 68, no. 6, pp. 980–992, 2015.
- [32] V. Macchi *et al.*, "Anatomical study of renal arterial vasculature and its potential impact on partial nephrectomy," *BJU Int.*, vol. 120, no. 1, pp. 83–91, Jul. 2017.
- [33] P. Shao *et al.*, "Precise segmental renal artery clamping under the guidance of dual-source computed tomography angiography during laparoscopic partial nephrectomy," *Eur. Urol.*, vol. 62, no. 6, pp. 1001–1008, 2012.
- [34] M. A. Bjurlin *et al.*, "Near-infrared fluorescence imaging: Emerging applications in robotic upper urinary tract surgery," *Eur. Urol.*, vol. 65, no. 4, pp. 793–801, 2014.
- [35] B. Sauer, M. Flocquet, T. Batch, A. Blum, and J. Hubert, "Vascular renal anatomy and the ureteropelvic junction: Preoperative multidetector CT scanning with split-bolus injection as a predictor of laparoscopic findings," *J. Endourol.*, vol. 22, no. 1, pp. 13–17, 2008.

- [36] A. Türkvatan, S. Akıncı, Ş. Yıldız, T. Ölçer, and T. Cumhuri, "Multidetector computed tomography for preoperative evaluation of vascular anatomy in living renal donors," *Surg. Radiol. Anat.*, vol. 31, no. 4, pp. 227–235, 2009.
- [37] U. Özkan, L. Oğuzkurt, F. Tercan, O. Kizilkiliç, Z. Koç, and N. Koca, "Renal artery origins and variations: Angiographic evaluation of 855 consecutive patients," *Diagn. Interv. Radiol.*, vol. 12, no. 4, pp. 183–186, 2006.
- [38] A. Türkvatan, M. Özdemir, T. Cumhuri, and T. Ölçer, "Multidetector CT angiography of renal vasculature: Normal anatomy and variants," *Eur. Radiol.*, vol. 19, no. 1, pp. 236–244, 2009.
- [39] A. J. Wein, *Campbell-Walsh Urology*, 9th ed. Elsevier Inc., 2007, p. 3323.
- [40] S. Kumar, Z. Neyaz, and A. Gupta, "The utility of 64 channel multidetector ct angiography for evaluating the renal vascular anatomy and possible variations: A pictorial essay," *Korean J. Radiol.*, vol. 11, no. 3, pp. 346–354, 2010.
- [41] K. Munnusamy *et al.*, "Variations in Branching Pattern of Renal Artery in Kidney Donors Using CT Angiography," *J. Clin. Diagn. Res.*, vol. 10, no. 3, pp. AC01-3, Mar. 2016.
- [42] O. C. Famurewa, C. M. Asaleye, B. O. Ibitoye, O. O. Ayoola, A. S. Aderibigbe, and T. A. Badmus, "Variations of renal vascular anatomy in a nigerian population: A computerized tomography studys," *Niger. J. Clin. Pract.*, vol. 21, no. 7, pp. 840–846, 2018.
- [43] C. F. de Mello Júnior, S. A. Araujo Neto, A. M. de Carvalho Junior, R. B. Rebouças, G. R. P. Negromonte, and C. D. de Oliveira, "Multidetector computed tomography angiography of the renal arteries: normal anatomy and its variations," *Radiologia Brasileira*, vol. 49, no. 3, pp. 190–195, 2016.
- [44] F. J. Sampaio and A. H. Aragão, "Anatomical relationship between the renal venous arrangement and the kidney collecting system," *J. Urol.*, vol. 144, no. 5, pp. 1089–1093, 1990.
- [45] S. S. Raman, S. Pojchamarnwiputh, K. Muangsomboon, P. G. Schulam, H. A. Gritsch, and D. S. K. Lu, "Surgically relevant normal and variant renal parenchymal and vascular anatomy in preoperative 16-MDCT evaluation of potential laparoscopic renal donors," *American Journal of Roentgenology*, vol. 188, no. 1, pp. 105–114, 2007.
- [46] A. Holden, A. Smith, P. Dukes, H. Pilmore, and M. Yasutomi, "Assessment of 100 live potential renal donors for laparoscopic nephrectomy with multi-detector row helical CT," *Radiology*, vol. 237, no. 3, pp. 973–980, 2005.
- [47] M. J. Truty and T. C. Bower, "Congenital Anomalies of the Inferior Vena Cava and Left Renal Vein: Implications during Open Abdominal Aortic Aneurysm Reconstruction," *Ann. Vasc. Surg.*, vol. 21, no. 2, pp. 186–197, 2007.
- [48] M. Elkoushy and S. Andonian, "Campbell-Walsh Urology: Surgical, Radiographic, and Endoscopic Anatomy of the Kidney and Ureter," 2015, pp. 967–977.
- [49] J. K. Anderson and J. Cadeddu, "Surgical Anatomy of the Retroperitoneum, Adrenals, Kidneys, and Ureters | Abdominal Key." [Online]. Available: <https://abdominalkey.com/surgical-anatomy-of-the-retroperitoneum-adrenals-kidneys-and-ureters/>.
- [50] G. E. Cacciamani *et al.*, "Impact of Surgical Factors on Robotic Partial Nephrectomy Outcomes: Comprehensive Systematic Review and Meta-Analysis," *J. Urol.*, vol. 200, no. 2, pp. 258–274, Aug. 2018.

- [51] C. A. Bravi *et al.*, "The IRON Study: Investigation of Robot-assisted Versus Open Nephron-sparing Surgery," *Eur Urol Open Sci*, vol. 49, pp. 71–77, Mar. 2023.
- [52] E. Ruiz Guerrero, A. V. O. Claro, M. J. Ledo Cepero, M. Soto Delgado, and J. L. Álvarez-Ossorio Fernández, "Robotic versus Laparoscopic Partial Nephrectomy in the New Era: Systematic Review," *Cancers*, vol. 15, no. 6, Mar. 2023.
- [53] G. G. Calpin, F. R. Ryan, F. T. McHugh, and B. B. McGuire, "Comparing the outcomes of open, laparoscopic and robot-assisted partial nephrectomy: a network meta-analysis," *BJU Int.*, May 2023.
- [54] A. Ingels *et al.*, "Comparison of open and robotic-assisted partial nephrectomy approaches using multicentric data (UroCCR-47 study)," *Sci. Rep.*, vol. 12, no. 1, p. 18981, Nov. 2022.
- [55] U. Capitanio *et al.*, "Epidemiology of Renal Cell Carcinoma," *European Urology*, vol. 75, no. 1. Elsevier B.V., pp. 74–84, 01-Jan-2019.
- [56] M. R. Cooperberg, K. Mallin, J. Ritchey, J. D. Villalta, P. R. Carroll, and C. J. Kane, "Decreasing size at diagnosis of stage 1 renal cell carcinoma: analysis from the National Cancer Data Base, 1993 to 2004," *J. Urol.*, vol. 179, no. 6, pp. 2131–2135, Jun. 2008.
- [57] R. L. Siegel, K. D. Miller, and A. Jemal, "Cancer Statistics, 2018."
- [58] B. C. Leibovich *et al.*, "Predicting oncologic outcomes in renal cell carcinoma after surgery," *Eur. Urol.*, vol. 73, no. 5, pp. 772–780, May 2018.
- [59] R. Bertolo *et al.*, "Resection Techniques During Robotic Partial Nephrectomy: A Systematic Review," *European Urology Open Science*, vol. 52, pp. 7–21, Jun. 2023.
- [60] R. H. Thompson *et al.*, "Renal function after partial nephrectomy: effect of warm ischemia relative to quantity and quality of preserved kidney," *Urology*, vol. 79, no. 2, pp. 356–360, Feb. 2012.
- [61] B. Nahar, A. Bhat, and D. J. Parekh, "Does every minute of renal ischemia still count in 2019? Unlocking the chains of a flawed thought process over five decades," *Eur. Urol. Focus*, vol. 5, no. 6, pp. 939–942, Nov. 2019.
- [62] D. J. Parekh *et al.*, "Tolerance of the human kidney to isolated controlled ischemia," *J. Am. Soc. Nephrol.*, vol. 24, no. 3, pp. 506–517, Feb. 2013.
- [63] A. Antonelli *et al.*, "Is off-clamp robot-assisted partial nephrectomy beneficial for renal function? Data from the CLOCK trial," *BJU Int.*, vol. 129, no. 2, pp. 217–224, Feb. 2022.
- [64] D. Cignoli *et al.*, "Risks and benefits of partial nephrectomy performed with limited or with zero ischaemia time," *BJU Int.*, Mar. 2023.
- [65] A. D. Antonelli *et al.*, "The role of warm ischemia time on functional outcomes after robotic partial nephrectomy: a radionuclide renal scan study from the clock randomized trial," *World J. Urol.*, vol. 41, no. 5, pp. 1337–1344, May 2023.
- [66] A. J. Hung, J. Cai, M. N. Simmons, and I. S. Gill, "'Trifecta' in partial nephrectomy," *J. Urol.*, vol. 189, no. 1, pp. 36–42, Jan. 2013.
- [67] M. Eid *et al.*, "Cinematic Rendering in CT: A Novel, Lifelike 3D Visualization Technique," *AJR Am. J. Roentgenol.*, vol. 209, no. 2, pp. 370–379, Aug. 2017.

- [68] T. J. van Oostenbrugge, J. J. Fütterer, and P. F. A. Mulders, "Diagnostic Imaging for Solid Renal Tumors: A Pictorial Review," *Kidney Cancer*, vol. 2, no. 2, pp. 79–93, Aug. 2018.
- [69] P. Ljung, J. Krüger, E. Groller, M. Hadwiger, C. D. Hansen, and A. Ynnerman, "State of the art in transfer functions for direct volume rendering," *Comput. Graph. Forum*, vol. 35, no. 3, pp. 669–691, Jun. 2016.
- [70] R. Kikinis, S. D. Pieper, and K. G. Vosburgh, "3D Slicer: A Platform for Subject-Specific Image Analysis, Visualization, and Clinical Support," in *Intraoperative Imaging and Image-Guided Therapy*, F. A. Jolesz, Ed. New York, NY: Springer New York, 2014, pp. 277–289.
- [71] J. A. Iglesias-Guitian, P. Mane, and B. Moon, "Real-Time Denoising of Volumetric Path Tracing for Direct Volume Rendering," *IEEE Trans. Vis. Comput. Graph.*, vol. 28, no. 7, pp. 2734–2747, Jul. 2022.
- [72] S. P. Rowe, A. R. Meyer, M. A. Gorin, P. T. Johnson, and E. K. Fishman, "3D CT of renal pathology: initial experience with cinematic rendering," *Abdom Radiol (NY)*, vol. 43, no. 12, pp. 3445–3455, Dec. 2018.
- [73] V. Ficarra *et al.*, "Preoperative aspects and dimensions used for an anatomical (PADUA) classification of renal tumours in patients who are candidates for nephron-sparing surgery," *Eur. Urol.*, vol. 56, no. 5, pp. 786–793, Nov. 2009.
- [74] A. Kutikov and R. G. Uzzo, "The R.E.N.A.L. nephrometry score: a comprehensive standardized system for quantitating renal tumor size, location and depth," *J. Urol.*, vol. 182, no. 3, pp. 844–853, Sep. 2009.
- [75] F. Porpiglia *et al.*, "Development and validation of 3D printed virtual models for robot-assisted radical prostatectomy and partial nephrectomy: urologists' and patients' perception," *World J. Urol.*, vol. 36, no. 2, pp. 201–207, Feb. 2018.
- [76] J. L. Silberstein, M. M. Maddox, P. Dorsey, A. Feibus, R. Thomas, and B. R. Lee, "Physical models of renal malignancies using standard cross-sectional imaging and 3-dimensional printers: a pilot study," *Urology*, vol. 84, no. 2, pp. 268–272, Aug. 2014.
- [77] G. E. Cacciamani *et al.*, "Impact of three-dimensional printing in urology: State of the art and future perspectives. A systematic review by ESUT-YAUWP group," *Eur. Urol.*, vol. 76, no. 2, pp. 209–221, Aug. 2019.
- [78] O. Ukimura, M. Nakamoto, and I. S. Gill, "Three-dimensional reconstruction of renovascular-tumor anatomy to facilitate zero-ischemia partial nephrectomy," *Eur. Urol.*, vol. 61, no. 1, pp. 211–217, Jan. 2012.
- [79] F. C. von Rundstedt, J. M. Scovell, S. Agrawal, J. Zaneveld, and R. E. Link, "Utility of patient-specific silicone renal models for planning and rehearsal of complex tumour resections prior to robot-assisted laparoscopic partial nephrectomy," *BJU Int.*, vol. 119, no. 4, pp. 598–604, 2017.
- [80] F. Porpiglia *et al.*, "Three-dimensional virtual imaging of renal tumours: a new tool to improve the accuracy of nephrometry scores," *BJU Int.*, vol. 124, no. 6, pp. 945–954, Dec. 2019.
- [81] N. Wake *et al.*, "3D printed renal cancer models derived from MRI data: application in pre-surgical planning," *Abdom. Radiol. (NY)*, vol. 42, no. 5, pp. 1501–1509, May 2017.
- [82] R. Bertolo *et al.*, "Expanding the Indications of Robotic Partial Nephrectomy for Highly Complex Renal Tumors: Urologists' Perception of the Impact of Hyperaccuracy Three-

Dimensional Reconstruction," *J. Laparoendosc. Adv. Surg. Tech. A*, vol. 29, no. 2, pp. 233–239, Feb. 2019.

[83] N. Wake *et al.*, "Patient-specific 3D printed and augmented reality kidney and prostate cancer models: impact on patient education," *3D Printing in Medicine*, vol. 5, no. 1, 2019.

[84] F. Piramide *et al.*, "Three-dimensional Model-assisted Minimally Invasive Partial Nephrectomy: A Systematic Review with Meta-analysis of Comparative Studies," *Eur Urol Oncol*, Oct. 2022.

[85] J. D. Shirk *et al.*, "Effect of 3-dimensional virtual reality models for surgical planning of robotic-assisted partial nephrectomy on surgical outcomes: A randomized clinical trial," *JAMA Netw. Open*, vol. 2, no. 9, p. e1911598, Sep. 2019.

[86] F. Porpiglia *et al.*, "Three-dimensional Augmented Reality Robot-assisted Partial Nephrectomy in Case of Complex Tumours (PADUA ≥ 10): A New Intraoperative Tool Overcoming the Ultrasound Guidance," *Eur. Urol.*, vol. 78, no. 2, pp. 229–238, Aug. 2020.

[87] I. S. Gill *et al.*, "'Zero ischemia' partial nephrectomy: Novel laparoscopic and robotic technique," *Eur. Urol.*, vol. 59, no. 1, pp. 128–134, 2011.

[88] G. Sharma *et al.*, "Off-clamp Versus On-clamp Robot-assisted Partial Nephrectomy: A Propensity-matched Analysis," *European Urology Oncology*, May 2023.

[89] A. Antonelli *et al.*, "Safety of on- vs off-clamp robotic partial nephrectomy: per-protocol analysis from the data of the CLOCK randomized trial," *World J. Urol.*, vol. 38, no. 5, pp. 1101–1108, May 2020.

[90] B. G. Anderson *et al.*, "Comparing off-clamp and on-clamp robot-assisted partial nephrectomy: A prospective randomized trial," *Urology*, vol. 126, pp. 102–109, Jan. 2019.

[91] I. S. Gill *et al.*, "Zero ischemia anatomical partial nephrectomy: a novel approach," *J. Urol.*, vol. 187, no. 3, pp. 807–814, Mar. 2012.

[92] M. S. Borofsky *et al.*, "Near-infrared fluorescence imaging to facilitate super-selective arterial clamping during zero-ischaemia robotic partial nephrectomy," *BJU Int.*, vol. 111, no. 4, pp. 604–610, Apr. 2013.

[93] F. Porpiglia, C. Fiori, E. Checcucci, D. Amparore, and R. Bertolo, "Hyperaccuracy three-dimensional reconstruction is able to maximize the efficacy of selective clamping during robot-assisted partial nephrectomy for complex renal masses," *Eur. Urol.*, vol. 74, no. 5, pp. 651–660, Nov. 2018.

[94] D. Amparore *et al.*, "Three-dimensional Virtual Models of the Kidney with Colored Perfusion Regions: A New Algorithm-based Tool for Optimizing the Clamping Strategy During Robot-assisted Partial Nephrectomy," *Eur. Urol.*, Apr. 2023.

[95] H. Baumert *et al.*, "Reducing warm ischaemia time during laparoscopic partial nephrectomy: a prospective comparison of two renal closure techniques," *Eur. Urol.*, vol. 52, no. 4, pp. 1164–1169, Oct. 2007.

[96] B. Peyronnet *et al.*, "Early unclamping technique during robot-assisted laparoscopic partial nephrectomy can minimise warm ischaemia without increasing morbidity," *BJU Int.*, vol. 114, no. 5, pp. 741–747, Nov. 2014.

[97] F. Becker *et al.*, "Assessing the impact of ischaemia time during partial nephrectomy," *Eur. Urol.*, vol. 56, no. 4, pp. 625–634, Oct. 2009.

- [98] I. S. Gill *et al.*, "Laparoscopic ice slush renal hypothermia for partial nephrectomy: the initial experience," *J. Urol.*, vol. 170, no. 1, pp. 52–56, Jul. 2003.
- [99] A. E. Canda *et al.*, "Robotic assisted partial nephrectomy with cold ischemia applying ice pieces and intraoperative frozen section evaluation of the mass: complete replication of open approach with advantages of minimally invasive surgery," *Cent European J Urol*, vol. 73, no. 2, pp. 234–235, Apr. 2020.
- [100] K. Kijvikai, D. P. Viprakasit, P. Milhoua, P. E. Clark, and S. D. Herrell, "A simple, effective method to create laparoscopic renal protective hypothermia with cold saline surface irrigation: clinical application and assessment," *J. Urol.*, vol. 184, no. 5, pp. 1861–1866, Nov. 2010.
- [101] D. S. Crain, C. R. Spencer, M. A. Favata, and C. L. Amling, "Transureteral saline perfusion to obtain renal hypothermia: potential application in laparoscopic partial nephrectomy," *JSLs*, vol. 8, no. 3, pp. 217–222, Jul-Sep 2004.
- [102] G. Janetschek, A. Abdelmaksoud, F. Bagheri, H. Al-Zahrani, K. Leeb, and M. Gschwendtner, "Laparoscopic partial nephrectomy in cold ischemia: renal artery perfusion," *J. Urol.*, vol. 171, no. 1, pp. 68–71, Jan. 2004.
- [103] M. Marberger and F. Eisenberger, "Regional hypothermia of the kidney: surface or transarterial perfusion cooling? A functional study," *J. Urol.*, vol. 124, no. 2, pp. 179–183, Aug. 1980.
- [104] F. Greco *et al.*, "Ischemia techniques in nephron-sparing surgery: A systematic review and Meta-analysis of surgical, oncological, and functional outcomes," *Eur. Urol.*, vol. 75, no. 3, pp. 477–491, Mar. 2019.
- [105] K. Decaestecker *et al.*, "Robot-assisted Kidney Autotransplantation: A Minimally Invasive Way to Salvage Kidneys," *Eur Urol Focus*, vol. 4, no. 2, pp. 198–205, Mar. 2018.
- [106] A. Minervini *et al.*, "Impact of resection technique on perioperative outcomes and surgical margins after partial nephrectomy for localized renal masses: A prospective multicenter study," *J. Urol.*, vol. 203, no. 3, pp. 496–504, Mar. 2020.
- [107] V. Vermooten, "Indications for conservative surgery in certain renal tumors: a study based on the growth pattern of the cell carcinoma," *J. Urol.*, vol. 64, no. 2, pp. 200–208, Aug. 1950.
- [108] A. Minervini and M. Carini, "Tumor enucleation is appropriate during partial nephrectomy," *Eur. Urol. Focus*, vol. 5, no. 6, pp. 923–924, Nov. 2019.
- [109] A. Minervini *et al.*, "Positive surgical margins and local recurrence after simple enucleation and standard partial nephrectomy for malignant renal tumors: systematic review of the literature and meta-analysis of prevalence," *Minerva Urol. Nefrol.*, vol. 69, no. 6, pp. 523–538, Dec. 2017.
- [110] A. Minervini *et al.*, "Tumor-parenchyma interface and long-term oncologic outcomes after robotic tumor enucleation for sporadic renal cell carcinoma," *Urol. Oncol.*, vol. 36, no. 12, p. 527.e1-527.e11, Dec. 2018.
- [111] G. N. Gupta, R. S. Boris, S. C. Campbell, and Z. Zhang, "Tumor enucleation for sporadic localized kidney cancer: Pro and con," *J. Urol.*, vol. 194, no. 3, pp. 623–625, Sep. 2015.

- [112] A. Minervini *et al.*, “Histopathological validation of the surface-intermediate-base margin score for standardized reporting of resection technique during nephron sparing surgery,” *J. Urol.*, vol. 194, no. 4, pp. 916–922, Oct. 2015.
- [113] L. Marconi, M. M. Desai, V. Ficarra, F. Porpiglia, and H. Van Poppel, “Renal preservation and partial nephrectomy: Patient and surgical factors,” *Eur. Urol. Focus*, vol. 2, no. 6, pp. 589–600, Dec. 2016.
- [114] A. Minervini, M. Carini, R. G. Uzzo, R. Campi, M. C. Smaldone, and A. Kutikov, “Standardized reporting of resection technique during nephron-sparing surgery: the surface-intermediate-base margin score,” *Eur. Urol.*, vol. 66, no. 5, pp. 803–805, Nov. 2014.
- [115] A. Khaddad *et al.*, “A survey of augmented reality methods to guide minimally invasive partial nephrectomy,” *World J. Urol.*, Jul. 2022.
- [116] S. Bernhardt, S. A. Nicolau, L. Soler, and C. Doignon, “The status of augmented reality in laparoscopic surgery as of 2016,” *Med. Image Anal.*, vol. 37, pp. 66–90, Apr. 2017.
- [117] C. Schneider, C. Nguan, M. Longpre, R. Rohling, and S. Salcudean, “Motion of the kidney between preoperative and intraoperative positioning,” *IEEE Transactions on Biomedical Engineering*, vol. 60, no. 6, pp. 1619–1627, 2013.
- [118] K. Chandelon *et al.*, “Kidney tracking for live augmented reality in stereoscopic minimally invasive partial nephrectomy,” *Computer Methods in Biomechanics and Biomedical Engineering: Imaging & Visualization*, vol. 11, no. 4, pp. 1251–1260, Jul. 2023.
- [119] F. Joeres, T. Mielke, and C. Hansen, “Laparoscopic augmented reality registration for oncological resection site repair,” *Int. J. Comput. Assist. Radiol. Surg.*, vol. 16, no. 9, pp. 1577–1586, Sep. 2021.
- [120] E. Wild *et al.*, “Robust augmented reality guidance with fluorescent markers in laparoscopic surgery,” *Int. J. Comput. Assist. Radiol. Surg.*, vol. 11, no. 6, pp. 899–907, Jun. 2016.
- [121] H. Zhou and J. Jagadeesan, “Real-Time Dense Reconstruction of Tissue Surface From Stereo Optical Video,” *IEEE Trans. Med. Imaging*, vol. 39, no. 2, pp. 400–412, Feb. 2020.
- [122] J. Seetohul, M. Shafiee, and K. Sirlantzis, “Augmented Reality (AR) for Surgical Robotic and Autonomous Systems: State of the Art, Challenges, and Solutions,” *Sensors*, vol. 23, no. 13, Jul. 2023.
- [123] Y. Wang, Y. Long, S. H. Fan, and Q. Dou, “Neural Rendering for Stereo 3D Reconstruction of Deformable Tissues in Robotic Surgery,” in *Medical Image Computing and Computer Assisted Intervention – MICCAI 2022*, 2022, pp. 431–441.
- [124] B. Kerbl, G. Kopanas, T. Leimkuehler, and G. Drettakis, “3D Gaussian Splatting for Real-Time Radiance Field Rendering,” *ACM Trans. Graph.*, vol. 42, no. 4, pp. 1–14, Jul. 2023.
- [125] M. Labrunie, D. Pizarro, and C. Tilmant, “Automatic 3D/2D deformable registration in minimally invasive liver resection using a mesh recovery network.” [Online]. Available: https://encov.ip.uca.fr/publications/pubfiles/2023_Labrunie_et_al_MIDL_network.pdf. [Accessed: 06-Sep-2023].
- [126] B. Ljungberg *et al.*, “European Association of Urology Guidelines on Renal Cell Carcinoma: The 2022 Update,” *Eur. Urol.*, vol. 82, no. 4, pp. 399–410, Oct. 2022.

- [127] F. Crocerossa *et al.*, “Estimated Glomerular Filtration Rate Decline at 1 Year After Minimally Invasive Partial Nephrectomy: A Multimodel Comparison of Predictors,” *Eur Urol Open Sci*, vol. 38, pp. 52–59, Apr. 2022.
- [128] L. Mutelica, P. Mouracadé, O. Kara, J. Dagenais, M. J. Maurice, and J. H. Kaouk, “No ischemia technique, parenchymal preservation and age are the most important determinants of renal function after partial nephrectomy,” *Prog. Urol.*, vol. 30, no. 1, pp. 3–11, Jan. 2020.
- [129] G. Di Lascio *et al.*, “Which factors can influence post-operative renal function preservation after nephron-sparing surgery for kidney cancer: a critical review,” *Cent European J Urol*, vol. 75, no. 1, pp. 14–27, Jan. 2022.
- [130] G. E. Cacciamani *et al.*, “Impact of renal hilar control on outcomes of robotic partial nephrectomy: Systematic review and cumulative meta-analysis,” *Eur. Urol. Focus*, vol. 5, no. 4, pp. 619–635, Jul. 2019.
- [131] J.-A. Long *et al.*, “Superselective Ischemia in Robotic Partial Nephrectomy Does Not Provide Better Long-term Renal Function than Renal Artery Clamping in a Randomized Controlled Trial (EMERALD): Should We Take the Risk?,” *Eur Urol Focus*, vol. 8, no. 3, pp. 769–776, May 2022.
- [132] L. Bianchi *et al.*, “Novel Volumetric and Morphological Parameters Derived from Three-dimensional Virtual Modeling to Improve Comprehension of Tumor’s Anatomy in Patients with Renal Cancer,” *Eur Urol Focus*, vol. 8, no. 5, pp. 1300–1308, Sep. 2022.
- [133] L. Bianchi *et al.*, “Interpreting nephrometry scores with three-dimensional virtual modelling for better planning of robotic partial nephrectomy and predicting complications,” *Urol. Oncol.*, vol. 39, no. 12, p. 836.e1-836.e9, Dec. 2021.
- [134] L. Bianchi *et al.*, “The impact of 3D digital reconstruction on the surgical planning of partial nephrectomy: A case-control study. Still time for a novel surgical trend?,” *Clin. Genitourin. Cancer*, vol. 18, no. 6, pp. e669–e678, Dec. 2020.
- [135] E. Checcucci *et al.*, “3D mixed reality holograms for preoperative surgical planning of nephron-sparing surgery: evaluation of surgeons’ perception,” *Minerva Urol Nephrol*, vol. 73, no. 3, pp. 367–375, Jun. 2021.
- [136] D. Amparore *et al.*, “Three-dimensional Virtual Models’ Assistance During Minimally Invasive Partial Nephrectomy Minimizes the Impairment of Kidney Function,” *Eur Urol Oncol*, vol. 5, no. 1, pp. 104–108, Feb. 2022.
- [137] T. Masago *et al.*, “The significance of predictable traumatic area by renorrhaphy in the prediction of postoperative ipsilateral renal function,” *Cent European J Urol*, vol. 71, no. 1, pp. 64–71, 2018.
- [138] S. Isotani *et al.*, “Feasibility and accuracy of computational robot-assisted partial nephrectomy planning by virtual partial nephrectomy analysis,” *Int. J. Urol.*, vol. 22, no. 5, pp. 439–446, May 2015.
- [139] C. Wang *et al.*, “Precise estimation of renal vascular dominant regions using spatially aware fully convolutional networks, tensor-cut and Voronoi diagrams,” *Comput. Med. Imaging Graph.*, vol. 77, p. 101642, Oct. 2019.
- [140] “Approval of Synapse 3D Liver and Kidney Analysis. Center for Devices and Radiological Health,” 2014. [Online]. Available: https://www.accessdata.fda.gov/cdrh_docs/pdf14/K142521.pdf. [Accessed: 30-Oct-2023].

- [141] G. Novara, S. La Falce, A. Kungulli, G. Gandaglia, V. Ficarra, and A. Mottrie, "Robot-assisted partial nephrectomy," *Int. J. Surg.*, vol. 36, no. Pt C, pp. 554–559, Dec. 2016.
- [142] P. Min, "Binvox 3D mesh voxelizer." [Online]. Available: <http://www.patrickmin.com/binvox>. [Accessed: 30-Oct-2023].
- [143] F. S. Nooruddin and G. Turk, "Simplification and repair of polygonal models using volumetric techniques," *IEEE Trans. Vis. Comput. Graph.*, vol. 9, no. 2, pp. 191–205, April–June 2003.
- [144] F. Porpiglia *et al.*, "The effects of warm ischaemia time on renal function after laparoscopic partial nephrectomy in patients with normal contralateral kidney," *World J. Urol.*, vol. 30, no. 2, pp. 257–263, Apr. 2012.
- [145] B. R. Lane, I. S. Gill, A. F. Fergany, B. T. Larson, and S. C. Campbell, "Limited warm ischemia during elective partial nephrectomy has only a marginal impact on renal functional outcomes," *J. Urol.*, vol. 185, no. 5, pp. 1598–1603, May 2011.
- [146] X. Rod *et al.*, "Impact of ischaemia time on renal function after partial nephrectomy: a systematic review," *BJU Int.*, vol. 118, no. 5, pp. 692–705, Nov. 2016.
- [147] R. H. Thompson *et al.*, "Every minute counts when the renal hilum is clamped during partial nephrectomy," *Eur. Urol.*, vol. 58, no. 3, pp. 340–345, Sep. 2010.
- [148] M. Menon *et al.*, "Robotic kidney transplantation with regional hypothermia: a step-by-step description of the Vattikuti Urology Institute-Medanta technique (IDEAL phase 2a)," *Eur. Urol.*, vol. 65, no. 5, pp. 991–1000, May 2014.
- [149] J. S. Taylor, "Kidney cooling in partial nephrectomy. Evaluation of a technique," *Urology*, vol. 5, no. 4, pp. 456–460, Apr. 1975.
- [150] F. Liu, H. Yuan, X. Li, X. Ma, and M. Wang, "Application of Hypothermic Perfusion via a Renal Artery Balloon Catheter During Robot-assisted Partial Nephrectomy and Effect on Renal Function," *Acad. Radiol.*, vol. 26, no. 8, pp. e196–e201, Aug. 2019.
- [151] S. Hruby, L. Lusuardi, S. Jeschke, and G. Janetschek, "Cooling mechanisms in laparoscopic partial nephrectomy: are really necessary?," *Arch. Esp. Urol.*, vol. 66, no. 1, pp. 139–145, Jan–Feb 2013.
- [152] M. Yin, R. T. Currin, X.-X. Peng, H. E. Mekeel, R. Schoonhoven, and J. J. Lemasters, "Different patterns of renal cell killing after warm and cold ischemia," *Ren. Fail.*, vol. 24, no. 2, pp. 147–163, Mar. 2002.
- [153] J. Steffens, U. Humke, M. Ziegler, and S. Siemer, "Partial nephrectomy with perfusion cooling for imperative indications: a 24-year experience," *BJU International*, vol. 96, no. 4, pp. 608–611, 2005.
- [154] J. E. Gschwend, R. de Petriconi, S. Maier, K. Kleinschmidt, and R. E. Hautmann, "Continuous in situ cold perfusion with histidine tryptophan ketoglutarate solution in nephron sparing surgery for renal tumors," *J. Urol.*, vol. 154, no. 4, pp. 1307–1311, Oct. 1995.
- [155] J. Simon, M. Meilinger, H. Lang, R. E. Hautmann, and R. de Petriconi, "Novel technique for in situ cold perfusion in laparoscopic partial nephrectomy," *Surg. Endosc.*, vol. 22, no. 10, pp. 2184–2189, Oct. 2008.

- [156] T. R. W. Herrmann, S. Kruck, and U. Nagele, "Transperitoneal in situ intraarterial cooling in laparoscopic partial nephrectomy," *World J. Urol.*, vol. 29, no. 3, pp. 337–342, Jun. 2011.
- [157] C. Van Praet, E. Lambert, L. Desender, B. Van Parys, C. Vanpeteghem, and K. Decaestecker, "Total Intracorporeal Robot Kidney Autotransplantation: Case Report and Description of Surgical Technique," *Front Surg*, vol. 7, p. 65, Dec. 2020.
- [158] A. Breda *et al.*, "Intracorporeal Versus Extracorporeal Robot-assisted Kidney Autotransplantation: Experience of the ERUS RAKT Working Group," *Eur. Urol.*, vol. 81, no. 2, pp. 168–175, Feb. 2022.
- [159] I. Verbakel *et al.*, "Pushing boundaries in extracorporeal Robot-Assisted Kidney Autotransplantation (eRAKAT): bench surgery for an oncologic partial nephrectomy in a patient with a solitary kidney," in *A joint meeting of the EAU Section for Urotechnology and the EAU Section of Urolithiasis*, 2022, vol. 39, pp. S44–S45.
- [160] A. West *et al.*, "Clinical outcomes of low-pressure pneumoperitoneum in minimally invasive urological surgery," *J. Robot. Surg.*, vol. 16, no. 5, pp. 1183–1192, Oct. 2022.
- [161] H. M. Hasson, "Open laparoscopy: a report of 150 cases," *J. Reprod. Med.*, vol. 12, no. 6, pp. 234–238, Jun. 1974.
- [162] E. H. Streeter, D. M. Little, D. W. Cranston, and P. J. Morris, "The urological complications of renal transplantation: a series of 1535 patients," *BJU Int.*, vol. 90, no. 7, pp. 627–634, Nov. 2002.
- [163] G. Sternbach, "Sven Ivar Seldinger: catheter introduction on a flexible leader," *J. Emerg. Med.*, vol. 8, no. 5, pp. 635–637, Sep-Oct 1990.
- [164] B. M. Benway, A. J. Wang, J. M. Cabello, and S. B. Bhayani, "Robotic partial nephrectomy with sliding-clip renorrhaphy: technique and outcomes," *Eur. Urol.*, vol. 55, no. 3, pp. 592–599, Mar. 2009.
- [165] D. Dindo, N. Demartines, and P.-A. Clavien, "Classification of surgical complications: a new proposal with evaluation in a cohort of 6336 patients and results of a survey," *Ann. Surg.*, vol. 240, no. 2, pp. 205–213, Aug. 2004.
- [166] P. De Backer *et al.*, "Surgical Phase Duration in Robot-Assisted Partial Nephrectomy: A Surgical Data Science Exploration for Clinical Relevance," Aug. 2023.
- [167] K. R. Henken, F. W. Jansen, J. Klein, L. P. S. Stassen, J. Dankelman, and J. J. van den Dobbelsteen, "Implications of the law on video recording in clinical practice," *Surg. Endosc.*, vol. 26, no. 10, pp. 2909–2916, Oct. 2012.
- [168] A. Schulze *et al.*, "Ensuring privacy protection in the era of big laparoscopic video data: development and validation of an inside outside discrimination algorithm (IODA)," *Surg. Endosc.*, May 2023.
- [169] E. Flouty, O. Zisimopoulos, and D. Stoyanov, "FaceOff: Anonymizing Videos in the Operating Rooms," in *OR 2.0 Context-Aware Operating Theaters, Computer Assisted Robotic Endoscopy, Clinical Image-Based Procedures, and Skin Image Analysis*, 2018, pp. 30–38.
- [170] A. P. Twinanda, S. Shehata, D. Mutter, J. Marescaux, M. de Mathelin, and N. Padoy, "EndoNet: A Deep Architecture for Recognition Tasks on Laparoscopic Videos," *arXiv [cs.CV]*, 09-Feb-2016.

- [171] J. A. Eckhoff *et al.*, “SAGES consensus recommendations on surgical video data use, structure, and exploration (for research in artificial intelligence, clinical quality improvement, and surgical education),” *Surg. Endosc.*, Jul. 2023.
- [172] B. Münzer, K. Schoeffmann, and L. Böszörményi, “Relevance Segmentation of Laparoscopic Videos,” in *2013 IEEE International Symposium on Multimedia*, 2013, pp. 84–91.
- [173] A. P. Twinanda, J. Marescaux, M. De Mathelin, and N. Padoy, “Towards Better Laparoscopic Video Database Organization by Automatic Surgery Classification,” in *Information Processing in Computer-Assisted Interventions*, 2014, pp. 186–195.
- [174] M. Zohar, O. Bar, D. Neimark, G. D. Hager, and D. Asselmann, “Accurate Detection of Out of Body Segments in Surgical Video using Semi-Supervised Learning.”
- [175] J. L. Lavanchy, A. Vardazaryan, P. Mascagni, AI4SafeChole Consortium, D. Mutter, and N. Padoy, “Preserving privacy in surgical video analysis using a deep learning classifier to identify out-of-body scenes in endoscopic videos,” *Sci. Rep.*, vol. 13, no. 1, p. 9235, Jun. 2023.
- [176] R. Farinha *et al.*, “Potential Contenders for the Leadership in Robotic Surgery,” *J. Endourol.*, vol. 36, no. 3, pp. 317–326, Mar. 2022.
- [177] C. A. Bravi *et al.*, “Robot-assisted Radical Prostatectomy with the Novel Hugo Robotic System: Initial Experience and Optimal Surgical Set-up at a Tertiary Referral Robotic Center,” *Eur. Urol.*, vol. 82, no. 2, pp. 233–237, Aug. 2022.
- [178] B. C. Thomas *et al.*, “Preclinical Evaluation of the Versius Surgical System, a New Robot-assisted Surgical Device for Use in Minimal Access Renal and Prostate Surgery,” *Eur Urol Focus*, vol. 7, no. 2, pp. 444–452, Mar. 2021.
- [179] J. Kaouk, J. Garisto, and R. Bertolo, “Robotic Urologic Surgical Interventions Performed with the Single Port Dedicated Platform: First Clinical Investigation,” *Eur. Urol.*, vol. 75, no. 4, pp. 684–691, Apr. 2019.
- [180] K. He, X. Zhang, S. Ren, and J. Sun, “Deep Residual Learning for Image Recognition,” in *2016 IEEE Conference on Computer Vision and Pattern Recognition (CVPR)*, 2016, pp. 770–778.
- [181] J. M. Johnson and T. M. Khoshgoftaar, “Survey on deep learning with class imbalance,” *Journal of Big Data*, vol. 6, no. 1, pp. 1–54, Mar. 2019.
- [182] “NVIDIA CLARA AGX DEVELOPER KIT FOR AI-ENABLED MEDICAL DEVICES,” <https://resources.nvidia.com/en-us-enabling-smart-hospitals-ai-ep/nvidia-clara-agx-dev?lx=kwljje5&xs=301547>. .
- [183] “DELTA-12G-ELP-KEY 11,” <https://www.deltacast.tv/products/developer-products/sdi-capture-cards/delta-12g-elp-key-11>. .
- [184] T. J. Loftus *et al.*, “Executive summary of the artificial intelligence in surgery series,” *Surgery*, vol. 171, no. 5, pp. 1435–1439, May 2022.
- [185] A. A. Shvets, A. Rakhlin, A. A. Kalinin, and V. I. Iglovikov, “Automatic Instrument Segmentation in Robot-Assisted Surgery using Deep Learning,” in *2018 17th IEEE International Conference on Machine Learning and Applications (ICMLA)*, 2018, pp. 624–628.
- [186] O. R. Meireles *et al.*, “SAGES consensus recommendations on an annotation framework for surgical video,” *Surg. Endosc.*, vol. 35, no. 9, pp. 4918–4929, Sep. 2021.

- [187] T. M. Ward *et al.*, “Computer vision in surgery,” *Surgery*, vol. 169, no. 5, pp. 1253–1256, May 2021.
- [188] T. M. Ward, D. M. Fer, Y. Ban, G. Rosman, O. R. Meireles, and D. A. Hashimoto, “Challenges in surgical video annotation,” *Comput Assist Surg (Abingdon)*, vol. 26, no. 1, pp. 58–68, Dec. 2021.
- [189] M. Allan *et al.*, “2018 Robotic Scene Segmentation Challenge,” *arXiv [cs.CV]*, 30-Jan-2020.
- [190] L. Maier-Hein *et al.*, “Can masses of non-experts train highly accurate image classifiers? A Crowdsourcing Approach to Instrument Segmentation in Laparoscopic Images,” *Med Image Comput Comput Assist Interv*, vol. 17(Pt 2), pp. 438–445, 2014.
- [191] H. F. Fuchs, D. T. Müller, J. M. Leers, W. Schröder, and C. J. Bruns, “Modular step-up approach to robot-assisted transthoracic esophagectomy-experience of a German high volume center,” *Transl Gastroenterol Hepatol*, vol. 4, p. 62, Aug. 2019.
- [192] D. A. Hashimoto, G. Rosman, and O. R. Meireles, *Artificial Intelligence in Surgery: Understanding the Role of AI in Surgical Practice*. McGraw-Hill Education, 2021.
- [193] L. Maier-Hein *et al.*, “Why rankings of biomedical image analysis competitions should be interpreted with care,” *Nat. Commun.*, vol. 9, no. 1, p. 5217, Dec. 2018.
- [194] A. S. Kornilov and I. V. Safonov, “An Overview of Watershed Algorithm Implementations in Open Source Libraries,” *Journal of Imaging*, vol. 4, no. 10, p. 123, Oct. 2018.
- [195] A. Reinke *et al.*, “Common Limitations of Image Processing Metrics: A Picture Story,” *arXiv [eess.IV]*, 12-Apr-2021.
- [196] L.-C. Chen, Y. Zhu, G. Papandreou, F. Schroff, and H. Adam, “Encoder-Decoder with Atrous Separable Convolution for Semantic Image Segmentation,” *arXiv [cs.CV]*, Feb. 2018.
- [197] T. Roß *et al.*, “Comparative validation of multi-instance instrument segmentation in endoscopy: Results of the ROBUST-MIS 2019 challenge,” *Med. Image Anal.*, vol. 70, p. 101920, May 2021.
- [198] L. Maier-Hein *et al.*, “Heidelberg Colorectal Data Set for Surgical Data Science in the Sensor Operating Room,” *arXiv [cs.CV]*, 07-May-2020.
- [199] M. M. Rahman and D. N. Davis, “Addressing the class imbalance problem in medical datasets,” *Int. J. Mach. Learn. Comput.*, pp. 224–228, 2013.
- [200] S. Madad Zadeh *et al.*, “SurgAI: deep learning for computerized laparoscopic image understanding in gynaecology,” *Surg. Endosc.*, vol. 34, no. 12, pp. 5377–5383, Dec. 2020.
- [201] P. Mascagni *et al.*, “Artificial Intelligence for Surgical Safety: Automatic Assessment of the Critical View of Safety in Laparoscopic Cholecystectomy Using Deep Learning,” *Ann. Surg.*, vol. 275, no. 5, pp. 955–961, May 2022.
- [202] A. Danzer, T. Griebel, M. Bach, and K. Dietmayer, “2D Car Detection in Radar Data with PointNets,” pp. 61–66, Oct. 2019.
- [203] “Surgical data science – from concepts toward clinical translation,” *Med. Image Anal.*, vol. 76, p. 102306, Feb. 2022.
- [204] M. Rodrigues, M. Mayo, and P. Patros, “Surgical Tool Datasets for Machine Learning Research: A Survey,” *Int. J. Comput. Vis.*, vol. 130, no. 9, pp. 2222–2248, Sep. 2022.

- [205] L. Maier-Hein *et al.*, “Surgical data science for next-generation interventions,” *Nat Biomed Eng*, vol. 1, no. 9, pp. 691–696, Sep. 2017.
- [206] K. Lam *et al.*, “A Delphi consensus statement for digital surgery,” *NPJ Digit Med*, vol. 5, no. 1, p. 100, Jul. 2022.
- [207] B. van Amsterdam *et al.*, “Gesture Recognition in Robotic Surgery With Multimodal Attention,” *IEEE Trans. Med. Imaging*, vol. 41, no. 7, pp. 1677–1687, Jul. 2022.
- [208] T. Ross *et al.*, “Robust Medical Instrument Segmentation Challenge 2019,” *arXiv [cs.CV]*, 23-Mar-2020.
- [209] H. Al Hajj *et al.*, “CATARACTS: Challenge on automatic tool annotation for cataRACT surgery,” *Med. Image Anal.*, vol. 52, pp. 24–41, Feb. 2019.
- [210] M. Allan *et al.*, “2017 Robotic Instrument Segmentation Challenge,” *arXiv*, pp. 1–14, 2019.
- [211] M. Carstens *et al.*, “The Dresden Surgical Anatomy Dataset for Abdominal Organ Segmentation in Surgical Data Science,” *Sci Data*, vol. 10, no. 1, p. 3, Jan. 2023.
- [212] V. S. Bawa *et al.*, “The SARAS Endoscopic Surgeon Action Detection (ESAD) dataset: Challenges and methods,” *arXiv [cs.CV]*, Apr. 2021.
- [213] X. Wang, “Laplacian operator-based edge detectors,” *IEEE Trans. Pattern Anal. Mach. Intell.*, vol. 29, no. 5, pp. 886–890, May 2007.
- [214] S. Roberts *et al.*, “‘Augmented reality’ applications in urology: a systematic review,” *Minerva Urol Nephrol*, vol. 74, no. 5, pp. 528–537, Oct. 2022.
- [215] F. Piramide *et al.*, “Augmented reality 3D robot-assisted partial nephrectomy: Tips and tricks to improve surgical strategies and outcomes,” *Urology Video Journal*, vol. 13, no. 100137, p. 100137, Mar. 2022.
- [216] D. Amparore *et al.*, “Indocyanine Green Drives Computer Vision Based 3D Augmented Reality Robot Assisted Partial Nephrectomy: The Beginning of ‘Automatic’ Overlapping Era,” *Urology*, vol. 164, pp. e312–e316, Jun. 2022.
- [217] A. Piana *et al.*, “Three-dimensional augmented reality-guided robotic-assisted kidney transplantation: Breaking the limit of atheromatic plaques,” *Eur. Urol.*, vol. 82, no. 4, pp. 419–426, Oct. 2022.
- [218] R. Schiavina *et al.*, “Augmented reality to guide selective clamping and tumor dissection during robot-assisted partial nephrectomy: A preliminary experience,” *Clin. Genitourin. Cancer*, vol. 19, no. 3, pp. e149–e155, Jun. 2021.
- [219] B. Acidi, M. Ghallab, S. Cotin, E. Vibert, and N. Golse, “Augmented reality in liver surgery,” *J. Visc. Surg.*, vol. 160, no. 2, pp. 118–126, Apr. 2023.
- [220] L. Qian, J. Y. Wu, S. P. DiMaio, N. Navab, and P. Kazanzides, “A Review of Augmented Reality in Robotic-Assisted Surgery,” *IEEE Transactions on Medical Robotics and Bionics*, vol. 2, no. 1, pp. 1–16, Feb. 2020.
- [221] R. Suzuki, A. Karim, T. Xia, H. Hedayati, and N. Marquardt, “Augmented Reality and Robotics: A Survey and Taxonomy for AR-enhanced Human-Robot Interaction and Robotic Interfaces,” in *Proceedings of the 2022 CHI Conference on Human Factors in Computing Systems*, New Orleans, LA, USA, 2022, pp. 1–33.

- [222] J. Fischer, D. Bartz, and W. Straßer, "Occlusion handling for medical augmented reality using a volumetric phantom model," in *Proceedings of the ACM symposium on Virtual reality software and technology*, Hong Kong, 2004, pp. 174–177.
- [223] O. Kutter *et al.*, "Real-time Volume Rendering for High Quality Visualization in Augmented Reality," 2008.
- [224] R. Frikha, R. Ejbali, and M. Zaied, "Handling occlusion in Augmented Reality surgical training based instrument tracking," in *2016 IEEE/ACS 13th International Conference of Computer Systems and Applications (AICCSA)*, 2016, pp. 1–5.
- [225] T.-Y. Lin, P. Dollár, R. Girshick, K. He, B. Hariharan, and S. Belongie, "Feature Pyramid Networks for Object Detection," in *2017 IEEE Conference on Computer Vision and Pattern Recognition (CVPR)*, 2017, pp. 936–944.
- [226] M. Tan and Q. Le, "EfficientNetV2: Smaller Models and Faster Training," in *Proceedings of the 38th International Conference on Machine Learning*, 18–24 Jul 2021, vol. 139, pp. 10096–10106.
- [227] "NVIDIA TensorRT." [Online]. Available: <https://developer.nvidia.com/tensorrt>. [Accessed: 30-Oct-2023].
- [228] "NVIDIA Nsight Systems." [Online]. Available: <https://docs.nvidia.com/nsight-systems/index.html>. [Accessed: 31-Oct-2023].
- [229] M. Hwang *et al.*, "Efficiently calibrating cable-driven surgical robots with RGBD fiducial sensing and recurrent neural networks," *IEEE Robot. Autom. Lett.*, vol. 5, no. 4, pp. 5937–5944, Oct. 2020.
- [230] D. Bouget, M. Allan, D. Stoyanov, and P. Jannin, "Vision-based and marker-less surgical tool detection and tracking: a review of the literature," *Med. Image Anal.*, vol. 35, pp. 633–654, 2017.
- [231] L. C. Garcia-Peraza-Herrera *et al.*, "ToolNet: Holistically-nested real-time segmentation of robotic surgical tools," *Rep. U. S.*, vol. 2017-Septe, pp. 5717–5722, 2017.
- [232] S. Bodenstedt *et al.*, "Comparative evaluation of instrument segmentation and tracking methods in minimally invasive surgery," *arXiv [cs.CV]*, 07-May-2018.
- [233] L. Tanzi, P. Piazzolla, F. Porpiglia, and E. Vezzetti, "Real - time deep learning semantic segmentation during intra - operative surgery for 3D augmented reality assistance," *Int. J. Comput. Assist. Radiol. Surg.*, no. 0123456789, 2021.
- [234] "PyTorch Segmentation models." [Online]. Available: https://github.com/qubvel/segmentation_models.pytorch. [Accessed: 02-Nov-2023].
- [235] T. Akiba, S. Sano, T. Yanase, T. Ohta, and M. Koyama, "Optuna: A Next-generation Hyperparameter Optimization Framework," *arXiv [cs.LG]*, 25-Jul-2019.
- [236] L. Maier-Hein *et al.*, "Metrics reloaded: Recommendations for image analysis validation," *arXiv [cs.CV]*, 03-Jun-2022.
- [237] B. Zhou and P. Krähenbühl, "Cross-view Transformers for real-time Map-view Semantic Segmentation," in *2022 IEEE/CVF Conference on Computer Vision and Pattern Recognition (CVPR)*, 2022, pp. 13750–13759.

- [238] G. Xu, J. Li, G. Gao, H. Lu, J. Yang, and D. Yue, "Lightweight real-time semantic segmentation network with efficient Transformer and CNN," *arXiv [cs.CV]*, 21-Feb-2023.
- [239] J. Jain, J. Li, M. T. Chiu, A. Hassani, N. Orlov, and H. Shi, *OneFormer: [CVPR 2023] OneFormer: One Transformer to Rule Universal Image Segmentation*. Github.
- [240] V. Celentano *et al.*, "Use of laparoscopic videos amongst surgical trainees in the United Kingdom," *Surgeon*, vol. 17, no. 6, pp. 334–339, Dec. 2019.
- [241] P. Mota, N. Carvalho, E. Carvalho-Dias, M. João Costa, J. Correia-Pinto, and E. Lima, "Video-Based Surgical Learning: Improving Trainee Education and Preparation for Surgery," *J. Surg. Educ.*, vol. 75, no. 3, pp. 828–835, May-Jun 2018.
- [242] J. M. Abdelsattar *et al.*, "Do You See What I See? How We Use Video as an Adjunct to General Surgery Resident Education," *J. Surg. Educ.*, vol. 72, no. 6, pp. e145-50, Oct. 2015.
- [243] T. R. Grenda, J. C. Pradarelli, and J. B. Dimick, "Using Surgical Video to Improve Technique and Skill," *Ann. Surg.*, vol. 264, no. 1, pp. 32–33, Jul. 2016.
- [244] R. Farinha *et al.*, "International expert consensus on metric-based characterization of robot-assisted partial nephrectomy," *Eur. Urol. Focus*, vol. 9, no. 2, pp. 388–395, Mar. 2023.
- [245] R. Farinha *et al.*, "Objective assessment of intraoperative skills for robot-assisted partial nephrectomy (RAPN)," *J. Robot. Surg.*, Jan. 2023.
- [246] C. J. R. Schlick, K. Y. Bilimoria, and J. J. Stulberg, "Video-Based Feedback for the Improvement of Surgical Technique: A Platform for Remote Review and Improvement of Surgical Technique," *JAMA Surg.*, vol. 155, no. 11, pp. 1078–1079, Nov. 2020.
- [247] S. Erridge, D. K. T. Yeung, H. R. H. Patel, and S. Purkayastha, "Telementoring of Surgeons: A Systematic Review," *Surg. Innov.*, vol. 26, no. 1, pp. 95–111, Feb. 2019.
- [248] D. S. Keller, R. C. Grossman, and D. C. Winter, "Choosing the new normal for surgical education using alternative platforms," *Surgery*, vol. 38, no. 10, pp. 617–622, Oct. 2020.
- [249] S. Balvardi *et al.*, "The association between video-based assessment of intraoperative technical performance and patient outcomes: a systematic review," *Surg. Endosc.*, vol. 36, no. 11, pp. 7938–7948, Nov. 2022.
- [250] A. Langerman and T. P. Grantcharov, "Are We Ready for Our Close-up?: Why and How We Must Embrace Video in the OR," *Ann. Surg.*, vol. 266, no. 6, pp. 934–936, Dec. 2017.
- [251] M. F. Zeeshan, A. E. Dembe, E. E. Seiber, and B. Lu, "Incidence of adverse events in an integrated US healthcare system: a retrospective observational study of 82,784 surgical hospitalizations," *Patient Saf. Surg.*, vol. 8, no. 1, p. 23, May 2014.
- [252] C. R. Garrow *et al.*, "Machine Learning for Surgical Phase Recognition," *Ann. Surg.*, vol. 273, no. 4, pp. 684–693, 2021.
- [253] B. Gibaud *et al.*, "Toward a standard ontology of surgical process models," *Int. J. Comput. Assist. Radiol. Surg.*, vol. 13, no. 9, pp. 1397–1408, Sep. 2018.
- [254] J. L. Lavanchy, C. Gonzalez, H. Kassem, P. C. Nett, D. Mutter, and N. Padoy, "Proposal and multicentric validation of a laparoscopic Roux-en-Y gastric bypass surgery ontology," *Surg. Endosc.*, vol. 37, no. 3, pp. 2070–2077, Mar. 2023.

- [255] A. Mottrie *et al.*, "Objective assessment of intraoperative skills for robot-assisted radical prostatectomy (RARP): results from the ERUS Scientific and Educational Working Groups Metrics Initiative," *BJU Int.*, vol. 128, no. 1, pp. 103–111, Jul. 2021.
- [256] E. Mazzone *et al.*, "A Systematic Review and Meta-analysis on the Impact of Proficiency-based Progression Simulation Training on Performance Outcomes," *Ann. Surg.*, vol. 274, no. 2, pp. 281–289, Aug. 2021.
- [257] H. Cheng, B. P.-H. Chen, I. M. Soleas, N. C. Ferko, C. G. Cameron, and P. Hinoul, "Prolonged Operative Duration Increases Risk of Surgical Site Infections: A Systematic Review," *Surg. Infect.*, vol. 18, no. 6, pp. 722–735, Aug/Sep 2017.
- [258] J. Y. S. Kim *et al.*, "Surgical duration and risk of venous thromboembolism," *JAMA Surg.*, vol. 150, no. 2, pp. 110–117, Feb. 2015.
- [259] T. D. Jackson, J. J. Wannares, R. T. Lancaster, D. W. Rattner, and M. M. Hutter, "Does speed matter? The impact of operative time on outcome in laparoscopic surgery," *Surg. Endosc.*, vol. 25, no. 7, pp. 2288–2295, Jul. 2011.
- [260] M. Ferriero *et al.*, "Impact of learning curve on perioperative outcomes of off-clamp minimally invasive partial nephrectomy: propensity score matched comparison of outcomes between training versus expert series," *Minerva Urol Nephrol*, vol. 73, no. 5, pp. 564–571, Oct. 2021.
- [261] P. De Backer *et al.*, "Automated intra-operative video analysis in robot-assisted partial nephrectomy: Paving the road for Surgical Automation," presented at the ERUS23 20th Meeting of the EAU Robotic Urology Section, Florence.
- [262] P. Mascagni *et al.*, "Computer vision in surgery: from potential to clinical value," *NPJ Digit Med*, vol. 5, no. 1, p. 163, Oct. 2022.
- [263] Z. Walker *et al.*, "Evaluating the Effectiveness of Deep Learning Contouring across Multiple Radiotherapy Centres," *Phys Imaging Radiat Oncol*, vol. 24, pp. 121–128, Oct. 2022.
- [264] X. Chen *et al.*, "A deep learning-based auto-segmentation system for organs-at-risk on whole-body computed tomography images for radiation therapy," *Radiother. Oncol.*, vol. 160, pp. 175–184, Jul. 2021.
- [265] T. Lustberg *et al.*, "Clinical evaluation of atlas and deep learning based automatic contouring for lung cancer," *Radiother. Oncol.*, vol. 126, no. 2, pp. 312–317, Feb. 2018.
- [266] M. J. Willeminck *et al.*, "Preparing Medical Imaging Data for Machine Learning," *Radiology*, vol. 295, no. 1, pp. 4–15, Apr. 2020.
- [267] "First online laboratory for 3D modelling of medical images," *Visible Patient*, 29-Nov-2019. [Online]. Available: <https://www.visiblepatient.com/en/>. [Accessed: 09-Aug-2023].
- [268] A. 3d, "Axial3D - Making patient specific care routine," *Axial3D*. [Online]. Available: <https://axial3d.com/>. [Accessed: 09-Aug-2023].
- [269] "SurgiPrint – 3D Intelligence." [Online]. Available: <https://www.surgiprint.com/>. [Accessed: 09-Aug-2023].
- [270] "Ceevra." [Online]. Available: <https://ceevra.com/>. [Accessed: 09-Aug-2023].

- [271] F. Isensee, P. F. Jaeger, S. A. A. Kohl, J. Petersen, and K. H. Maier-Hein, “nnU-Net: a self-configuring method for deep learning-based biomedical image segmentation,” *Nat. Methods*, vol. 18, no. 2, pp. 203–211, Feb. 2021.
- [272] J. Wasserthal *et al.*, “TotalSegmentator: Robust Segmentation of 104 Anatomic Structures in CT Images,” *Radiology: Artificial Intelligence*, vol. 5, no. 5, p. e230024, Sep. 2023.
- [273] “MONAI Model Zoo.” [Online]. Available: <https://monai.io/model-zoo.html>. [Accessed: 09-Aug-2023].
- [274] N. Heller *et al.*, “The state of the art in kidney and kidney tumor segmentation in contrast-enhanced CT imaging: Results of the KiTS19 Challenge,” *arXiv*, 2019.
- [275] N. Sennesael *et al.*, “Ex-Vivo Renal Vascular Dominant Region Mapping using Artery-Selective Contrast Injections,” in *ISMRM & SMRT Annual Meeting & Exhibition*, 2021.
- [276] L. C. Sanmiguel Serpa, A. Hillaert, and P. Pullens, “Measurement of renal perfusion using ASL-MRI and renal oxygenation using BOLD-MRI in dogs,” in *Faculty of Engineering and Architecture Research Symposium 2022 (FEARS 2022)*, 2022.
- [277] M. Tan and Q. V. Le, “EfficientNet: Rethinking Model Scaling for Convolutional Neural Networks,” *arXiv [cs.LG]*, 28-May-2019.
- [278] C. Wang *et al.*, “Ultrasound 3D reconstruction of malignant masses in robotic-assisted partial nephrectomy using the PAF rail system: a comparison study,” *Int. J. Comput. Assist. Radiol. Surg.*, vol. 15, no. 7, pp. 1147–1155, Jul. 2020.
- [279] L. Ayala *et al.*, “Spectral imaging enables contrast agent-free real-time ischemia monitoring in laparoscopic surgery,” *Sci Adv*, vol. 9, no. 10, p. eadd6778, Mar. 2023.
- [280] J. Sancho, M. Villa, M. Chavarrías, E. Juárez, A. Lagares, and C. Sanz, “SLIMBRAIN: Augmented reality real-time acquisition and processing system for hyperspectral classification mapping with depth information for in-vivo surgical procedures,” *Int. J. High Perform. Syst. Archit.*, vol. 140, p. 102893, Jul. 2023.
- [281] S. Vermijs, B. Cornette, P. De Backer, K. Decaestecker, L. Desender, and C. Debbaut, “A preoperative planning tool for lung segmentectomy procedures : a case study,” in *The European Association of Endoscopic Surgery (EAES 2022)*, 2022.
- [282] Y. Liu *et al.*, “LoViT: Long Video Transformer for Surgical Phase Recognition,” *arXiv [cs.CV]*, 15-May-2023.
- [283] S. Nag, G. Datta, S. Kundu, N. Chandrachoodan, and P. A. Beereel, “ViTA: A Vision Transformer Inference Accelerator for Edge Applications,” *arXiv [cs.AR]*, 17-Feb-2023.
- [284] “Stream Deck XL Trailer,” 12-May-2023. [Online]. Available: <https://www.elgato.com/us/en/p/stream-deck-xl>. [Accessed: 11-Aug-2023].
- [285] J. M. Brandenburg *et al.*, “Active learning for extracting surgomic features in robot-assisted minimally invasive esophagectomy: a prospective annotation study,” *Surg. Endosc.*, vol. 37, no. 11, pp. 8577–8593, Nov. 2023.
- [286] C. Shearer, “The CRISP-DM Model: The New Blueprint for Data Mining,” *Journal of Data Warehousing*, vol. 5, no. 4, 2000.

The risk I took was calculated,

but man,

am I bad at math.



ACKNOWLEDGMENTS

« Ik wou dat ik een xylofoonspeler was zodat ik elke dag hout kon afkloppen »

- Maud Vanhauwaert

Acknowledgments

The shortest path between two points is and always has been a straight line. Looking back on the journey of preparing for and finally pursuing a PhD, quite some plot twist repeatedly deviated me from the most straightforward route. As Van Gogh would say “Normality is a paved road: It’s comfortable to walk, but no flowers grow on it.”

Whilst writing these acknowledgements, I once more realize that I have been very privileged up to present and that Van Gogh’s quote has only been applicable and appropriate because of all this luck. As such, I should knock on wood daily, just like a xylophone.

In the light of all the above, I will start off with a small twist to the classical PhD acknowledgements. While my PhD supervisors were instrumental in achieving this career milestone, one person was most instrumental and deserves nothing but the first acknowledgement: my loving wife **Tine**. Arriving up to this point would simply not have been possible without your deep understanding and unconditional continuous support.

From a surgical point of view, I was very lucky to have two promotors, both innovators as well as top notch surgeons, in different stages of their respective careers. Not only was I able to learn from them through an academic point-of-view, up to present they have also taught me numerous clinical skills and I hope they will be doing so for many years to follow. I am amazed each time I see them perform the most challenging cases or interact with their patients. They make surgery seem so simple and I learned over the last couple of years that this is what defines a true master.

From an academic and mentorship point-of-view, I was fortunate to have my path crossed by my main promotor professor Karel Decaestecker in 2018. **Karel**, thank you for taking me under your wings, providing me with unwavering support and all freedom to explore different paths whilst at the same time also putting in place a safety net when developments or progress were hampered. It has been inspiring to see you take on a global leadership role in robotic surgery whilst always staying so close to your patients. I look forward to many more years of innovating together.

All the above also counts for my industrial promotor professor Alexandre Mottrie. **Alex**, thank you for reminding me that technology should be there to serve our patients and not the other way around. Not only did you show me how to navigate a world where technology and medicine cross through your decades of experience, you added the fine-grained details of the MedTech industry to that complex mix. You showed me how these three together can be an even more potent medicine, allowing developments to reach the real operating theater. Thank you for taking on the risk to let me build and expand Orsi InnoTech. I think the best is yet to come and I look forward to keep building under your supervision.

Lastly there is no technology without engineering. My heartfelt gratitude goes out to my engineering co-promotor professor Charlotte Debbaut. **Charlotte**, just as the 2 clinical promotors, you let me wander and do my own thing, but you were always available for feedback and guidance. You kept me sharp on the scientific side, motivated at critical times and made sure that from an engineering point-of-view, this thesis was also a success. I might have been the first rather clinically inclined PhD student you supervised, but I always felt very well understood and I cannot be more grateful for your guidance.

Now comes the harsh point of heartfelt upfront apologies. So many individuals have supported this PhD from the academic, industrial, and personal side and I noticed I am quite unable to name all individuals who impacted the journey during the last couple of years, but here it goes...

Team InnoTech, you grew together with the PhD, and I am so happy to be working together. **Jente**, **Jasper** and **Marco**, you guys are the brute workforce of Orsi InnoTech and the world should know. I am happy you took the risk of joining the team throughout the years and I believe the surgical AI

world can expect a lot of things from what we are building throughout the years to come. All three of you have different characters, bring very complementary skills to the table and I think this is truly special. I enjoy the way all three of you have taken ownership and I realize it might not always be simple to navigate this complex field especially at times when I am performing clinical duties. Thank you for your flexibility and your belief in building towards our dream of improving surgery and surgical training through digitalization. MedTech innovation requires several other management skills and I thank you **Inge** from bringing this to our team daily. I truly enjoy working with you, you juggle quite some tasks at Orsi but your ever optimism and can-do mentality still make things happen. Let's keep pushing together! **Jeroen**, I know I sometimes offloaded too many items towards you while you had to manage a ton of other things. Nevertheless, Innotech would have been nowhere without your efforts in 3D design and video recording infrastructure which are the fuel of what we do today, and I thank you for your hard work and all the good laughs. As you generated videos, all this data needed to be stored in a safe manner and I thank **Hannah**, subsequently **Margot** and finally **Mieken** for their support. Mieken, since your arrival, InnoTech really received a strong boost on datacollection, warehousing, legislation, and administration. You entered the team with zero medical or technical background. Nonetheless, I have not met anyone at Orsi who is so meticulous, and your hard work and hyperflexibility pays off strongly. I enjoy how you engage with a problem, and you do not let go of it until it is fixed.

Just as good data storage is essential, there is a need for structuring and annotating data. Through the insights and tenacity of **Kenzo**, **Heleen**, **Charlotte**, **Tim**, **Julie**, **Amélie** and many others, we were able to build unique datasets which continuously help us propel the field through young and innovative ideas. Thanks!

Building Orsi Innotech has been an opportunity I had not really anticipated. Despite having a broad medical and technological background, I had little industrial experience when starting at Orsi. As such, I want to thank **Niek** for introducing me to these aspects, **Carl** for getting our organization structured and **Philippe** to push it to the next level where we are today. I still have so much to learn from you and look forward to that very much.

Ofcourse, InnoTech is only a small part of our Orsi organization. As such, apart from **Alex**, I want to thank our leadership **Luc**, **Korneel** and **Geert**. **Luc**, not only did you teach me business diplomacy as a true gentleman, you were always available for feedback or discussion, no matter what time of day. Apart from converting me from Windows to Apple and a lot of good laughs, you provided me with plenty of advice that will stick with me throughout my professional life. **Korneel**, I truly enjoy your mix of enthusiasm and sobriety. When I was once more overwhelmed or fed up, you managed to de-escalate troublesome situations whilst also continuously connecting the dots between Orsi Academy and Innotech. On a sidenote, I enjoy our proverb contests a lot during meetings and we should make more time to ping pong rather than our incidental monthly match. I think you might have inherited quite some of that sobriety and composure from **Geert**. Geert, I am also very grateful for your trust and freedom to expand InnoTech aligned with the general Orsi goals.

At Orsi, we perform a lot of training which also creates a setting where engineers have ample possibility to perform test and experiments. Even though we were not always equipped with enough (wo)manpower, I thank **Eva**, **Marieken**, and everyone in "team OK" for your animal trial support and testing and **Kevin** for endless material and technical tips. Without your flexibility, InnoTech would not have had the current impact, nor innovation pace it has achieved. Impact means nothing without good communication, hospitality, and events, and I hope while writing this that our first surgical AI congress has been a true highlight. Thank you for (in my opinion) the real Peppi & Kokki, **Odile & Jana** and your team for making this happen. **Veerle & Lars**, also a heartfelt thank you: you are doing a fantastic effort streamlining our internal financial processes and it has aided tremendously. Lastly, Orsi is nothing without proficiency based progression.

Thank you **professor Gallagher** for showing me why proficiency matters and for keeping me sharp on the scientific side. I expect the impact of PBP to only increase in coming years and I hope A.I. can be a meaningful accelerator in spreading that message. I also appreciate the friendship and help of scientific fellows (**Stefano, Marco(s), Carlo, Nicola, Maria, Luca, Pietro, Angelo, Rui**, and many many others) who passed through Orsi in the last couple of years. I also want to thank Orsi and VLAIO for jointly financing this PhD trajectory.

Rita, Kim, Sabrina and team ISS, thanks for your friendship, laughter and for always providing me and the team with a healthy and clean working space, including all Nalus to get us through the afternoons after another delicious lunch.

This PhD was also the result of strong collaboration with Ghent University and partnering hospitals. More specifically, the urology departments of Ghent University Hospital, OLV Aalst and AZ Maria Middelaere have been very open to co-innovate and I can only be grateful for that. In Ghent University Hospital, I would specifically like to acknowledge prof. Van Praet, prof. De Visschere & Dr. Berquin. **Charles**, I learned a ton of things whilst being under your clinical supervision. I admire your scientific but human approach, your availability for discussions and laughter, your working attitude and authenticity. **Pieter**, I truly appreciate your insightful teaching on all renal radiological aspects. **Camille**, also thank you for a lot of clinical guidance and fun moments.

At OLV, I would like to thank **Tinneke** for all administrative help as well as Dr De Groote and Dr De Naeyer on the clinical side. **Ruben & Geert**, you were and are always available to try out any new technology, whilst providing honest feedback or support in yet another scientific article. I look forward to the upcoming year under your mentorship and that of your colleagues and I thank the department for the flexibility in letting me combine a career in applied research and surgery. This gratitude also extends deeply to **prof. Hoebeke, prof. Van Laecke, prof. Everaert and Dr Ameye**.

At Ghent University, I would like to thank the BioMMeda department as a whole and **Saar** in specific. **Saar**, I have seen you expand the field of predicting perfusion zones from a master student into your PhD and I could have not wished for anyone else to overtake and tremendously improve this research line in the way you did. I am looking forward to your defense soon and I am convinced you will ace it. **Joris**, I am happy you will continue the clinical side of perfusion prediction and despite having just started, I wish you the best and I am likewise convinced you hold all cards to ace this.

Throughout this PhD, I also got involved in several academic initiatives. As such, I would like to thank my friends at the EAES AI subcommittee and the EAU YAU Urotech committee for all insightful and fruitful discussions, as well as for all exciting joint projects which lie ahead. Furthermore, I would like to thank the collaborators at KU Leuven as well as all other partner universities such as Modena (**Federica & Stefano**) and Cologne (**Hans, Jennifer & Dolores**) and all master students in medicine, computer science and biomedical engineering who interned and all aided toward this PhD in their own way.

Apart from the above-mentioned hospitals and international universities, large parts of this manuscript would have been impossible without all collaborating surgeons whose expertise span all body parts, all robotic systems and all continents. A special thanks to **Dr. D'Hondt, Van Eetvelde, Van Den Bossche, Jobczyk, Quackels, Dekuyper, Moschovas, Patel**, and many more for your support, trust, and friendship.

As we tested our technology on several robotic systems, I might also have troubled some of the robotic surgery trainers at Orsi. Thank you, **Luc** and **Andy**, your Xi system was instrumental in our publication output, and we would have not ended up with such impactful stories if we could

not have tested all of this upfront. Likewise, my heartfelt gratitude goes out to **Olivier, Marianne, Karl, Sandra & Romain** for introducing me to your new HUGO RAS ecosystem whilst facilitating the need for decent data capture.

From a computational point-of-view, I want to thank **Thijs, Nadime, Oliver, Zhijin** and the whole NVIDIA team for your collaborative spirit and support towards achieving real-time surgical AI applications. Also thank you to the whole Deltacast crew for supporting us in successful video capture for minimized latency. From a 3D visualization and rendering point-of-view, I thank **Robo** and **Jaro** for your kind introduction to 3D rendering and advanced visualisation techniques. Also thank you **Bram** and **Lubo** for the final PhD shaping and editing.

Despite my tendency to go off the beaten path, as a man of tradition, I want to close by thanking my family and friends. After all, this work reflects on the last 5 years but was enabled by a much stronger foundation.

Thank you, **mama**, for all instilled social values, for giving me a sense to try and give back to society where possible and being sensitive to injustice. I realize this value instillation backfired quite heavily when I decided to pursue medicine after engineering, but I am forever grateful for the way you immediately understood and had seen this coming for many years without me explicitly stating. Still today, you are the first to support me when I get another crazy idea, like lengthening my residency for a PhD in collaboration with a company, but you are always rightfully critical as well to challenge me on beforehand. I think my perfectionist trait also came from your end, and with that a tendency to work till early morning when needed. We both don't mind it so much during the night but we both hate it in the mornings!

Papa, thank you for showing me that perseverance pays off and for convincing me that difficult roads often lead to beautiful destinations even when I was still too young to understand. You taught me that I should not always get things right the first time (balancing our mamie's perfectionism) and that repetition is the mother of all learning. Thank you for also guiding me on the balance between leisure, work, and dedicated focus. You showed me the relativity of things when once more I overcooked and together with mama provided a stable and loving environment for personal growth. If anyone wonders where I got my situational jokes from - talk to my dad over a beer.

Lies, my big sister. You had quite some stuff going on while your little brother kept running around the house (or school) with too much energy. Still, you were always there for me when something was wrong, being it a problematic high school task or the 10th time forgetting my lunch box or swimming trousers. I saw how your diligence at university paid off and it inspired me to go for it as well when you graduated law school. Now, you are still there for any troubles that arise and while I keep forgetting my towel when we go swimming, you are always there to discuss the more important issues in life.

With life and love, also comes family-in-law. Once more, I was privileged. Thank you **Pieter**, for your friendship, laughs and discussions throughout the years. Thank you **Marc** and **Gerda**, for being wonderful loving parents-in-law who we can always rely on, day and night. Thank you, **Ruben, Joke, Maarten & Kaat** for your support and love throughout all these years.

Thank you to my whole family, also those who are no longer here, for always understanding when once more work or 'urgent' obligations took over. Your unwavering support means more to me than words, graphs, or even meticulously crafted citations ever could.

Apart from family, I have plenty of friends to thank but I will keep it to groups for conciseness. I am very grateful to be sharing this milestone with all of you. I apologize for being absent so much in the last year and I thank you for all your support and fun times.

Thanks to all 'old' friends: the **boykes**, and by extension the **RenDVoe** group. I think it is quite unique to have such a wonderful and tight group of high school friends still together. Because I know the boykes will make a competition of looking up their names and seeing who is cited first, I will just put you here in alphabetic order - just because I can: **Filip, Fredo, Gigi, Japie, Jelle, Munckie, Nick, PJ, Rein, Stef & Tombo**. Thanks amigos, you have seen me through the highs and lows and were always there, and that is what friendship is all about.

Another big thanks to all 'newer' friends: the **geruste tsjuus & darters**, the **amicas**, and **PrintPlace**. A special thanks to Maarten, for writing a poem for the PhD opening! I am sure your hidden bundle will be a success once you decide to publish it.

Last but not least, my dear **Tine**... I have put you through quite some unexpected tests in the last 12 years. You started off dating an electromechanical engineer, but you married a urology resident. I moved to Switzerland right after we met. I started medical school at a time when all our friends started their professional lives and went on living together. Still, we made it work. I decided to do a PhD during my residency when the opportunity arose, during which I figured to have some more flexibility and family time compared to residency. The risk I took was calculated, but man, am I bad at math. You had just finished your PhD and thought I was somewhat insane. You were right, but still you went ahead and supported me. We had our lovely **Suzan** join us in the meantime and started to build our house, with all problems on the construction side. You shifted from academics to the hospital setting while I had to travel more and more. Working late nights, weekends and sometimes even holidays became more of a standard than having time for the three of us. And still you kept on supporting me. Now, whilst juggling residency with applied research, things have taken another turn. While this new dust settles, I realize every day how lucky I am to have you in my life, and I most certainly stress this way too little. You can pull the handbrake when things get out of hand and even protect me against myself. Your sense of humor still makes me laugh every day. Apart from a fantastic partner, you are a wonderful mother to **Suzan**. Suzannie, no matter how bad my day was, getting back home and seeing your smile warms my heart while your love, hugs, and laughter make me forget all troubles. I look forward to our future together and the upcoming arrival Suzan's little brother, surrounded by our loving and supporting family and friends.

*Pieter De Backer
December 2023*

Pieter De Backer

Personalia

 Born in Aalst, Belgium
 pieter.de.backer@orsl.be
 linkedin.com/in/pdebacker
 @pidebacker

Languages

Dutch
French (C1)
English (C2)
Spanish (A2)
German (A2)

3D Modeling Software

Abaqus, Simpleware,
Mimics, 3Matic, 3DSlicer,
Fusion 360, Netfabb,
AutoCAD, SolidWorks,
Cura, MatterControl

Programming

Matlab, Python, Pytorch,
TensorFlow, Linux, JAVA,
HTML, Joomla, LaTeX
ClewIn, Ms. Office, Maple

Interests

Travelling,
Technology,
Football/Futsal,
Snowboarding,
Running

About me

I am an engineer who had a late calling for medicine. After graduation and a short stop in the robotics industry, I pursued my passion for medicine and subsequently fell in love with urology. I have a technical background in A.I. & computer vision, micro-electronics, and 3D design. Actively enabling image guidance and computer vision for error detection and surgical training in minimally invasive surgery.

Education

Current - Master of Medicine in Specialist Medicine: Urology

2023 - 2024: Resident Urology @ OLV Ziekenhuis Aalst
2020 - 2023: Resident Urology @ Ghent University Hospitals
2019 - 2020: Resident Urology @ AZ Sint-Blasius Dendermonde
2018 - 2019: Resident General Surgery @ OLV Ziekenhuis Aalst

2019-2023: Joint PhD programme

Biomedical Engineering and Medical Sciences

"Peri-operative Digital Planning in Robot-Assisted Partial Nephrectomy:
Bridging the gap between A.I., A.R. and surgical data science"

2018 - M.D. - Master of Medicine (Magna Cum Laude), VUB, UZ Brussels

2015 - Bachelor of Science in Medicine (Cum Laude), VUB, UZ Brussels

- Webmaster at local Belgian Medical Students' Association (BeMSA)

2013 - Master of Science: Biomedical Engineering (Cum Laude)

- Specialization in micro-electronics, Ghent University & VUB
- Master thesis: Design and Fabrication of a Tunable Artificial Iris
(see publication list)

2012 - Exchange semester at EPFL - Swiss Federal Institute of Technology in Lausanne

2011 - Bachelor of Science: Mechanical and Electro-technical Engineering (Cum Laude), Ghent University

- Bachelor project: Design and production of a Foucault brake

2008 - Secondary School: Mathematics and Sciences, DvM Humaniora Aalst

- Mathematics Valedictorian

Experience

2020 – present

Artificial Intelligence Lead • Orsi Academy

At Orsi Academy, global training centre for robotic surgery, I set up the activities involving the use of artificial intelligence for robotic surgery to enhance surgical training and performance. I obtained an individual research grant from the Flanders Innovation and Entrepreneurship agency (VLAIO) for research on digital surgery planning.

2016 – present

Co-founder & Advisor PrintPlace 3D Printing • 3D Guided Surgery

PrintPlace.be aims to leverage 3D Printing providing consumers easy access to personalised objects. After co-founding the company in 2016, I have evolved from founder and 3D printing research engineer to an advisory role. I have a specific interest in and focus on medical 3DPrinting at the PrintPlace subsidiary 3DGuidedSurgery.com. Amongst others, we printed patient-specific carotid artery molds for validation of biomechanical simulations, pre-operative kidney and pulmonary vein models, dosimetry phantoms, ... My built-up expertise is the design and automation of new 3D printing techniques allowing easy integration into clinical practice while significantly reducing costs.

2017

Bolivian Prosthetics Foundation • internship,

Volunteered for the 'Bolivian Prosthetics Foundation FunProBo' in La Paz to make free prostheses for impoverished amputees. Optimization of the 3D printing process to produce artificial hands. Tripling of the average output and giving 3 patients a primitive active opponent finger grip by means of personalized 3D printed hands

2016 – 2017

Clinical internships,

Neurosurgery, Cardiology, Rehabilitation Medicine, Ophthalmology, Otolaryngology, Dermatology, Radiology, Family Medicine, Urology, Cardiac Surgery, Gynecology, Pediatrics, Gastro-enterology, Oncologic Surgery

Summer 2014

B-PHOT - Brussels Photonics Team, internship

Design and fabrication of an interferometric setup using Digital Optical Phase Conjugation to obtain focused light out of a multimode optical fiber used for micro-endoscopes with 200 micron fiber diameter.

Summer 2013

P&G - Global Go To Market Engineering, Research Engineer

Investigation of opportunities for increased automation in the global production line of Head and Shoulders. Left the position to pursue my passion for surgery and start medical school.

2012 - 2013

CMST + EPFL - Development and Fabrication of a Tunable Artificial Iris, Master project

Spent 4 months in the Renaud lab at EPFL and 4 months in the De Smet lab at CMST(Imec). Investigation of patient groups benefitting from an artificial iris contact lens, reviewing most suitable technology platform, design and cleanroom fabrication of an artificial iris contact lens by use of a curved liquid crystal display. Electro-optical characterization and programming to physiologically mimic the human iris. Now being productized as Azalea Vision. [Final Thesis Result \(video\)](#) - read about it online [here](#) (Dutch)

>2012

Various student summer jobs such as teaching, maintenance technician, administrator, ...

Awards & Funding

- 2023** - BVU Elaut prize Antwerp – Best scientific presentation for work on automated surgical scene understanding
- Vattikuti Foundation Robotic Surgery symposium “Humans at the Cutting Edge of Robotic Surgery” – Finalist video for work on A.I. assisted surgical scene understanding in partial nephrectomy, Ghent, Belgium
- AE-CAI workshop MICCAI 2023 Vancouver, Canada - Outstanding paper award for work on Realtime A.R. deployment in robotic surgery
- 2022** - Belgian Association of Urology 2022 congress, Brussels – best poster for work on A.R.
- European Association of Urology 2022, Robotic Session, Barcelona – best video for work on A.R.
- Top 10 best technology abstracts EAES2022 (Gerhard Buess session) for work on surgical annotation
- CLINICAI day 2022, Singapore - 2nd best presentation for work on video anonymization
- Fonds voor Innovatie en Klinisch Onderzoek, grant for the development of patient-specific 3D modelling at Ghent University Hospital. Ranked first out of 18 projects
- 2021** - Audience award Belgian Association of Urology, for poster on 3D clamping strategies in robot-assisted partial nephrectomy
- 2020** - Abundance 360 scholarship
- VLAIO Baekeland Mandate, individual PhD Grant in collaboration with Orsi Academy
- 2017** - Hamlyn Winter School Travel Grant, Imperial College London
- VLIR UOS Travel Grant for collaboration at Bolivian Prosthetics Foundation
- 2015** - Jozef Plateau prize for "Design and Fabrication of a Tunable Artificial Iris", site
Yearly award for the best master thesis of the Faculty of Engineering and Architecture UGent
- Flanders Transition Fellowship for research at the Mechanobiology lab, Cape Town
- Award 'Medische Wereld' VUB for research at the Mechanobiology lab, Cape Town: site, video.
- 2013** - Shortlist Vlaamse Scriptieprijs for "Design and Fabrication of An Artificial Iris": video

Memberships

- 1 Society of American Gastrointestinal and Endoscopic Surgeons (SAGES)
- 2 European Association of Urology (EAU)
 - Elected associate member of the Young Academic Urologist Urotechnology Working Group (YAU UroTech)
- 3 European Association of Endoscopic Surgery (EAES)
 - Elected full member of the EAES Artificial Intelligence Subcommittee
- 4 Medical Image Computing and Computer Assisted Intervention (MICCAI)
- 5 Advisory Committee bachelor and master of Biomedical Engineering

Tutoring & Teaching

Supervisor Master's dissertation - Master of Science in Biomedical Engineering:

- 2018** Sarah Vandenbulcke - Development of a planning tool for robot-assisted partial nephrectomy surgery based on 3D reconstructions of kidneys
- 2019** Saar Vermijs - Development of a preoperative assessment tool for the planning of robot assisted partial nephrectomies based on 3D reconstructions of kidneys
- 2020** Jordi Martens - Development of an automatic segmentation method for kidneys in support of robot-assisted partial nephrectomy surgery

Supervisor Master's dissertation - Master of Medicine:

- 2019** Maryse Lejoly & Stefanie Vanderschelden - Analysis and optimization of 3D renal anatomy reconstruction for Robot-Assisted Partial Nephrectomy planning
- 2020** Rania Matthys & Roberto Ciani - Analysis of renal morphology and vasculature in neoplastic kidney disease by 3D-reconstruction

- 2021** Gerben Michiels & Jerome Callebaut - optimalisatie van 3d-anatomische niermodellen bij preoperatieve planning van robot-geassisteerde partiële nefrectomie
- 2021** Heleen Creemers - Phase Assessment in Radical Prostatectomy: Exploratory analysis of clinical relevance
- 2022** Victor Chi Shan & Mereth Demuyck - Quantitative video analysis in robot-assisted partial nephrectomy: analysis of phase definitions and tumour complexity
- 2022** Karel Van Regemorter & Aube Wastyn - Artificial Intelligence in Surgery: Phase Recognition and Analysis in Robot-Assisted Partial Nephrectomy

Supervisor Master's dissertation – Master of Science in Computer Science Engineering:

- 2022** Mathias Delue – Improving robotic surgery phase detection using self-supervised learning
- 2023** Marco Mezzina - Harnessing Self-Supervised Learning and Explainability for Enhanced Surgical Phase Recognition in Robot-Assisted Surgery Procedures
- 2023** Ilaria Manghi - Real-time Instrument Segmentation and Augmented Reality in Robot-Assisted Partial Nephrectomy
- 2023** Kevin Marchesini - Surgical Tools and Organs Segmentation in Robot-Assisted Procedures
- 2023** Giulio Besi - Automated Robotic Surgical Skill Assessment in the Era of Proficiency-Based Progression: A Study on the Effectiveness of Classical Computer Vision Metrics
- 2023** Francesco Cisternino - deep learning based surgical scene segmentation in robot-assisted procedures

Supervisor Honours Programme Ghent University

- 2022** Kenzo Mestdagh & Fiebe Maris
Renal Volumetric Analysis in Robot-Assisted Partial Nephrectomy:
Impact of Surgical Techniques, PADUA Score and Arterial Calcifications

Teaching

- 2022** Interuniversity Certificate in Artificial Intelligence in Medicine and Digital Health (ULB – UMONS – CHU Charleroi)
- 2020** Computational biofluid dynamics course – Master of Biomedical Engineering - Ghent University 2020 &
- 2021 2021
- 2022** Tutor anatomical sessions – bachelor of Medicine
Anatomy course 2022
- 2011** EPFL - Swiss Federal Institute of Technology, Lausanne, Teaching assistant
Tutoring Mechanics exercise sessions in French to first year Physics students.

Extracurricular courses & certifications

- 2023** HUGO RAS course
- 2023** CC-ERUS: ORSI Academy Robotic Skills Course
- 2022** Explainability of Deep Learning Systems, UGent
- 2022** Deep Learning, UGent
- 2022** Artificiële Intelligentie in de gezondheidszorg – KU Leuven
- 2021** General Adversarial Networks – Ghent University
- 2021** Machine Learning with Python – Ghent University
- 2021** Advanced Academic writing – Ghent University
- 2021** Leadership foundation – Ghent University
- 2019** Deep Learning specialization Coursera
- 2018** Business Engineering and Surgical Technology Course – IRCAD/IHU Strasbourg
International summer school on development of new surgical technologies and the corresponding business aspect.
- 2017** Hamlyn Winter School on Surgical Imaging and Vision – Imperial College London
International winter school on the engineering of state of the art robotics and image guided surgical interventions
- 2017** Spanish level A2 – DELE certificate
- 2017** Good Clinical Practice
- 2017** Intercultural competences day UCOS vzw
- 2015** Let's talk Science! Summer School on scientific communication, Leuven

- 2012** French level C1 - Centre de langues Lausanne certificate
2011 Summer School: Aircraft system integration, UC3M, Madrid
 International summer school on avionics and aircraft system engineering. Selected 20 out of 400 applicants.

Public Speaking

- 11 March 2021** Junior Orsi event - 'The future of artificial intelligence in healthcare'
- 9 April 2021** AFT – Academics for Technology Student Startup Trip – Orsi Academy
- 19 May 2021** BAST Expert in the field webinar
 - 'A.I. in Surgery: From Neural Networks to 3D models'
- 25 Sept 2021** Indian society of genito-urinary surgeons
 - 'AI and ML in robotic urology and training'
- 12 Oct 2021** OncoTech panel Ehealth valley
- 13 Oct 2021** Proasca Global Congress on Prostate Cancer
 - 'AI and robotics: a combination that is changing the operating room'
- 10 Feb 2022** Digital Health expert panel The Big Score
- 11 Feb 2022** Research Lunch 'Robot Assisted Surgery' – UZGent Department of Human Structure and Repair)
- 17 March 2022** Belgian MedTech Meetup
 - 'Challenging the status quo in surgical training'
- 19 March 2022** De Arts Van Morgen Symposium De Arts van Morgen 'Modernizing Medicine: AI'
 - 'AI voor robotchirurgie'
- 19 April 2022** Vlerick Entrepreneurship Academy
 - 'AI as a service: How to get started with AI in your business without breaking the bank'
- 21 April 2022** AI in surgery (AI4Health webinar)
- 30 April 2022** Junior Orsi event - Surgery of tomorrow
- 9 June 2022** European Society of Pediatric Urology - local keynote lecture
 - 'Surgery 4.0.: The impact of A.I. on the future of surgery'
- 16 June 2022** Vlaamse Vereniging Obstetrie en Gynaecologie - Artificiële intelligentie, Innovatieve Technologie en Digital Health
 - 'AI & robotchirurgie: opportuniteit of dreiging?'
- 3 July 2022** European Association of Urology 2022 Amsterdam
 - Surgery In Motion panellist and speaker: 'AI and automation'
- 26 August 2022** Belgian Association of Urology – Brussels
 - 'Artificial Intelligence: How can we improve treatment planification?'
- 28 Sept 2022** Lokaal Overleg Comité Urologie Aalst
 - '3D modellen in nierchirurgie: hoe, wat en waar?'
- 21 Nov 2022** LVS0 Leuven, Belgium; speaker Event "Artificial Intelligence: the future is now"
- 7 Dec 2022** Edu4Health webinar "Going beyond Hardware", panelist and speaker: The world is our oyster – implementation of Artificial Intelligence in Robotics
- 14 Jan 2023** Teaching « Intelligence Artificielle en médecine et santé digitale Université Libre de Bruxelles et Université de Mons – Belgium
- 4 March 2023** Keynote "AI in vascular surgery: what's next?", Belgian Society for Vascular Surgery – Dolce La Hulpe

- 30 March 2023** Research day Ghent University - Keynote "Surgery 4.0.: The Impact of A.I. on the Future of Surgery"
- 22 April 2023** ESRU Day Belgium - Keynote "AI in partial nephrectomy"
- 2 June 2023** Robotic Abdominal Wall Surgery congress – "AI in robotic surgery"
- 20-23 June 2023** 31st international congress European Association of Endoscopic Surgery, Rome, Italy.
- Technology Symposium Session– Simulation and Training:
 - 'AI for surgical training'
 - Session 'Towards clinical applications of AI - ready for primetime?'
 - 'Robotics as a platform for AI in surgery'
 - Masterclass 'Artificial Intelligence in Surgery'
 - 'Surgical robotics as a key platform'
- 28 June 2023** E-Health Venture keynote: AR & VR in Robotic Surgery
- 29 June 2023** Hamlyn Symposium on Medical Robotics – workshop Robotic systems for surgery training and assistance: recent advances and future perspectives
- 'AI assisted surgical scene and error understanding'
- 29 June 2023** European School of Urology Webinar
- 'The ABC of A.I. : A practical guide for the modern urologist'
- 5 July 2023** Summer school: Computer vision in surgery
- 'Introduction to Surgical Data Science'
- 11 Aug 2023** Urology Grand Rounds – University of Southern California – Keck School of Medicine 'Digital Urology: Advancements in surgical AI'
- 9 Sept 2023** International Symposium on A.I. in Urology, Banjara Hills Hyderabad India
- The Art of Building Computer Vision Models and the Role Urologists must play
- 11 Sept 2023** 5th Renal Imaging Meeting, Ghent
- Imaging in urological interventions
- 8 Oct 2023** Vattikuti Foundation KS International Innovation Awards, Ghent, Belgium
- 11 Oct 2023** Surgery Grand Rounds – University of British Columbia
- 'AI and Augmented Reality (AR) in Surgery – Report from the front lines'
- 24 Oct 2023** Interview "A.I. in Surgery" for the "A.I. Ready Healthcare" podcast by Anirban Mukhopadhyay
- 22 Nov 2023** Keynote "A.I. in surgery" - COEHRE Symposium: Innovation in technology, leadership and healthy ageing, Artevelde Hogeschool Gent
- 28 Nov 2023** UROwebinar: New Technologies in Robotics
- Integration of novel imaging modalities and robotic surgery
- 15 Dec 2023** Surgical AI Day, Orsi Academy Belgium
- Session 'Surgical Skill Assessment'
 - Proficiency-based progression in surgical training: what is it & can we automate it?

Publications

PhD Related First Author Articles

Published

1. Multicentric exploration of tool annotation in robotic surgery: lessons learned when starting a surgical artificial intelligence project
P De Backer, J Eckhoff, J Simoens, D Müller, C Allaey, H Creemers, A Hallemeesch, K Mestdagh, C Van Praet, C Debbaut, K Decaestecker, C Bruns, O Meireles, A Mottrie, H Fuchs
Surgical Endoscopy 2022
2. A Novel Three-dimensional Planning Tool for Selective Clamping During Partial Nephrectomy: Validation of a Perfusion Zone Algorithm
P De Backer*, S Vermijs*, C Van Praet, P De Visschere, S Vandenbulcke, A Mottaran, C A Bravi, C Berquin, E Lambert, S Dautricourt, W Goedertier, A Mottrie, C Debbaut, K Decaestecker
European Urology 2023 – Surgery in Motion
*shared first author
3. Improving Augmented Reality Through Deep Learning: Real-time Instrument Delineation in Robotic Renal Surgery
P De Backer, C Van Praet, J Simoens, M Peraire Lores, H Creemers, K Mestdagh, C Allaey, S Vermijs, P Piazza, A Mottaran, C A Bravi, M Paciotti, L Sarchi, R Farinha, S Puliatti, F Cisternino, F Ferraguti, C Debbaut, G De Naeyer, K Decaestecker, A Mottrie
European Urology 2023 – Case Series of the Month
4. Robot Assisted Partial Nephrectomy using Intra-Arterial Renal Hypothermia for Highly Complex Endophytic or Hilar Tumors: Case series and Description of Surgical Technique
P De Backer, J Vangeneugden, C Berquin, S Vermijs, P Dekuyper, A Mottrie, C Debbaut, T Quackels, C Van Praet, K Decaestecker
European Urology Open Science 2023
5. Surgical Phase Duration in Robot-Assisted Partial Nephrectomy: A surgical data science exploration for clinical relevance
P De Backer, M Peraire Lores, M Demuynck, F Piramide, J Simoens, T Oosterlinck, W Bogaert, CV Shan, K Van Regemorter, A Wastyn, E Checcucci, C Debbaut, C Van Praet, R Farinha, R De Groote, A Gallagher, K Decaestecker, A Mottrie
Diagnostics 2023 (in Press)
6. First-in-Human Realtime AI-Assisted Instrument Deocclusion during Augmented Reality Robotic Surgery
J Hofman*, **P De Backer***, I Manghi, J Simoens, R De Groote, H Van Den Bossche, M D'Hondt, T Oosterlinck, J Lippens, C Van Praet, F Ferraguti, C Debbaut, Z Li, O Kutter, A Mottrie, K Decaestecker
Wiley's Healthcare Technology Letters - MICCAI 2023 AE-CAI Workshop
*shared first author

Under revision

7. Privacy-proof live surgery streaming: Development and validation of a low-cost, real-time robotic surgery anonymization algorithm

P De Backer, J Simoens, K Mestdagh, J Hofman, JA Eckhoff, M Jobczyk,
E Van Eetvelde, M D'Hondt, MC Moschovas, V Patel, C Van Praet, HF Fuchs,
C Debbaut, K Decaestecker, A Mottrie

Resubmitted for second revision round – Annals of Surgery

PhD Related Patent Filed

- EP23163230.8: European patent application “Real-time instrument delineation in robotic surgery”
- US18/211,269: US patent application “Real-time instrument delineation in robotic surgery”

First pages of published manuscripts are appended.



Multicentric exploration of tool annotation in robotic surgery: lessons learned when starting a surgical artificial intelligence project

Pieter De Backer^{1,3,4,5} · Jennifer A. Eckhoff² · Jente Simoens¹ · Dolores T. Müller² · Charlotte Allaeys³ · Heleen Creemers³ · Amélie Hallemeesch³ · Kenzo Mestdagh³ · Charles Van Praet⁵ · Charlotte Debbaut⁴ · Karel Decaestecker⁵ · Christiane J. Bruns² · Ozanan Meireles⁶ · Alexandre Mottrie^{1,7} · Hans F. Fuchs²

Received: 10 May 2022 / Accepted: 16 July 2022

© The Author(s), under exclusive licence to Springer Science+Business Media, LLC, part of Springer Nature 2022

Abstract

Background Artificial intelligence (AI) holds tremendous potential to reduce surgical risks and improve surgical assessment. Machine learning, a subfield of AI, can be used to analyze surgical video and imaging data. Manual annotations provide veracity about the desired target features. Yet, methodological annotation explorations are limited to date. Here, we provide an exploratory analysis of the requirements and methods of instrument annotation in a multi-institutional team from two specialized AI centers and compile our lessons learned.

Methods We developed a bottom-up approach for team annotation of robotic instruments in robot-assisted partial nephrectomy (RAPN), which was subsequently validated in robot-assisted minimally invasive esophagectomy (RAMIE). Furthermore, instrument annotation methods were evaluated for their use in Machine Learning algorithms. Overall, we evaluated the efficiency and transferability of the proposed team approach and quantified performance metrics (e.g., time per frame required for each annotation modality) between RAPN and RAMIE.

Results We found a 0.05 Hz image sampling frequency to be adequate for instrument annotation. The bottom-up approach in annotation training and management resulted in accurate annotations and demonstrated efficiency in annotating large datasets. The proposed annotation methodology was transferrable between both RAPN and RAMIE. The average annotation time for RAPN pixel annotation ranged from 4.49 to 12.6 min per image; for vector annotation, we denote 2.92 min per image. Similar annotation times were found for RAMIE. Lastly, we elaborate on common pitfalls encountered throughout the annotation process.

✉ Pieter De Backer
pieter.de.backer@orsi.be

¹ ORSI Academy, Proefhoevestraat 12, 9090 Melle, Belgium

² Robotic Innovation Laboratory, Department of General, Visceral, Tumor and Transplantsurgery, University Hospital Cologne, Cologne, Germany

³ Department of Human Structure and Repair, Faculty of Medicine and Health Sciences, Ghent University, Ghent, Belgium

⁴ IBiTech-Biommeda, Faculty of Engineering and Architecture, and CRIG, Ghent University, Ghent, Belgium

⁵ Department of Urology, Ghent University Hospital, Ghent, Belgium

⁶ Surgical Artificial Intelligence and Innovation Laboratory, Massachusetts General Hospital, Boston, USA

⁷ Department of Urology, OLV Hospital Aalst-Asse-Ninove, Aalst, Belgium

available at www.sciencedirect.com
journal homepage: www.europeanurology.com



European Association of Urology



Surgery in Motion

A Novel Three-dimensional Planning Tool for Selective Clamping During Partial Nephrectomy: Validation of a Perfusion Zone Algorithm

Pieter De Backer^{a,b,c,d,*†}, Saar Vermijs^{b,c,e,†}, Charles Van Praet^{a,c}, Pieter De Visscher^f, Sarah Vandenbulcke^b, Angelo Mottaran^{d,g,h}, Carlo A. Bravi^{d,h,i}, Camille Berquin^a, Edward Lambert^a, Stéphanie Dautricourt^a, Wouter Goedertier^a, Alexandre Mottrie^{d,h}, Charlotte Debbaut^{b,e,‡}, Karel Decaestecker^{a,c,j,‡}

^a Department of Urology, ERN eUROGEN Accredited Centre, Ghent University Hospital, Ghent, Belgium; ^b IBiTech-Biommeda, Department of Electronics and Information Systems, Faculty of Engineering and Architecture, Ghent University, Ghent, Belgium; ^c Department of Human Structure and Repair, Faculty of Medicine and Health Sciences, Ghent University, Ghent, Belgium; ^d ORSI Academy, Melle, Belgium; ^e Cancer Research Institute Ghent, Ghent University, Ghent, Belgium; ^f Department of Radiology and Nuclear Medicine, Ghent University Hospital, Ghent, Belgium; ^g Division of Urology, IRCCS Azienda Ospedaliero-Universitaria di Bologna, Bologna, Italy; ^h Department of Urology, Onze-Lieve-Vrouweziekenhuis Hospital, Aalst, Belgium; ⁱ Division of Oncology/Unit of Urology, URI, IRCCS Ospedale San Raffaele, Milan, Italy; ^j Department of Urology, AZ Maria Middelaers Hospital, Ghent, Belgium

Article info

Article history:
Accepted January 6, 2023

Associate Editor:
Alexandre Mottrie

Keywords:
Three-dimensional models
Indocyanine green
Partial nephrectomy
Perfusion zone algorithm
Renal cell carcinoma
Selective clamping

Abstract

Background: Selective clamping during robot-assisted partial nephrectomy (RAPN) requires extensive knowledge on patient-specific renal vasculature, obtained through imaging.

Objective: To validate an in-house developed perfusion zone algorithm that provides patient-specific three-dimensional (3D) renal perfusion information.

Design, setting, and participants: Between October 2020 and June 2022, 25 patients undergoing RAPN at Ghent University Hospital were included. Three-dimensional models, based on preoperative computed tomography (CT) scans, showed the clamped artery's ischemic zone, as calculated by the algorithm.

Surgical procedure: All patients underwent selective clamping during RAPN. Indocyanine green (ICG) was administered to visualize the true ischemic zone perioperatively. Surgery was recorded for a postoperative analysis.

Measurements: The true ischemic zone of the clamped artery was compared with the ischemic zone predicted by the algorithm through two metrics: (1) total ischemic zone overlap and (2) tumor ischemic zone overlap. Six urologists assessed metric 1; metric 2 was assessed objectively by the authors.

Results and limitations: In 92% of the cases, the algorithm was sufficiently accurate to plan a selective clamping strategy. Metric 1 showed an average score of 4.28 out of 5. Metric 2 showed an average score of 4.14 out of 5. A first limitation is that ICG can be evaluated only at the kidney surface. A second limitation is that mainly patients with

[†] These authors shared first authorship.

[‡] These authors shared last authorship.

* Corresponding author. Proefhoevestraat 12, 9090 Melle, Belgium. Tel. 0032 472 394 735.
E-mail address: pieter.de.backer@orsi.be (P. De Backer).





Case Series of the Month

Improving Augmented Reality Through Deep Learning: Real-time Instrument Delineation in Robotic Renal Surgery

Pieter De Backer^{a,b,c,d,e,*}, Charles Van Praet^{c,d}, Jente Simoens^a, Maria Peraire Lores^a, Heleen Creemers^c, Kenzo Mestdagh^c, Charlotte Allaey^{c,d}, Saar Vermijs^{b,c,e}, Pietro Piazza^{a,f}, Angelo Mottaran^{a,f}, Carlo A. Bravi^{a,g,h}, Marco Paciotti^{a,g,i}, Luca Sarchi^{a,g}, Rui Farinha^{a,g}, Stefano Puliatti^{a,j}, Francesco Cisternino^k, Federica Ferraguti^k, Charlotte Debbaut^{b,e}, Geert De Naeyer^g, Karel Decaestecker^{c,d,l,†}, Alexandre Mottrie^{a,g,†}

^aORSI Academy, Melle, Belgium; ^bIbitech-Biommeda, Department of Electronics and Information Systems, Faculty of Engineering and Architecture, Ghent University, Ghent, Belgium; ^cDepartment of Human Structure and Repair, Faculty of Medicine and Health Sciences, Ghent University, Ghent, Belgium; ^dDepartment of Urology, ERN eUROGEN accredited centre, Ghent University Hospital, Ghent, Belgium; ^eCancer Research Institute Ghent, Ghent University, Ghent, Belgium; ^fDivision of Urology, IRCCS Azienda Ospedaliero-Universitaria di Bologna, Bologna, Italy; ^gDepartment of Urology, Onze-Lieve-Vrouwziekenhuis Hospital, Aalst, Belgium; ^hDivision of Oncology/Unit of Urology, Urological Research Institute, IRCCS Ospedale San Raffaele, Milan, Italy; ⁱDepartment of Urology, Humanitas Clinical and Research Center, Rozzano, Milan, Italy; ^jDepartment of Urology, University of Modena and Reggio Emilia, Modena, Italy; ^kDepartment of Sciences and Methods for Engineering, University of Modena and Reggio Emilia, Modena, Italy; ^lDepartment of Urology, AZ Maria Middelaers Hospital, Ghent, Belgium

Article info

Article history:
Accepted February 13, 2023

Associate Editor:
Sarah P. Psutka

Keywords:
Three-dimensional models
Augmented reality
Instrument segmentation
Partial nephrectomy
Kidney transplantation
Robotic surgery
Renal cell carcinoma
Deep learning
Real time

Abstract

Several barriers prevent the integration and adoption of augmented reality (AR) in robotic renal surgery despite the increased availability of virtual three-dimensional (3D) models. Apart from correct model alignment and deformation, not all instruments are clearly visible in AR. Superimposition of a 3D model on top of the surgical stream, including the instruments, can result in a potentially hazardous surgical situation. We demonstrate real-time instrument detection during AR-guided robot-assisted partial nephrectomy and show the generalization of our algorithm to AR-guided robot-assisted kidney transplantation. We developed an algorithm using deep learning networks to detect all nonorganic items. This algorithm learned to extract this information for 65 927 manually labeled instruments on 15 100 frames. Our setup, which runs on a standalone laptop, was deployed in three different hospitals and used by four different surgeons. Instrument detection is a simple and feasible way to enhance the safety of AR-guided surgery. Future investigations should strive to optimize efficient video processing to minimize the 0.5-s delay

† Joint last authors.

* Corresponding author. ORSI Academy, Proefhoevestraat 12, 9090 Melle, Belgium. Tel. +32 472 394735.

E-mail address: pieter.de.backer@orsi.be (P. De Backer).



available at www.sciencedirect.comjournal homepage: www.eu-openscience.europeanurology.com

European Association of Urology

**Surgery in Motion: Open Science****Robot-assisted Partial Nephrectomy Using Intra-arterial Renal Hypothermia for Highly Complex Endophytic or Hilar Tumors: Case Series and Description of Surgical Technique**

Pieter De Backer^{a,b,c,*}, Joris Vangeneugden^a, Camille Berquin^a, Saar Vermijs^b, Peter Dekuyper^d, Alexandre Mottrie^{c,e}, Charlotte Debbaut^b, Thierry Quackels^f, Charles Van Praet^a, Karel Decaestecker^{a,d}

^a Department of Urology, ERN eUROGEN Accredited Centre, Ghent University Hospital, Ghent, Belgium; ^b IBiTech-Biommeda, Department of Electronics and Information Systems, Faculty of Engineering and Architecture, Ghent University, Ghent, Belgium; ^c ORSI Academy, Melle, Belgium; ^d Department of Urology, AZ Maria Middelaers Hospital, Ghent, Belgium; ^e Department of Urology, Onze-Lieve-Vrouwziekenhuis Hospital, Aalst, Belgium; ^f Department of Urology, Hôpital Erasme, Brussels, Belgium

Article info**Article history:**

Accepted October 16, 2023

Associate Editor:

M. Carmen Mir

Keywords:

Partial nephrectomy
Renal cell carcinoma
Intra-arterial cooling
Ischemia time
Three-dimensional models
Robot-assisted surgery

Abstract

Background: In partial nephrectomy for highly complex tumors with expected long ischemia time, renal hypothermia can be used to minimize ischemic parenchymal damage.

Objective: To describe our case series, surgical technique, and early outcomes for robot-assisted partial nephrectomy (RAPN) using intra-arterial cold perfusion through arteriotomy.

Design, setting, and participants: A retrospective analysis was conducted of ten patients with renal tumors (PADUA score 9–13) undergoing RAPN between March 2020 and March 2023 with intra-arterial cooling because of expected arterial clamping times longer than 25 min.

Surgical procedure: Multiport transperitoneal RAPN with full renal mobilization and arterial, venous, and ureteral clamping was performed. After arteriotomy and venotomy, 4°C heparinized saline is administered intravascular through a Fogarty catheter to maintain renal hypothermia while performing RAPN.

Measurements: Demographic data, renal function, console and ischemia times, surgical margin status, hospital stay, estimated blood loss, and complications were analyzed.

Results and limitations: The median warm and cold ischemia times were 4 min (interquartile range [IQR] 3–7 min) and 60 min (IQR 33–75 min), respectively. The median rewarming ischemia time was 10.5 min (IQR 6.5–23.75 min). The median pre- and postoperative estimated glomerular filtration rate values at least 1 mo after surgery were 90 ml/min (IQR 78.35–90 ml/min) and 86.9 ml/min (IQR

* Corresponding author. ORSI Academy, Proefhoevestraat 12, 9090 Melle, Belgium. Tel. +32 472 394 735.

E-mail address: pieter.de.backer@orsi.be (P. De Backer).




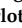

<https://doi.org/10.1016/j.euros.2023.10.004>

2666-1683/© 2023 The Authors. Published by Elsevier B.V. on behalf of European Association of Urology. This is an open access article under the CC BY-NC-ND license (<http://creativecommons.org/licenses/by-nc-nd/4.0/>).



Article

Surgical Phase Duration in Robot-Assisted Partial Nephrectomy: A Surgical Data Science Exploration for Clinical Relevance

Pieter De Backer^{1,2,3,4,5,*}, Maria Peraire Lores¹, Meret Demuyne³, Federico Piramide^{1,6}, Jente Simoens¹, Tim Oosterlinck⁷, Wouter Bogaert², Chi Victor Shan³, Karel Van Regemorter³, Aube Wastyn³, Enrico Checcucci^{4,6}, Charlotte Debbaut², Charles Van Praet^{3,5}, Rui Farinha¹, Ruben De Grootte⁸, Anthony Gallagher¹, Karel Decaestecker^{3,5,9} and Alexandre Mottrie^{1,8}

- ¹ ORSI Academy, 9090 Melle, Belgium
 - ² IbiTech-Biommeda, Department of Electronics and Information Systems, Faculty of Engineering and Architecture, Ghent University, 9000 Ghent, Belgium
 - ³ Department of Human Structure and Repair, Faculty of Medicine and Health Sciences, Ghent University, 9000 Ghent, Belgium; charles.vanpraet@uzgent.be (C.V.P.)
 - ⁴ Young Academic Urologist—Urotechnology Working Group, NL-6803 Arnhem, The Netherlands
 - ⁵ Department of Urology, ERN eUROGEN Accredited Centre, Ghent University Hospital, 9000 Ghent, Belgium
 - ⁶ Department of Surgery, Candiolo Cancer Institute, FPO-IRCCS, 10060 Turin, Italy
 - ⁷ Faculty of Medicine, KU Leuven, 3000 Leuven, Belgium
 - ⁸ Department of Urology, Onze-Lieve Vrouweziekenhuis Hospital, 9300 Aalst, Belgium
 - ⁹ Department of Urology, AZ Maria Middelaers Hospital, 9000 Ghent, Belgium
- * Correspondence: pieter.de.backer@orsi.be; Tel.: +32-933-469-26



Citation: De Backer, P.; Peraire Lores, M.; Demuyne, M.; Piramide, F.; Simoens, J.; Oosterlinck, T.; Bogaert, W.; Shan, C.V.; Van Regemorter, K.; Wastyn, A.; et al. Surgical Phase Duration in Robot-Assisted Partial Nephrectomy: A Surgical Data Science Exploration for Clinical Relevance. *Diagnostics* **2023**, *13*, 3386. <https://doi.org/10.3390/diagnostics13213386>

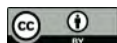
Academic Editor: Fabiano Bini

Received: 25 August 2023

Revised: 29 October 2023

Accepted: 3 November 2023

Published: 5 November 2023



Copyright: © 2023 by the authors. Licensee MDPI, Basel, Switzerland. This article is an open access article distributed under the terms and conditions of the Creative Commons Attribution (CC BY) license (<https://creativecommons.org/licenses/by/4.0/>).

Abstract: (1) Background: Surgical phases form the basic building blocks for surgical skill assessment, feedback, and teaching. The phase duration itself and its correlation with clinical parameters at diagnosis have not yet been investigated. Novel commercial platforms provide phase indications but have not been assessed for accuracy yet. (2) Methods: We assessed 100 robot-assisted partial nephrectomy videos for phase durations based on previously defined proficiency metrics. We developed an annotation framework and subsequently compared our annotations to an existing commercial solution (Touch Surgery, Medtronic™). We subsequently explored clinical correlations between phase durations and parameters derived from diagnosis and treatment. (3) Results: An objective and uniform phase assessment requires precise definitions derived from an iterative revision process. A comparison to a commercial solution shows large differences in definitions across phases. BMI and the duration of renal tumor identification are positively correlated, as are tumor complexity and both tumor excision and renorrhaphy duration. (4) Conclusions: The surgical phase duration can be correlated with certain clinical outcomes. Further research should investigate whether the retrieved correlations are also clinically meaningful. This requires an increase in dataset sizes and facilitation through intelligent computer vision algorithms. Commercial platforms can facilitate this dataset expansion and help unlock the full potential, provided that the phase annotation details are disclosed.

Keywords: phase duration assessment; partial nephrectomy; video analysis; surgical data science


1. Introduction

Surgical video recordings have become an indispensable tool in surgery, and their uses can be categorized into three main groups [1]:

1. **Surgical Education and Training:** Video recordings provide a valuable resource for trainees to observe and learn surgical procedures from experts [2,3]. By capturing critical moments during surgery, videos also allow for retrospective analysis and discussions among surgical teams and aid in complex decision making. Literature reports have documented the utility of surgical video review in assessing anatomical

LETTER

First-in-human real-time AI-assisted instrument deocclusion during augmented reality robotic surgery

Jasper Hofman^{1,#}  | Pieter De Backer^{1,2,3,4,#} | Ilaria Manghi⁵ | Jente Simoens¹ | Ruben De Groot^{1,6} | Hannes Van Den Bossche⁷ | Mathieu D'Hondt⁸ | Tim Oosterlinck⁹ | Julie Lippens² | Charles Van Praet⁴ | Federica Ferraguti⁵ | Charlotte Debbaut³ | Zhijun Li¹⁰ | Oliver Kutter¹⁰ | Alex Mottrie^{1,6,##} | Karel Decaestecker^{4,##}

¹ORSI Academy, Melle, Belgium²Faculty of Medicine and Health Sciences, Department of Human Structure and Repair, Ghent University, Ghent, Belgium³IBiTech-Biommeda, Faculty of Engineering and Architecture, and CRIG, Ghent University, Ghent, Belgium⁴Department of Urology, Ghent University Hospital, Ghent, Belgium⁵Department of Sciences and Methods for Engineering, University of Modena and Reggio Emilia, Modena, Italy⁶Department of Urology, OLV Hospital, Aalst, Belgium⁷Department of Urology, AZ West Hospital, Veurne, Belgium⁸Department of Digestive and Hepatobiliary/Pancreatic Surgery, AZ Groeninge Hospital, Kortrijk, Belgium⁹Faculty of Medicine, KU Leuven, Leuven, Belgium¹⁰NVIDIA, Santa Clara, California, USA**Correspondence**

Pieter De Backer, ORSI Academy, Proefhoevestraat 12, 9090 Melle, Belgium.
Email: Pieter.De.Backer@orsi.be

Shared first author

Shared senior author

Funding information

Ipsen NV, Grant/Award Number: A20/TT/1655; Ghent University, Grant/Award Numbers: BOFSTA201909015, A20/TT/0337; Flanders Innovation & Entrepreneurship, Grant/Award Number: HBC.2020.2252

Abstract

The integration of Augmented Reality (AR) into daily surgical practice is withheld by the correct registration of pre-operative data. This includes intelligent 3D model superposition whilst simultaneously handling real and virtual occlusions caused by the AR overlay. Occlusions can negatively impact surgical safety and as such deteriorate rather than improve surgical care. Robotic surgery is particularly suited to tackle these integration challenges in a stepwise approach as the robotic console allows for different inputs to be displayed in parallel to the surgeon. Nevertheless, real-time de-occlusion requires extensive computational resources which further complicates clinical integration. This work tackles the problem of instrument occlusion and presents, to the authors' best knowledge, the first-in-human on edge deployment of a real-time binary segmentation pipeline during three robot-assisted surgeries: partial nephrectomy, migrated endovascular stent removal, and liver metastasectomy. To this end, a state-of-the-art real-time segmentation and 3D model pipeline was implemented and presented to the surgeon during live surgery. The pipeline allows real-time binary segmentation of 37 non-organic surgical items, which are never occluded during AR. The application features real-time manual 3D model manipulation for correct soft tissue alignment. The proposed pipeline can contribute towards surgical safety, ergonomics, and acceptance of AR in minimally invasive surgery.

This is an open access article under the terms of the [Creative Commons Attribution-NonCommercial-NoDerivs](https://creativecommons.org/licenses/by-nc-nd/4.0/) License, which permits use and distribution in any medium, provided the original work is properly cited, the use is non-commercial and no modifications or adaptations are made.

© 2023 The Authors. *Healthcare Technology Letters* published by John Wiley & Sons Ltd on behalf of The Institution of Engineering and Technology.

Other Articles (First and Co-author)

8. Role of robotics as a key platform for digital advancements in surgery
P De Backer, F Nickel
British Journal of Surgery, Editorial 2023 (in Press)
9. Point-of-care 3D printing: a low-cost approach to teaching carotid artery stenting
P De Backer, C Allaey, C Debbaut, R Beelen
3D Printing in Medicine 2021
10. Artificial Intelligence in Surgical Training for Kidney Cancer: A Systematic Review of the Literature,
N Rodriguez Peñaranda, A Eissa, S Ferretti, G Bianchi, S Di Bari, R Farinha, P Piazza, E Checcucci, I Rivero Belenchón, A Veccia, J Gomez Rivas, M Taratkin, K-F Kowalewski, S Rodler, **P De Backer**, GE Cacciamani, R De Groot, AG Gallagher, A Mottrie, S Micali, S Puliatti,
Diagnostics (Basel, Switzerland) 13 (19) 2023
11. Robot-assisted Radical Prostatectomy Performed with Different Robotic Platforms: First Comparative Evidence Between Da Vinci and HUGO Robot-assisted Surgery Robots,
C A Bravi, E Balestrazzi, M De Loof, S Rebuffo, F Piramide, A Mottaran, M Paciotti, G Sorce, L Nocera, L Sarchi, M Peraire, C Colla'-Ruvolo, N Frego, A Piro, M Ticonosco, **P De Backer**, R Farinha, H Van Den Bossche, G De Naeyer, F D'Hondt, R De Groot, A Mottrie,
European Urology Focus, 2023
12. Robot-assisted sacropexy with the novel HUGO robot-assisted surgery system: initial experience and surgical setup at a tertiary referral robotic center
A Mottaran, C A Bravi, L Sarchi, M Paciotti, L Nocera, A Piro, P Piazza, **P De Backer**, R Farinha, R De Groot, G De Naeyer, A Mottrie
Journal of Endourology 37 (1), 35-41, 2023
13. Outcomes of robot-assisted radical prostatectomy with the Hugo RAS surgical system: initial experience at a high-volume robotic center
C A Bravi, M Paciotti, E Balestrazzi, A Piro, F Piramide, M Peraire, L Sarchi, A Mottaran, L Nocera, **P De Backer**, G De Naeyer, F D'Hondt, R De Groot, A Mottrie
Eur Urol Focus 2023 Jul;9(4):642-644, 2023
14. Robot-assisted adrenalectomy: Step-by-step technique and surgical outcomes at a high-volume robotic center
F Piramide, C A Bravi, M Paciotti, L Sarchi, L Nocera, A Piro, M Peraire Lores, E Balestrazzi, A Mottaran, R Farinha, H Nicolas, **P De Backer**, F D'hondt, P Schatteman, R De Groot, G De Naeyer, A Mottrie
Asian Journal of Urology, 2023
15. Nerve-sparing robot-assisted radical prostatectomy with the HUGO™ robot-assisted surgery system using the 'Aalst technique'
M Paciotti, C A Bravi, A Mottaran, L Nocera, L Sarchi, A Piro, R Farinha, M Peraire Lores, E Balestrazzi, F Piramide, E Roussel, **P De Backer**, F D'Hondt, G De Naeyer, R De Groot, A Mottrie
BJU international, 2023
16. Peritoneal tuberculosis caused by intravesical instillation with Bacillus Calmette-Guérin (BCG) following nephroureterectomy in a patient with bladder and upper tract urothelial

cancer: a case report

C Allaeyns, **P De Backer**, K Decaestecker, C Berquin, K Decaestecker, S Callens, C Van Praet
Acta Clinica Belgica 78 (3), 257-260, 2023

17. Robot-assisted simple prostatectomy with the novel HUGO™ RAS System: feasibility, setting, and perioperative outcomes.
A Mottaran, M Paciotti, C A Bravi, L Sarchi, L Nocera, A Piro, R Farinha, **P De Backer**, P Piazza, K Pauwaert, M van Herwaarden, R De Groote, A Mottrie, G De Naeyer
Minerva Urol Nephrol 2023;75:235-9.
18. Techniques and outcomes of robot-assisted partial nephrectomy for the treatment of multiple ipsilateral renal masses.
N M Buffi, A Uleri, M Paciotti, G Lughezzani, P Casale, P Diana, R De Groote, L Sarchi, A Mottaran, C Bravi, **P De Backer**, D Amparore, C Fiori, F Porpiglia, A Mottrie
Minerva Urol Nephrol. 2023 Apr;75(2):223-230.
19. Robot-assisted sutureless partial nephrectomy for the treatment of fifteen bilateral renal masses in a patient with Von Hippel-Lindau syndrome: a case report from a high-volume robotic center
M Peraire Lores, J Domínguez, C A Bravi, A Mottaran, L Sarchi, M Paciotti, A Piro, L Nocera, E Balestrazzi, R Farinha, K Pauwaert, M Van Herwaarden, M-H Vinckier, **P De Backer**, R De Groote, F D'Hondt, G De Naeyer, A Mottrie
CEN Case Reports, 2023 Aug;12(3):335-340
20. Different approaches for bladder neck dissection during robot-assisted radical prostatectomy: the Aalst technique
C A Bravi, A Mottaran, L Sarchi, A Piro, M Paciotti, L Nocera, E Balestrazzi, M Peraire, R Farinha, K Pauwaert, M Van Herwaarden, M-H Vinckier, **P De Backer**, F D'Hondt, R De Groote, G De Naeyer, A Mottrie
Int Braz J Urol. 2023 Jul-Aug;49(4):521-522.
21. Re: Robot-assisted Radical Prostatectomy With the Novel Hugo Robotic System: Initial Experience and Optimal Surgical Set-up at a Tertiary Referral Robotic Center
CA Bravi, M Paciotti, L Sarchi, A Mottaran, L Nocera, R Farinha, **P De Backer**, M-H Vinckier, G De Naeyer, F D'Hondt, R De Groote, A Mottrie
JOURNAL OF UROLOGY 209 (1), 279-279
22. Robot-assisted radical prostatectomy with the novel Hugo robotic system: initial experience and optimal surgical set-up at a tertiary referral robotic center
C A. Bravi, M Paciotti, L Sarchi, A Mottaran, L Nocera, R Farinha, **P De Backer**, M-H Vinckier, G De Naeyer, F D'Hondt, R De Groote, A Mottrie
European Urology 82 (2), 233-237
23. Feasibility and optimal setting of robot-assisted partial nephrectomy with the novel "HUGO" robotic system: a pre-clinical study
CA Bravi, L Sarchi, A Mottaran, M Paciotti, R Farinha, P Piazza, **P De Backer**, S Puliatti, R. De Groote, G De Naeyer, A Gallagher, A Breda, A Mottrie
May 2022, Urology Video Journal 15:100164,
24. Assessing pentafecta achievement after robot-assisted radical cystectomy and its association with surgical experience: results from a high-volume institution
P Piazza, C A Bravi, S Puliatti, G E Cacciamani, S Knipper, M Amato, P Dell'Oglio, E Mazzone, G Rosiello, R Farinha, L Sarchi, S Scarcella, P Wisz, R Schiavina,

D Develtere, **P De Backer**, R De Groote, F D'Hondt, A Mottrie
Urol Oncol. 2022 Jun;40(6):272.e11-272.e20.

25. Will renorrhaphy become obsolete? Evaluation of a new hemostatic sealant
R Farinha, R De Groote, P Zondervan, M Paciotti, E Roozen, S Head, L Sarchi,
C A Bravi, A Mottaran, S Puliatti, **P De Backer**, G De Naeyer, A Mottrie
J Endourol. 2023 Jan;37(1):105-111.
26. Kinematic boundary conditions substantially impact in silico ventricular function
M Peirlinck, K L Sack, **P De Backer**, P Morais, P Segers, T Franz, M De Beule
International Journal for Numerical Methods in Biomedical Engineering 35 (1) e3151
27. Curved Guest-Host LCD used as a dynamic artificial iris
H De Smet, J De Smet, **P De Backer**, P Joshi, E Islamaj, X Shang, D Cuypers
SID-ME Chapter Spring Meeting 2014, 22-22
28. Paper No P17: A Spherically Shaped Display for Use as an Artificial Iris
J De Smet, **P De Backer**, E Islamaj, P Joshi, D Cuypers, H De Smet
SID Symposium Digest of Technical Papers 44, 61-64

First Author Abstracts

29. Automated intra-operative video analysis in robot-assisted partial nephrectomy: Paving the road for Surgical Automation
P De Backer, M Peraire Lores, J Simoens, M Mezzina, J Hofman, T Oosterlinck,
M Demuyne, C Debbaut, C Collà Ruvolo, F Piramide, H Van Den Bossche,
R De Groote, C Van Praet, K Decaestecker, A Mottrie
ERUS 2023 Firenze
30. Deep learning video anonymization: Breaking GDPR boundaries in robotic urology
P De Backer, J. Simoens, K. Mestdagh, C.A. Bravi, L Sarchi, A Mottaran, M Paciotti,
R Farinha, M Peraire, S Puliatti, A Piro, R. De Groote, C Van Praet, K. Decaestecker,
A Mottrie
ERUS 2022 Barcelona - European Urology Open Science 44:S404
31. Augmented reality instrument detection: Enabling 3D model-instrument interaction through deep learning
P De Backer, J. Simoens, H. Creemers, S. Vermijs, R. Matthys, C.A. Bravi, L Sarchi,
P Piazza, M Paciotti, R Farinha, C Debbaut, L Desender, C Van Praet, A Mottrie,
K. Decaestecker
ERUS 2022 Barcelona - European Urology Open Science 44:S406
32. Deep learning in robot-assisted partial nephrectomy: Advent of realistic augmented reality
P De Backer, C Allaey, H Creemers, A Hallemeesch, K Mestdagh, F Cisternino,
F Ferraguti, S Vermijs, R Janssens, C Van Praet, J Dambre, C Debbaut, K Decaestecker,
A Mottrie
EAU 2022 Amsterdam - EUROPEAN UROLOGY 81
33. Predicting selective arterial clamping strategy in robot assisted partial nephrectomy using 3d simulations
P De Backer, S Vermijs, C Van Praet, R Matthys, R Ciani, P De Visschere, A Mottrie,

C Debbaut, K Decaestecker
EAU 2022 Amsterdam - EUROPEAN UROLOGY 81

34. Robot-assisted partial nephrectomy using intra-arterial renal hypothermia for highly complex endophytic or hilar tumors
P De Backer, J Vangeneugden, C Van Praet, M Lejoly, S Vermijs, C Vanpeteghem, K Decaestecker
AUA 2022 New Orléans V04-12 - The Journal of Urology 206 (Supplement 3), e295-e295
35. 3D Selective arterial clamping in robot assisted partial nephrectomy
P De Backer, S Vermijs, C Van Praet, S Vandebulcke, M Lejoly, S Vanderschelden, P De Visschere, A Mottrie, C Debbaut, K Decaestecker
AUA2022 New Orléans V04-07 - The Journal of Urology 206 (Supplement 3), e293-e293
36. Peri-operatieve planning in Partiële Nefrectomie met behulp van Artificiële Intelligentie
P De Backer, et al. BVU Elautprijs 2022 AZ Maria Middelaes Gent
37. Reliable Anonymization of Robotic Surgical Video Data using Deep Learning
P De Backer, et al. Amazing Technology Session - European Association of Endoscopic Surgery 2022 – Kraków
38. Step-by-step Guide to spatial Annotation of Robotic Tools – Stumbling Stones and valuable Insights from two European Expert Centers
P De Backer, et al. Gerhard Buess Technology – European Association of Endoscopic Surgery 2022 – Kraków
39. Automated Anonymization of Robotic Surgical Video Data using Deep Learning
P De Backer, et al. CLINICAI – Clinical Day at MICCAI 2022 – Singapore
40. Augmented Reality Instrument Detection: Realtime 3D model interaction in Robotic Liver Surgery through Deep Learning
P De Backer, et al. How new technology can improve your surgical outcome - European Association of Endoscopic Surgery 2023, Rome
41. Automated Robotic Surgical Video Anonymization: Enabling Privacy Proof Video Sharing through Deep Learning
P De Backer, et al. Useful techniques for your future OR - European Association of Endoscopic Surgery 2023, Rome
42. Improving Augmented Reality Surgery through first-in-human real time AI-powered instrument segmentation
P De Backer, et al. CLINICAI – Clinical Day at MICCAI 2023 – Vancouver
43. Intra-operatieve A.I. ondersteuning tijdens partiële nefrectomie: automatische weefselinterpretatie en fase-analyse als mijlpalen richting autonome navigatie
P De Backer, et al. BVU Elautprijs 2023, Elisabeth center, Antwerpen

Co-Authored Abstracts

44. Robot-assisted simple prostatectomy versus holmium laser enucleation for the treatment of benign prostatic hyperplasia in large (>100 ml) prostates: updated comparative analysis from a high-volume center
A Mottaran, E Balestrazzi, CA Bravi, L Nocera, M Paciotti, A Piro, MP Lores, L Sarchi, F Piramide, **P De Backer**, R De Groote, G De Naeyer, P Schatteman, A Mottrie.
The Journal of Urology 209 (Supplement 4), e178, 2023
45. The impact of 3D models on surgical outcomes of RAPN: is CT scan becoming obsolete?
L Nocera, C Bravi, A Mottaran, A Piro, L Sarchi, M Paciotti, MP Lores, E Balestrazzi, F Piramide, R Farinha, **P De Backer**, R De Groote, A Mottrie
The Journal of Urology 209 (Supplement 4), e798, 2023
46. Robot-assisted radical prostatectomy in large (≥ 100 gr) prostate glands: Results from an high-volume robotic center
CA Bravi, A Mottaran, L Sarchi, A Piro, M Pacciotti, L Nocera, M Peraire Lores, R Farinha, **P De Backer**, F D'Hondt, R De Groote, G De Naeyer, A Mottrie
European Urology Open Science 44, S306
47. Robot-assisted radical prostatectomy with HUGO RAS robotic platform: First case series from an European high-volume robotic center
CA Bravi, M Paciotti, A Mottaran, A Piro, L Sarchi, L Nocera, R Farinha, M Peraire Lores, **P De Backer**, F D'Hondt, R De Groote, G De Naeyer, A Mottrie
European Urology Open Science 44, S409
48. Robot-assisted radical prostatectomy with HUGO RAS robotic platform: Step-by-step description of the technique according to validated performance metrics
CA Bravi, A Mottaran, L Sarchi, M Paciotti, L Nocera, A Piro, M Peraire Lores, **P De Backer**, R Farinha, R De Groote, G De Naeyer, A Mottrie
European Urology Open Science 44, S407
49. Feasibility and optimal setting of robot-assisted simple prostatectomy with the novel HUGO RAS System
A Piro, A Mottaran, M Paciotti, L Sarchi, C Bravi, L Nocera, M Peraire Lores, **P De Backer**, G De Naeyer, R De Groote, A Mottrie
European Urology Open Science 44, S276
50. Preoperative planning of partial nephrectomy procedures based on kidney perfusion zones
S Vermijs, **P De Backer**, P De Visschere, C Van Praet, K Decaestecker, C Debbaut
WCB 2022, 9th World Congress of Biomechanics, Abstract book
51. Pushing boundaries in extracorporeal Robot-Assisted Kidney Autotransplantation (eRAKAT): bench surgery for an oncologic partial nephrectomy in a patient with a solitary kidney
I Verbakel, M Wirtz, **P De Backer**, B Van Parys, L Desender, C Van Praet, K Decaestecker
A joint meeting of the EAU Section for Urotechnology and the EAU Section of Urolithiasis
52. Development of an interactive, patient-specific planning tool for partial nephrectomy procedures

S Vermijs, **P De Backer**, R Matthys, R Ciani, C Van Praet, K Decaestecker, C Debbaut
OncoDot. 3 symposium 2021

53. External validation of radical cystectomy pentafecta, achievement assessment and its association with surgical experience

P Piazza, CA Bravi, S Puliatti, GE Cacciamani, S Knipper, M Amato, P Dell'Oglio, E Mazzone, G Rosiello, A Mottaran, L Sarchi, M Paciotti, R Farinha, S Scarcella, P Wisz, R Schiavina, E Brunocilla, L Bianchi, D Develtere, C Sinatti, C Berquin, R De Groote, **P De Backer**, F D'Hondt, A Mottrie
European Urology Open Science 33, S69-S70

54. Ex-vivo renal vascular dominant region mapping using artery-selective contrast injections

N Sennesael, **P De Backer**, K Decaestecker, P De Visschere, M Speeckaert, S Vermijs, G Villeirs, C Debbaut, P Pullens
ISMIRM & SMRT Annual Meeting & Exhibition

Posters

55. Automated Surgical Phase Recognition in Robot-Assisted Radical Prostatectomy (RARP): Feasibility exploration
H Creemers, ML Peraire, J Simoens, M Mezzina, F Piramide, N Frego, C Debbaut, K Decaestecker, A Mottrie, **P De Backer**
ERUS 2023 Firenze
56. Phase Assessment in Robot-Assisted Radical Prostatectomy (RARP) : Exploratory analysis of feasibility and clinical relevance
H Creemers, ML Peraire, J Simoens, C Debbaut, A Piro, S Rebuffo, K Decaestecker, A Mottrie, **P De Backer**
ERUS 2023 Firenze
57. A preoperative planning tool for lung segmentectomy procedures: a case study
S Vermijs, B Cornette, **P De Backer**, K Decaestecker, L Desender, C Debbaut
The European Association of Endoscopic Surgery (EAES 2022)
58. Development of a planning tool for robot-assisted partial nephrectomy surgery based on 3D reconstructions of kidneys
S Vandembulcke, **P De Backer**, D Babin, P Segers, K Decaestecker, C Debbaut
18th National Day on Biomedical Engineering: Artificial Intelligence in Medicine
59. Virtual clamping tool for RAPN
P De Backer, S Vandembulcke, M Lejoly, S Vanderschelden, C Van Praet, D Babin, C Debbaut, K Decaestecker
Annual Congress of the Belgian Association of Urology, BAU Congress 2019
60. Augmented Reality Partial Nephrectomy: Pushing Boundaries through Instrument Detection
P De Backer, J Simoens, S Vermijs, G Michiels, J Callebaut, J Lippens, T Oosterlinck, C Berquin, C Debbaut, C Van Praet, A Mottrie, K Decaestecker
Annual Congress of the Belgian Association of Urology, BAU Congress 2022

Book Chapters

61. Pushing the Boundaries in Robot—Assisted Partial Nephrectomy for Renal Cancer
C Van Praet, **P De Backer**, R Campi, P Piazza, A Pecoraro, A Mottrie, A Minervini,
K Decaestecker
Robotic Surgery for Renal Cancer, 43-62
62. Renal Anatomy, Physiology, and Its Clinical Relevance to Renal Surgery
R De Groote, C Sundaram and **P De Backer**
(2022) Robotic Urologic Surgery. p.407-420
63. Technical Advances in Robotic Renal Surgery
S Puliatti, CA Bravi, **P De Backer**, E Canda
(2022) Robotic Urologic Surgery. p 593-603
64. Current Imaging Modalities and Virtual Models for Kidney Tumors
F Porpiglia, C Rogers, **P De Backer** and F Piramide
(2022) Robotic urologic surgery. p.427-439
65. AI and XR in Robotics
P De Backer, R Matthys, N Rashidian
(2023) Textbook of Robotic Liver Surgery (in press)

"Gutta cavat lapidem non vi, sed saepe cadendo"
- Choirilos of Samos

